Porosity and dynamics in crystalline materials of transition metal complexes based on dipodal N-donor ligands and related solid-state phenomena

Author: Simran Chaudhary

Supervisor: dr hab. Liliana Dobrzańska, prof. UMK
Co-Supervisor: dr hab. Zbigniew Rafiński, prof. UMK

A dissertation submitted in partial fulfillment of the requirements for the degree of Doctor of Philosophy

Faculty of Chemistry
Doctoral School of Exact and Natural Sciences
Nicolaus Copernicus University in Toruń

Toruń, December 2025

Dedicated to my grandparents
(Amma and Babaji)

....while it's tempting to play it safe, the more we're willing to risk, the more alive we are. In the end, what we regret most are the chances we never took.

Christopher Lloyd & Joe Keenan ("Frasier")

The research conducted in the doctoral dissertation was funded by the National Science Centre Poland; project:
Sonata Bis 2014/14/E/ST5/00611

Acknowledgments

"Alone, we can do so little; together, we can do so much." – Helen Keller

The journey of a research scholar weaves through a tapestry of triumphs and tribulations, positives and pitfalls. Just like it takes a village to raise a child, it takes a village to get a PhD candidate to the point of thesis submission. This section is a heartfelt tribute to those remarkable individuals who have profoundly shaped my professional and personal growth throughout my PhD journey.

I am greatly indebted to my supervisor, dr hab. Liliana Dobrzańska, prof. UMK for providing me with this opportunity to pursue my doctoral studies under her guidance and introducing me to the exciting world of crystallography. Her support, guidance, and encouragement throughout my research journey have been invaluable and always pushed me to learn and grow immensely. Furthermore, I would like to express my profound gratitude to my co-supervisor, dr hab. Zbigniew Rafiński, prof. UMK whose guidance introduced me to the domain of organic synthesis. His invaluable expertise played a pivotal role in overcoming challenges encountered during the synthesis of ligands, ensuring the successful resolution of each issue. I am also grateful to our collaborator, dr hab. Marek Wiśniewski, prof. UMK for carrying out the sorption studies and all the discussions about those results that broadened my horizons further into material sciences.

Lab mates play a vital role in making life easy through the bumpy ride of a Ph.D. journey. I express gratitude to Krzysztof, Karina, and Iza for their constant support in addressing organic synthesis queries, engaging in productive discussions, and assisting me with various non-lab aspects as an international student in Poland. Their presence has consistently made my lab experience enjoyable. I would also like to acknowledge Renny and Paul for their consistent support, engaging discussions, and great conference trips together. These conversations have often provided valuable insights into the topics we have explored, fostering mutual learning and contributing to our collective knowledge.

I would also like to acknowledge the technical staff of our faculty for carrying out the NMR, PXRD, and thermal analysis. In particular, I am grateful to Mrs. Aleksandra Cyganiuk for her close collaboration and efforts in coordinating schedules for the PXRD studies.

It was not easy being an international student, but having incredible friends by my side here made all the difference. I want to express my heartfelt gratitude to Anuradha, Tilak, Drashti, and Thiliban for being my family from day one and never letting me feel homesick. To Ganesh, Ecem, Jola, Seiji, Tom, and Sylwia, thank you for all the amazing memories in Toruń. Special thanks to Abinash for organizing PhD getaway trips, and to my Warsaw friends, Rajeev and Suhani, for always providing a warm roof over my head and making every visit to Warsaw enjoyable and memorable. To Asia, a sister I never knew I needed, thank you for your unwavering support throughout this journey. Life in Toruń was easier because of you. To my best friend, Ayush, thank you for constantly checking in on my progress, offering valuable ideas, and making Toruń feel like home. Your encouragement and insights, even as an astrophysicist from a completely different field, embody the true spirit of science, where boundaries are nonexistent. Thanks to you all for simply being there, your encouragement during tough times, celebration during victories, and presence throughout this journey have been invaluable. I would also like to express my appreciation to Ola and Ola for being my first friends in Poland. Your kindness and guidance helped me navigate the department and the city of Toruń with ease, and your readiness to assist will always be remembered.

I am thankful to my best friends, Priyanshi back in India and Avleen in the USA for always listening to my academic as well as personal blasphemies and providing solace and unwavering support throughout this challenging journey. Most importantly, I want to appreciate myself for not giving up and keeping my spirit up regardless of the circumstances. Thanks to these four years of Ph.D. for preparing me to handle hardships, failures, disappointments, stress, and everything else that comes my way.

Last, but not least, I am extremely grateful to my family, for their love, encouragement, sacrifice, trust, and support throughout this journey. Despite my parents, Mrs. Sangeeta and Mr. Pawan Kumar, having limited knowledge of chemistry and research, they wholeheartedly supported my decision to pursue a doctorate in a foreign country. Their unwavering belief in me speaks volumes, and I am immensely grateful for their trust and encouragement. If it weren't for them, I wouldn't be who I am today. My brothers, Aniket and Harshit are my pillars of strength and I am thankful to them for taking good care of me during my PhD journey as well as taking care of my parents back home while I was away

all this time. Their love and support have been instrumental in reaching this milestone, and I am fortunate to have them by my side where I can share everything.

I had been brought up mostly by my beloved grandfather, Late Mr. Dhoomsingh, and grandmother, Late Mrs. Dayawati. During my PhD journey, the sudden demise of my grandparents within 1.5 years apart marked the lowest point for me. It breaks my heart that they're not here to witness my success but I am confident that they are watching me from heaven and would find great joy in witnessing my academic achievements. They are no longer with me, but their love, values, enduring resilience and optimism continues to inspire me everyday and will do so forever. This thesis is dedicated to them.

Abstract

Porous materials capable of adsorbing molecules have received considerable attention in recent decades due to their potential in applications like pollutant removal, gas storage, and chemical separation. Coordination bonds, known for their directionality and versatility, provide a solid foundation for creating crystalline frameworks with diverse microporous structures. While metal-organic frameworks (MOFs) have been extensively explored in the past decade, these materials often encounter challenges related to stability and scalability. Consequently, there is an increasing demand for alternative porous materials. Notably, systematic investigations into the porosity of materials based on 0D metallocycles are still limited. These materials, with their confined cavities, have the potential to selectively differentiate guest molecules based on properties such as size and electrostatic interactions, making them promising candidates for applications in sensing and separation. This thesis aimed to investigate alternative microporous crystalline materials, focusing on discrete metallocycles synthesized with semi-rigid and flexible dipodal imidazole-based ligands. During synthesizing these metallocycles, potentially porous 1D coordination polymers (CPs) were also obtained and studied. The work started with the synthesis of a series of bipodal ligands, varying in aromatic core length, rigidity, and substitution patterns, which were further utilized to construct discrete metallocycles in combination with various transition metal salts. Moreover, the solid-state studies were also performed on these ligands, revealing among others their conformational flexibility that enhances their suitability for constructing dynamic crystalline coordination compounds. Some of the isolated coordination compounds displayed remarkable solid-state transformations, triggered via external stimuli such as heat or vacuum. For instance, metallocycle **MC2**, $[Co_2(\mathbf{L3})_2Cl_4]\cdot 0.8CH_3CN$ containing ligand 2,6-bis((2-methylimidazol-1-yl)methyl)naphthalene **(L3)**, **MC8** $[Cd_2(\mathbf{L7})_2Cl_4]\cdot 2MeOH$ constructed with 4,4′-bis((2-methyl-imidazol-1-yl)methyl)-1,1′-biphenyl **(L7)**, **MC10** $[Zn_2(\mathbf{L9})_2Cl_4]\cdot xS$ containing 4,4′-bis((1H-benzimidazol-1-yl)methyl)-1,1′-biphenyl **(L9)**, and 1D coordination polymers, **CP2**, $\{[Cu(\mathbf{L3})Cl_2]\cdot CH_3CN\}_n$ and **CP3**, $\{[Cd(\mathbf{L3})Cl_2]\cdot CH_3CN\cdot 0.2H_2O\}_n$ synthesized using ligand 2,6-bis((2-methylimidazol-1-yl)methyl)naphthalene **(L3)**, underwent structural transformations to form phases with distinct ligand conformations. These transformations were analyzed using thermogravimetric analysis, single-crystal and powder X-ray diffraction techniques, providing valuable insights into their dynamic behavior. Additionally, sorption studies revealed selective gas uptake properties, CO_2 in

the case of **MC2** and H_2 in the case of **CP2** and **CP3**, highlighting potential of these materials for applications such as hydrogen storage and molecular sieving. Concluding, the results obtained demonstrate the potential of cyclic coordination compounds and low-dimensional (1D) coordination polymers with respect to their sorption properties; nevertheless, further systematic investigations are necessary for their optimization.

Publications

1. **S. Chaudhary**, M. Wiśniewski, A. Hoser, R. Maria Losus, Z. Rafiński, L. Dobrzańska, Reversible phase transformations upon water uptake/removal in crystalline material of a bipodal *N*-donor ligand and evaluation of the stability of the hydrates formed, *CrystEngComm*, **2025**, 27, 3891-3898. (+cover)
2. **S. Chaudhary**, R.M. Losus, L. Dobrzańska, Polymorphism and the phenomenon of whole-molecule disorder revealed in a novel dipodal thiopyridine ligand, *Crystals*, **2025**, 15, 289. (Invited by **Prof. Dr. Edward R.T. Tiekink**)
3. **S. Chaudhary**, D. Kędziera, Z. Rafiński, L. Dobrzańska, Solvent-induced polymorphism in dipodal N-donor ligands containing a biphenyl core, *RSC Adv*, **2023**, 13, 30625-30632.
4. **S. Chaudhary**, D. Kędziera, L. Dobrzańska, Structural diversity of Ag(I) complexes with the flexible ligand 1,3-bis[(imidazol-2-yl)thiomethyl]benzene, *Polyhedron*, **2022**, 224, 115989.
5. R.M. Losus, **S. Chaudhary**, L. Dobrzańska, Solvation, hydration, and counterion effect on the formation of Ag(I) complexes with the dipodal ligand 2,6-bis[(imidazol-2-yl)thiomethyl]naphthalene, *Crystals*, **2024**, 14, 248.
6. P. Le. Garff, R.M. Losus, **S. Chaudhary**, L. Dobrzańska, Tailoring the dimensionality of metal complexes via ligand modifications, *Acta Cryst*, **2024**, B80, 19-26.

Conferences

International:

1. 34th European Crystallographic Meetings (ECM34), Padova, Italy, 26-30 August 2024 (Received **Bursary** supported by **IUCR** to attend this conference)

Oral Presentation: *Isostructurality, supramolecular isomerism, and single-crystal to single-crystal transformations in a family of metal complexes with a new bipodal ligand*
Authors: Simran Chaudhary, Renny Louis Anto Maria Losus, Zbigniew Rafiński, Liliana Dobrzańska

2. 8th European Crystallography School (ECS8), HZB, Berlin, Germany, 18-24 June 2023

Poster Presentation: *Polymorphism of the flexible molecule 1,4-bis(thiopyridine)benzene*
Authors: Simran Chaudhary, Zbigniew Rafiński, Liliana Dobrzańska

3. 33rd European Crystallographic Meetings (ECM33), Versailles, France, 23-27 August 2022

Poster Presentation: *Polymorphism in a series of dipodal N-donor ligands containing a biphenyl core*
Authors: Simran Chaudhary, Dariusz Kędziera, Zbigniew Rafiński, Liliana Dobrzańska

National:

1. XVII Copernican Doctoral Seminar (KSD), Nicolaus Copernicus University, Toruń, Poland, 6-7 June 2024

Oral Presentation: *Solute concentration, solvent, temperature, and time as factors controlling the polymorphic outcome*
Authors: Simran Chaudhary, Dariusz Kędziera, Zbigniew Rafiński, Liliana Dobrzańska

2. 65th Scientific Congress of the Polish Chemical Society (PTChem), Toruń, Poland, 18-22 September 2023

Oral Presentation: *Tailoring the dimensionality of metal complexes via ligand modifications* ***(Received outstanding oral presentation award for this talk)***
Authors: Simran Chaudhary, Paul Le Garff, Renny Louis Anto Maria Losus, Liliana Dobrzańska

3. 8th Young Scientist Symposium (SMN), University of Warsaw, Poland, 20-22 September 2022

Oral Presentation: *Conformational polymorphism of 1,4-bis(thiopyridine)benzene*
Authors: Simran Chaudhary, Zbigniew Rafiński, Liliana Dobrzańska

4. XV Copernican Doctoral Seminar (KSD), Nicolaus Copernicus University, Toruń, Poland, 20-22 June 2022

Oral Presentation: *The effect of ligand modifications on the final products of metal complexation reactions*
Authors: Simran Chaudhary, Zbigniew Rafiński, Liliana Dobrzańska

5. 63rd Scientific Congress of the Polish Chemical Society (PTChem), Toruń, Poland, 18-22 September 2021

Poster Presentation: *Polymorphic behavior of 4,4'-bis(pyridin-4-ylmethyl)-1,1'-biphenyl*
Authors: Simran Chaudhary, Dariusz Kędziera, Zbigniew Rafiński, Liliana Dobrzańska

6. XIV Copernican Doctoral Seminar (KSD), Nicolaus Copernicus University, Toruń, Poland, 20-22 September 2021

Oral Presentation: *Imidazole and pyridine-derived organic ligands for metal complexation*
Authors: Simran Chaudhary, Zbigniew Rafiński, Liliana Dobrzańska

Research Internship

1. Carried out a one-month internship at Vellore Institute of Technology (VIT), Vellore, Tamil Nadu, India from 30-10-23 to 27-11-23 under the supervision of Prof. S. Kalainathan, funded by “Excellence Initiative - Research University" (IDUB) program, UMK, to study the nonlinear optical activity of polymeric Ag(I) complexes.

Fundings

1. Mobility grant recipient for participation in conferences in France **(ECM33, 2022)** and Germany **(ECS8, 2023)** from Doctoral School of Exact and Natural Sciences (AST), Nicolaus Copernicus University.

2. Annual young scientist grant recipient– Faculty of chemistry, Nicolaus Copernicus University (2021 & 2022).

3. Involvement into the realisation of the project: 'Application of quantum chemistry computational methods in crystal engineering' funded by the Center of Excellence 'Astrophysics and Astrochemistry' (UMK), PLN 40,000, (May 1, 2021-December 31, 2022).

4. Member of the Crystal Engineering and Advanced Solid-State Characterisation research group, funded through IDUB (2023-2025).

List of Abbreviations

0D	Zero Dimensional
1D	One Dimensional
2D	Two Dimensional
3D	Three Dimensional
MC	Metallocycle
CP	Coordination Polymer
MOF	Metal-Organic Framework
DCC	Discrete Coordination Compounds
COF	Covalent-Organic Framework
SBU	Secondary Building Unit
CIF	Crystallographic Information File
CSD	Cambridge Structural Database
EtOAc	Ethyl Acetate
DCM	Dichloromethane
DMF	N, N-Dimethylformamide
DME	Dimethoxyethane
EtOH	Ethanol
MeOH	Methanol
CH_3CN	Acetonitrile
$CHCl_3$	Chloroform
THF	Tetrahydrofuran
DMSO	Dimethylsulfoxide
TLC	Thin-Layer Liquid Chromatography
UV	Ultraviolet
TGA	Thermogravimetric Analysis
DTA	Differential Thermal Analysis
NMR	Nuclear Magnetic Resonance
MHz	Megahertz
FT-IR	Fourier-Transform Infrared Spectroscopy
PXRD	Powder X-ray Diffraction
SC-XRD	Single-Crystal X-ray Diffraction
RB flask	Round Bottom Flask
KOH	Potassium Carbonate
$MgSO_4$	Magnesium Sulfate
IUPAC	International Union of Pure and Applied Chemistry
IUCr	International Union of Crystallography
SC-SC	Single-Crystal to Single-Crystal
SE	Slow Evaporation
SL	Solvent Layering

Atomic color symbols

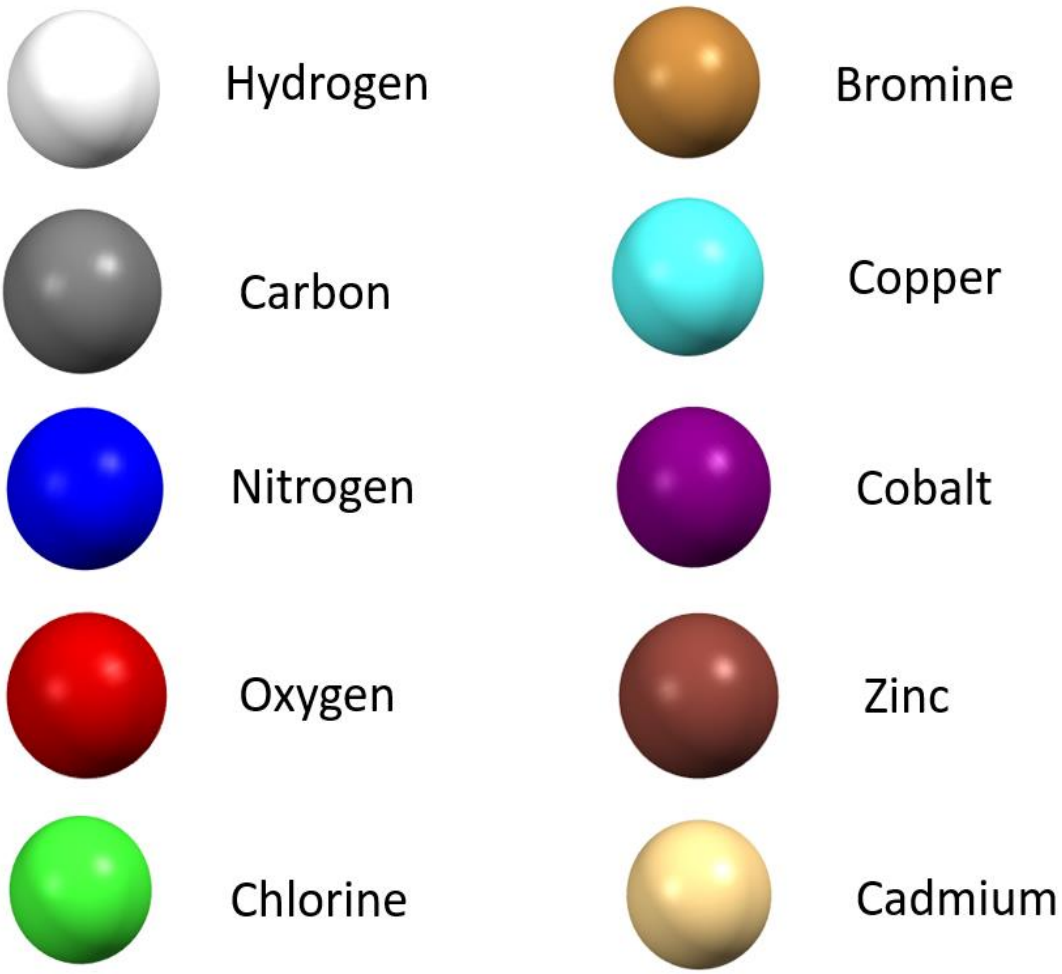

Table of Contents

Thesis Motivation and Aim

"To strive, to seek, to find, and not to yield"- Alfred, Lord Tennyson

In recent decades, one of the key trends in material science has been the development of materials capable of trapping molecules through adsorption. A particular focus has been put on developing highly crystalline, chemically stable materials with extensive surface areas and well-defined, modifiable pores. Metal-organic frameworks (MOFs) and covalent organic frameworks (COFs) have gained significant attention for their potential in applications such as pollutant removal, fuel storage, water harvesting in arid regions, and separating specialized chemicals like pharmaceuticals. MOFs are composed of organic molecules connected by metal ion nodes, whereas COFs are entirely organic in structure. Despite their promise, MOFs face challenges, including instability under operational conditions. Conversely, COFs often suffer from poor crystallinity and a restricted range of structural designs. These limitations highlight the need for alternative porous materials that meet the requirements for efficient chemical separation and storage. Additionally, porous materials, such as MOFs with large voids and/or internal surface areas are highly desirable for applications where guest storage capacity is crucial. In contrast, discrete coordination compounds, with their confined cavities, hold the potential to selectively distinguish between guest molecules based on factors such as size and electrostatic interactions. This makes them highly promising for sensing and separation applications.

The aims of this project were as follows: **1)** synthesis of dipodal imidazole based ligands and their further characterisation in the solid state (Figure 1) **2)** synthesis and crystallization of discrete 0D metallocycles utilizing imidazole-based ligands of different aromatic core length and rigidity, as well as substituents on imidazole moieties with application of a variety of 3d transition metal salts **3)** systematic investigation of the factors that influence the formation of particular supramolecular architectures (e.g. the effects of altering solvent, counterions etc.) **4)** dynamics and sorption studies on the selected crystalline material **5)** studying how modification of the ligands relates to their sorption properties.

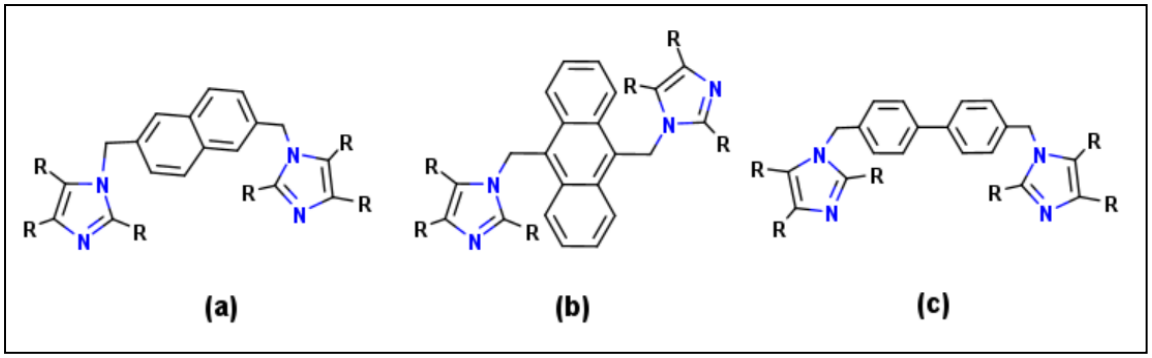

Figure 1: *Schematic representation of imidazole-based ligands containing rigid (a and b) and flexible cores (c) studied as part of the preparation of the PhD dissertation.*

Section 1
Introduction

"The beginning is the most important part of the work." – Plato, The Republic

This doctoral dissertation focuses on the synthesis, characterization, studies of dynamics and porosity of crystalline materials. The thesis as a whole deals with a range of aspects of Crystal Engineering, thus this section lays a foundation for readers to fully grasp and value the findings presented in the subsequent chapters. Additionally, it includes a concise summary of significant historical milestones in the research areas in focus, enhancing the context and depth of understanding.

1. Crystal Engineering

Designing crystalline solids with specific physical and chemical properties is a central focus in modern chemical research, and this area of study is generally referred to as Crystal Engineering. The term 'crystal engineering' was first introduced by the physicist Pepinsky at the meeting of the American Physical Society in August 1955 in an abstract entitled Crystal Engineering: A New Concept in Crystallography [1]. However, it is commonly accepted that the term 'crystal engineering' and the concept was elaborated by Schmidt almost two decades later (1971) while investigating the photo-dimerization reactions of cinnamic acids and amides in the solid state [2]. In 1988, Prof. Desiraju provided the modern definition of 'crystal engineering' as "***the understanding of intermolecular interactions in the context of crystal packing and the utilization of such understanding in the design of new solids with desired physical and chemical properties***" [3].

The noteworthy contributions of Desiraju's published work and a review by Zaworotko and colleagues [4,5] highlight the progression of the crystal engineering approach and its consequential effects on crystal structure, packing, and physicochemical properties. Crystal engineers employ single-crystal X-ray diffraction, one of the most powerful techniques for the characterization and detailed analysis of crystal structures. The subject started with the study of organic solids and their crystal structures but today is a mainline interdisciplinary research activity, dealing with the self-assembly of molecular (organic and metal-organic) crystals as well as coordination polymers using non-covalent interactions [6-10]. The

ultimate aim of crystal engineering concept is to gain control over the formation of products of crystallization enabling us to prepare solids with desired structures and properties [11]. It encompasses the deliberate design of functional three-dimensional crystal structures from molecular-scale components, aiming for specific properties. While accurately predicting crystal structures remains a considerable challenge, notable progress has been made in prediction of the structures of relatively simple molecules [12-14] and the field holds fundamental significance in advancing functional materials (e.g., optical and nonlinear optical properties, electrical conductivity, magnetism, solubility, photochemical stability, and porosity) [15].

The solids that are actively studied by the crystal engineering scientific community include, among others, supramolecular host-guest systems (organic and metal-organic) which can lead to the formation of porous crystalline materials and/or undergo single-crystal to single-crystal transformations [16, 17]. Moreover crystal engineering covers examination of a range of solid-state phenomena such as polymorphism (Figure 2), particularly prominent in the pharmaceutical industry [18-20], supramolecular isomerism, isostructurality, formation of solvates or multicomponent crystals of organic molecules which came into light in the early 20s [21, 22].

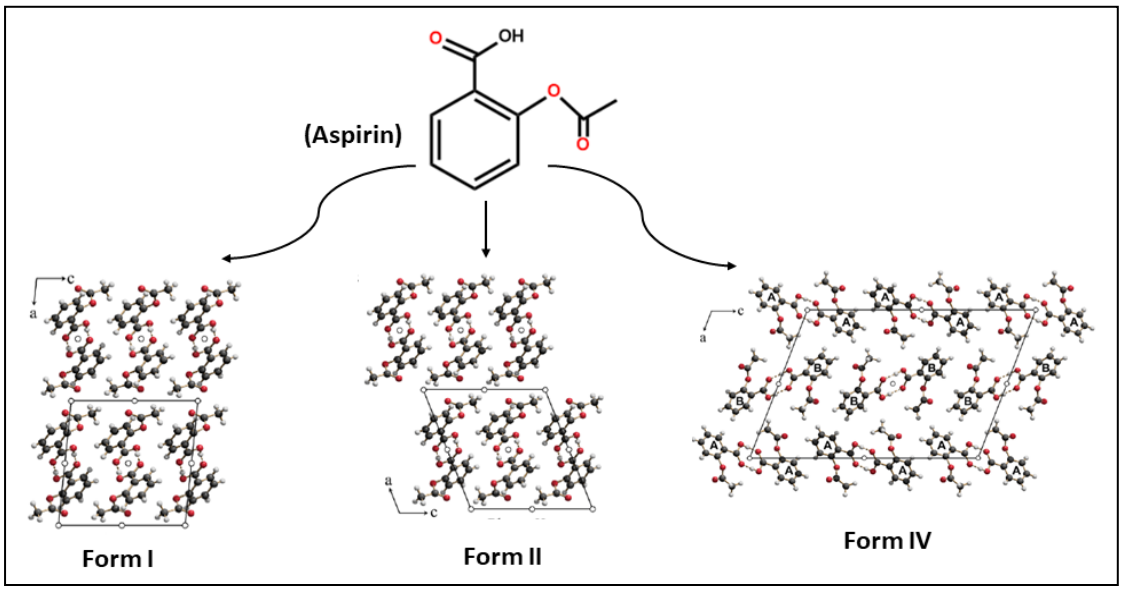

Figure 2: *Three polymorphs of aspirin reported in the literature so far, extracted from [23].*

We could say that the major application of crystal engineering in the field of metal-organic materials is in the engineering of open metal-organic framework structures [24, 25]. Similarly, the concept of crystal engineering can be applied to design porous materials of discrete built, which is the focus of this thesis. Our group has already showcased several

examples in this regard. In one recent report, it was shown that the ligand composition has a huge effect on the final structure i.e., introducing methyl groups on the organic spacer of an imidazole based ligand can lead to the formation of a discrete metallocycle instead of a polymeric metal complex [26] as illustrated in the figure 3.

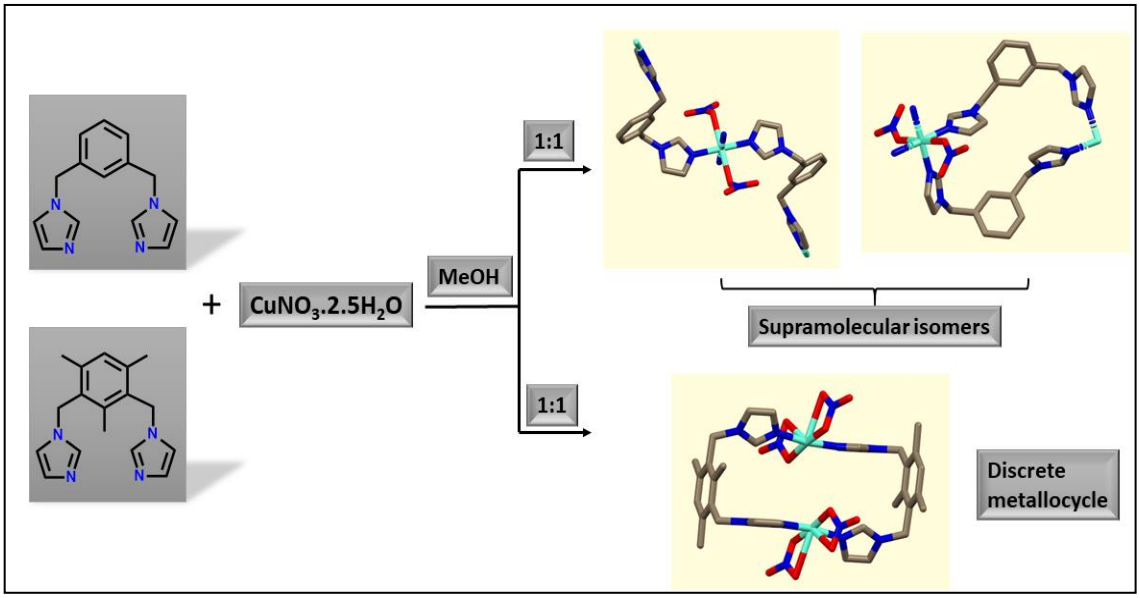

Figure 3*: Schematic representation showing the effect of ligand modification to synthesize a discrete metallocycle.*

2. Intermolecular Interactions

Crystal engineering heavily relies on principles of supramolecular chemistry, which involves the study of non-covalent interactions between molecules [27]. These non-covalent forces are crucial not only for advancements in crystal design but also for the entire living world and play a vital role in various biological processes [28]. These interactions include among others hydrogen bonding, halogen bonding, van der Waals forces, interactions between aromatic rings, and electrostatic interactions (ion-ion, ion-dipole and dipole-dipole interactions) (Figure 4). To construct supramolecular assemblies in a more predictable way, a fundamental understanding of various interaction aspects such as their strengths, geometric characteristics, and the directional properties of acceptors are prerequisite [29]. Once these interactions are understood, they can be leveraged for the rational design and construction of functional materials [6, 30]. To achieve this, statistical analyses of numerous crystal structures are essential, particularly when examining weaker interactions [31, 32].

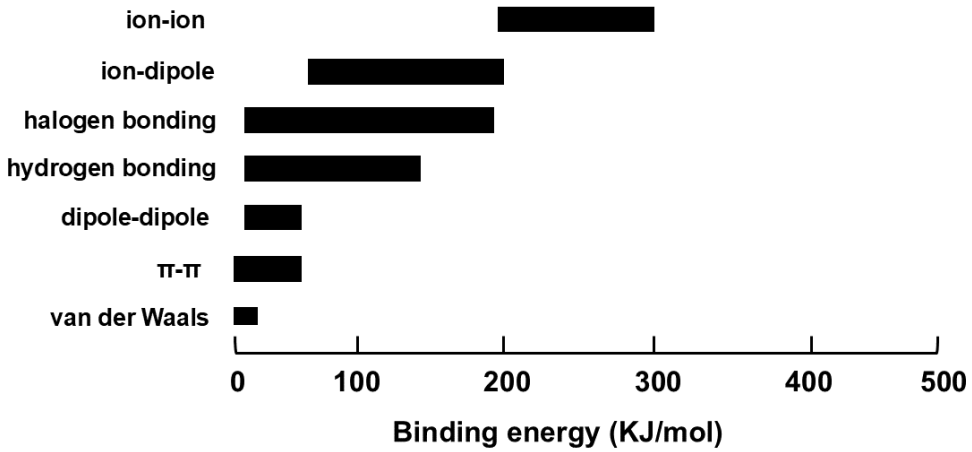

Figure 4: *Relative strengths of common intermolecular interactions, extracted from [33].*

Records of such interactions are now easily accessible through crystallographic databases like the Cambridge Structural Database (CSD), which is known for its user-friendly interface. The CSD also offers tools for searching, retrieving, and displaying structural data, providing valuable insights into intermolecular bonds [34, 35]. Recent advancements in diffractometers design and computational technologies have also shortened the time required for data collection and structure determination, resulting in a growing number of structures being added to the CSD annually. For crystal engineers, categorizing intermolecular interactions based on their distance dependence and directionality is the most effective approach. The packing of molecules in the solid state, leading to crystal formation, is influenced by two main types of interactions. The first involves medium-range isotropic forces, such as close packing and the consideration of molecular shape and size. These forces typically involve interactions like C···H, C···C, and H···H, and are more localized. The second type consists of long-range electrostatic and anisotropic forces, which usually occur between heteroatoms such as N, O, S, Cl, Br, and I, or between these atoms and carbon or hydrogen [31]. Supramolecular assembly relies on the careful balance of these crystal packing forces, which vary in strength, directionality, and dependence on distance [36]. These intermolecular forces, often described as supramolecular 'glue' or 'cement,' play a crucial role in determining the structure and stability of the crystal [37]. Among several types of intermolecular interactions hydrogen bonds are the most widely studied.

Below is a brief overview of the major types of intermolecular interactions which are the basis of work carried out in this thesis.

2.1. Hydrogen Bonding

Hydrogen bonding is the most important directional intermolecular interaction [4, 38]. As George A. Jeffrey and Wolfram Saenger mentioned in their book "***The discovery of the hydrogen bond could have won someone the Nobel Prize, but it didn't***" [39]. This statement itself highlights the crucial role of hydrogen bonding as without it, there would be no water on Earth, and therefore, no life.

The literature on the subject dates back to the 20th century [40], whereas it was first referred to as a 'bond' by Latimer and Rodebush in 1920 [41] and became a key concept in chemistry through Pauling's 1939 work, defining it as a primarily ionic interaction between electronegative atoms [42]. Later definitions, including those by Pimentel, Atkins, and Steiner, expanded its scope, considering various bond types and experimental evidence [43-45]. Despite ongoing research, no single definition fully captures the complexity of this interaction. In 2011, a novel definition of hydrogen bond was proposed by IUPAC taking into account the experimental and theoretical knowledge accumulated over the past century: *"**The hydrogen bond is an attractive interaction between a hydrogen atom from a molecule or a molecular fragment X–H in which X is more electronegative than H, and an atom or a group of atoms in the same or a different molecule, in which there is evidence of bond formation"*** [46]. This interaction may be represented as X–H···Y–Z, where the three dots denote the hydrogen bond, where X–H acts as the hydrogen bond donor, while the acceptor can be an atom, anion (Y), or a fragment (Y–Z), where Y is bonded to Z. Sometimes, X and Y are the same, and in specific cases, the distances between X–H and Y–H are equal, forming symmetric hydrogen bonds. The donor here is electron deficient, contrary to the conventional donor in chemistry and the acceptor is always an electron-rich species, such as a lone pair on Y or a π-bond in Y–Z. They listed six criteria that could be used as evidence for the presence of a hydrogen bond which are as follows:

1) Hydrogen bond formation involves electrostatic forces, charge transfer between the donor and acceptor leading to partial covalent bonding, and dispersion forces.
2) In an X–H covalent bond, the bond is polarized, and the H···Y bond becomes stronger as X's electronegativity increases.
3) The X–H···Y angle is typically linear (180º). The closer the angle is to 180º, the stronger the hydrogen bond and the shorter the H···Y distance.

4) Hydrogen bond formation lengthens the X–H bond, causing a red shift in its infrared stretching frequency and increasing absorption. The greater the bond lengthening, the stronger the H···Y bond, and new vibrational modes appear.
5) X–H···Y–Z hydrogen bonds show unique NMR features, including pronounced proton deshielding, spin–spin couplings between X and Y, and nuclear Overhauser enhancements.
6) For a hydrogen bond to be experimentally detectable, its Gibbs energy of formation must exceed the system's thermal energy.

Hydrogen bonds are defined by four parameters: d, D, θ, and φ (Figure 5). The distances X···Y and H···Y are denoted by D and d, whereas θ and φ represent the angles: X-H-Y and Z-Y-H, respectively.

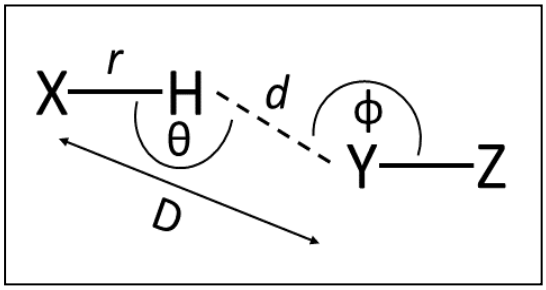

Figure 5: *A schematic representation of a hydrogen bond showcasing geometrical parameters* d, D, θ, and φ, *adapted from [47].*

The angle φ determines the directionality of the hydrogen bond. The closer the angle is to 180º, the more directional and stronger the hydrogen bond becomes, and this angle should preferably be greater than 110º [46]. The D and d must be smaller than the sum of the atoms' van der Waals radii in order for a hydrogen bond to form. In structure determination using single-crystal X-ray diffraction, the distance D between the donor (X) and acceptor (Y) is particularly important because the hydrogen atom positions in this case are not accurately defined. In contrast, neutron diffraction provides precise information about the position of hydrogen atoms, as well as the angle θ and distance d [47].

Hydrogen bonding interactions can be classified into three categories based on their strength [48]:

(1) Very strong: These hydrogen bond occurs when X and Y atoms are highly electronegative non-metals, and such that X-H is sufficiently polarized to be electrostatically attracted to Y. The proton is often highly shared between the donor and the acceptor atoms.

(2) Strong: The hydrogen is still attracted strongly to both the donor and acceptor, but it does not exhibit the same degree of proton sharing as very strong hydrogen bonds. However, they are more common than very strong hydrogen bonds and found in many biological molecules, like DNA base pairing (A-T and G-C).

(3) Weak: Hydrogen bonds involving less electronegative atoms or in environments where the distance between donor and acceptor is greater. These bonds typically occur in less organized structures, where the electronegative atoms are not positioned as favorably to form stronger interactions and hence are less directional often longer in distance, leading to a weaker attraction.

For more detailed parameters of each type of the bond, refer to the Table 1.

Table 1: *Properties of the different types of hydrogen bonds [49].*

	Very Strong	**Strong**	**Weak**
Bond Energy (kcal/mol)	15-40	4-15	< 4
Examples	$[F\cdots H\cdots F]^-$ $[N\cdots H\cdots N]^+$ P–OH···O=P	O–H···O=C N–H···O=C O–H···O-H	C–H···O O–H···π C–H···N
D (X···Y) range (Å)	2.2–2.5	2.5–3.2	3.0–4.0
d (H···Y) range (Å)	1.2–1.5	1.5-2.2	2.0–3.0
θ (X-H···Y) range (^{0})	175–180	130–180	110–180
Lengthening of X–H bond (Å)	0.05–0.2	0.01–0.05	< 0.01
Bonds shorter than vdW	100%	Almost 100%	30-80%
Effect on crystal packing	Strong	Distinctive	Variable
Utility in Crystal Engineering	Useful	Useful	Partly useful

Ongoing advancements in X-ray crystallography are enabling chemists to gain a deeper insight into the nature of hydrogen bonds, as the geometric measurements illustrated in Figure 5 can now be determined with considerable precision. A common observation is that the distance D is notably smaller than the combined van der Waals radii of atoms X and Y [50]. However, using van der Waals radii alone to define a hydrogen bond can be quite misleading [51], as experimental evidence shows that hydrogen bonds can be detected at distances well beyond the van der Waals contact limit [49].

Hydrogen bonding is not just limited to single donor-acceptor interactions. Multifurcated hydrogen-bonded interactions are quite common and occur when a donor atom engages with two or more acceptor atoms. Similarly, an acceptor can also interact with multiple

donors [47]. Examples of bifurcated and trifurcated hydrogen bond donors, along with a bifurcated acceptor, are depicted in Figure 6.

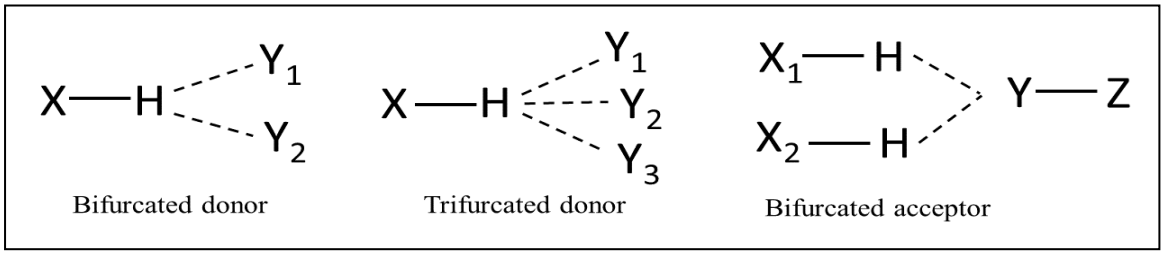

Figure 6: *A schematic representation of multifurcated hydrogen bonding interactions, adapted from [47].*

There was once a time when it was considered that X and Y had to be extremely electronegative atoms like N, O, and F in order to form a hydrogen bond. However, the concept of hydrogen bonding has evolved over time to include C–H···O/N and O/N–H···π interactions, with hardly any covalent character, and even C–H···π interactions that are more of the van der Waals interactions (dispersion-repulsion) type [47]. It is worth noting that some of the stronger hydrogen bonds have comparable energy to the weakest covalent bonds, whilst the weakest hydrogen bonds have similar energy to van der Waals interactions [52]. These interactions have been at the forefront of the Crystal Engineering field since the beginning [53], with particular emphasis on pharmaceutically important compounds [15, 17-19, 21].

2.2. π-π Interactions

π-π interactions (also called **aromatic stacking interactions**) are one of the most important non-covalent interactions that are prominent in crystals build of aromatic molecules and also in systems containing π-bonds, where the π-electron clouds overlap [54]. These interactions are non-directional interactions of weak to moderate strength (8–42 kJ/mol) and play an important role in the structure and stability of various biological and chemical systems, including proteins with around 60% of aromatic side chains participating in π-π interactions, DNA, RNA, and materials science applications [55-57]. These interactions have been at the forefront since the beginning of the field of Crystal Engineering but are less well-defined than the hydrogen bonds [4, 6].

Sanders and Hunter were among the first researchers to provide a detailed description of π-π interactions in the early 1990s that emphasized electrostatic considerations rather than just the overlap of delocalized π-electrons and explained these interactions in terms of a quadrupole moment highlighting partial negative electrostatic potential above aromatic

faces and partial positive potential around edges [58]. This uneven charge distribution drives **T-shaped (edge-to-face)** or **parallel-displaced** stacking in neutral aromatic molecules like benzene. Electron-withdrawing groups, such as in hexafluorobenzene, reverse this distribution, making the ring electron-deficient with a positive face and negative edges. This facilitates **cofacial parallel stacking (face-to-face)** between electron-deficient and electron-rich aromatic rings due to opposing quadrupole interactions (Figure 7) [59, 60].

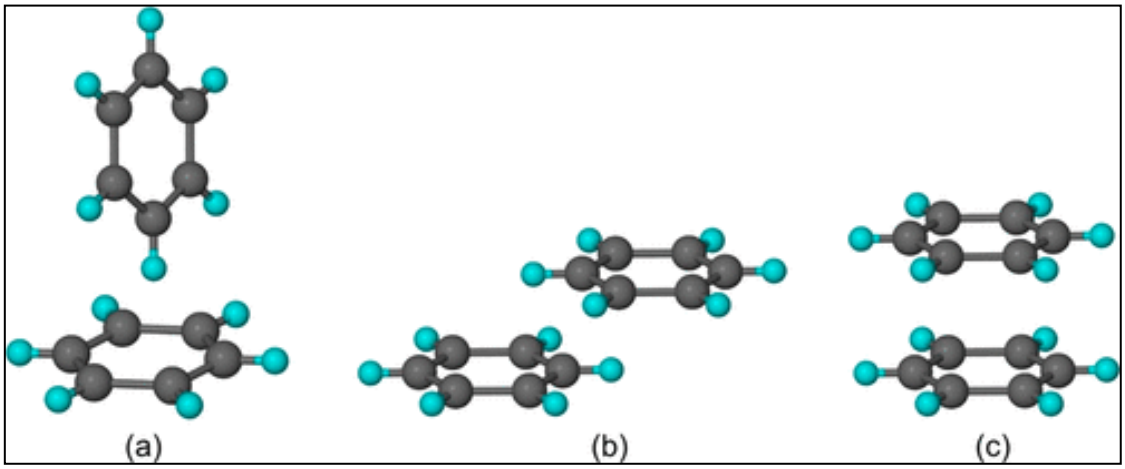

Figure 7: *A schematic representation of (a) edge-to-face T-shape, (b) parallel displaced, and (c) cofacial parallel stacked geometries of π–π interactions between aromatic systems, extracted from [56].*

Upon a follow-up of these findings, Sherrill and colleagues provided theoretical support predicting that the T-shaped and parallel-displaced geometries are the most stable and almost isoenergetic, while the cofacial parallel-stacked arrangement is the least favorable for benzene dimers [61]. In contrast, Wheeler and Houk, based on their observation of substituent effects, argued that substituents do not alter the π-cloud density as suggested by Sanders and Hunter. Instead, they proposed that the substituents contribute directly to electrostatic interactions between aromatic systems [62]. Further experimental and theoretical studies have supported this view.

Sanders and Hunter's model suggests that electron-rich aromatic rings repel in stacked arrangements. However, theoretical studies on monosubstituted benzene dimers show that electron-donating and electron-withdrawing groups enhance attraction in sandwich orientations due to stabilizing London dispersion forces, as explained by Sherrill using symmetry-adapted perturbation theory (SAPT) [63]. Diederich, Castellano, and Meyer further highlighted solvent effects on aromatic interactions [55]. Moreover, it was recently reported that it is also important to emphasize the statistical likelihood of interactions based

on geometry, with greater offsets (larger radii and angles) being more probable. This geometry-dependent entropic effect favors parallel or near-parallel stacking due to increased interaction probabilities at higher offsets and angles (Figure 8) [56].

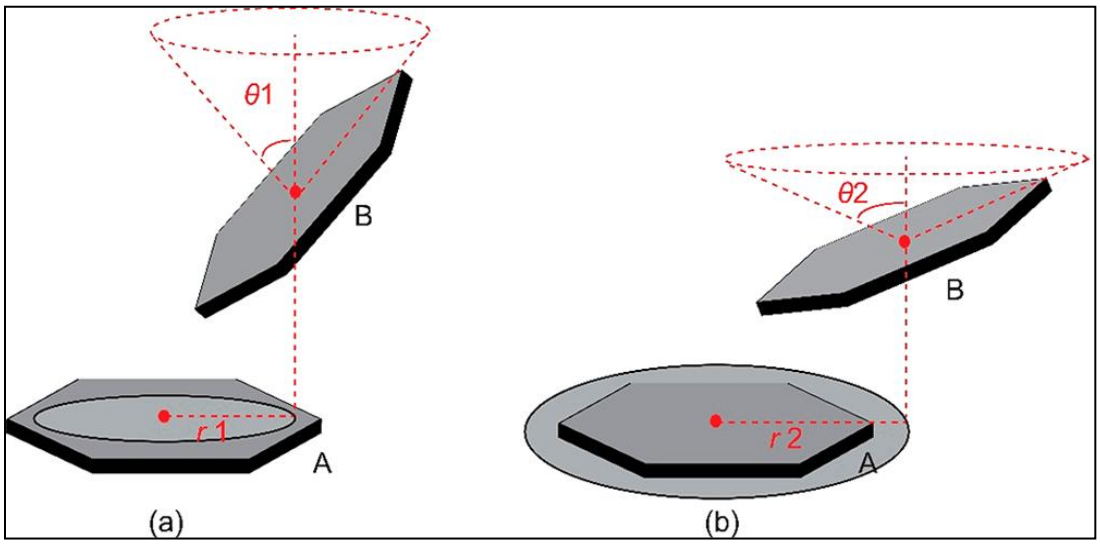

Figure 8: *(a, b) Stacking representations showing higher probabilities of interactions with larger offset and parallel or near parallel stacking, extracted from [56].*

So, various theories have been proposed to explain the nature of π-π interactions in aromatic systems since the 1990s till now considering quadrupole and dipole moments, charge transfer, direct interactions between substituents and the aromatic ring, dispersion forces, and the influence of solvent effects. The importance of these factors varies with the type and shape of aromatic compounds, ranging from small benzene molecules to large structures like graphene, nanotubes, and fullerenes—and is influenced by heteroaromatics and substituents, making these interactions highly system-dependent [64, 65].

The distance between two aromatic rings in π-π interactions is typically described by the centroid-to-centroid separation. According to Janiak, the typical range for facial π-π interactions falls between 3.3 and 3.8 Å, which is close enough to allow significant overlap of π-orbitals but not too close to introduce repulsive forces [66]. Unlike hydrogen bonds, which tend to involve a single point of contact, π-π interactions involve multiple contact points between molecules. Although individual π-π interactions are relatively weak, when considered within the framework of close packing, they contribute significantly to the overall stability of the crystal structure [3, 58]**.**

These interactions have been widely utilized in the field of Crystal Engineering for the last two decades for their potential in diverse functional materials. For example, devices exhibiting exceptional photoconductivity have been realized in both π-π stacked single-component and multicomponent organic crystals [67, 68] and they have also proven useful

in detecting nitroaromatic explosives [69, 70]. Thanks to their tunable electronic characteristics and established methods for structural control, these interactions continue to offer significant promise for future sensing and electronic applications.

2.3. Van der Waals Interactions

Van der Waals interactions are non-directional, weak, short-range forces that occur between atoms or molecules, and they arise from the interactions of electron clouds [71]. These forces are much weaker than covalent or ionic bonds, but they play an important role in a variety of physical and biological processes. Among these interactions, London dispersion is the weakest type, and they occur due to the temporary, instantaneous dipoles that arise when electrons in an atom or molecule are unevenly distributed at a given moment. These forces are inherently attractive and decrease in strength as the distance between atoms increases, following an inverse relationship proportional to the sixth power of the distance between them. Their magnitude also depends on the size of the molecules involved. In contrast, repulsive forces, commonly known as exchange-repulsion forces, act to stabilize the attractive forces and vary inversely with the twelfth power of the distance [72]. Together, these two types of non-directional interactions, dispersion, and repulsion, are collectively termed van der Waals forces. London forces are universal; they exist between all molecules, regardless of their polarity. While all atoms in organic molecules can contribute to van der Waals forces, these interactions are primarily linked to C···C, C···H, and H···H contacts due to the high prevalence of carbon and hydrogen in organic systems. Although van der Waals forces rarely play a decisive role in supramolecular architecture, they become significant in inclusion compounds [73]. Their contribution is most noticeable when stronger electrostatic forces are absent and when a large number of van der Waals interactions are present to collectively influence the system.

3. Coordination Bond: Metallocycles vs MOFs

Coordination bond, also known as dative covalent bond, forms between a metal cation, acting as a Lewis acid, and an organic ligand, which donates a lone pair of electrons as a Lewis base [74]. The metal cation (often a transition metal) with vacant d or f orbitals accepts electron density from a ligand donor, which typically possesses lone pairs of electrons, most commonly from heteroatoms like nitrogen, oxygen, or sulfur. These interactions are partially electrostatic, and the formation of these bonds results in strong and directional interactions, with bond strengths ranging between 30 and 70 kcal/mol

depending on the metal and ligand involved [39]. This combination of strength and directionality makes coordination bonds highly desirable for the construction of stable, yet flexible, hybrid materials. The formation and stability of coordination bonds depend on several factors, including the coordination preferences of the metal ion, the geometry of the available coordination sites, the nature of the organic ligand, and the overall reaction conditions. Transition metals, especially those with available d and f orbitals, display a variety of coordination geometries, including octahedral, tetrahedral, and square planar arrangements. This versatility allows for the design of diverse coordination compounds ranging from discrete (mononuclear or polynuclear), 1D CPs to higher-dimensionality 2D CPs and 3D CPs with tailored properties (Figure 9). In addition, the counter anions, temperature and solvent can also significantly influence the final structure of these materials [75].

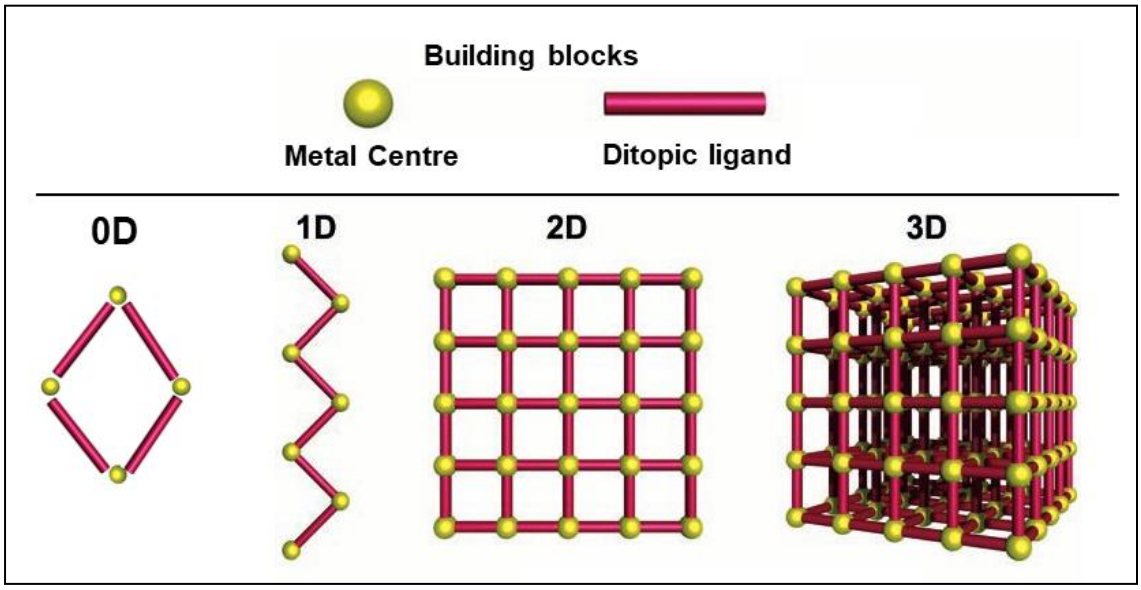

Figure 9: *A schematic representation of different coordination compounds, adapted from [76].*

3.1. Discrete Coordination Compounds

Discrete coordination compounds (DCCs) are a distinct class of coordination complexes characterized by their well-defined molecular architecture, in which metal ions are coordinated to organic or inorganic ligands in a specific geometric arrangement. DCCs consist of individual, finite molecular entities. The foundation of modern coordination chemistry largely stems from the pioneering work of Alfred Werner (1866–1919), who was awarded the Nobel Prize in Chemistry in 1913 and his work on DCCs initiated the development of coordination chemistry [77, 78]. DCCs exhibit isolated structures, which

can range from simple mononuclear complexes to intricate multinuclear assemblies, depending on the number of metal centers and the coordination geometry imposed by the ligands [79, 80]. By exploring different coordination environments and ligand designs, chemists can tailor these compounds for specific uses, contributing to advancements in both fundamental research and applied science [81]. Their well-defined architecture allows for precise control over their chemical behavior, making them valuable in various applications. One of the fascinating classes of DCCs are supramolecular coordination complexes which are discrete assemblies of metal ions and ligands that form larger, often highly symmetric, molecular architectures such as cages, spheres, cycles, or polyhedral [82]. These complexes are held together by coordination bonds as well as secondary interactions like hydrogen bonding or π-π stacking. Their ability to encapsulate guest molecules within their cavities makes them valuable in supramolecular chemistry, and they find application in molecular recognition, drug delivery, sensing and separation [83].

3.1.1. Metallocycles (MCs):

Discrete MCs are obtained by coordination-driven self-assembly of metal ions and organic ligands, wherein the coordinate bond forms between the metal atom and donor atom of the ligand, by using a 'bottom to up' approach, either by classic solution reactions or solvothermal synthesis. Dinuclear metallocycles are discrete metal-organic complexes made up of two metal centers bridged by two exobidentate mostly C-shaped ligands, and so on. Such cyclic structures are appealing because of their precise geometries and ability to facilitate communication between metal centers. Although they are not fully enclosed like molecular cages, metallocycles feature defined cavities and active sites that can effectively bind guest molecules, and several N-donor ligand bases dinuclear metallocycles have been shown to form porous crystals that exhibit structural stability during guest transport, offering potential uses in guest storage and separation [84-92]. Metallocycles represent a highly promising category of porous materials suitable for investigating structure-property correlations using single-crystal X-ray diffraction (SC-XRD) techniques. These materials possess comparatively simple zero-dimensional structures, and their guest-accessible space is sufficiently compact, facilitating the straightforward localization of included guests within the host. Usually, it is observed that upon solvent removal, molecular crystals rearrange themselves to achieve closely packed structures [93]. However, there are certain examples in the literature showing that the guest molecules (solvent) present inside metallocycles structure can be removed to yield guest-free

(apohost) structures in a single-crystal to single-crystal manner, to use them further for sorption studies, although this number is quite small [85-87].

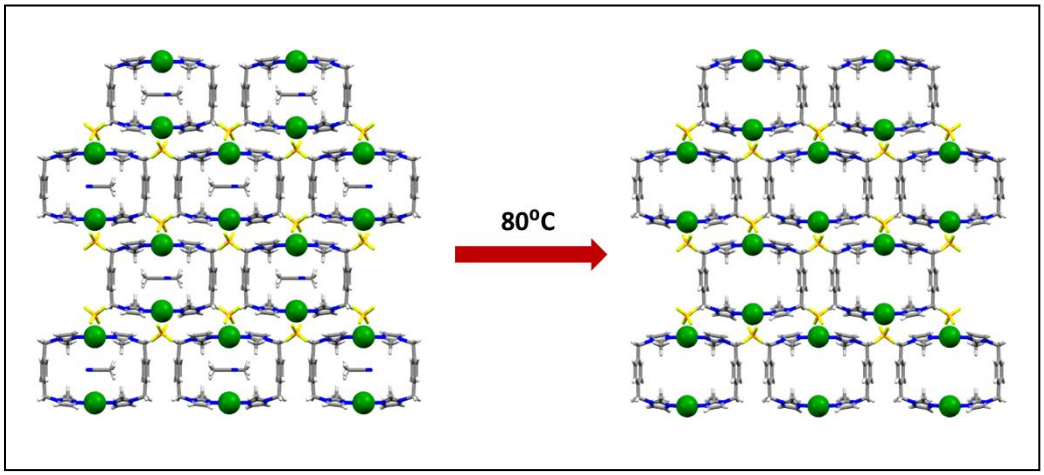

Figure 10: *Figure showing the unaltered packing of a metallocycle $[Ag_2L_2](BF_4)_2{\cdot}2CH_3CN$ after solvent removal in a SC-SC manner [85].*

Even though the first example of a metallocycle was reported in 1990 by Fujita and co-workers, the molecular square $[\{Pd(en)(\mu{-}4,4'\text{-bipy})\}_4](NO_3)_8$, based on the linear linker 4,4′-bipyridine [94], the sorption properties of this system were not in focus, and the subject of porosity studies in metallocycles was initiated in 2004 by Chatterjee *et al.* [95] followed by Dobrzańska *et al.* [85]. In the latter report a discrete cyclic dinuclear Ag(I) complex was described containing ditopic ligand 1,4-bis(2-methylimidazol-1-ylmethyl)benzene in acetonitrile, which formed a discrete rectangular type of complex which had solvent (acetonitrile) molecules inside, and upon solvent removal, the packing arrangement of the host was unaltered (see figure 10) yielding a porous lattice capable of absorbing various gases [85].

Following this example attempts to obtain porous discrete metallocycles based on dipodal imidazole-based ligands were achieved by the same group. The solvent templation effect on the formation of metallocycles [96], heat or solvent-induced SC-SC transformations [87, 97] and, more recently, the mechanism of chromatic changes for a series of common solvents as guest molecules were also shown [98]. However, no systematic studies focused on porosity have been performed on this group of compounds. Recently, a very interesting example of the conversion of pyrene functionalized Ru-based interlocked metallacycles to mono-rectangle through aging was reported, which is the first-ever example of such a case in metallocycles [99].

The unoccupied space (voids) in the crystalline materials build of discrete metallocycles is lower than that of the MOFs, and it is believed that smaller pore dimensions increase van

der Waals contact area, thereby enhancing gas binding affinity. Moreover, the confined cavity of MCs gives rise to a variety of host-guest chemistry and displays encapsulation ability for diverse guests. Recently, a dinuclear Cu-based metallocycle $[Cu_2L_2Cl_4]$ where (L = 1,3-bis(imidazol-1-ylmethyl)-2,4,6-trimethylbenzene) was reported to show exceptional selectivity for *p-xylene*, distinguishing it effectively from other xylene isomers [91]. Notably, this material is the first metal-organic compound to exclusively absorb *p-xylene* from liquid xylene mixtures and uniquely removes trace amounts of *p-xylene* from *o-xylene*. All the above-mentioned examples demonstrated that porosity in molecular crystals can be achieved when channels or discrete cavities form due to inefficient packing supported via intermolecular interactions.

A range of rigid and flexible ligands containing N-donors, specifically imidazole-based have been employed to create discrete metal-organic complexes [100]. Recently, there has been a growing interest in the structures of metal-complexes formed using flexible bridging ligands. These ligands possess flexibility, enabling them to bend and rotate during coordination to metal centers, adapting to various coordination geometries. Apart from the ligand's structure and composition [26, 101], factors such as counter-ions [102-104], metal-to-ligand ratio [105], solvent utilized [96] during crystallization, etc., significantly impact the formation of coordination architectures. Understanding these factors is crucial for the rational design of crystalline materials.

Discrete metallocycles are mainly stabilized by weak non-covalent interactions, such as hydrogen bonds, π-π interactions, and van der Waals forces, thus systematic studies with respect to these intermolecular interactions are required.

3.2. Coordination Polymers/Metal-Organic Frameworks (MOFs)

Coordination polymers (CPs) are extensive network structures formed by the coordination of metal ions or clusters with organic ligands. Based on their dimensionality, CPs are categorized into 1D, 2D, and 3D frameworks (Figure 11), each offering distinct structural attributes and functionalities [75]. **1D CPs** are chain-like structures where metal ions are sequentially connected by organic ligands. These chains can adopt diverse configurations, such as linear, zigzag, helical, or ladder-like arrangements, depending on the coordination geometry and flexibility of the ligands [106]. These 1D coordination chains can further interact with neighboring chains through non-covalent interactions, such as hydrogen bonding or π-π stacking, often resulting in fascinating supramolecular architectures and various applications [107]. While simpler in structure compared to 2D and 3D CPs, 1D CPs

offer inherent flexibility and unique adsorption properties with some advantages over their higher dimensionality counterparts [108]. While this flexibility offers the potential for significant structural transformations, it often leads to a marked decrease in crystal quality not being able to follow these transformations in a single-crystal to single-crystal manner [109]. Consequently, although this area holds considerable promise, materials of this nature are often set aside due to possible challenges. However, there have been published examples of 1D coordination polymers with notable applications [110-112]. **2D CPs** consist of sheet-like architectures formed by the coordination of metal ions with ligands in two dimensions, resulting in planar networks [113]. These frameworks often feature topologies such as square grids, honeycomb, or Kagome patterns, dictated by the coordination geometry and connectivity of the components. Their layered structure has led to significant interest in their use for catalysis, sensing, and energy storage [114, 115]. **3D CPs** are constructed from metal ions or clusters (secondary building units, SBUs) connected by polytopic organic ligands, forming intricate three-dimensional networks [116, 117]. **3D CPs** based on carboxylates were the first type of MOFs representing permanently porous systems introduced by Yaghi and colleagues [118]. These materials exhibited remarkable versatility in gas storage and separation [119], catalysis [120], drug delivery [121], and sensing [122], with some frameworks achieving record-breaking surface areas, such as NU-110E [123]. However, due to the widespread use of the term "MOF", a definition by the IUPAC task group was given specifically to coordination networks (1D, 2D or 3D) with organic ligands containing potential voids/displaying porosity [124].

Each class of CPs offers distinct advantages, with 3D CPs excelling in porosity-driven applications, 2D CPs standing out for their anisotropic and electronic properties, and 1D CPs showcasing unique flexibility and adaptability. Collectively, CPs remain at the forefront of materials research, with growing applications fueled by their structural diversity and tunability.

While research on high-dimensional 2D [114] and 3D [125] materials is abundant less attention was given to 1D coordination polymers [108] in the context of solid-state dynamics and porosity studies.

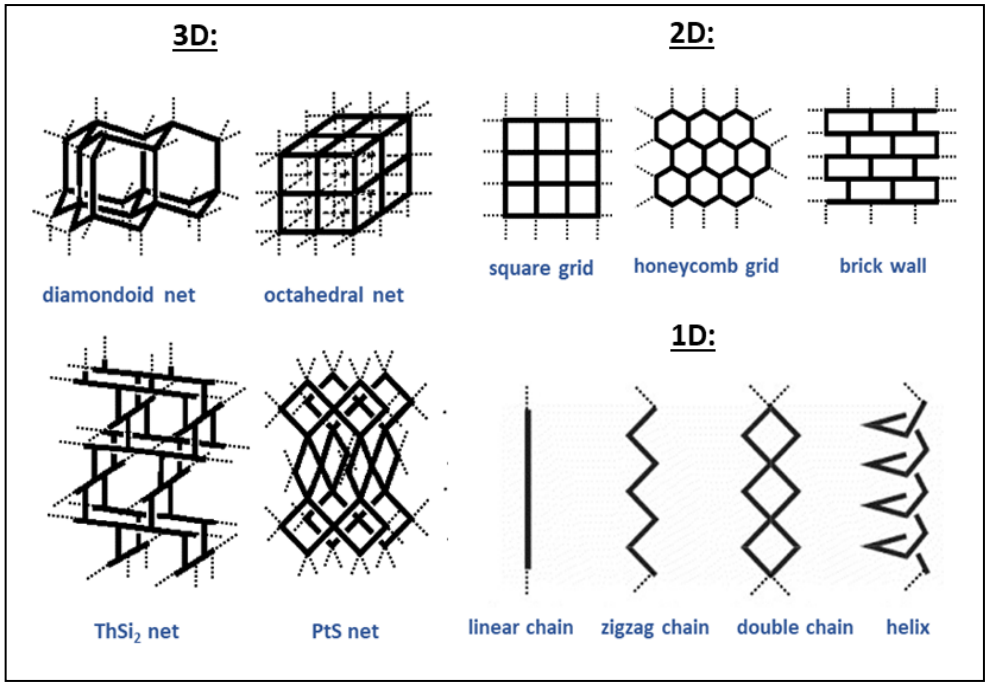

Figure 11: *Few common motifs in 3D, 2D and 1D CPs. Adapted from [74].*

4. Structural Diversity: From Polymorphs to Solvates

The solid-state phenomena described below are central topics in Crystal Engineering and are worth emphasizing in the context of this dissertation.

4.1. Polymorphism: Polymorphism occurs when a material forms two or more different crystal structures, either due to the change in molecular conformation (conformational polymorphs) or the packing arrangement of molecules in the lattice (packing polymorphs) [126-128]. Although the polymorphs consist of the same compound, they can display significantly different physical and chemical properties, such as solubility, density, diffraction patterns, melting points, stability, and more due to variations in their solid-state architecture. This phenomenon is critically important in the pharmaceutical industry, as even minor changes in crystal structure can drastically impact the physical properties essential for drug effectiveness [129].

4.2. Supramolecular isomerism: The term *polymorphism* is typically used for molecular crystals, whereas in the case of network structures, the term *supramolecular isomerism* is preferred. Supramolecular isomerism refers to the presence of multiple types of structures formed from the same molecular building blocks and can be categorized into four main types: structural, conformational,

catenane/interpenetration, and optical isomerism [5]. This phenomenon is particularly common in coordination polymers, where factors such as temperature, solvent, concentration, crystallization methods, additives, and templates can influence the formation of different supramolecular isomers [130].

4.3. Isostructurality: Isostructurality, as defined by the International Union of Crystallography (IUCr), refers to two crystals having the same structure but not necessarily identical cell dimensions or chemical composition, with a comparable variability in atomic coordinates relative to these factors [131]. In the 1990s, the Kálmán group systematically studied isostructurality, introducing quantitative descriptors such as the unit-cell similarity and isostructurality indices, leading to the creation of the ISOS program [132-134]. More recently, Bombicz *et al.* proposed a broader definition, emphasizing structural resemblance demonstrated through quantitative measures that consider atomic coordinates, unit-cell parameters, and overall structural patterns. This approach accommodates subtle variations and provides a comprehensive framework for analysis, extending the concept's applicability in Crystal Engineering [135].

4.4. Solvates: Solvates are crystalline substances where solvent molecules, referred to as guests, are incorporated into the crystal lattice of a host compound. These guests are not covalently bonded to the host; instead, they interact through various electrostatic interactions ranging from strong hydrogen bonds and ionic forces to weaker π- π interactions and van der Waals forces. Hydrogen bonding is particularly significant due to its strength, directional nature, and frequent occurrence. When water acts as the guest molecule, the resulting crystalline compound is specifically termed a *hydrate* [136].

5. Single-Crystal to Single-Crystal (SC-SC) Transformations

An important feature of coordination bonds is their structural flexibility. While covalent bonds tend to fix atoms in rigid geometries, coordination bonds can tolerate slight angular distortions, allowing dynamic transformations in the solid state [137, 138]. This flexibility is crucial for applications where materials must respond to external stimuli, such as in gas adsorption, molecular recognition, or catalysis [139]. This dynamic behavior is further enhanced by incorporating weaker interactions like hydrogen bonding or van der Waals forces into the frameworks. For instance, many MOFs combine coordination bonds with

hydrogen bonding, resulting in materials with improved structural stability and tunable properties [140].

Single-crystal to single-crystal (SC-SC) transformations, a type of solid-state reaction well utilized in the field of crystal engineering and supramolecular chemistry have been known since 1970s [141] and have gained considerable interest from researchers in the field in the last two decades, especially in CPs [142]. The so-called single-crystal to single-crystal (SC-SC) transformation is a distinct type of solid-state reaction that happens in a single-crystal to single-crystal manner [143]. SC-SC transformations occur when crystals are exposed to an external stimulus such as temperature, light, pressure, mechanochemical forces, and loss/uptake of solvent vapors, resulting in structurally transformed products [109, 144, 145]. They offer detailed snapshots of the structural changes that occur when materials are exposed to external stimuli, allowing researchers to observe the mechanisms driving these changes in real time.

However, the major challenge in SC-SC transformation is to retain the crystallinity of the transformed single crystal, as single crystals tend to lose their crystallinity when exposed to external forces, however if maintained, analyzing these transformation processes through single-crystal X-ray diffraction can provide valuable insights into molecular transport and reactions in the solid state for the rational design of crystalline materials [146]. These transformations are usually accompanied by a change in the physical properties such as color, magnetism, dimensionality, porosity, chirality, coordination geometry, etc., leading to the formation of products that often could not be obtained by routine conventional methods [147]. These dynamic processes involve among others the breakage and formation of covalent [148, 149] or non-covalent bonds, accompanied by structural rearrangement in the crystalline phase. In many complexes, SC-SC transformation is facilitated by a change in the color of the crystals which makes them a potential candidate for sensor technology.

There is a growing interest in the research of single crystals exhibiting adaptive crystal lattices that respond to external stimuli [147]. This structural flexibility offers a promising avenue for developing advanced adsorption materials, tunable magnetic properties, and ferroelectric materials. Although there is ample documentation on SC-SC transformations in high-dimensionality coordination polymers (CPs) and metal-organic frameworks (MOFs) [142, 144, 145], SC-SC transformations at the discrete molecular level are still very uncommon [147].

5.1. SC-SC Transformations in Discrete 0D MCs

As mentioned above, SC-SC transformations at the discrete molecular level remain scarce as compared to coordination polymers, and the efforts to understand this phenomenon in discrete compounds are ongoing, yet there are some great examples where the physical properties of the discrete metal complexes are changed with the structural transformation. In some cases, even the transformation from 0D to higher dimensionality 1D, 2D, or 3D could be observed after treating the single crystals of zero-dimensionality to external stimulus [147].

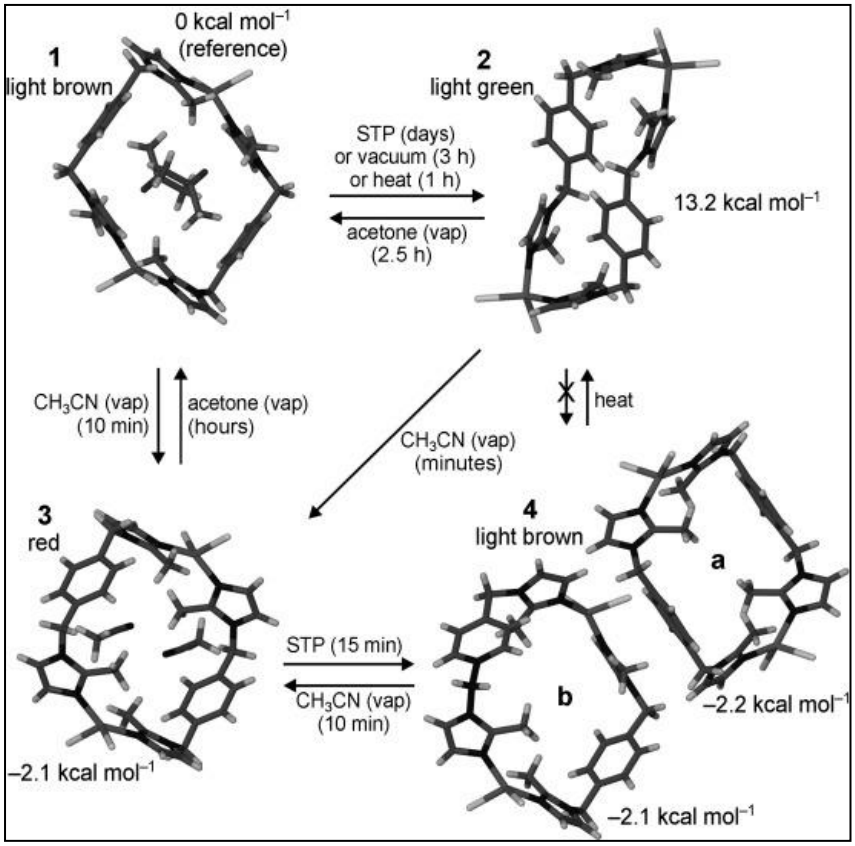

Figure 12: *Figure showing the interconversion of the four dinuclear metal complexes (1-4), (vap: vapor, STP: ambient conditions) along with energies calculated by nonlocal DFT level of theory with the B3LYP/LANL2DZ basis set, extracted from [87].*

However, the first documented instance of single-crystal to single-crystal (SC-SC) transformations in zero-dimensional molecular crystals was presented by L. Dobrzańska *et al.* In this study, the reversible interconversion between four distinct molecular crystal forms composed of neutral, dinuclear metal complexes was demonstrated. This transformation was driven by the uptake and release of solvent vapors, leading to notable changes in the conformation and position of the host molecules with each structural modification accompanied by a vapochromic response [87] (Figure 12).

Recently, the first example of a transformation of imidazolyl-based 0D metallocycle to a 1D coordination polymer was reported by Wei *et al.*, wherein a novel 0D metallocycle transforms in SC-SC fashion to a 1D coordination polymer upon the loss of solvent (acetonitrile) [150] (see figure 13).

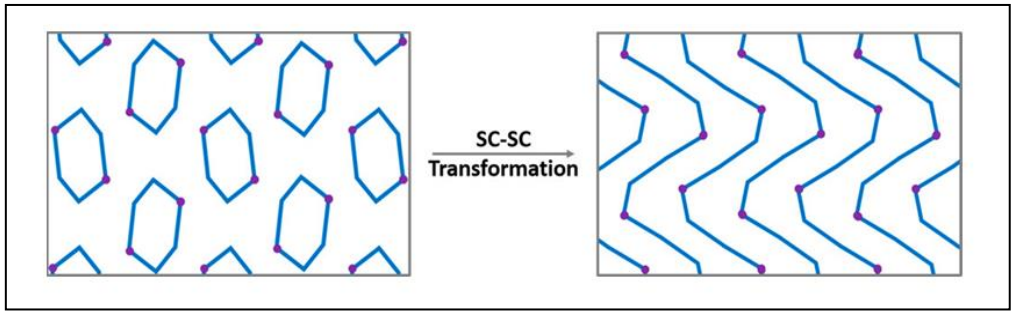

Figure 13: *Figure showing the structural transformation of a 0D Cu(II) metallocycle to 1D coordination polymer, extracted from [150].*

SC-SC transformations from the last decade continued to be studied widely in discrete compounds as they allow for studying structure-property relationships in great detail [147]. While there are quite a few reports about the packing changes upon SC-SC transformation in 0D MCs due to bonds rearrangements [108, 147]. There are a handful of examples reporting purely conformational changes in a single-crystal to single-crystal manner in these structures upon subjecting crystals to external stimulus [87, 90, 97]. For instance, solvent-induced transformations have been shown in a seemingly non-porous single crystals of a dinuclear complex $[Ag_2(\mathbf{bitmb})_2](BF_4)_2$ [97]. The desolvated form (**1**) upon exposure to ethanol and acetone resulted in monosolvated (**3b**, **4b**) forms and exposure to acetonitrile resulted in monosolvated (**2b**) and disolvated (**2a**) forms. The molecular structures of the Ag(I) complex in **1** and **2a** stay more or less the same, this could lead to the assumption that the process is based on minor rearrangements involving the layers consisting of metallocycles in the crystal lattice. However, deeper insight into the process revealed that the transition from form **1** to **2a** and back actually involves a few intermediate steps including the formation of monosolvated form **2b**. The transformations taking place involve not only a rearrangement of the molecules, but also conformational changes within the complexes, such as swinging of the mesitylene rings or flapping of the imidazole rings, to facilitate the solvent diffusion process. Remarkably, these changes occur rapidly and in a coordinated manner within a single crystal, making them easy to overlook, especially since the solvent molecules do not form stable solvates but merely pass through the crystal. Prolonged exposure of **1** to the vapours of all three solvents (over 1 month) leads to the regrowth of crystals and formation of a 1D polymeric Ag(I) complex,

showing a wave-like chain structure. These transformations demonstrate that even seemingly non-porous crystals can undergo dynamic structural changes. However, capturing every phase of this process is challenging, as the observed forms represent only brief glimpses into a much more complex and continuous transformation. Many intermediate states may occur rapidly and transiently, making them easy to miss.

5.2. SC-SC Transformations in CPs

There have been a lot of reports on SC-SC transformations in coordination polymers in the literature, yet the quest to obtain some new coordination supramolecular systems, which cannot be obtained using routine synthetic methods is still ongoing.

Vittal and co-workers contributed a lot in the field of solid-state reactivity and structural transformations involving coordination polymers [151, 152]. Among these transformations, research on UV-induced [2+2] photochemical reactions stand out as the most well-established and advanced field [153]. In this context, recently in 2020, Vittal *et al*. showed the first example of a one-dimensional coordination polymer (CP) containing a post-transition metal ion Pb(II) showing photo salient (PS) properties triggered by [2 + 2] cycloaddition of olefinic ligands (Figure 14). Upon UV illumination, crystals of CP showed various photomechanical effects such as jumping, splitting, rolling, and breaking [154].

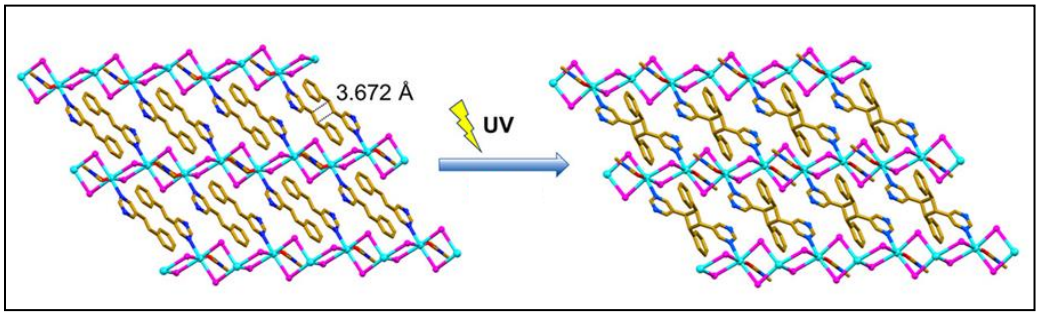

Figure 14: *Single-crystal structures of the photoreactive and photosalient 1D CP **1** and the dimerized 2D sheet structure **2** showing the structural transformation, extracted from [154].*

Another, most common, and direct method that prompts these various solid-state transformations is elevated temperature [109], either by solvent removal or sometimes without solvent participation. In 2022, Kaskel and colleagues demonstrated that a desolvated DUT-8(Ni); $Ni_2(2,6\text{-ndc})_2(dabco)$ (2,6-ndc=2,6-naphthalenedicarboxylate, DUT – Dresden University of Technology) MOF undergoes an irreversible phase transformation from a closed pore phase (cp) to an interpenetrated confined closed pore

phase (ccp) (see Figure 15) showing a huge thermal effect, implying the metal-ligand (Ni-O) bond-breaking and reformation during the phase transition [148].

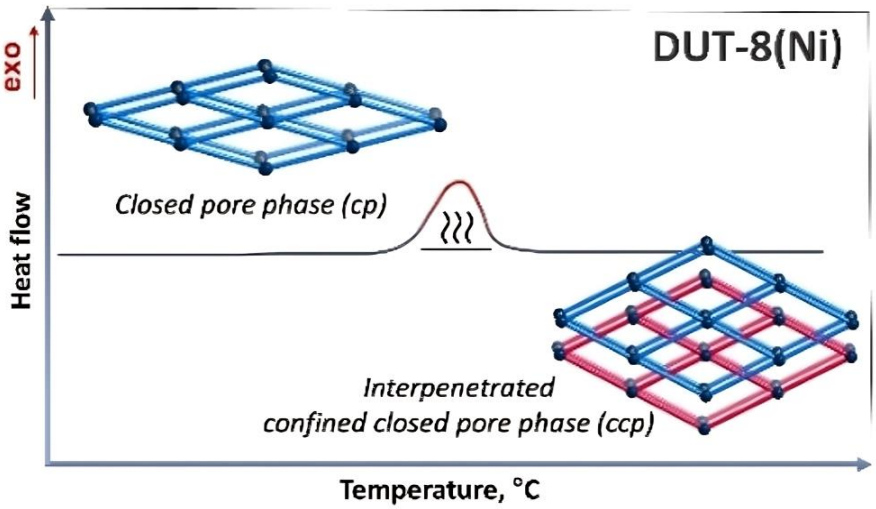

Figure 15: *Figure showing the structural transformation of DUT-89(Ni) cp to ccp. extracted from [148].*

The literature on the SC-SC transformations in CPs contains many good reviews as already cited above covering a range of stimuli and conditions [142-146, 151-153], which are suggested for further reading for anyone interested in the topic.

6. Porosity

Porosity in materials refers to the presence of voids or channels that allow for the diffusion and selective sorption of guest molecules. Porous materials exhibit the ability to adsorb and store gases or liquids and play significant roles in our daily activities. Porous materials are often ordered (crystalline) solids comprised of a framework, or discrete molecules [155, 156] but can be amorphous too. This type of materials have been used by humankind since antiquity, starting with their use in medicine. Historical examples of porous materials include activated carbons and zeolites, which were recognized well before the twentieth century. Since, these materials are amorphous solids having undefined pore arrangements and irregularities, making it challenging to establish clear structure-property relationships, research on porous materials has increasingly focused on developing well-structured, customizable compounds for diverse applications [156, 157]. Coordination polymers (CPs) gained attention in the mid-late 90s, with Robson's team pioneering work [158], followed by Kitagawa's study exploring and advancing functional porous coordination polymers [159]. Yaghi later advanced metal-organic frameworks (MOFs) for gas storage,

significantly impacting the field [160]. Their groundbreaking work on the development of MOFs laid the foundation for transformative applications such as carbon dioxide capture, removal of poluttants from water, targeted drug delivery and harvesting water from desert air and they were jointly awarded ***2025 Nobel Prize*** in Chemistry. Although traditionally uncommon in coordination compounds (specifically molecular compounds) due to the close-packing principle, the field of crystal engineering has developed several approaches to create porous structures, particularly metal-organic frameworks (MOFs). They are recognized for their high surface areas and adjustable pore sizes/characteristics, rendering them excellent candidates for a range of gas adsorption and separation [161]. An alternative for MOFs could be porous materials based on metal complexes built from discrete molecules, but molecular crystals rarely exhibit open channels or isolated voids larger than approximately 25 $Å^3$ and this type of research is still in its early stages due to the greater challenge of creating porous materials solely bound by weak intermolecular forces. Nevertheless, various engineering strategies have been employed to achieve this, such as designing frameworks with irregularly shaped molecules, such as metallocycles [84-91] that resist close-packing and thus maintain intrinsic or extrinsic porosity. Functionalization of the cavities and channels can also enhance selectivity and guest affinity, opening up diverse applications in fields that rely on controlled molecular transport and storage [93]. Unlike MOFs, which exhibit 3D polymeric structures formed through chemical bonds between metal ions and ligands with free electron pairs, the development of porous materials relying solely on weak intermolecular forces is more intricate and there still remains a need for systematic study of porosity in 0D discrete metallocycles.

The recent interest in porous materials, especially MOFs, has led to the frequent, sometimes broad, application of the term "porous." According to Barbour, a material can be classified as porous (in traditional sense) if it meets two main criteria: first, the voids or channels must be accessible to guest molecules, allowing permeability; second, the host structure must remain intact during guest uptake and removal [93].
Barbour actually categorized porosity into three distinct types: conventional, transient, and virtual.

1. Conventional porosity involves the presence of permanent channels within a host material which can release guest molecules without compromising the host's structural integrity. Often, these materials are prepared as inclusion compounds with removable guest molecules, resulting in a stable porous framework upon their extraction.

Porous materials can further be classified by the dimensionality of their channels, from zero-dimensional (discrete voids) to three-dimensional (intersecting channels in multiple directions). Kitagawa and colleagues described these classes as 0D, 1D, 2D, and 3D, reflecting the spatial characteristics of the voids [159]. In addition to structural dimensionality, porosity is also distinguished by pore size, ranging from ultramicroporous (<2 nm) to macroporous (>50 nm) [162, 163]. Ultramicropores and micropores (<2 nm) enable adsorption similar to molecular filling, while mesopores (2-50 nm) undergo capillary condensation, and macropores (>50 nm) behave more like open surfaces due to their size.

Generally, porous materials derived from discrete compounds can be categorized into two types:

Intrinsic: It refers to the rigid molecules, which contain shape-persistent cavities or clefts within the material's structure. Examples include calixarenes, cucurbiturils, or cage compounds [164].

Extrinsic: It means that the molecules themselves do not possess any predefined voids, clefts, cavities, or internal free molecular volume, but rather involve void spaces intentionally introduced or modified in the material, often through external treatments or alterations [165].

The interplay between these two types of porosity contributes to the overall performance and versatility of discrete porous materials in various applications.

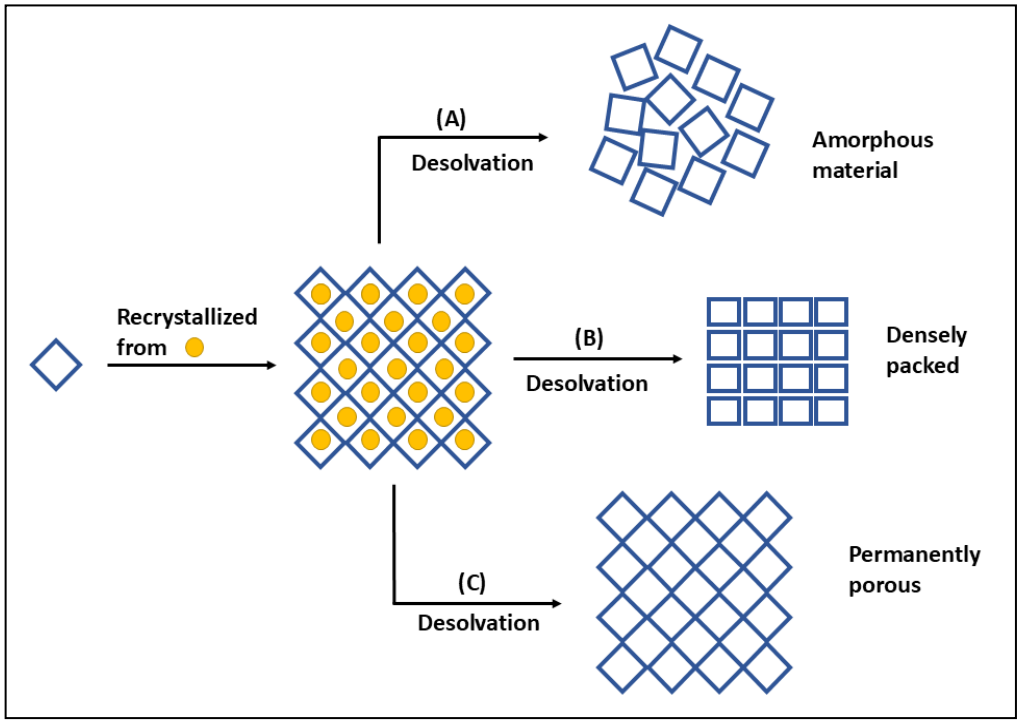

Figure 16: *Routes showing possible outcomes after desolvation for intrinsic porous materials, adapted from [165].*

Figure 16 provides a simplified depiction of a discrete porous material [165], where each square symbolizes a discrete molecule possessing an intrinsic pore. The material's permanent porosity relies on its shape persistence, meaning that even when the pores are emptied, the molecules remain 'open.' The illustration present three potential outcomes during desolvation: a) the development of an amorphous material, which may still retain porosity; b) the loss of extrinsic pores while retaining access to intrinsic pores forming a densely packed structure, which might be porous or non-porous; c) and the 'ideal' scenario where the material preserves intrinsic porosity, resulting in permanent porosity.

2. Transient porosity allows guest molecules to move through the structure without permanent channels linking internal cavities to the external environment. Here, molecular motion or structural shifts permit temporary connectivity, facilitating guest diffusion even in the absence of continuous channels. This type of porosity is intriguing because it enables guest access without stable, open channels, achieved through dynamic structural flexibility, and interestingly several examples of such systems are reported in the literature [84, 86, 88, 90, 91, 166-168].

3. Virtual porosity arises when guest molecules or counter ions are computationally removed from a crystallographic model, artificially creating voids or channels that do not exist in reality. This type of porosity is often visualized through structural models, which can be misleading if atom sizes, or actual spatial occupancy are not accurately depicted.

6.1. Gas Sorption

Gas sorption studies provide critical insights into materials' porosity and structural integrity. Through gas adsorption-desorption isotherm analysis, researchers can identify pore sizes, evaluate whether a material maintains its framework during adsorption and desorption, and detect the presence of hysteresis [169]. These experiments are pivotal for understanding whether the guest molecules are only interacting with the surface (adsorption) or permeating the internal structure (absorption). When there is ambiguity about whether adsorption or absorption is occurring, the term *sorption* is used to encompass both processes. During sorption, a material (the *sorbent*) takes up guest molecules (the *sorptive*) which may be gases, vapors, or liquids. Sorption can occur through two main mechanisms: physisorption and chemisorption. Physisorption involves relatively weak van

der Waals forces that do not significantly alter the geometry of the sorptive. In contrast, chemisorption involves stronger, typically covalent, interactions, resulting in a greater enthalpic gain compared to physisorption [170].

The amount of gas taken is typically plotted as a sorption isotherm, showing the relationship between guest molecule uptake and relative pressure (P/P_0) at a constant temperature [162, 163, 169]. Here, P_0 represents the saturation pressure of the sorptive at the experiment's temperature, which shifts to absolute pressure P if the temperature is above the sorptive's critical temperature. When experiments are conducted consecutively, both adsorption and desorption isotherms are plotted, often revealing hysteresis if they do not align. Such hysteresis is indicative of the presence of pores within the host material or its structural flexibility, with the International Union of Pure and Applied Chemistry (IUPAC) defining six types of adsorption isotherms (Type I to VI) based on specific sorption behaviors and material characteristics [162, 169] (Figure 17).

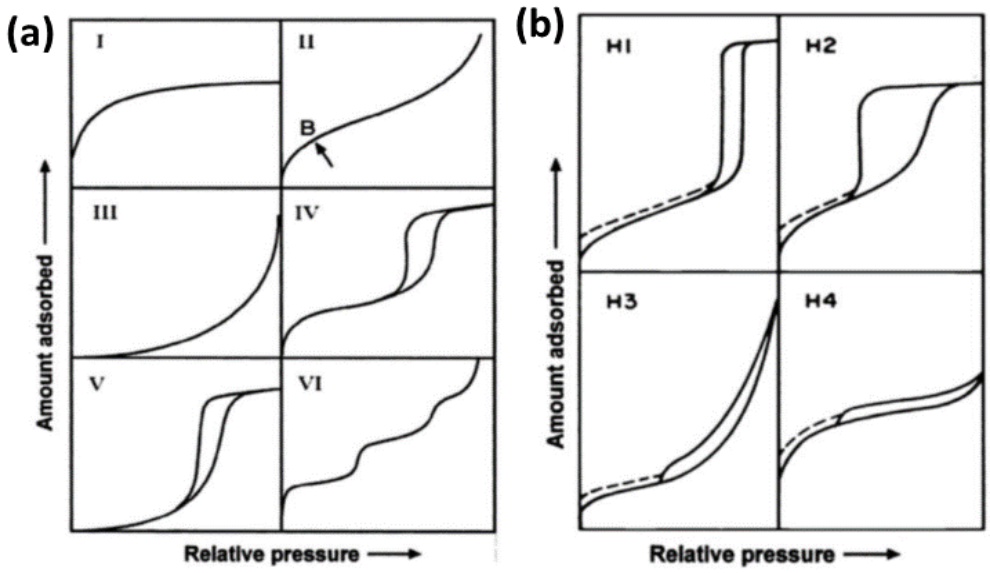

Figure 17: *IUPAC classification of **(a)** the gas physisorption isotherms and **(b)** idealised hysteretic loops, extracted from [169].*

The isotherm type often correlates with pore size: **Type I** isotherms occur in microporous materials (<2 nm) with rapid adsorption at low pressures. **Type II**, found in macroporous materials (>50 nm), show unrestricted monolayer-multilayer adsorption. **Type III** indicates stronger guest-guest interactions, resulting in a convex curve. **Type IV**, typical of mesoporous materials (2-50 nm), displays multilayer adsorption with hysteresis due to pore condensation, while **Type V** is similar but with weaker host-guest interactions. **Type VI** represents stepwise multilayer adsorption on non-porous surfaces, often with non-polar

adsorbates. In addition to this they also classified four idealized hysteretic loops, H1 to H4 (Figure 17). These type are linked to specific pore structures and adsorption mechanisms: H1 is for materials with a narrow distribution of uniform mesopores, H2 is exhibited by materials with more complex pore structures with network effects or pore-blocking, H3 is for aggregates of plate-like particles or if the pore network consists of macropores that are not completely filled with pore condensates, and H4 is for narrow slit-shaped micropores. An updated classification also includes sub-tyes like H2(a) and H2(b) and an unusual type H5 for some plugged mesoporous materials [162, 169].

Sorption isotherms can be recorded using either volumetric or gravimetric methods. In volumetric sorption, uptake is determined by monitoring pressure changes at a set volume, while gravimetric sorption tracks the mass change of the host at constant pressure. Key factors influencing sorption behavior include guest size and shape, thermodynamic interactions, and diffusion kinetics, which together dictate how effectively a guest molecule associates with a host material [163].

6.2. Vapour Sorption

Vapour sorption involves the adsorption of vapours, typically water, organic solvents, or other condensable vapours at controlled relative humidities or vapour pressures. Vapour sorption measurements are typically gravimetric and involve exposing a sample to a stepwise increase and decrease in vapour concentration while continuously recording mass changes using a high-precision microbalance. The resulting sorption isotherms, often classified similarly to gas sorption isotherms, provide insights into the pore structure, surface area, pore connectivity, and the hydrophilic or hydrophobic nature of the material.

7. Dipodal Imidazole-based Ligands

The key factor for the construction of novel coordination architectures with fascinating structures and functions is the rational choice of organic ligands as building blocks. The two most important classes of ligands that are broadly explored for the construction of such materials are aromatic polycarboxylic acids and polydentate N-heterocyclic bases (such as imidazoles, triazoles, tetrazoles, and pyrazoles) [159]. In this work, we utilized N-donor ligands because M-N coordination bonds (M = metal) tend to be weaker and more labile compared to the M-O carboxylate coordination bond. This characteristic renders the structures more adaptable and capable of rearrangement during self-assembly, which

supports further structural optimization. Various approaches for improving these outcomes include exchanging anions, removing or substituting guest molecules, or temperature-induced crystal transformations [159]. Kitagawa and colleagues, for instance, demonstrated a dynamic Cu(II) and bipyridine system containing AF_6 anions (where A represents Si, Ge, or P) that can undergo multiple transformations or guest exchanges [171]. This versatility allows the design of coordination compounds with diverse dimensionalities and pore configurations.

Imidazoles are one of the most widely employed out of all N-donor heterocyclic ligands for the construction of metal complexes varying from discrete to extended (1D, 2D and 3D) coordination compounds, because of their great ability to coordinate to metals [172-174]. Imidazole can be equipped with additional functional groups to form multi-functional ligands, generating extra coordination diversity (Figure 18). 1-imidazole-containing ligands are limited to functioning solely as electrically neutral ligands, as only 1 N-atom is available for coordination in this case, but when two or more of these imidazole groups are combined into a single ligand, it can function as a multi-topic organic linker, bridging metal ions to form coordination polymers and metallocycles [172]. In contrast, derivatives 2- or 4-containing imidazole ligands exhibit the ability to act as both neutral and anionic ligands. The anionic nature of these ligands arises when the amine NH group of the imidazole ring undergoes deprotonation, resulting in the formation of an imidazolate anion, in this case, the imidazolate can act as a bridge to bind two metal ions for the construction of metallocycles, and coordination polymers. The unique attributes of these substituted derivatives offer significant promise for diverse applications in the field of coordination chemistry [172].

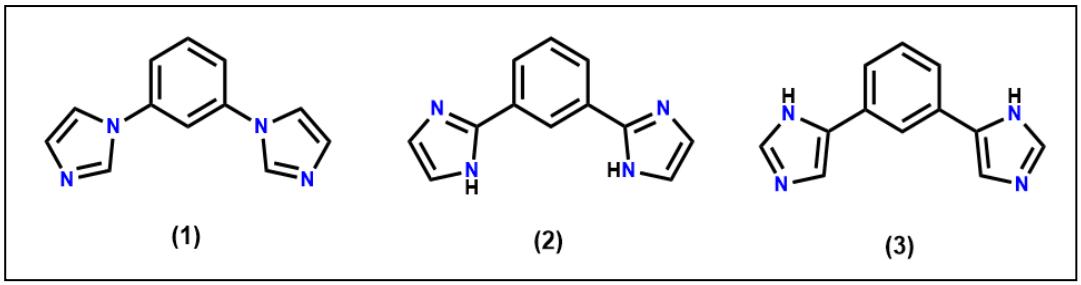

Figure 18: *Representative example of (1) 1-imidazole-substitution, (2) 2-imidazole-substitution, and (3) 4-imidazole-substitution.*

1-Imidazole-containing dipodal ligands can be easily synthesized using Ullmann condensation methods, such as the reaction of aryl halides and imidazole or the substitution

reaction of benzylic halides and imidazole, resulting in rigid or flexible ligands, respectively.

As mentioned above, 1-imidazole-containing dipodal ligands can function as multi-topic organic linkers depending on the number of imidazole moieties combined into a single ligand. When two imidazole groups are attached to one aromatic core, it is called a di-topic or dipodal ligand. Similarly, a ligand featuring three imidazole groups is referred to as a tripodal ligand, and this nomenclature extends accordingly for ligands with additional imidazole groups. If two or more such imidazole groups are integrated into one ligand, it can act as the multi-topic organic linkers for bridging metal ions to construct metallocycles and coordination polymers [172].

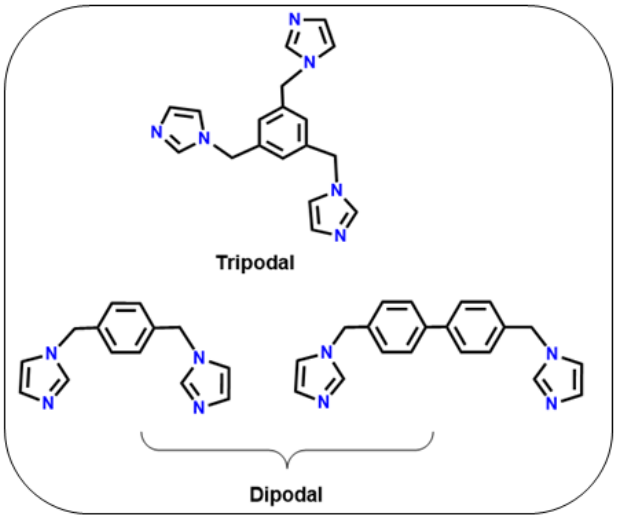

Figure 19: *Representative example of flexible 1-imidazole-containing multipodal ligands, adapted from [172].*

These ligands can be further divided into two categories [172]:

- **Rigid:** The term "rigid" typically refers to ligands with a well-defined and inflexible structure, which means they possess a certain rigidity and stability, which can reduce the uncertainty in the assembly process, and in most situations, result in a densely packed coordination architecture.
- **Flexible:** On the other hand, these ligands have a more flexible structure compared to their rigid counterparts. The flexibility in these ligands can be attributed to the presence of flexible linkers or substituents, allowing for a certain degree of conformational freedom. This flexibility further adds complexity to the resulting coordination architectures, as well as gives room to design architectures with tailored properties. See Figure 19 for a few representative examples of flexible 1-imidazole-containing ligands.

Many supramolecular coordination compounds (e.g. MOFs, CPs, and MCs), ZIFs (zeolitic imidazolate frameworks) being the most famous one, with attractive structures and advanced functions have been reported incorporating imidazole or its derivatives-based ligands and various metal ions [159, 160, 172-174].

In this thesis, we explored semi-rigid and flexible dipodal 1-imidazole-containing ligands, by varying aromatic core length and rigidity, and substitution on imidazole moiety, to further use them for the construction of porous metallocycles. These dipodal ligands can coordinate via N-atoms of imidazole moiety with metal ions in a different fashion to yield a variety of coordination compounds.

Section 2

Experimental Part

"The important thing in science is not so much to obtain new facts as to discover new ways of thinking about them." – Sir William Henry Bragg (1862–1942), Nobel Prize for Physics 1915.

This section includes the experimental techniques used for the prepared ligands and metal-complexes crystallization and characterization, as well as detailed ligand synthesis and basic procedure to obtain metal-complexes.

8. Experimental methodology

8.1. Single-Crystal X-Ray Diffraction (SC-XRD)

Single-crystal X-ray diffraction data were collected on a Rigaku XtaLab Synergy-S diffractometer equipped with graphite-monochromated CuKα radiation (λ = 1.5418 Å). The crystals were coated with Paratone-N oil and mounted on a nylon loop. Data collection was carried out at 100(2) K to minimize solvent loss, possible structural disorder, and thermal motion effects. Data frames were processed (unit cell determination, intensity data integration, correction for Lorentz and polarisation effects, and empirical absorption correction) by using the corresponding diffractometer's software package [175]. The structures were solved by using intrinsic phasing methods with SHELXT-2018/3 or direct methods with SHELXS-2018/3 [176] and refined by using full-matrix least-squares methods based on F^2 by using SHELXL-2018/3 [177] through the Olex [178] interface. Non-hydrogen atoms were refined with anisotropic displacement parameters. The hydrogen atoms were included in idealized positions and were refined according to the riding model except the water hydrogen atoms which were located in the difference electron density maps and refined freely with restrained O-H bond lengths. The structures: **MC2-b, MC7, MC10-a** and **CP2-a** were solved as a two-component non-merohedral twin with a twin-component ratio of 0.52:0.48, 0.87:0.13, 0.7:0.3 and 0.52:0.48, respectively. Highly disordered solvent molecules in some of the structures of metal-complexes were squeezed with Platon application: **MC1**- shows presence of 207 electrons in a void volume of 1001 $Å^3$ per unit cell, which accounts for approximately 2.5

acetonitrile molecules per metallocycle, **MC6-** shows 7 electrons count in a void volume of 152 $Å^3$ per unit cell, which could correspond to 0.7 H_2O molecules per formula unit, **MC7-** shows 39 electrons in a void volume of 317 $Å^3$ per unit cell corresponding to around 1 MeOH molecule per formula unit, **MC10-** 367 electrons per unit cell having a void volume of 1693 $Å^3$ which correlates roughly with the presence of 4.5 DMF molecules per formula unit and **MC11 –** shows 239 electrons in a void volume of 817 $Å^3$ per unit cell, which corresponds to around 6 DMF molecules per formula unit out of which 2 DMF molecules per asymmetric unit were refined and other were squeezed due to diffuse residual electron density. Representations of all crystal structures were generated using the program Mercury [179] and POV-Ray [180].

8.2. Powder X-Ray Diffraction (PXRD)

PXRD patterns for the samples used in this thesis were obtained on a Philips X'Pert diffractometer using CuKα radiation. The samples were measured at the 2θ range of 4-45º with a scan speed of 4º/min. The PXRD data were analyzed using the Match [181], PowderCell [182] and Profex [183] software packages.

8.3. Nuclear Magnetic Resonance (NMR) Spectroscopy

This technique was used for the characterization of the ligands used in the work presented here. ^1H and ^{13}C spectra were recorded in $CDCl_3$ solution on a Bruker Avance NMR spectrometer operating at 700, 400, and 300 MHz. The chemical shifts are referenced with respect to tetramethylsilane.

8.4. Melting Point Determination

The melting points of the compounds were determined using a Stuart SMP50 automated melting point apparatus, starting at a temperature of 30°C and ramping up at 2°C/min.

8.5. Thermogravimetric Analysis

Thermal analysis (TGA, DTA) was performed on a TA Instruments SDT 650 analyzer or on a Perkin Elmer Pyris STA9 analyzer at a heating rate of 2 °C min^{-1} under dry nitrogen with a flow rate of 100 ml min^{-1} and 20 mL $min^{-1,}$ respectively, covering the temperature range: 25-600 °C.

8.6. Computational Studies

Hirshfeld surface analysis [184] was performed using CrystalExplorer 17 [185], generating 2D fingerprint plots for all interactions present in various ligand forms within the range of 0.4–2.8 Å. These plots, including reciprocal contacts, quantified the contribution of different interactions in each form. The same software was utilized to calculate crystal lattice energies using the dispersion-corrected CE-B3LYP/6-31G(d,p) model. Additionally, PIXEL [186, 187] with MP2/6-31G level of theory, using the Gaussian09/16 quantum chemistry package [188, 189], and DFT [190] were employed for lattice energy calculations in certain cases. Molecular packing similarity was assessed using the Mercury [179] and XPac program [191].

8.7. Gas/Vapour Adsorption

Adsorption isotherms were determined at a temperature of 25°C using a gravimetric adsorption apparatus equipped with Baratron pressure transducers (MKS Instruments, Germany). Each sample was thermally desorbed before the measurement under high vacuum until a constant mass was obtained (after ca. 2 days).

8.8. Crystallization Techniques

The crystals of ligands suitable for SCXRD were obtained via slow evaporation and vapour diffusion. A number of methods were used especially for crystallization of metal-complexes as described below.

8.8.1. Slow Evaporation

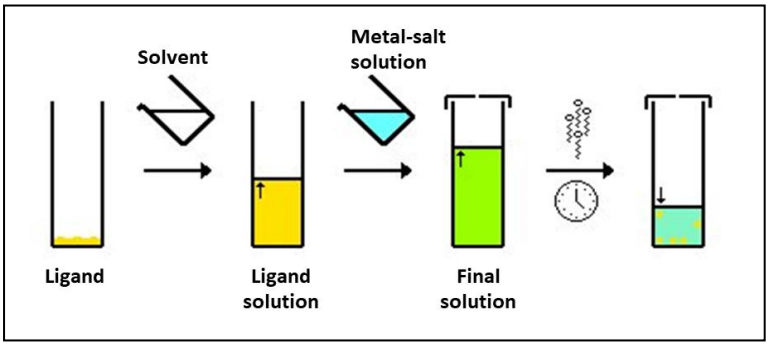

Figure 20: *Figure showing single-crystal growth of metal-complexes by slow evaporation of solvent.*

Good quality crystals in most of the cases were obtained using this method for both ligands and metal-complexes (Figure 20). To obtain the crystals of a particular product, a reaction solution was covered with parafilm punctured with holes and was allowed to undergo slow

evaporation. Solvents such as MeOH, EtOH, CH_3CN, DCM, $CHCl_3$, acetone, THF, etc. were used.

8.8.2. Vapour Diffusion

This procedure was applied in case of obtaining crystals of some metal complexes. The solution after reaction of complexation was transferred into a smaller vial (Figure 21). This vial was then placed inside a larger vial filled with an anti-solvent. After covering the vial, it was left undisturbed to facilitate the formation of single crystals. Common pairs of solvent and antisolvent used were MeOH and hexane, DCM and diethyl ether, THF and cyclohexane, etc.

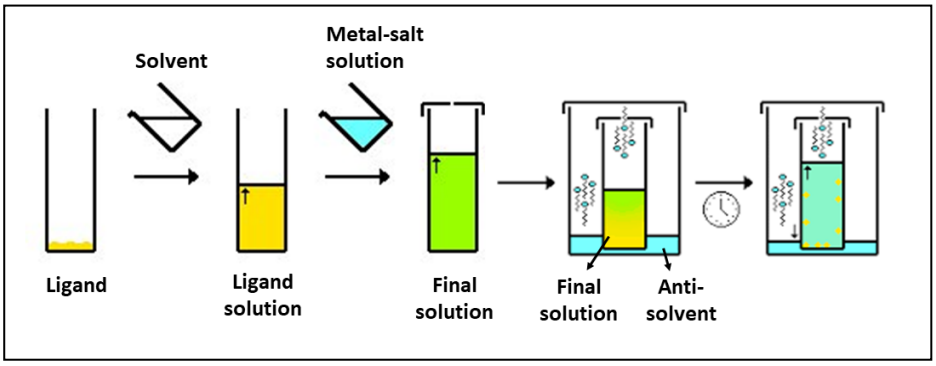

Figure 21: *Figure showing single-crystal growth of metal-complexes by the vapour diffusion method.*

8.8.3. Solvent Layering or Liquid Diffusion

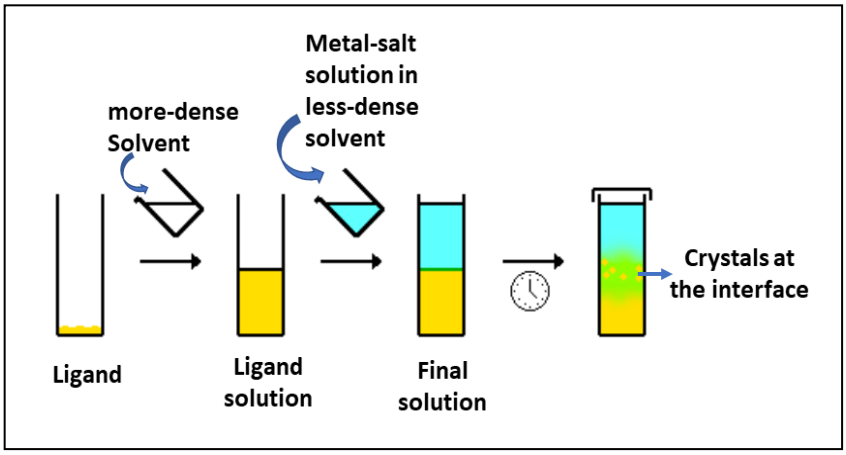

Figure 22: *Figure showing the growth of single-crystals of metal-complexes by the liquid diffusion method.*

This procedure as above was applied to obtain crystals of some of the metal complexes. In this method, a solution of metal salt in a less-dense solvent was carefully layered over a solution of ligand in a more-dense solvent to form two distinct layers (Figure 22). Crystals

were obtained at the interface of two layers. Common pairs of solvent and antisolvent that lead to good quality crystals by this method were $CHCl_3$/DCM and MeOH, DMF/DMSO and EtOH, methanol and hexane, etc.

8.8.4. Solvothermal Synthesis

In rare instances, crystals of metal-complexes were obtained through solvothermal crystallization. In this approach, all reaction components such as the ligand, metal salt in specific ratios, and solvent were combined in a Teflon-lined, sealed autoclave, which was then heated in an oven at a set temperature for several days, after which it was gradually cooled to room temperature at a controlled rate (Figure 23).

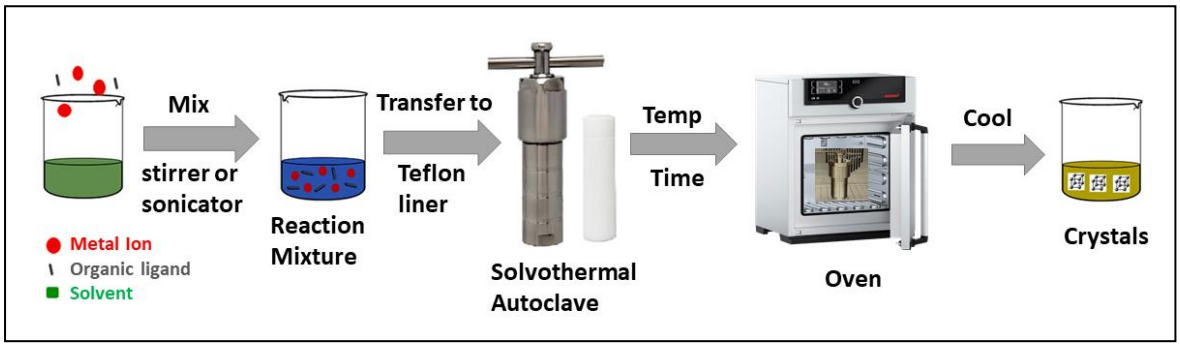

Figure 23: *Figure showing the growth of single-crystals of metal-complexes by solvothermal method.*

The primary solvents used in this work were CH_3CN and DMF, though, depending on solubility requirements, single or mixed solvents can be advantageous.

9. Synthesis and Basic Characterization of Dipodal Ligands (L1-L12)

Several N-donor ligands based on pyridine and imidazole moieties were attempted to synthesize for this project. As the synthesis with pyridine-based ligands did not work well, the focus was shifted more towards imidazole-based ligands. The Figure 24 presents the schematic representation of the synthesized ligands: 1) ligands utilized in obtaining metal complexes discussed in the chapter 12 (highlighted in circle), 2) ligands that didn't result in the formation of good quality single crystals of metal complexes but were used in further solid-state studies (not highlighted ones). The ligands highlighted in red are the novel ones and were utilized for the first time for metal-complexation.

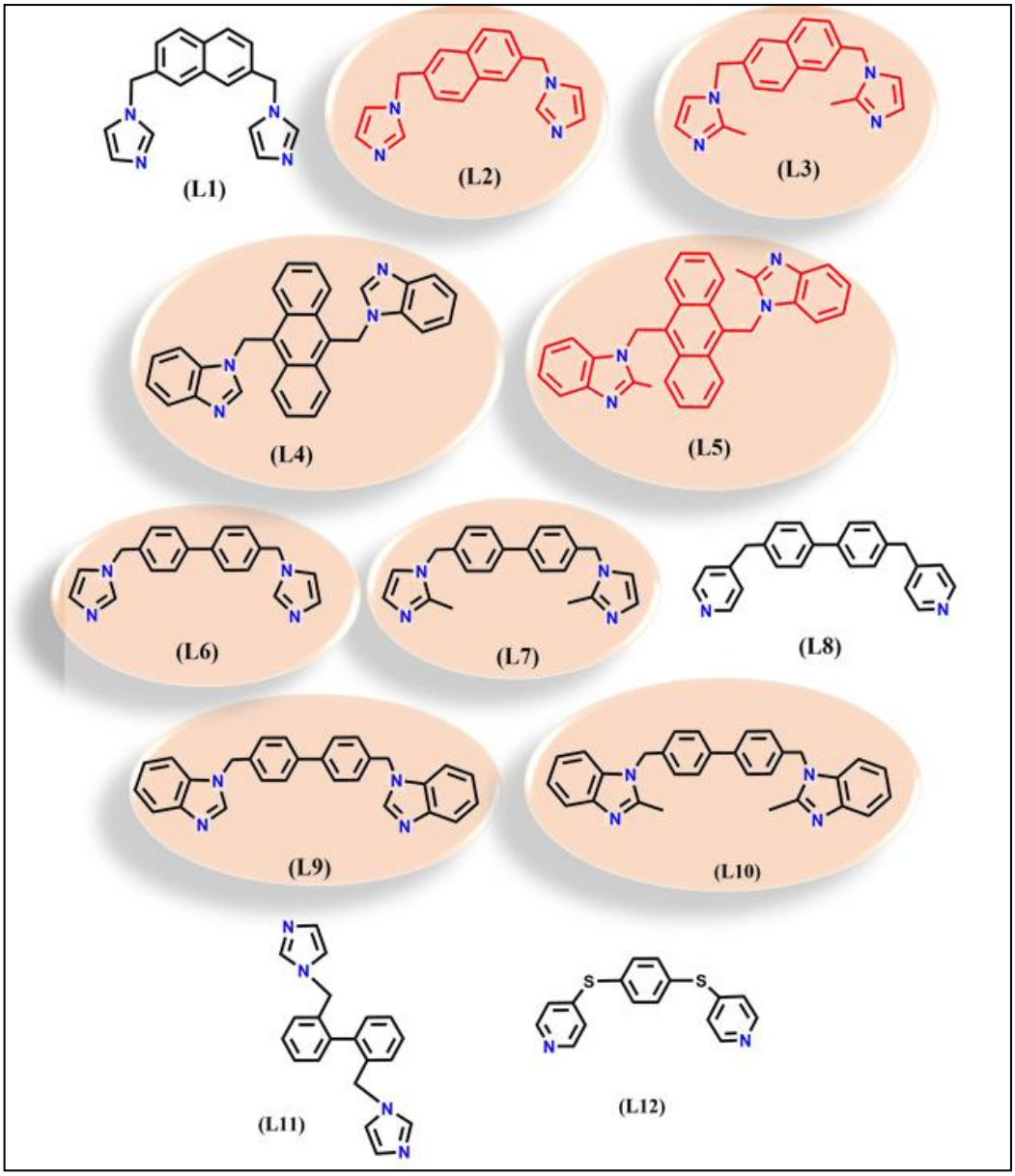

Figure 24: *Schematic representation of the synthesized ligands.*

9.1. Synthetic Procedures

The ligands were synthesized using conventional methods of organic chemistry, mostly nucleophilic substitution [192]. The melting point of each solid sample was recorded and % yield was calculated. The compounds were characterized by ^{1}H-NMR and ^{13}C-NMR.

9.1.1. 2,7-Bis((imidazol-1-yl)methyl)naphthalene (L1):

Although the synthesis of ligand **L1** has been previously reported during the preparation of naphthalenophane ligand [193], I employed an alternative method, detailed below.

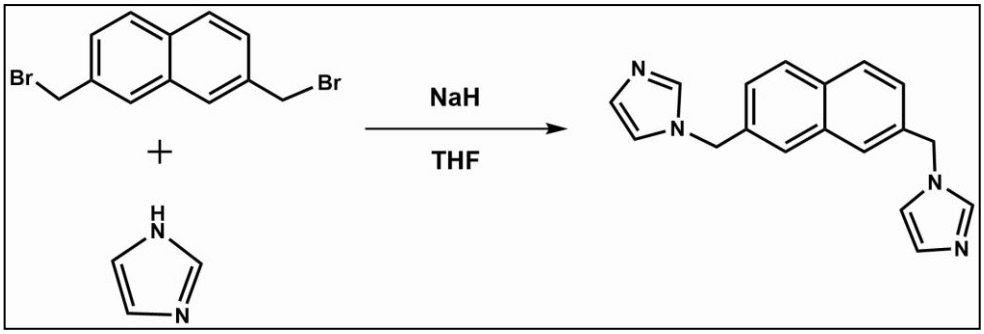

Imidazole (1.3 g, 19.08 mmol) dissolved in 20 ml dry THF was slowly added to sodium hydride (60% in oil, 0.763 g, 19.08 mmol) in dry THF (20 mL) at 0ºC, and the resulting suspension was stirred at rt for 2 h (until the hydrogen gas evolution ceased). 2,7-bis(bromomethyl)naphthalene (1 g, 3.18 mmol) solution in 25 ml dry THF was then added to the resulting mixture slowly and was refluxed for another 12 h. The obtained mixture was dissolved in water and extracted with DCM (3*50 mL). The combined organic layers were washed with water (100 mL), dried over anhydrous magnesium sulfate and filtered. After removal of the solvent under reduced pressure, the product was re-dissolved in ethyl acetate and hexane was added dropwise until the cloudiness and left at rt to precipitate the pure product as a yellow solid.

Yield - 52% **Melting point- 138-141^{0}C**

^{1}H NMR (700 MHz, $CDCl_3$): δ 7.83-7.84(d, 2H), 7.61(s, 2H), 7.54(s, 2H), 7.28-7.30(d, 2H), 7.13(s, 2H), 6.95(s, 2H), 5.28(s, 4H)

^{13}C NMR (175 MHz, $CDCl_3$): δ 137.52, 134.57, 133.19, 132.57, 129.97, 128.84, 126.16, 125.46, 119.37, 50.86

9.1.2. 2,6-Bis((imidazol-1-yl)methyl)naphthalene (L2):

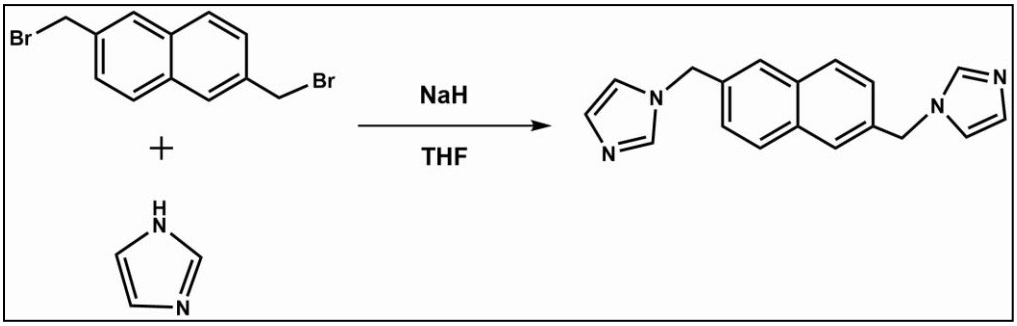

Similar procedure as above was employed for the synthesis of **L2**. Sodium hydride (0.695 g, 18 mmol) was weighed in an RB flask, 30 ml dry THF was added to it under an argon atmosphere and a solution of imidazole (1.23 g, 18 mmol) in 30 ml dry THF was added to this solution dropwise at room temperature and stirred for 2

hours. After 2 hours, 2,6-bis(bromomethyl)naphthalene (2 g, 6.37 mmol) solution in 40 ml dry THF was added to the above mixture slowly and refluxed overnight. The resulting solution was evaporated, quenched with water, and extracted using DCM, and recrystallized with MeOH to yield the product as a yellow solid.

Yield- 95% **Melting Point- 178-180^{o}C**

^{1}H NMR ($CDCl_3$, 400 MHz): δ 7.78-7.80(d, 2H), 7.64(s, 2H), 7.58(s, 2H), 7.28-7.31(dd, 2H), 7.13(t, 2H), 6.94-6.95(t, 2H), 5.29(s, 4H)

^{13}C NMR ($CDCl_3$, 100 MHz): δ 137.52, 134.35, 132.86, 129.92, 128.91, 126.07, 125.66, 119.38, 50.83

9.1.3. 2,6-Bis((2-methylimidazol-1-yl)methyl)naphthalene (L3):

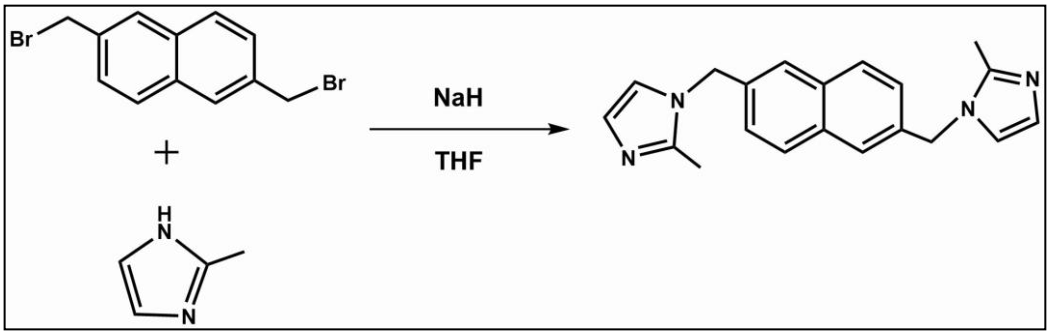

Similar procedure like for **L1** an **L2** was employed for the synthesis of another new ligand **L3**. Sodium hydride (0.695 g, 18 mmol) was weighed in an RB flask, 30 ml dry THF was added to it under an argon atmosphere, a solution of 2-methylimidazole (1.478 g, 18 mmol) in 30 ml dry THF was added to the above solution dropwise at room temperature and stirred for 2 hours. After 2 hours, 2,6-bis(bromomethyl)naphthalene (2 g, 6.37 mmol) solution in 40 ml dry THF was added to the above mixture slowly and refluxed overnight. The resulting solution was evaporated, quenched with water, and extracted using DCM, and recrystallized with MeOH to yield the product as an off-white solid.

Yield- 94% **Melting Point- 202-204^{o}C**

^{1}H NMR ($CDCl_3$, 400 MHz): δ 7.77-7.79(d, 2H), 7.43(s, 2H), 7.23-7.24(d, 2H), 7.06(d, 2H), 6.92(d, 2H), 5.24(s, 4H), 2.45(s, 6H)

^{13}C NMR ($CDCl_3$, 100 MHz): δ 144.99, 134.39, 132.78, 128.84, 127.35, 125.22, 125.19, 120.02, 49.80, 13.08

9.1.4. 9,10-bis((benzimidazol-1-yl)methyl)anthracene (L4):

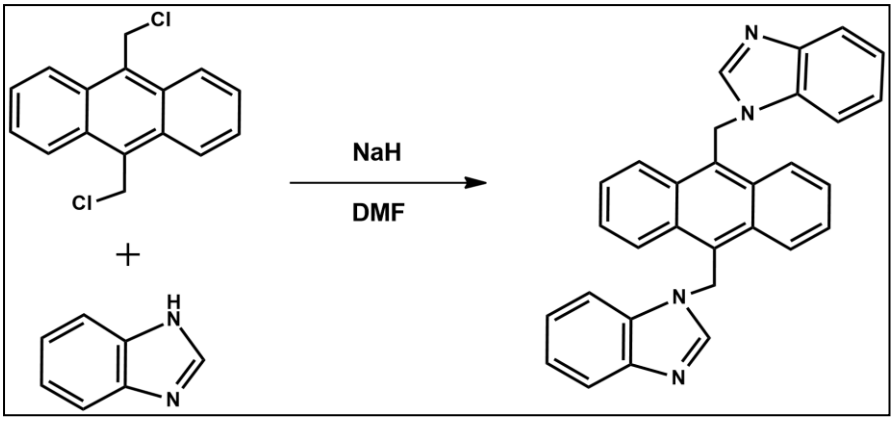

The procedure for the synthesis of **L4** was adapted from [194], wherein it was used to synthesize a new fluorescent probe 9,10-bis[1-(2-naphthalenylbenzimidazolium)-3-methyl]anthracene.

Sodium hydride (0.43 g, 11 mmol) was weighed in an RB flask, 15 ml dry DMF was added to it under an argon atmosphere, a solution of benzimidazole (1.3 g, 11 mmol) in 15 ml dry DMF was added to the above solution dropwise at room temperature and stirred for 2 hours. After 2 hours, 9,10-bis(chloromethyl)anthracene (1 g, 3.63 mmol) solution in 20 ml dry DMF was added to the above mixture slowly and refluxed overnight. The resulting solution was quenched with water and extracted using DCM. The resulting solid was purified by flash chromatography (Eluent- 0 to 2% MeOH in DCM).

Yield- 30% **Melting Point- 190-192^{0}C**

^{1}H NMR ($CDCl_3$, 400 MHz): δ 8.25-8.27(dd, 4H), 7.85-7.87(dt, 2H), 7.74-7.76(dt, 2H), 7.57-7.60(dd, 4H), 7.44-7.49(m, 2H), 7.37-7.41(m, 2H), 7.32(s, 2H), 6.29(s, 4H).

9.1.5. 9,10-bis((2-methyl-1H-benzimidazol-1-yl)methyl)anthracene (L5):

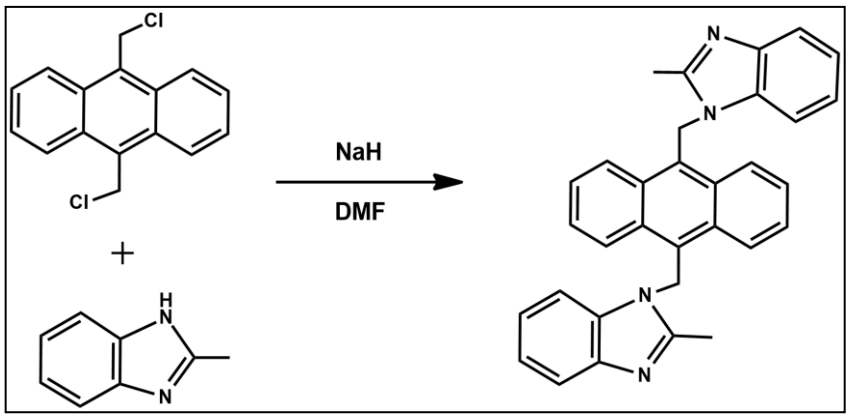

Similar procedure like for **L4** was used for the synthesis of **L5**. Sodium hydride (0.43 g, 11 mmol) was weighed in an RB flask, 15 ml dry DMF was added to it under an argon atmosphere, a solution of 2-methylbenzimidazole (1.45 g, 11 mmol) in 15 ml dry DMF was added to the above solution dropwise at room temperature and stirred for 2 hours. After 2 hours, 9,10-bis(chloromethyl)anthracene (1 g, 3.63 mmol) solution in 20 ml dry DMF was added to the above mixture slowly and refluxed overnight. The resulting solution was quenched with water and extracted using DCM. The resulting solid was purified by flash chromatography (Eluent- 0 to 3% MeOH in DCM).

Yield- 27% **Melting Point- 215-217^{0}C**

^{1}H NMR ($CDCl_3$, 400 MHz): δ 8.25-8.28(dd, 4H), 7.80-7.82(d, 2H), 7.66-7.68(d, 2H), 7.51-7.63(dd, 4H), 7.14-7.17(m, 2H), 6.94-6.98(m, 2H), 6.33(s, 4H), 2.38(s, 6H)

9.1.6. 4,4′-bis((1H-imidazol-1-yl)methyl)-1,1′-biphenyl (L6):

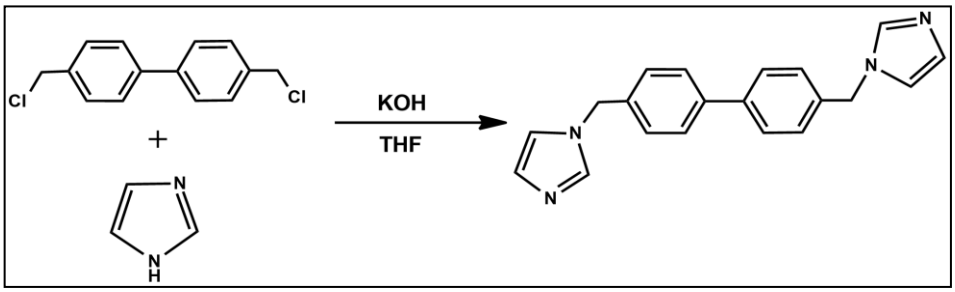

The ligand was reported previously [195] but I used a modified procedure. A mixture of imidazole (3.36 g, 60 mmol) and KOH (4.08 g, 60 mmol) in 100 ml THF was stirred in an RB flask for 4h at room temperature. Then, a solution of 4,4'-bis(chloromethyl)biphenyl in 100 ml THF was added dropwise to the above solution. After complete addition, the resulting solution was stirred for 2 days at room temperature, and then the solvent was evaporated. 50 ml water was added to the obtained yellow solid and the aqueous layer was extracted with DCM. The organic layer was washed with water, dried with $MgSO_4$ and concentrated under reduced pressure. The product was obtained as an off-white solid.

Yield: 80% **Melting Point- 162-165^{0}C**

^{1}H NMR ($CDCl_3$, 700 MHz) δ 7.65 (s, 2H), δ 7.58 (d, 4H), δ 7.26 (d, 4H), 7.15(t, 2H), 6.96(t, 2H), 5.20 (s, 4H)

^{13}C NMR (CDCl$_3$, 100 MHz) δ 140.34, 137.44, 135.58, 129.89, 127.81, 127.60, 119.29, 50.43

9.1.7. 4,4′-bis((2-methyl-imidazol-1-yl)methyl)-1,1′-biphenyl (L7):

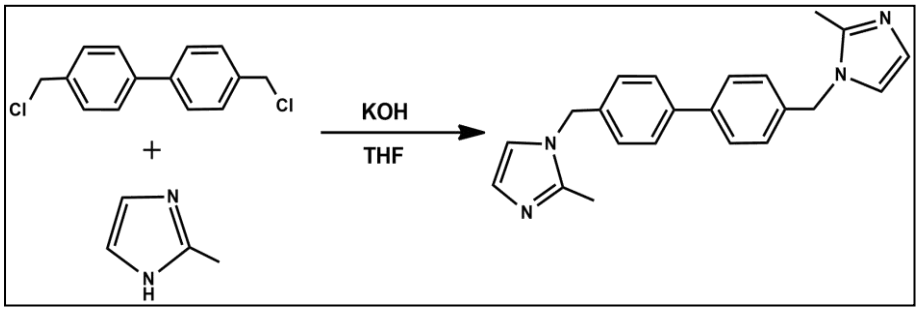

L7 was synthesized using a similar procedure like for **L6** and was reported previously during the synthesis of bisimidazolium salts [196]. 2-methylimidazole (2.463 g, 30 mmol) and KOH (2.04 g, 30 mmol) were combined in 50 ml THF and stirred in a round-bottom flask for 4 hours at room temperature. Subsequently, a solution of 4,4'-bis(chloromethyl)biphenyl (2.55 g, 10 mmol) in 50 ml THF was slowly added dropwise to the above mixture. Following the complete addition, the resulting solution was stirred for 2 days at room temperature, and then the solvent was evaporated. To the resulting yellow solid, 50 ml of water was added, and the aqueous layer was extracted with DCM. The organic layer was washed with water, dried using $MgSO_4$, and concentrated under reduced pressure. The product was obtained in the form of a yellow solid.

Yield: 81% **Melting Point: 168-170^{0}C**

^{1}H NMR (CDCl$_3$, 700 MHz) δ 7.55-7.56 (d, 4H), 7.14-7.15(d, 4H), 7.01(d, 2H), 6.90(d, 2H), 5.12(s, 4H), 2.40(s, 6H)

^{13}C NMR (CDCl$_3$, 100 MHz) δ 144.94, 140.09, 135.73, 127.57, 127.49, 127.17, 119.90, 49.42, 13.16

9.1.8. 4,4′-bis((pyridin-4-yl)methyl)-1,1′-biphenyl (L8):

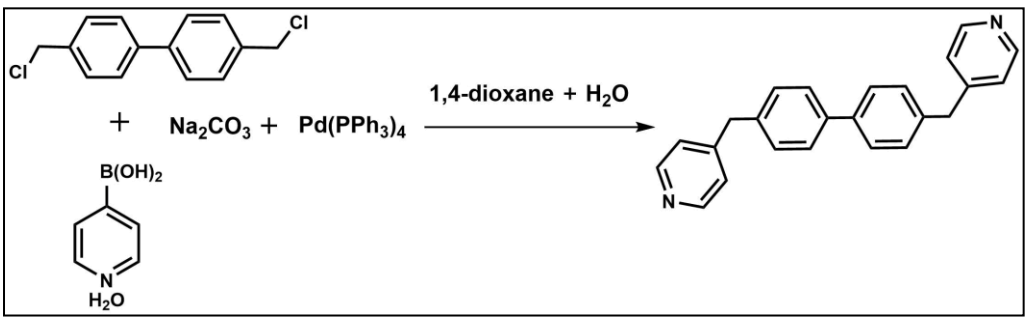

This ligand was also reported elsewhere [197] but I used a modified procedure. 4,4'-bis(chloromethyl)biphenyl (2 g, 7.96 mmol), 4-pyridinylboronic acid (2.4 g, 19.52 mmol) and Na_2CO_3 (3.446 g, 32.51 mmol) were weighed and added in an RB flask. Under argon, $Pd(PPh_3)_4$ (0.462 g, 0.4 mmol) was added to the same flask. 1,4-dioxane (32 ml) and water (16 ml) were added to the above flask, and the reaction mixture was refluxed at 100^0C for 4 hours. Upon reaction completion (after 4 h, monitored by TLC), the mixture was cooled down, and quenched with water. The aqueous layer was extracted with DCM, and the organic layer was dried over $MgSO_4$ and evaporated under reduced pressure. The resulting solid was purified by flash chromatography (Eluent- 0 to 3% MeOH in DCM).

Yield- 13% **Melting Point- 112-116^{0}C**

^{1}H NMR ($CDCl_3$, 700 MHz) δ 8.54 (d, 4H), 7.55 (d, 4H), 7.27 (d, 4H), 7.19 (d, 4H), 4.04 (s, 4H)

^{13}C NMR ($CDCl_3$, 100 MHz) δ 149.89, 139.17, 137.97, 129.47, 127.31, 124.91, 40.87

9.1.9. 4,4′-bis((1H-benzimidazol-1-yl)methyl)-1,1′-biphenyl (L9):

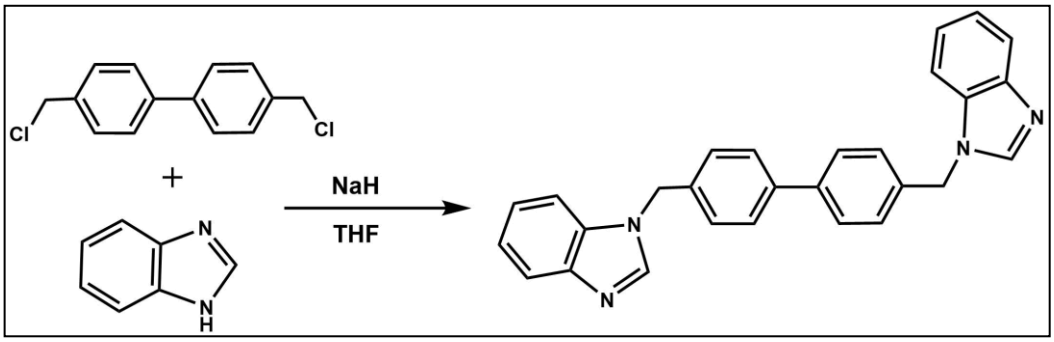

Similar procedure as for **L1, L2** and **L3** was used for the synthesis of **L9**. Sodium hydride (0.695 g, 18 mmol) was weighed in an RB flask, 30 ml dry THF was added to it under an argon atmosphere and a solution of benzimidazole (2.12 g, 18 mmol) in 30 ml dry THF was added to the above solution dropwise at room temperature and stirred for 2 hours. After 2 hours, 4,4'-bis(chloromethyl)biphenyl (2 g, 5.88 mmol) solution in 40 ml dry THF was added to the above mixture slowly and refluxed overnight. The resulting solution was evaporated, quenched with water, and extracted using DCM. The resulting solid was purified using flash chromatography (DCM: MeOH in 90:10).

Yield: 72% **Melting Point: 162-165^{0}C**

^{1}H NMR (CDCl$_3$, 700 MHz) δ 7.99 (s, 2H), 7.83-7.85(dt, 2H), 7.50-7.53(dt, 4H), 7.23-7.33(m, 10H), 5.40(s, 4H)

^{13}C NMR (CDCl$_3$, 100 MHz) δ 143.87, 143.20, 140.30, 134.81, 133.89, 127.64, 123.22, 122.43, 120.39, 110.11, 48.52

9.1.10. 4,4′-bis((2-methyl-1H-benzimidazol-1-yl)methyl)-1,1′-biphenyl (L10):

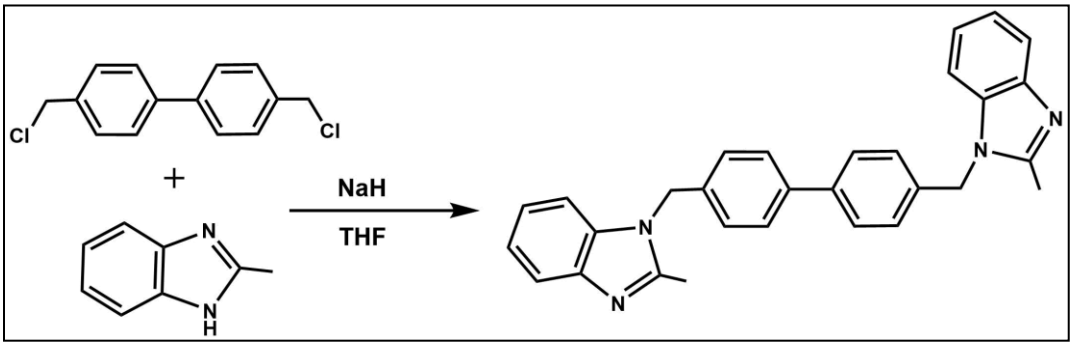

L10 was also synthesized using the similar procedure as for **L9**. Sodium hydride (0.765 g, 19.75 mmol) was weighed in an RB flask, 30 ml dry THF was added to it under an argon atmosphere, a solution of 2-methylbenzimidazole (2.6 g, 19.75 mmol) in 30 ml dry THF was added to the above solution dropwise at room temperature and stirred for 2 hours. After 2 hours, 4,4'-bis(chloromethyl)biphenyl (2 g, 7.96 mmol) solution in 40 ml dry THF was added to the above mixture slowly and refluxed overnight. The resulting solution was evaporated, quenched with water, and extracted using DCM. The resulting solid was purified using flash chromatography (DCM: MeOH in 97:3).

Yield: 25% **Melting Point: 209-211^{0}C**

^{1}H NMR (CDCl$_3$, 400 MHz) δ 7.76-7.79(dt, 2H), 7.46-7.50(dt, 4H), 7.23-7.31(m, 6H), 7.10-7.13(d, 4H), 5.38(s, 4H), 2.65(s, 6H)

^{13}C NMR (CDCl$_3$, 100 MHz) δ 151.80, 142.45, 140.07, 135.37, 135.10, 127.62, 126.77, 122.43, 122.13, 119.16, 109.36, 46.84, 13.98

9.1.11. 2,2′-bis((1H-imidazol-1-yl)methyl)-1,1′-biphenyl (L11):

Preparation of **L11** was carried out according to the procedure reported in the literature [198].

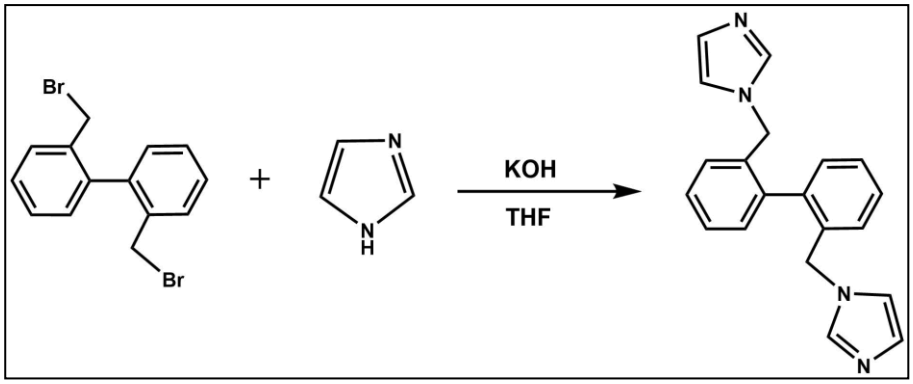

Imidazole (3.36 g, 60 mmol) and KOH (4.08 g, 60 mmol) were weighed in an RB flask and stirred at room temperature in 100 ml THF. After 4h, a solution of 2,2'-bis(bromomethyl)biphenyl (3.4 g, 10 mmol) in 100 ml THF was added dropwise to the above solution. After complete addition, the resulting solution was stirred for 2 days at room temperature. Then, the solvent was evaporated, and 50 ml of water was added to the resulting pale yellow solid. The aqueous layer was extracted 3 times (*50 ml) with DCM, and the combined organic fractions were washed with water, dried with $MgSO_4$, filtered, and concentrated under reduced pressure, yielding the product as a yellow solid.

Yield: 55% **Melting point: 117-119 ^{0}C**

^{1}H NMR ($CDCl_3$, 700 MHz) δ 7.42-7.46(m, 4H), 7.21-7.23(d, 2H), 7.14-7.15(d, 2H), 7.04(s, 2H) 7.02(d, 2H), 6.67(t, 2H), 4.5(dd, 4H)

^{13}C NMR ($CDCl_3$, 100 MHz) δ 139.0, 137.3, 134.5, 129.6, 129.0, 128.8, 128.6, 119.0, 48.6

9.1.12. 1,4-bis(thiopyridine)benzene (L12):

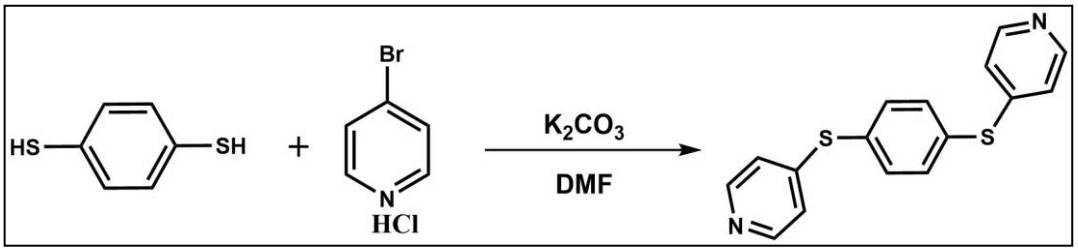

The novel ligand 1,4-bis(thiopyridine)benzene was synthesized using a modified procedure adapted from the method reported for the synthesis of 2-benzenesulfonyl-pyridine [199]. A 25 ml flask was charged with 4-bromopyridine hydrochloride (1.45 g, 7.5 mmol), 1,4-benzenedithiol (0.5 g, 3.5 mmol), and DMF (5 mL). K_2CO_3 (2.21 g, 16 mmol) was added to the above flask, and the mixture was heated to 110°C and stirred for 24 h. The resulting

mixture was extracted using water and ethyl acetate. The organic layer was washed with water, dried using $MgSO_4$ and concentrated to give yellowish solid as a pure product.

Yield: 88% **Melting Point: 133-135^{0}C**

^{1}H NMR ($CDCl_3$, 700 MHz) δ 7.14-7.15(d, 4H), 7.60-7.64(t, 4H), 8.47(s, 4H)

^{13}C NMR ($CDCl_3$, 100 MHz) δ 49.81, 148.54, 135.34, 132.05, 121.69

10. Synthesis of Coordination Compounds

10.1. Based on Naphthalene Core Ligands: L2 and L3

10.1.1. L2: MC1: $[Cu_2(L2)_2Cl_4]\cdot xS$

The reaction of naphthalene core-based ligand **L2** with $CuCl_2\cdot H_2O$ was performed in different ratios in different solvents using different crystallization methods (Figure 25), and all these setups resulted in the formation of the same metallocycle **(MC1)**. Each of these complexation reactions yielded crystals suitable for single-crystal X-ray diffraction. Since all the crystallisation products were isostructural, the metallocycle (**MC1**) obtained via the slow evaporation of an equimolar mixture of **L2** (0.1 mmol) with $CuCl_2\cdot H_2O$ (0.1 mmol) in acetonitrile was studied further.

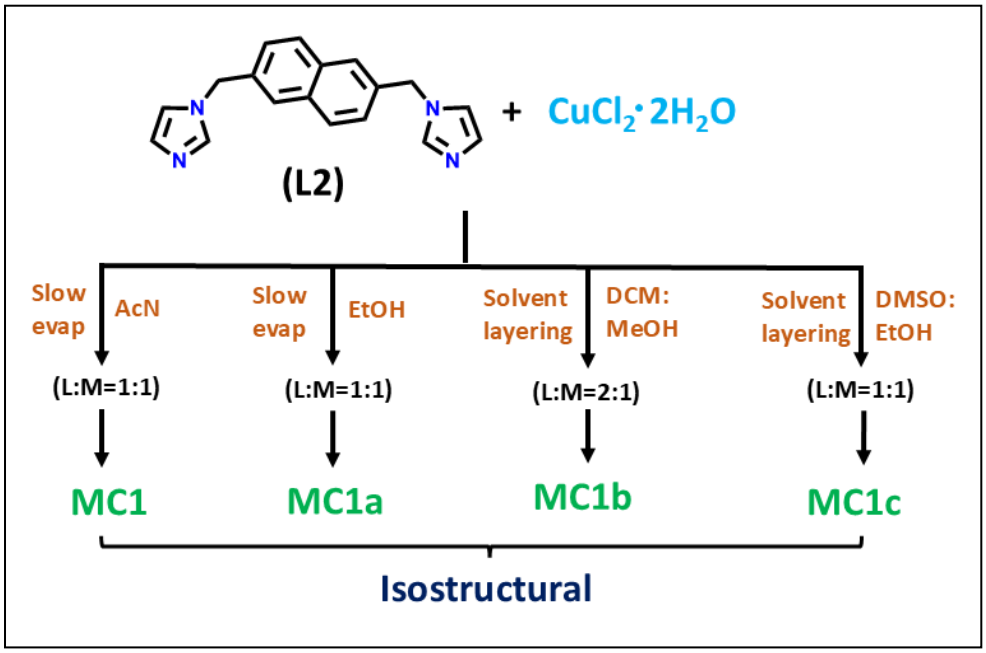

Figure 25: *Schematic representation of the synthetic conditions and crystallization setups resulted in metallocycle **MC1**.*

10.1.2. L3: MC2: $[Co_2(L3)_2Cl_4]\cdot 0.8CH_3CN$, CP1: $[Co(L3)Cl_2]_n$, CP2: $\{[Cu(L3)Cl_2]\cdot CH_3CN\}_n$ and CP3:$\{[Cd(L3)Cl_2]\cdot CH_3CN\cdot 0.2H_2O\}_n$

L3, a novel ligand containing a rigid naphthalene core that was synthesized for the first time for this study, was used for metal-complexation with various metal salts. But not all the set ups successfully produced crystals. Interestingly, crystals of a 0D metallocycle (**MC2**) was exclusively formed by reacting **L3** (0.1 mmol) with $CoCl_2 \cdot 6H_2O$ (0.1 mmol) through slow evaporation in acetonitrile. However, performing a similar reaction in a different solvent system using solvent layering resulted instead in a 1D zig-zag chain coordination polymer **(CP1)**. Good quality crystals of **CP1** were obtained by layering the solution of $CoCl_2 \cdot 6H_2O$ (0.1 mmol) in MeOH (10 ml) over the solution of **L3** (0.1 mmol) in $CHCl_3$ (10 ml), respectively. These results demonstrate the challenge of controlling crystallization outcomes, as even minor changes in conditions can significantly alter the final product. Additionally, attempts to react **L3** with $CuCl_2 \cdot 2H_2O$ and $CdCl_2 \cdot 2.5H_2O$ in equimolar amount via slow evaporation in acetonitrile led to formation of 1D coordination polymers: **CP2** and **CP3** respectively (Figure 26).

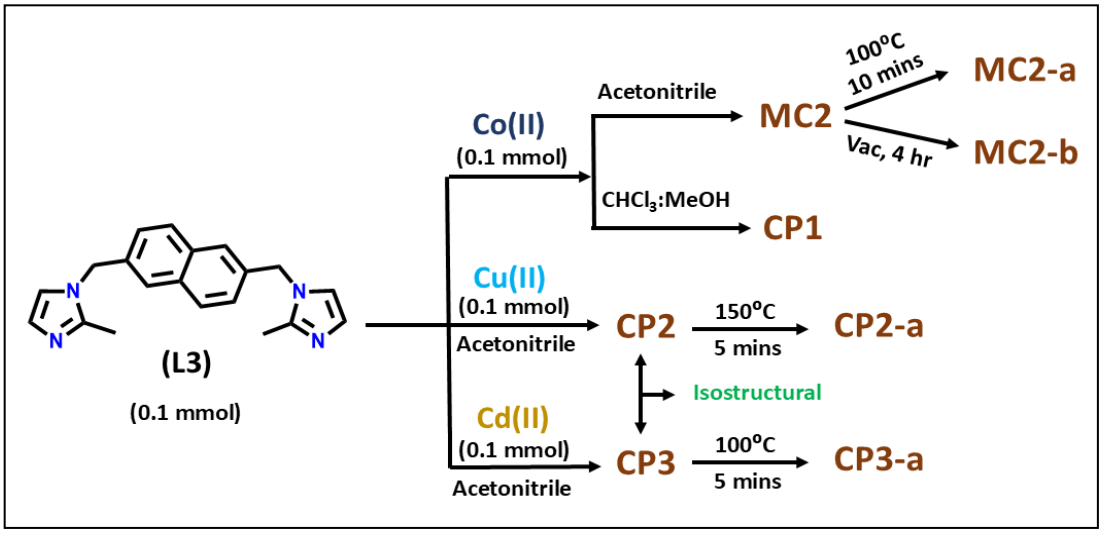

Figure 26: *Schematic representation of synthetic conditions to obtain **MC2**, **CP1**, **CP2** and **CP3** and corresponding SC-SC transformation conditions.*

10.2. Based on Partially Embedded Anthracene Moiety/ Ligands L4 and L5

Due to the limited solubility of anthracene-based ligands, all the metal-complexations conducted at room temperature resulted in a precipitate formation, with no crystal formation observed using slow evaporation, vapor diffusion, and solvent layering crystallization methods. To address this, solvothermal synthesis was employed in autoclaves at elevated temperatures, followed by controlled cooling to room temperature. While most attempts still did not yield crystals, a few crystallizations were successful.

10.2.1. L4: MC3 $[Co_2(L4)_2Cl_4]\cdot CH_3CN$ and MC4:$[Co_2(L4)_2Br_4]\cdot 4CH_3CN$

The metallocycles **MC3** and **MC4** were obtained by the reaction of equimolar amounts of $CoCl_2\cdot 6H_2O$ and $CoBr_2\cdot H_2O$ (0.1 mmol) with **L4** (0.1 mmol) in 10 ml acetonitrile at 120°C in an autoclave for 3 days in the oven, which on subsequent cooling until the room temperature at the rate of 5°C/h resulted in blue and bluish-green block crystals, respectively.

10.2.2. L5: MC5 $[Co_2(L5)_2Br_4]$

MC5 was obtained by the reaction of equimolar amounts of $CoCl_2\cdot 6H_2O$ (0.1 mmol) and **L5** (0.1 mmol) in 10 ml acetonitrile at 120ºC in an autoclave for 3 days in the oven, which on subsequent cooling until the room temperature at the rate of 5ºC/h resulted in blue block crystals, respectively.

10.3. Based on Biphenyl Core Ligands: L6, L7, L9 and L10

10.3.1. L6: MC6 $[Cu_2(L6)_2Cl_4]\cdot xS$ and MC7 $[Zn_2(L6)_2Cl_4]\cdot xS$

Two metallocycles **MC6** and **MC7** were obtained by the slow evaporation of the solution of $CuCl_2\cdot 2H_2O$ (0.1 mmol) and $ZnCl_2$ (0.1 mmol) salts with **L6** (0.1 mmol) in 40 ml methanol at room temperature.

Both solutions formed cloudy suspensions, yielding only a few single crystals upon crystallization. Efforts to improve crystal quality and quantity were made by exploring various solvents and crystallization methods; however, none of these approaches successfully produced single crystals. Notably, even when methanol was used again as the solvent, crystal formation could not be replicated.

10.3.2. L7: MC8 $[Cd_2(L7)_2Cl_4]\cdot 2CH_3OH$

The solution of $CdCl_2\cdot 2.5H_2O$ (0.1 mmol) in MeOH was layered over the solution of ligand 4,4′-bis(2-methylimidazol-1-ylmethyl)biphenyl **(L7)** (0.1 mmol) in $CHCl_3$ to afford colourless block-shaped crystals suitable for X-ray diffraction studies (SCXRD).

10.3.3. L9: MC9 $[Cu_2(L9)_2Cl_4]\cdot CH_2Cl_2$ and MC10 $[Zn_2(L9)_2(Cl)_4]$.xS

MC9 was obtained by the solvent layering of the solution of $CuCl_2 \cdot 2H_2O$ (0.1 mmol) in 10 ml MeOH over the solution of **L9** (0.1 mmol) in 10 ml DCM at RT which resulted in the formation of yellow block crystals between the two layers.

MC10 was obtained by layering EtOH solution of $ZnCl_2$ over DMF solution of **L9** in a molar ratio of 1:1 which yielded colorless block-shaped single crystals after a few days.

10.3.4. L10: MC11 $[Zn_2(L10)_2(Cl)_4] \cdot 4DMF \cdot xS$ and MC12 $[Zn_2(L10)_2(Cl)_4] \cdot 1DMF$

Both **MC11** and **MC12** were obtained concomitantly upon layering the EtOH solution of $ZnCl_2$ over a DMF solution of **L10** in a molar ratio of 1:1 which yielded colorless block-shaped single crystals.

11. Structural Studies on the Synthesized Ligands: SCXRD and Solid-State Investigation

SCXRD and supportive solid-state studies were conducted on the synthesized ligands, which, led to the isolation of polymorphs and hydrates. The crystallographic data of all isolated forms are summarized in the tables below. Results of **L1**, **L6**, **L8** and **L12** are published (mentioned in publications section).

Table 2: *Crystallographic data and structure refinement parameters for the anhydrate form **(a)** and hydrates (**b**, **c** and **d**) of **L1**.*

Compound reference	**L1a**	**L1b**	**L1c**	**L1d**
Chemical formula	$C_{18}H_{16}N_4$	$C_{18}H_{17}N_4O_{0.5}$	$C_{18}H_{18}N_4O$	$C_{18}H_{20}N_4O_2$
Formula Mass	288.35	297.35	306.36	324.38
Crystal system	Triclinic	Monoclinic	Orthorhombic	Monoclinic
a/Å	9.0492(3)	20.5410(4)	9.72620(10)	18.149(4)
b/Å	9.5052(4)	5.46830(10)	10.12810(10)	9.6466(19)
c/Å	9.9724(3)	26.6872(5)	31.3817(5)	9.3799(19)
α/°	62.525(4)	90	90	90
β/°	75.236(3)	102.478(2)	90	93.06(3)
γ/°	80.607(3)	90	90	90
Unit cell volume/$Å^3$	734.86(5)	2926.82(10)	3091.35(7)	1639.9(6)
Temperature/K	100(2)	100(2)	100(2)	100(2)
Space group	*P*-1	*C*2/*c*	*Pbca*	$P2_1/c$
No. of formula units per unit cell, Z	2	8	8	4
Radiation type	CuKα	CuKα	CuKα	CuKα
Absorption coefficient, μ/mm^{-1}	0.632	0.676	0.680	0.089

No. of reflections measured	26217	10042	26217	8358
No. of independent reflections	3044	2997	3187	2892
R_{int}	0.0441	0.0307	0.0644	0.0470
Final R_1[a] values ($I > 2\sigma(I)$)	0.0391	0.0371	0.0383	0.0581
Final wR_2[b] values ($I > 2\sigma(I)$) [b]	0.1008	0.0936	0.1030	0.1174
Final R_1[a] values (all data)	0.0444	0.0421	0.0428	0.0880
Final wR_2[b] values (all data)	0.1042	0.0973	0.1061	0.1293
Goodness of fit on F^2	1.056	1.048	1.039	1.057

Table 3: *Crystallographic data and structure refinement parameters for the polymorphs of **L6**, **L8**, **L11**, and **L12**.*

Compound reference	**L6a**	**L6b**	**L8a**	**L8b**	**L11a**	**L11b**	**L12a**	**L12b**
Chemical formula	$C_{20}H_{18}N_4$	$C_{20}H_{18}N_4$	$C_{24}H_{20}N_2$	$C_{24}H_{20}N_2$	$C_{20}H_{18}N_4$	$C_{20}H_{18}N_4$	$C_{16}H_{12}N_2S_2$	$C_{16}H_{12}N_2S_2$
Formula Mass	314.38	314.38	336.42	336.42	314.38	314.38	296.40	296.40
Crystal system	Monoclinic	Orthorhombic	Monoclinic	Monoclinic	Monoclinic	Orthorhombic	Monoclinic	Monoclinic
a/Å	5.66180(10)	18.2880(5)	20.7777(2)	5.76800(5)	10.0008(3)	7.83430(10)	10.5963(3)	7.6480(2)
b/Å	14.6008(2)	7.9130(2)	10.58810(10)	9.98210(10)	9.0946(2)	17.0456(2)	14.4449(3)	5.85520(10)
c/Å	19.1251(3)	22.3941(5)	8.25020(10)	15.60390(10)	18.1298(5)	24.4392(3)	10.0761(3)	17.5179(5)
α/°	90	90	90	90	90	90	90	90
β/°	90.6510(10)	90	94.6050(10)	100.4410(10)	99.927(3)	90	113.933(3)	118.578(4)
γ/°	90	90	90	90	90	90	90	90
Unit cell volume/Å^3	1580.91(4)	3240.72(14)	1809.16(3)	883.546(11)	1624.28(8)	3263.62(7)	1409.67(7)	688.89(4)
Temperature/K	100(2)	100(2)	100(2)	100(2)	100(2)	100(2)	100(2)	100(2)
Space group	$P2_1/n$	$Pbca$	$P2_1/c$	$P21$	$P2_1/n$	$Pbca$	$P2_1/c$	$P2_1/c$
No. of formula units per unit cell, Z	4	8	4	2	4	8	4	2
Radiation type	CuKα	CuKα	CuKα	CuKα	CuKα	CuKα	CuKα	CuKα
Absorption coefficient, μ/mm^{-1}	0.633	0.618	0.556	0.570	0.616	0.613	3.329	3.406
No. of reflections measured	18651	27548	39998	29193	8832	18909	14327	6681
No. of independent reflections	3263	2985	3774	3501	3062	3372	2904	1385
R_{int}	0.0290	0.0638	0.0347	0.0238	0.0264	0.0636	0.0311	0.0324

Final R_1[a] values (I > 2σ(I))	0.0342	0.0382	0.0373	0.0256	0.0412	0.0437	0.0324	0.0290
Final wR_2[b] values (I > 2σ(I))[b]	0.0863	0.0921	0.0936	0.0674	0.1093	0.1151	0.0928	0.0768
Final R_1[a] values (all data)	0.0384	0.0520	0.0440	0.0260	0.0484	0.0468	0.0368	0.0299
Final wR_2[b] values (all data)	0.0892	0.0989	0.0978	0.0677	0.1136	0.1184	0.0958	0.0773
Goodness of fit on F^2	1.052	1.033	1.028	1.038	1.048	1.042	1.075	1.088
Flack Parameter				-0.13(10)				
KPI	71.6	69.7	68.4	70.3				

11.1. Hydrates of 2,7-bis(imidazol-1-ylmethyl)naphthalene (L1):

11.1.1. Structural Analysis:

Crystallization of 2,7-bis(imidazol-1-ylmethyl)naphthalene (**L1)** from a range of solvents led to the isolation of the anhydrous form **(L1a)** of the ligand alongside three distinct hydrates: the hemihydrate (**L1**·0.5H_2O, **L1b**), monohydrate (**L1**·H_2O, **L1c**), and dihydrate (**L1**·2H_2O, **L1d**). Single-crystal X-ray diffraction (SCXRD) analysis revealed that **L1a** crystallizes in a *P*-1 space group of the triclinic crystal system, featuring a single molecule in the asymmetric unit (molecular structure is illustrated in Figure 27). The angle between the mean planes of the two imidazole rings measures 53°, while the angles between each imidazole ring and the naphthalene core are 84° and 89°, respectively. The molecules align into rows along the *a* axis, adopting alternating orientations related by an inversion center. A network of C–H···N hydrogen bonds leads to the formation of a three-dimensional supramolecular architecture, further supported by C–H···π interactions. In these interactions, methylene groups, naphthalene core, and imidazole rings serve as hydrogen donors, while the naphthalene core and imidazole rings act as acceptors (Table S1).

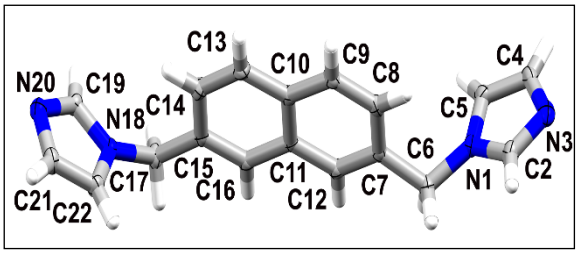

Figure 27: *Molecular structure of **L1a** with atomic displacement plot shown at 50% probability.*

L1b crystallizes as a hemihydrate in the monoclinic system, adopting the *C*2/*c* space group, wherein the asymmetric unit consists of one ligand molecule and half of a water molecule, with the oxygen atom of the water molecule situated on an inversion center (Figure 28). The dihedral angle between the mean planes of the two imidazole rings is 46°, while the angles between the mean planes of each imidazole ring and the naphthalene core are 77° and 85°, respectively, indicating notable conformational differences compared to the anhydrous form (Figure 31). The water molecule connects two ligand molecules via strong O–H···N hydrogen bonds, specifically the O23–H23···N3 interaction, characterized by an O···N distance of 2.897(1) Å and an O–H···N angle of 170°. Moreover, the water molecule acts as a hydrogen bond acceptor, engaging in C-H···O interactions that lead to the formation of two-dimensional supramolecular layers oriented along the *a*-*b* plane. These layers are further stabilized by C–H···π interactions and are interconnected along a third dimension through weak C–H···N hydrogen bonds (see Table S1).

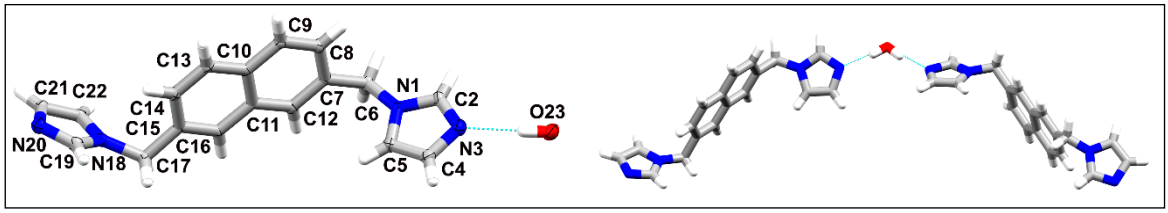

Figure 28: ***On the left:*** *asymmetric unit of* ***L1b*** *with atomic displacement plot shown at 50% probability;* ***on the right:*** *the supramolecular discrete motive stabilised by a water molecule.*

L1c crystallizes as a monohydrate in the orthorhombic crystal system, having the *Pbca* space group, where one ligand molecule and one water molecule are present in the asymmetric unit (Figure 29). The angle between the mean planes of the two imidazole rings is 54°, while the angles between each imidazole ring and the naphthalene core are 90° and 86°, respectively, suggesting greater structural similarity to **L1a** than to **L1b** (Figure 31). The water molecule in this case forms strong O–H···N hydrogen bonds with both imidazole rings: O23–H23B···N3 (O···N distance of 2.887(1) Å, O–H···N angle of 170°) and O23–H23A···N20 (O···N distance of 2.873(1) Å, O–H···N angle of 178°), resulting in the formation of one-dimensional zigzag chains. These chains are further extended into a three-dimensional framework through additional C–H···O, C–H···N hydrogen bonds as well as π-π stacking interactions present between adjacent naphthalene cores, with a centroid-to-centroid distance of approximately 3.8 Å. C–H···π interactions are absent in this hydrate.

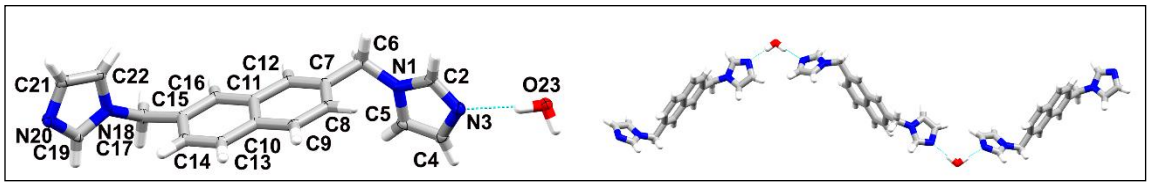

Figure 29: ***On the left:*** *asymmetric unit of* ***L1c*** *with atomic displacement plot shown at 50% probability;* ***on the right:*** *fragment of the 1D supramolecular chain, bridged by water molecules.*

L1d crystallizes as a dihydrate in the monoclinic $P2_1/c$ space group with two water molecules and one ligand molecule in the asymmetric unit (Figure 30). The dihedral angle between the mean planes of the imidazole rings is measured at 64°, while the respective angles between each imidazole ring and the naphthalene core are 84° and 87°. In this structure, the two water molecules engage in mutual hydrogen bonding, forming one-dimensional chiral chains that propagate along the *c* axis via O–H···O interactions. These interactions involve O23–H23B···O24 (O···O distance = 2.754(3) Å, O–H···O angle = 174°) and O24–H24A···O23 (O···O distance = 2.791(3) Å, O–H···O angle = 167°), which subsequently connect to the ligands via O–H···N interactions, giving rise to layered assemblies in the *a*-*c* plane. These layers are reinforced by π-π interactions between adjacent naphthalene cores and are further extended into a three-dimensional architecture via weak C–H···O and C–H···N hydrogen bonds (Table S1). Similar to **L1c**, no C–H···π interactions are observed in this case. Interestingly, the formation of water-mediated one-dimensional chains correlates with a greater tendency for π-π stacking, which is consistent with previous reports on hydrates of nitrogen-containing aromatic systems [201].

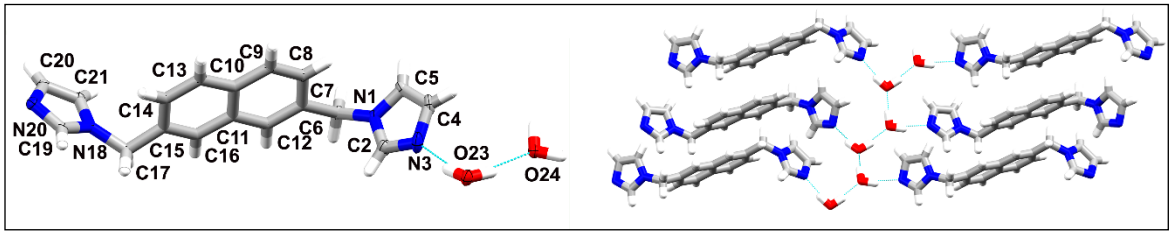

Figure 30: ***On the left:*** *asymmetric unit of* ***L1d*** *with atomic displacement plot shown at 50% probability;* ***on the right:*** *fragment of the 2D supramolecular layers, bridged by water molecules.*

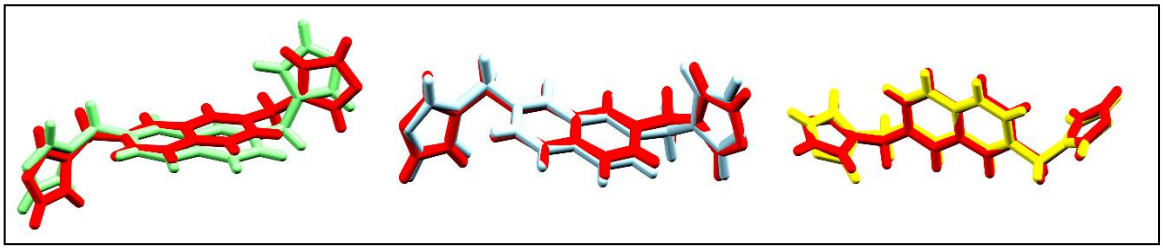

Figure 31: *Overlays of the ligands:* ***L1a/L1b****,* ***L1a/L1c*** *and* ***L1a/L1d****,* ***L1a*** *(red),* ***L1b*** *(light*

*green), **L1c** (blue), and **L1d** (yellow); the RMS deviations (after inversion) are as follows: 0.6794, 0.3927, 0.7943 Å.*

Hirshfeld surface analysis was performed to quantify the relative contributions (percentages) of specific intermolecular contacts to the overall Hirshfeld surface, providing deeper insight into the distribution of intermolecular interactions. The results revealed that upon hydration, C–H···N and C–H···π hydrogen bonds progressively diminish, while hydrogen bonds involving oxygen atoms and π-π interactions become increasingly dominant (see Figure 32 and Table S1).

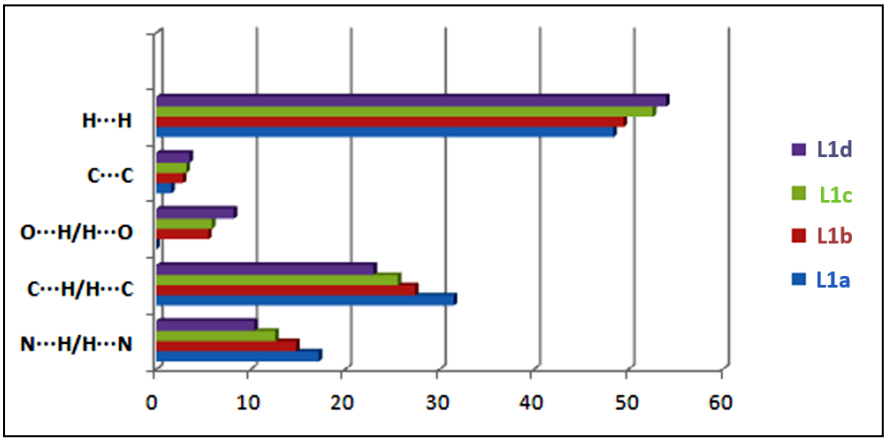

Figure 32: *The relative contributions (percentages) of selected intermolecular contacts to the Hirshfeld surface.*

11.1.2. Bulk Solid-State Studies and Hydrate Conversions

Supportive bulk material studies, including powder X-ray diffraction (PXRD), thermogravimetric analysis (TGA), and H_2O adsorption/desorption isotherms, were performed to understand the transformations between the anhydrate and hydrate forms in depth.

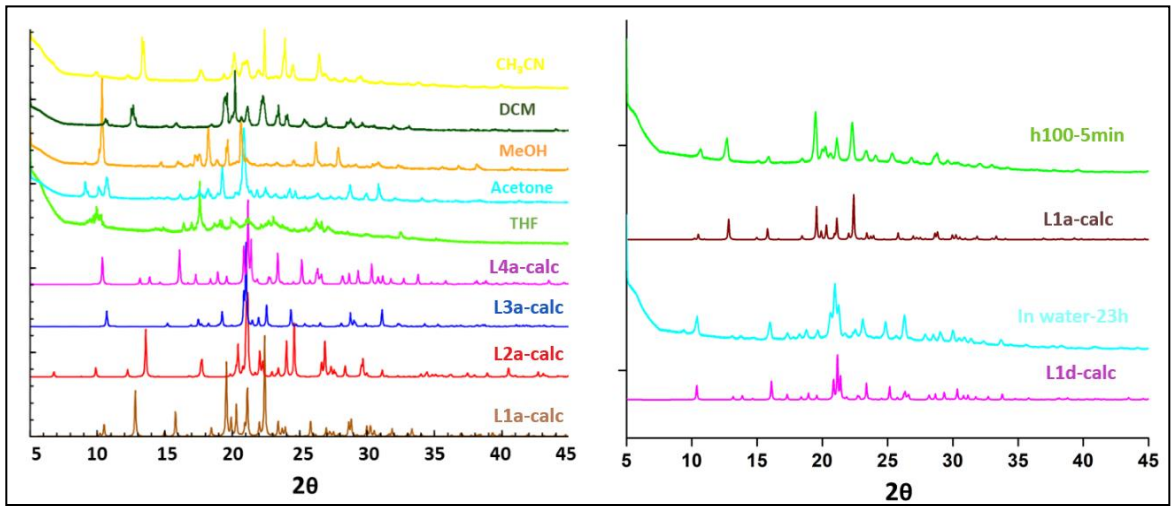

Figure 33: ***On the left:*** *experimental PXRD patterns obtained for the products isolated from different solvents and simulated traces generated for* ***L1a-L1d****,* ***on the right:*** *experimental PXRD patterns of a sample obtained by crystallization from THF heated for 5 minutes at 100°C, immersed for 23h in water upon heating, and the simulated PXRD patterns for the anhydrate* ***L1a*** *and the dihydrate* ***L1d****, respectively.*

PXRD analysis revealed that all samples obtained from various solvents are mixtures comprising products with varying degrees of hydration, and the proportions of these phases depend on both time and storage conditions (Figure 33). However, upon heating the samples at 100 °C for a few minutes, the material undergoes complete transformation to anhydrous form, which, upon immersion of the powdered sample in water, directly transforms to dihydrate form (Figure 33).

Moreover, sorption studies confirmed that the transformation from anhydrous to dihydrate form occurs in a single step, while the dehydration path follows a stepwise transition from dihydrate to anhydrous form via monohydrate and hemihydrate forms which can also be seen on thermogram indicating distinct steps: the first stage up to approximately 45 °C, the second extending to around 70 °C, and the final one occurring near 141 °C, which is associated with melting (Figure 34).

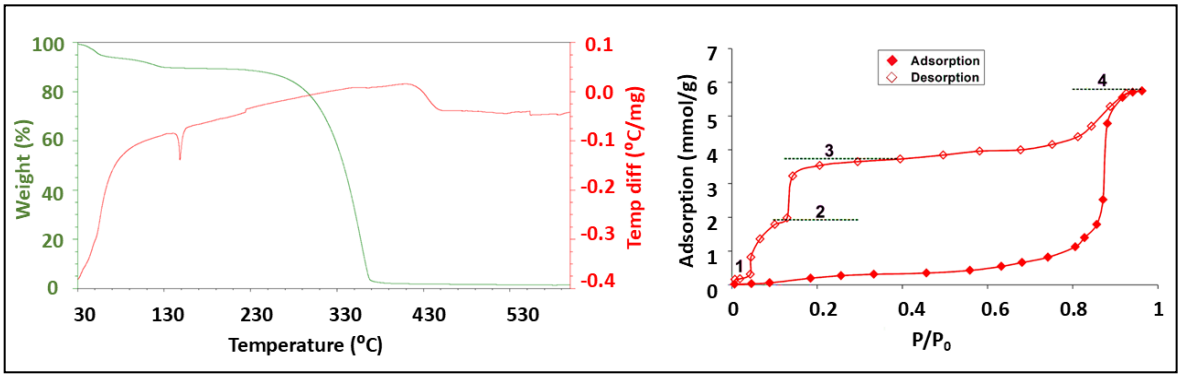

Figure 34: ***On the left:*** *thermogram of bulk hydrated sample of* ***L1****;* ***on the right:*** *water adsorption/desorption isotherms as a function of relative pressure, with markings indicating the formation of* ***L1a-L1d****.*

Water vapor adsorption/desorption isotherm measurements indicate that the adsorption curve remains nearly flat up to a relative pressure of about 0.8 P/P_0, suggesting that the material exhibits considerable hydrophobic character. Once the relative pressure exceeds approximately 0.85 P/P_0, structural reorganization facilitates capillary condensation, leading to a sharp increase in water uptake and approaching maximum adsorption capacity. The resulting type V isotherm is indicative of limited multilayer adsorption within the pores, a behavior typically associated with hydrophobic surfaces. The weak interactions

between the adsorbent and water molecules, compared to the stronger water-water interactions, favors condensation within the pores only at higher relative pressures, resulting in significant hysteresis mainly because of the formation of bridged water molecules via hydrogen bonds in micropores. Notably, the desorption branch of the isotherm provides clear evidence of the gradual dehydration process, corresponding to transitions between different hydration states (Figure 34). At the highest relative pressures, a plateau corresponding to roughly 1.7 water molecules per adsorbent unit is observed. The slight discrepancy between the number of water molecules determined by single-crystal X-ray diffraction (SCXRD) and those observed in adsorption studies likely arises from the statistical distribution of crystallite sizes. Another plateau, appearing around 0.7 P/P_0, represents the formation of the monohydrate phase (approximately 1.1 H_2O molecules per ligand). Finally, at relative pressures below 0.15 P/P_0, further desorption occurs, leading to a third plateau corresponding to the hemihydrate form, with about 0.5 water molecules associated with each adsorbent molecule.

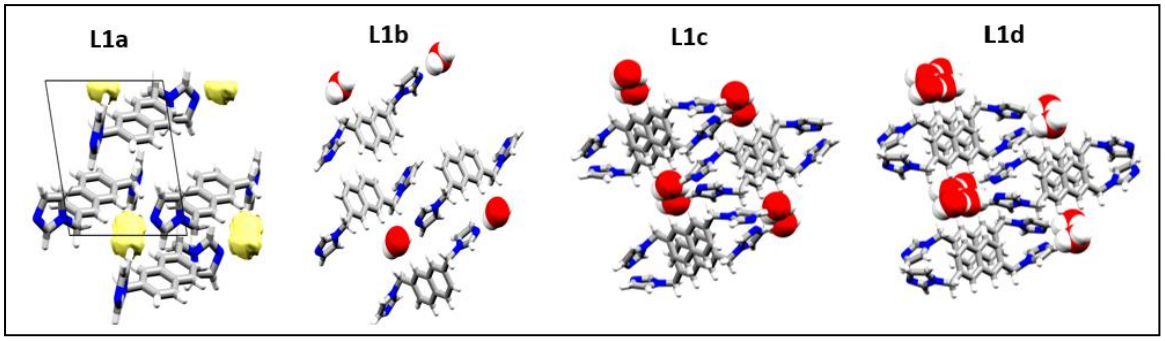

Figure 35: *Packing diagrams of **L1a-L1d** shown along the b (**L1a-L1c**) and c (**L1d**) axis, small apertures present in **L1a** indicated in yellow, water molecules shown in space filling representation.*

The observed structural transitions in the bulk samples prompt a closer examination of crystal structures **L1a-L1d**. Despite noticeable changes in crystallographic parameters (Table 2), the similarities in their packing arrangements further support a gradual dehydration mechanism. This process involves significant molecular-level reorganization, where new intermolecular interactions form during water removal, facilitated by slight molecular shifts and minor conformational changes of the ligand (Figure 31), changes of which were followed in a single-crystal to single-crystal fashion. In the anhydrous structure, small apertures which could be mapped using a contact surface probe radius of 0.9 Å in Mercury appear sufficient to initiate the adsorption of water molecules (Figure 35). A comparable behavior has been documented for an apohost organic macrocycle capable

of reversibly adsorbing tetrahydrofuran (THF) in a single crystal [201]. However, the transformation of the anhydrous bulk material to the dihydrate phase occurs via recrystallization.

11.1.3. Crystal Lattice Energy Calculations

Moreover, it was observed that the lattice energy decreases relative to the anhydrous form in these hydrates, demonstrating the typical effect of water incorporation into the crystal structure, i.e., the introduction of water molecules enhances the intermolecular bonding network, primarily through the formation of additional hydrogen bonds, thus reducing the lattice energy per unit cell. Additionally, to predict the formation and stability of specific hydrates, the stabilisation energy (E_{stab}) was determined following the methodology proposed by Braun *et al.* [202], which relates the energy differences between hydrates of varying stoichiometries, the anhydrate, and ice. The calculated stabilization energies (E_{stab}) for the hydrates (Table 4) indicate that all forms are thermodynamically stable, with values lower than the lattice energies of the ordered ice polymorphs (ranging from −60 to −64 kJ mol^{-1}). This finding is consistent with the experimental observations.

Table 4: *The results of crystal lattice energy calculations and the stabilisation energy of the hydrates*

	L1a	**L1b**	**L1c**	**L1d**
E_{latt}/per unit cell (kJ/mol)	-198.7	-263.3	-266.9	-365.8
E_{stab} (kJ/mol)		-67.0	-68.2	-83.6

11.2. Polymorphism of Ligands Containing Biphenyl Spacer:

11.2.1. Polymorphism of 4,4′-bis((1H-imidazol-1-yl)methyl)-1,1′-biphenyl (L6):

Crystallization of **L6** was conducted using various solvents differing in polarity and geometry, including acetone, CH_3CN, DCM, EtOH, MeOH, and THF, maintaining a concentration of 10 mg of **L6** per 10 mL of solvent via slow evaporation. Among these, only DCM, MeOH, and EtOH produced crystals, though those obtained from EtOH were of relatively poor quality and less suitable for single-crystal X-ray diffraction (SCXRD) analysis, and the screening led to the isolation of two new polymorphs **(L6a** and **L6b)**. Two distinct solid forms of **L6**, a monohydrate **(L6c)** and an anhydrous form **(L6d)**, had previously been reported whereas monohydrate was serendipitously obtained during metal

complexation (by the slow diffusion of an ethanolic $AgBF_4$ solution into a chloroform solution of the ligand), while the anhydrate resulted from the slow diffusion of an aqueous $AgNO_3$ solution into a ligand solution prepared in acetone [203].

11.2.1.1. Structural Analysis

L6a and **L6d** crystallize in monoclinic crystal system, adopting the $P2_1/n$ and $P2_1/c$ space groups, respectively, while **L6c** crystallizes in the higher symmetry *Pbca* space group of the orthorhombic crystal system, where all of them have one molecule in the asymmetric unit. As noted in the reported study one of the imidazole rings in **L6d** exhibits positional N/C disorder in a 50:50 ratio, complicating direct and precise comparisons between **L6d** and the other two polymorphs (**L6a** and **L6b**). So, it was separated into two parts (**L6d1** and **L6d2**) to facilitate better comparison. A comparison between the ligand conformation in **L6a** and the two disordered components of **L6d** (designated **L6d1** and **L6d2**) reveals notable differences, particularly in the positioning of one imidazole ring (Figure 36), with root-mean-square (RMS) deviations of 1.1590 Å for **L6d1** and 0.8922 Å for **L6d2**. In **L6b**, an alternative orientation of the imidazole ring is observed, as a result of the inherent flexibility of the molecule.

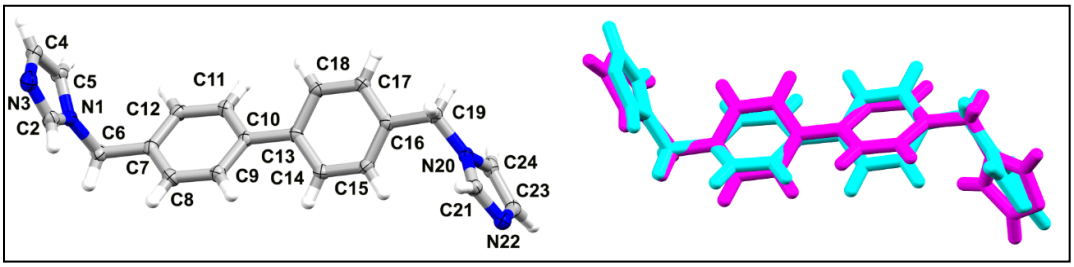

Figure 36: ***On the left:*** *molecular structure of* ***L6*** *with atomic displacement plot shown at 50% probability;* ***on the right:*** *overlay of two polymorphs* ***L6a*** *(cyan) and* ***L6b*** *(magenta) of* ***L6****; RMSD 0.9791 Å.*

The torsion angles C7-C6-N1-C2 and C16-C19-N20-C21, as labeled in Figure 36, are measured at 87°/-99° for **L6a**, 92°/-148° for **L6b**, and 89°/102° for **L6d**. The dihedral angles between the benzene ring planes are 31°, 34°, and 33° for **L6a**, **L6b**, and **L6d** respectively. In contrast, the corresponding dihedral angles between the imidazole ring planes are 11°, 61°, and 10° for **L6a**, **L6b**, and **L6d**, respectively.

The crystal structures of **L6a**, **L6b** and **L6d** are stabilized primarily by weak C–H···N hydrogen bonding, leading to the formation of three-dimensional supramolecular frameworks, with additional support from C–H···π interactions (Table S1). Notably, π–π stacking interactions are absent in this series of polymorphs.

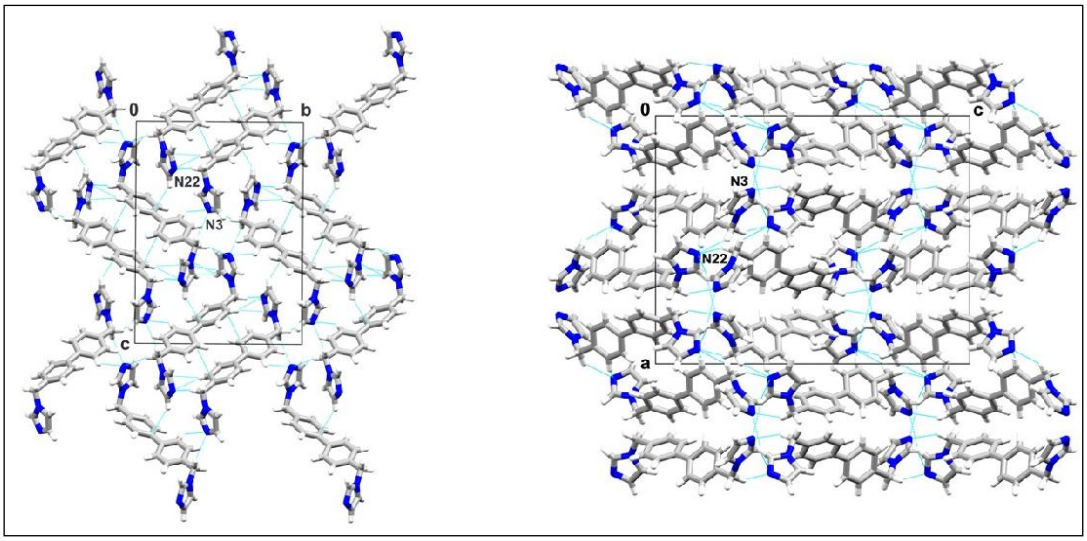

Figure 37: *Packing diagrams of **L6a** (on the left) and **L6b** (on the right). The N-H···N interactions present are shown in blue.*

Analysis of the intermolecular interactions in the two disordered components of **L6d**, designated **L6d1** and **L6d2**, was carried out using Crystal Explorer. The evaluation revealed that H···N and H···H contacts dominate, contributing 16% and 17.9%, and 52.6% and 51.4%, for **L6d1** and **L6d2**, respectively. After averaging these values, comparisons were made with the interactions present in **L6a** and **L6b** (Figure 38). The results highlight that **L6a** exhibits the highest proportion of hydrogen-bonding interactions, correlating with its status as the most thermodynamically stable phase.

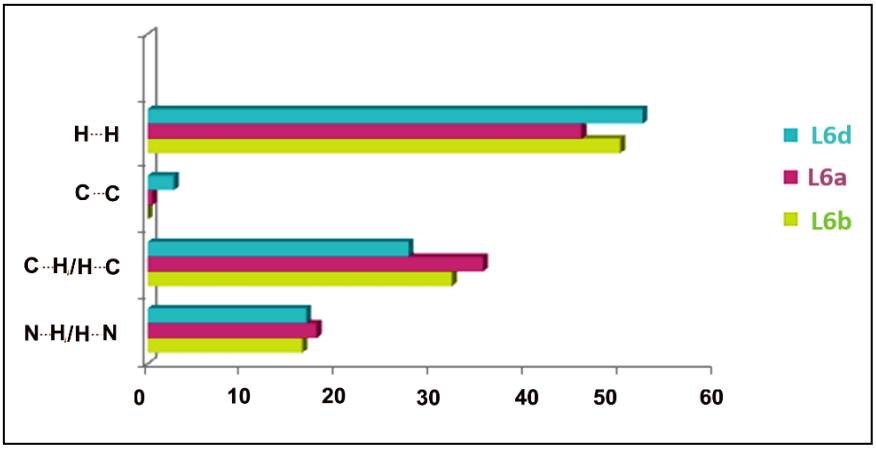

Figure 38: *Estimated contributions (percentage) of selected intermolecular contacts to the Hirshfeld surface in **L6a**, **L6b** and **L6c**.*

11.2.1.2. Bulk Solid-State Studies

Powder X-ray diffraction (PXRD) analysis of solids crystallized from various solvents revealed that the bulk grown from DCM and THF corresponds exclusively to form **L6a**. In

contrast, crystallization from solvents such as MeOH, acetone, CH_3CN, and EtOH produced mixtures of **L6b** and **L6c**, with **L6a** accounting for over 70% of the composition in each case (Figure 39). Notably, acetone led to the highest proportion of **L6a** at 92%. An intriguing observation was made with ethanol: the PXRD pattern of the resulting solid indicated the formation of **L6b**, constituting approximately 74% of the sample, coexisting with **L6c** and showing no presence of **L6a**.

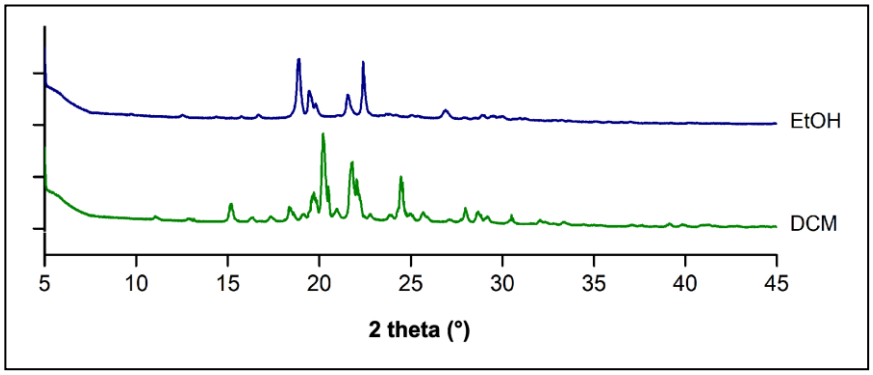

Figure 39: *PXRD patterns obtained for samples of **L6** after recrystallization from DCM and EtOH.*

To gain deeper insight into the system further, thermal analyses (TG/DTA) were conducted on the solids obtained from DCM and EtOH. These studies revealed a phase transition occurring near 140 °C for the material grown from ethanol (**L6b**) (Figure 40).

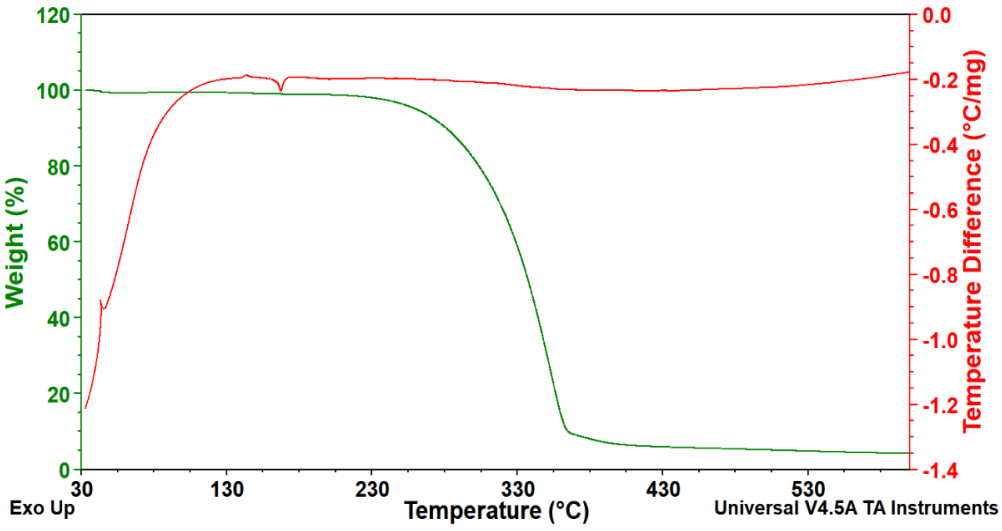

Figure 40: *Thermogram of **L6b**.*

Subsequent PXRD analysis demonstrated that heating this sample at 150 °C for 3 minutes led to the complete transformation of the monohydrate (**L6c**) into **L6a**, while **L6b** underwent only partial conversion to **L6a** initially. Prolonged heating ultimately resulted

in the full conversion of **L6b** to **L6a**. Notably, a comparison of the molecular packing in the monohydrated **L6c** and the anhydrous **L6d** structures revealed similar key packing motifs, suggesting that these similarities may facilitate the dehydration process.

11.2.1.3. Crystal Lattice Energy Calculations

Crystal lattice energy calculations (Table 5) further confirmed that **L6a** is the most stable form, which is consistent with its highest Kitaigorodskii packing index (KPI values summarized in Table 3).

Table 5. *Interaction energies calculated by the program PIXEL for the polymorphs of **L6** (kJ/mol units).*

Energy component/ Form	Coulombic	Polarisation	Dispersion	Repulsion	Energy in total
L6a	-72.7	-31.1	-202.8	103.9	-202.7
L6b	-74.8	-29.6	-196.1	100.2	-200.3
L6d1	-43.3	-23.6	-172.1	69.3	-169.7
L6d2	-56.5	-27.1	-174.2	82.5	-175.2
L6d(av)	- 49.9	-25.35	-173.15	75.9	- 172.45

The energy differences between phases are quite significant variations with particularly the low stability of **L6d**. This is noteworthy, as **L6d** was absent among the solids obtained in this study and was previously only isolated through silver salt complexation. The relatively low contribution from Coulombic and polarization forces in **L6d** may be attributed to a reduced presence of C-H$\cdots\pi$ interactions, as illustrated in the histogram in Figure 38. Overall, the findings emphasize that dispersion forces play the most critical role in stabilizing all three crystalline forms.

11.2.2. Polymorphism of 4,4′-bis((pyridin-4-yl)methyl)-1,1′-biphenyl (L8):

Crystallization of **L8** was also carried out via slow evaporation using a range of solvents, such as acetone, CH_3CN, DCM, EtOH, MeOH, and THF, using a concentration of 10 mg of **L8** per 10 mL of solvent, which allowed us to obtain good-quality crystals in all the vials and the screening led to the isolation of two new conformational polymorphs **L8a** from THF vial and **L8b** from MeOH vial.

11.2.2.1. Structural Analysis

Both the conformational polymorphs **L8a** and **L8b** crystallize in monoclinic systems, with **L8a** adopting the $P2_1/c$ space group and **L8b** crystallizing in the $P2_1$ space group, both having one molecule in the asymmetric unit. It is noteworthy that polymorphic pairs exhibiting both centrosymmetric and non-centrosymmetric space groups have attracted considerable interest, as understanding their formation can provide valuable insights into directing the assembly of non-centrosymmetric structures [204].

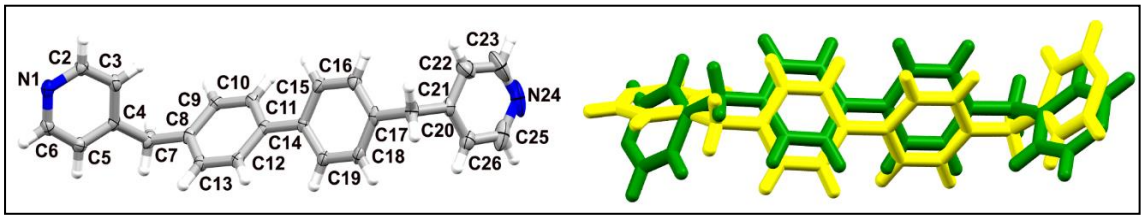

Figure 41: ***On the left:*** *molecular structure of* ***L8*** *with atomic displacement plot shown at 50% probability;* ***on the right:*** *overlay of two polymorphs* ***L8a*** *(green) and* ***L8b*** *(yellow) of* ***L8****; RMSD 1.0522 Å.*

In these two crystal forms, the molecules adopt distinct conformations, as illustrated in Figure 41. Specifically, the dihedral angles between the benzene ring planes are measured at 34° for **L8a** and 35° for **L8b**, while the angles between the planes of the pyridine rings are 57° and 20°, respectively.

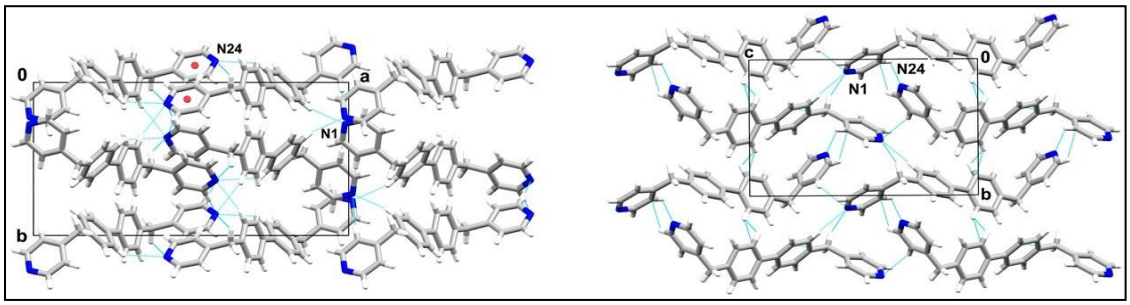

Figure 42: *Packing diagrams of* ***L8a*** *(on the left) and* ***L8b*** *(on the right). The N-H···N interactions present are shown in blue, two centroids (in red) indicate an exemplary pair of π-π interactions.*

In both crystalline forms, molecular packing is directed by a limited but distinct set of intermolecular interactions (Figure 42). As expected, C–H···N hydrogen bonds make a significant contribution, giving rise to three-dimensional supramolecular architectures. These assemblies are further stabilized by C–H···π interactions (Table S1) where in the case of **L8a**, methylene groups and pyridine rings serve as hydrogen donors while benzene rings act as acceptors. For **L8b**, the situation is more varied: either pyridine rings serve both as donors and acceptors, or a combination of benzene and pyridine rings function in these roles. Moreover, **L8a** displays weak π-π interactions between neighbouring pyridine rings

containing the N24 atom (symmetry code: 1-x, 1-y, -z), with a centroid-centroid distance measured at 3.7092(6) Å. The key differences between the two crystal structures lie in the variation of interaction strengths, the differing molecular components involved in the interactions, and the presence or absence of π-π stacking.

Hirshfeld surface analysis, performed using Crystal Explorer, was employed to quantify the contributions of intermolecular interactions stabilizing the crystal structures of both polymorphs. The analysis confirmed, among other findings, the presence of stronger C–H···π interactions in **L8b** (Figure 43), consistent with previous observations. Enrichment ratio calculations further emphasized the key role of C–H···N and C–H···π contacts in stabilizing the structures of **L8a** and **L8b**. In **L8a**, C–H···N interactions are slightly more prominent (enrichment ratio 1.33 compared to 1.15 for C–H···π), whereas in **L8b**, C–H···π interactions become more dominant (1.27 versus 1.20).

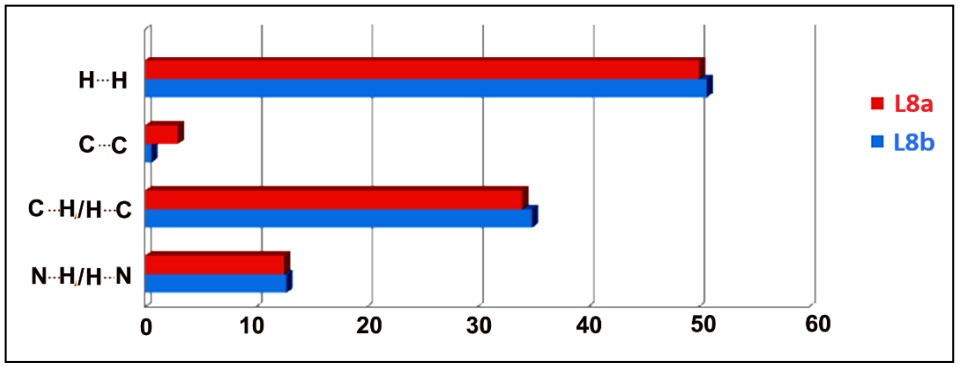

Figure 43: *Estimated contributions (percentage) of selected intermolecular contacts to the Hirshfeld surface in **L8a** and **L8b**.*

11.2.2.2. Bulk Solid-State Studies

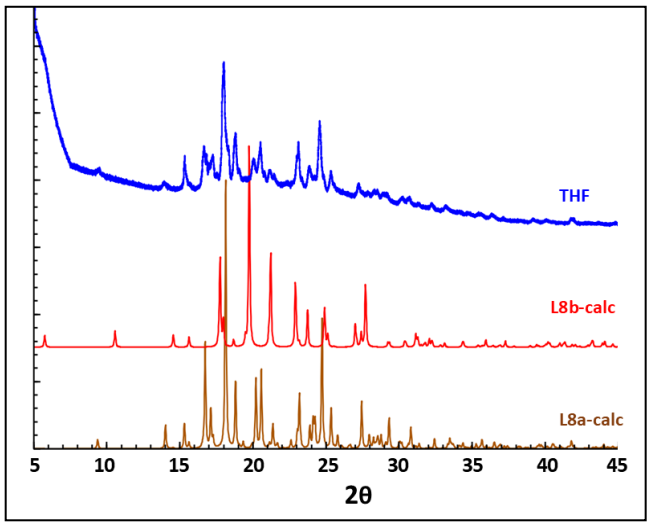

Figure 44: *Comparison of the calculated PXRD patterns of **L8a** and **L8b** with experimental patterns obtained for samples of **L8** after recrystallization from THF.*

The powder X-ray diffraction (PXRD) pattern recorded for the crystalline material grown from THF was notably distinct (Figure 44), showing a strong match with the simulated powder pattern of **L8a**. In contrast, Powder Cell analysis confirmed that **L8a** was absent in the solid recrystallized from MeOH. In samples obtained from other solvents, phase **L8b** was found to be the predominant form. However, in the THF-grown sample, the presence of **L8b** was minimal, accounting for only about 2% of the composition.

Furthermore, thermal analysis (TG/DTA) was carried out on both **L8a** and **L8b** (Figure 45), revealing that **L8a** undergoes a phase transition at approximately 100 °C. This observation was further supported by PXRD measurements: upon heating **L8a** at 110 °C for 2 minutes, an irreversible transformation into **L8b** was observed. Remarkably, this phase change could also be monitored in a single-crystal to single-crystal manner, with the crystal maintaining its integrity and crystallinity throughout the transition.

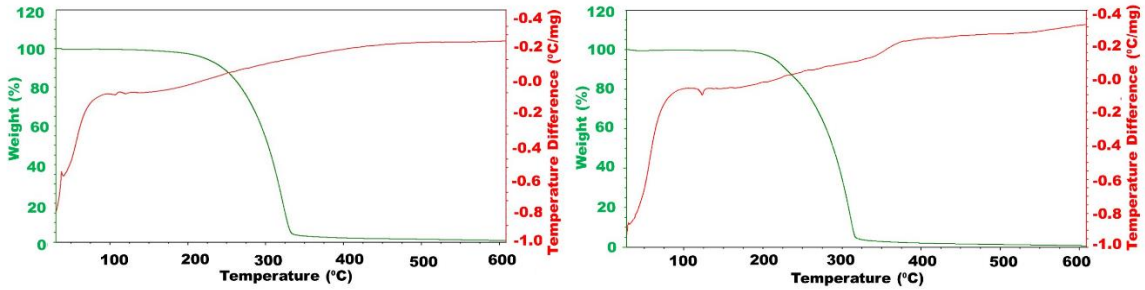

Figure 45: *Thermogram of **L8a** (on the left) and **L8b** (on the right).*

11.2.2.3. Crystal Lattice Energy Calculations

Additionally, crystal lattice energy calculations (Table 6) revealed that form **L8a** is less stable than **L8b**, which aligns with its lower Kitaigorodskii packing index (refer to Table 3). Overall, the energy decomposition highlights similar contributions from various interaction types in both forms, with the most significant differences arising from the dispersion component, which remains the major factor stabilizing both crystalline phases.

Table 6. *Interaction energies calculated by the program PIXEL for the polymorphs of **L8** **(L8a and L8b)** in kJ/mol units.*

Energy component/ Form	**Coulombic**	**Polarisation**	**Dispersion**	**Repulsion**	**Energy in total**
L8a	-51.0	-22.9	-198.3	94.9	-177.4
L8b	-50.8	-21.9	-208.8	96.7	-184.9

11.2.3. Polymorphism of 2,2′-bis((1H-imidazol-1-yl)methyl)-1,1′-biphenyl (L11):

Crystallization of **L11** by slow evaporation from a range of solvents resulted in isolation of two new polymorphs **L11a** and **L11b**, both from DCM. One polymorph was already reported in the literature for this molecule (refcode at CSD: **MIDJEP**) which was obtained by vapor diffusion from DCM and heptane which was measured by SCXRD at room temperature so to facilitate better comparison of **L11a**, **L11b** and **MIDJEP**, the data for **MIDJEP** was recollected at 100K, denoted as **MIDJEPLN**. PXRD studies indicated that the products formed from EtOH and THF were amorphic.

11.2.3.1. Structural Analysis

L11a and **L11b** crystallize in $P2_1/n$ of a monoclinic system and the *Pbca* space group of an orthorhombic system, respectively, with one molecule in the asymmetric unit.

In both the phases, the molecules adopt very similar conformations with dihedral angles between the planes of the benzene rings of 77° and 75° for **L11a** and **L11b**, respectively (Figure 46). The corresponding angles between the planes of the imidazole rings are 78° and 70°. There is a slightly bigger difference in the conformations adopted by the two crystallographically independent molecules present in **MIDJEPLN**, where the dihedral angles between the planes of the benzene rings are 70° and 72° and between the planes of the imidazole rings 88° and 86°, respectively.

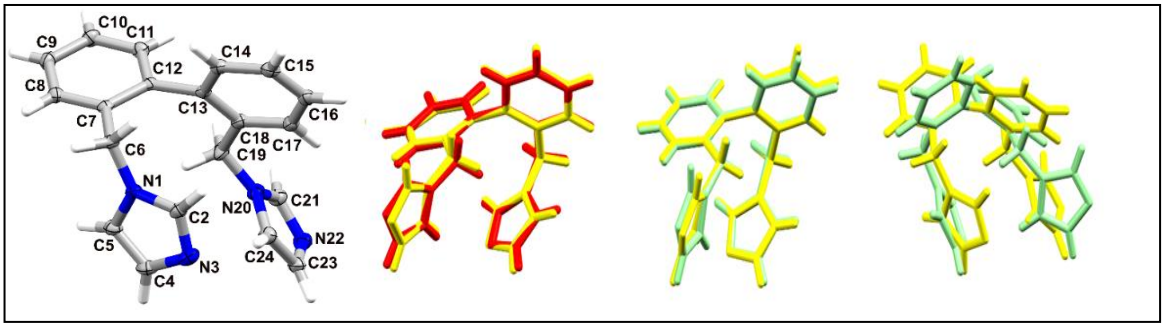

Figure 46: ***On the left:*** *Molecular structure of* ***L11*** *(representation of* ***L11a*** *with atomic displacement plot shown at 50% probability;* **L11a** and **L11b** *show the same labelling);* ***on the right:*** *overlay of* ***L11a*** *(red) with* ***L11b*** *(yellow), RMSD of 0.143 Å; overlays of two crystallographically independent molecules present in the asymmetric unit of* ***MIDJEPLN*** *(light green) with* ***L11a*** *(yellow): RMSDs of 0.146 Å and 2.825 Å, respectively; RMSD for the latter after inversion is 0.2185 Å.*

Analysis of the molecular packings reveals that all phases are stabilized by C–H···N and C–H···π interactions (Table S1), and that there are no π-π interactions present. C–H···N

interactions are formed via N3 with either the benzene rings (**L11a**) or with a methylene group, an imidazole and a benzene ring (**L11b**) and via N22 with either the benzene rings and a methylene group (**L11a**) or with the imidazoles and a benzene ring (**L11b**) of adjacent molecules. The C–H···N interactions in **MIDJEPLN**, containing two crystallographically independent molecules in the asymmetric unit, are for N1 resembling of the interactions formed by N22 in **L11b** (involving the imidazole and benzene rings), whereas the hydrogen bonds formed by N4 involve the imidazole ring and the methylene group. Furthermore, the interactions formed by N5 are reminiscent of the hydrogen bonds formed by N22 in **L11a** (involving the benzene ring and the methylene group) and N8 is getting involved, similarly to N4, in interactions with the imidazole ring and the methylene group.

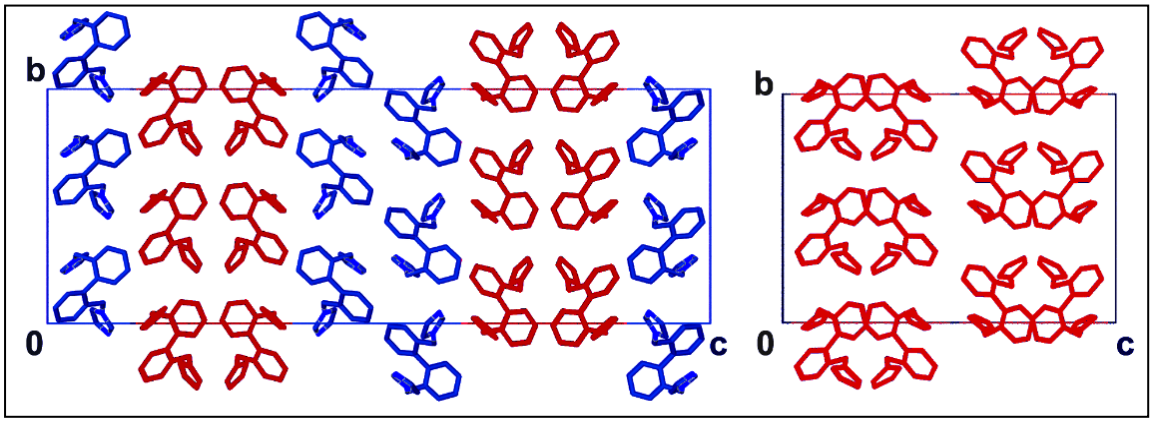

Figure 47: *Schematic packing of **MIDJEPLN** (on the left) and **L11b** (on the right) shown along the a axis with the similar motives marked in red.*

The C–H···π interactions are more diverse in **L11a**, with the involvement of methylene groups, benzene rings, as well as imidazole rings, whereas only aromatic units, i.e. benzene and imidazole rings are involved in **L11b** and **MIDJEPLN**. Furthermore, the molecular packings of **L11b** and **MIDJEPLN** which crystallize in the same space group, show the presence of similar motives (Figure 47), namely double columns of molecules which is **MIDJEPLN** are separated by double columns of differently ordered molecules as a result of the presence of a second crystallographically independent molecule in the asymmetric unit. The distance between the centroids of the benzene rings of adjacent molecules in a single column is 8.599 Å for **L11b** and 8.843 Å for **MIDJEPLN** whereas between the rings originating from adjacent column, this is 5.355 Å for **L11b** and 4.998 Å for **MIDJEPLN**, respectively.

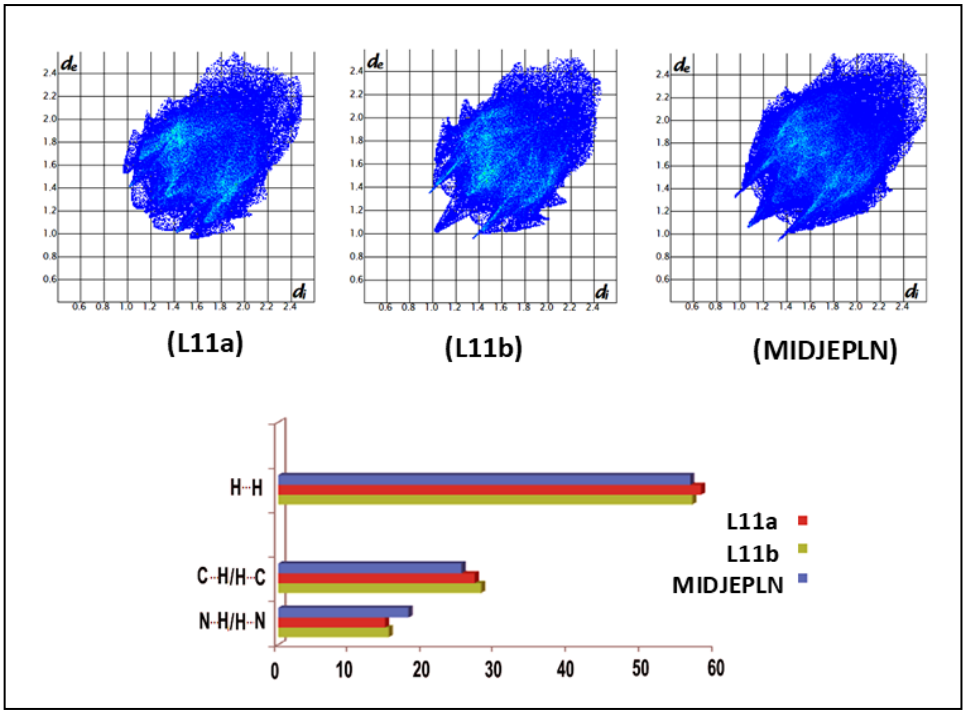

Figure 48: *Top: 2D fingerprint plots for **MIDJEPLN**, **L11a** and **L11b**; bottom: the relative contributions (percentages) of selected intermolecular contacts to the Hirshfeld surface.*

Hirshfeld surface analysis and finger prints plots generated also indicate the similarity in molecular packing for **L11b** and **MIDJEPLN** (Figure 48). There are two features most noticeably differentiating these fingerprints from **L11a**, namely characteristic pairs of sharp spikes indicating the presence of stronger C–H···N interactions and rather short H···H contacts appearing at $d_e \cong d_i$ around 1.0 Å. The fingerprint of **L11a** indicates the presence of stronger C–H···π interactions (see also Table S1). The histograms presenting the percentage contributions of different contacts to the Hirshfeld surface clearly indicate a higher contribution of N···H and a lower involvement of C···H contacts in **MIDJEPLN** than in the remaining two structures.

11.2.3.2. Bulk Solid-State Studies

Analysis of the PXRD pattern collected from solid shortly after crystallization of 10 mg of **1** from 10 ml DCM indicated the presence of a mixture of 3 phases (**L11a**, **L11b** and **MIDJEPLN**, Figure 49). Initially, only a 5% contribution of **MIDJEPLN** was present, but the values change over time, and after leaving the sample in air for 4 days, phase **MIDJEP** was dominant (50%) and the inputs of **L11a** (26%) and **L11b** (24%) were almost equal. The solid over time converts to only one phase **MIDJEPLN**, which can alternatively be achieved by heating the initial sample at 110°C (Figure 49).

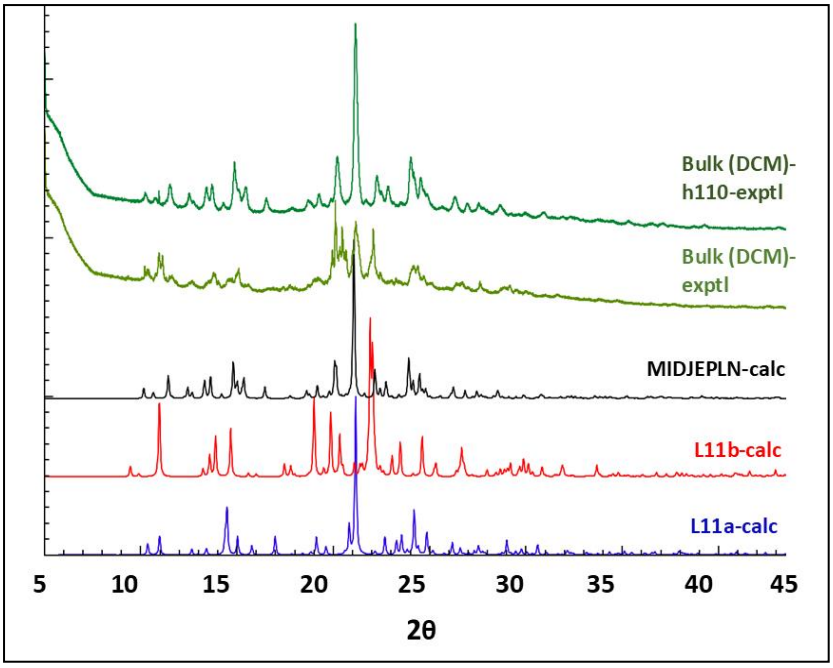

Figure 49: *PXRD pattern obtained for **L11** after crystallization from DCM (light green) followed by heating the sample at 110°C (dark green) and simulated PXRD patterns generated from the crystal structures of: **L11a** (blue), **L11b** (red), **MIDJEPLN** (black).*

This phase transition was initially observed on the DTA curve and takes place shortly before the melting point (Figure 50).

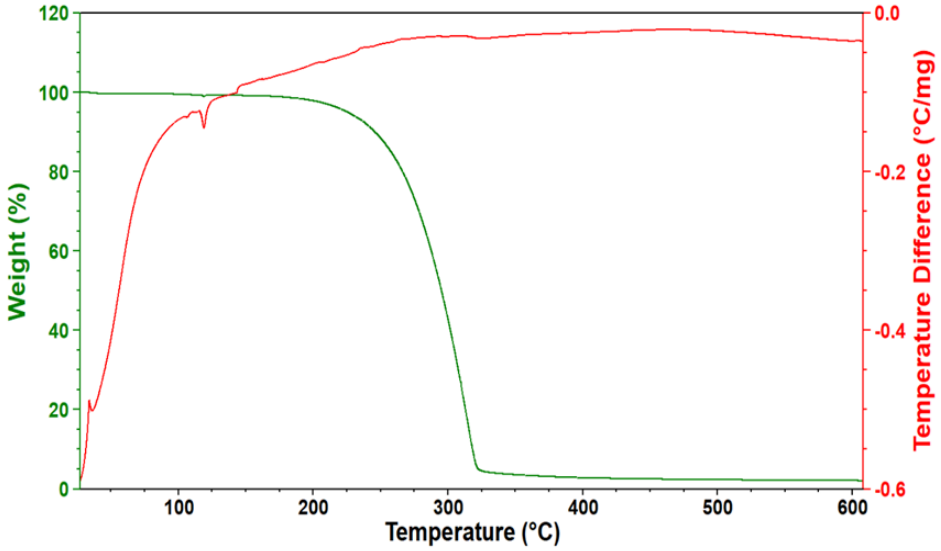

Figure 50: *Thermal analysis data of bulk **L11** crystallized from DCM.*

Furthermore, the percentage contributions of the phases formed can be tuned by adjusting the solute concentration. Crystallization from DCM containing 10 mg of solute in 10 ml of DCM leads (as shown above) to the occurrence of three phases with the lowest input of **L11b**. In the batch which crystallized from 20 mg of solute, only traces of **L11a** were left. Starting from 30 mg, the **L11a** phase was no longer present, so it was not observed in

crystalline material obtained from a corresponding saturated solution. A similar observation, highlighting the influence of solute concentration on the outcome of the crystallization process, was reported for paracetamol, where low initial concentration led to the formation of a metastable phase, which was not observed with an initial solute concentration close to the saturation point, leading exclusively to formation of the stable phase [205].

11.2.3.3. Crystal Lattice Energy Calculations

The results of crystal lattice energy calculations (Table 7) do not agree well with the experimental results. Further calculations are ongoing in the UK (University of Southampton, Prof. Graeme Day's group) aiming to account for the entropy factor which could change the order of stability.

Table 7: *Interaction energies calculated by the program PIXEL for the three forms of* ***L11 (****kJ/mol units).*

Energy Component/Form	Coulombic	Polarisation	Dispersion	Repulsion	Total Energy
L11a	-63.2	-23.7	-172.1	93.9	-165.1
L11b	-63.8	-26.0	-168.1	90.5	-167.5
MIDJEPLN	-48.2	-19.5	-146.0	58.1	-155.6

11.3. Polymorphism of 1,4-bis(thiopyridine)benzene (L12):

While this ligand didn't result in any interesting metallocycles, two new concomitant polymorphs, **L12a** and **L12b** of **L12**, were isolated from the slow evaporation of the MeOH solution, with the latter also being isolated from slow evaporation from the THF solution.

11.3.1. Structural Analysis

Single-crystal X-ray diffraction (SCXRD) revealed that both forms crystallize in the same $P2_1/c$ space group of a monoclinic crystal system, wherein form **L12a** contains one molecule of 1,4-bis(thiopyridine)benzene in the asymmetric unit, unlike form **L12b**, which contains half a molecule with the other half being generated by an inversion center. Interestingly, form **L12a** exhibits a case of whole molecule disorder (approximately 93:7), and the two components were separated (major - **L12a1** and minor - **L12a2**) to use them for further comparisons.

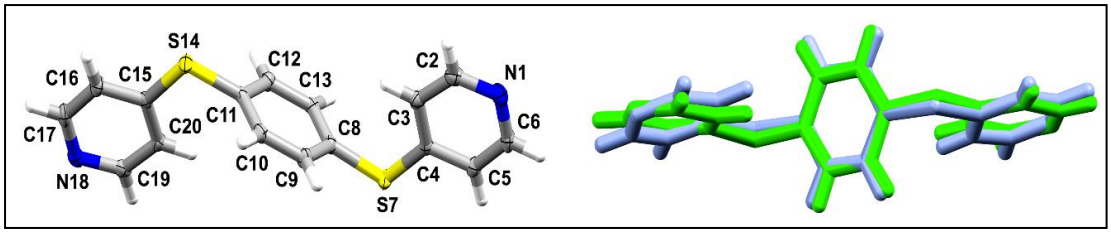

Figure 51: ***On the left:*** *Molecular structure of* ***L12*** *(representation of* ***L12b*** *with atomic displacement plot shown at 50% probability);* ***on the right:*** *overlay of* ***L12a1*** *(light green) with* ***L12b*** *(light blue), RMSD of 0.2081 Å.*

The molecules in the two polymorphs adopt largely the same *'anti'* conformation, exhibiting only minor variations in the orientation of the pyridine rings (Figure 51). These variations are attributed to differences in molecular packing, which in turn give rise to distinct sets of intermolecular interactions. In polymorph **L12a1**, the angles between the mean planes of the benzene ring and the pyridine rings are 81° and 82°, while in polymorph **L12b**, this angle is measured at 84°. Additionally, the angles between the planes of the two pyridine rings are 9° in **L12a1** and 0° in **L12b**. Despite the conformational similarities, the molecular packing arrangements in **L12a1** and **L12b** are markedly different, as illustrated in Figure 52. Packing analyses performed using both XPac and Mercury software confirm that there are no significant packing similarities between these two phases.

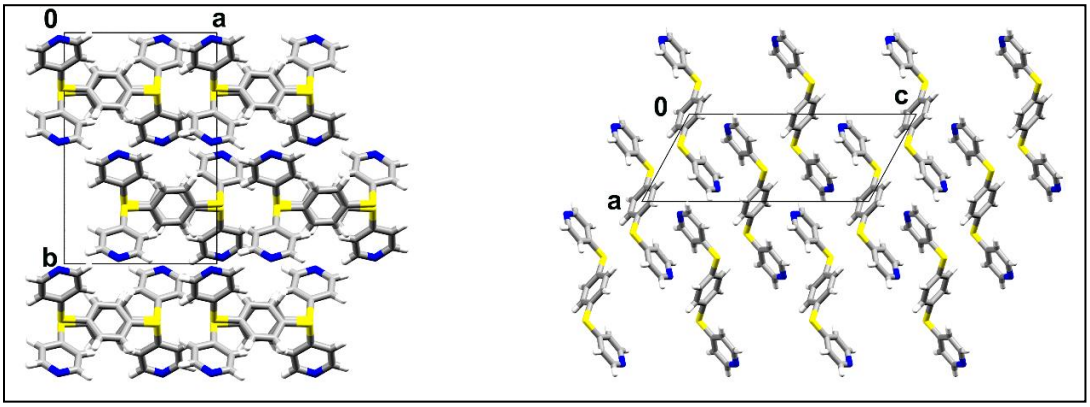

Figure 52: *Packing diagram shown along the c axis for* ***L12a1*** *(on the left) and along the b-axis for* ***L12b*** *(on the right).*

The 3D supramolecular assembly of both the polymorphs is stabilized by an abundant net of C-H···N hydrogen bonds, with **L12a1** additionally containing π-π interactions formed between the pyridine rings (N18) with a distance of 3.619 Å (Table S1). Moreover, S···S interactions [206] appear to contribute to the stabilization of the packing in polymorph **L12b**, with an observed S···S distance of 3.5541(6) Å, which is shorter than the sum of the van der Waals radii of two sulfur atoms (3.66 Å) [207]. In contrast, the corresponding S···S distances in polymorph **L12a1** are longer, measuring 3.7321(6) Å.

A comparison of the packing arrangements of the ligand molecules in polymorphs **L12a1** and **L12a2** (Figure 53) reveals that the primary difference between the major and minor components lies in the relative positioning of the AB layers, which are composed of ligands aligned parallel to the *ac* plane. This conclusion was further supported by the analysis performed using the program XPac, which is particularly useful for assessing structural similarities in isostructural systems and polymorphs. The program identified the formation of two-dimensional supramolecular constructs, characterized by layers that match internally but differ in their stacking arrangements. XPac calculated a dissimilarity index of 1.7, indicating a high degree of similarity between α_a and α_b. For comparison, dissimilarity values around 1 are typical when small substituents such as chlorine are replaced with bromine (x = 1), while more substantial changes, like the replacement of a methyl group with a trifluoromethyl group, yield values around x = 2.8 [208]. Complementary analysis using the Mercury program also suggested a high structural similarity between **L12a1** and **L12a2**, showing an overlap of 8 molecules out of 15 with a root-mean-square (RMS) deviation of 0.063 Å. Standard settings were applied during this analysis, with a 20% tolerance for bond lengths and angles.

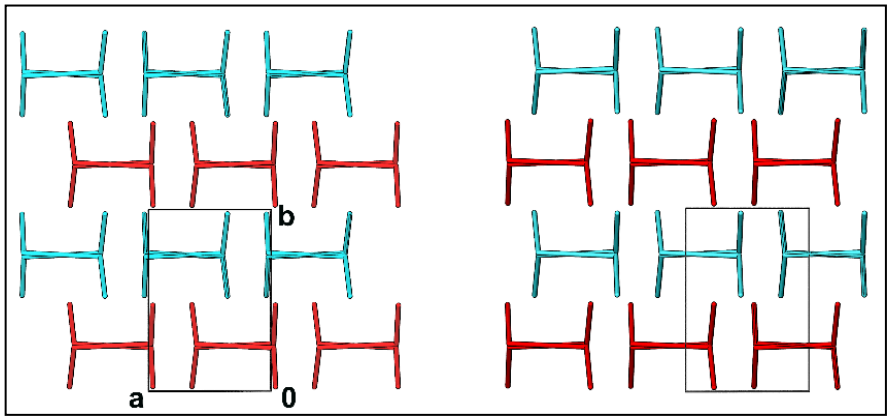

Figure 53: *Simplified packing representation of the ligand molecules in **L12a1** (left) and **L12a2** (right).*

Both components (**L12a1** and **L12a2**) exhibit distinct sets of intermolecular interactions. It should be noted, however, that the analysis for **L12a2** is only an approximate estimation, given its low occupancy within the crystal structure. In **L12a2**, the formation of two-dimensional supramolecular layers parallel to the *ac* plane is driven by hydrogen bonding involving atoms C17A and C6A, as well as S7A···S14A contacts measuring 3.725 Å. This layered arrangement is similar to the structural motif found in **L12a1**. However, **L12a2** also displays additional short-range interactions between the AB layers, notably involving atoms C9A and N18A, along with unusually short π-π interactions between pyridine rings

(N18A) at a distance of approximately 2.86 Å. These new contacts arise from slight shifts in the relative positioning of the layers. The exceptionally short distances suggest that the **L12a2** component may not represent a fully distinct phase but rather a localized structural irregularity, such as a stacking fault or stacking disorder. This interpretation is corroborated by the appearance of diffuse scattering features along the reciprocal b* axis, as depicted in the Figure 54.

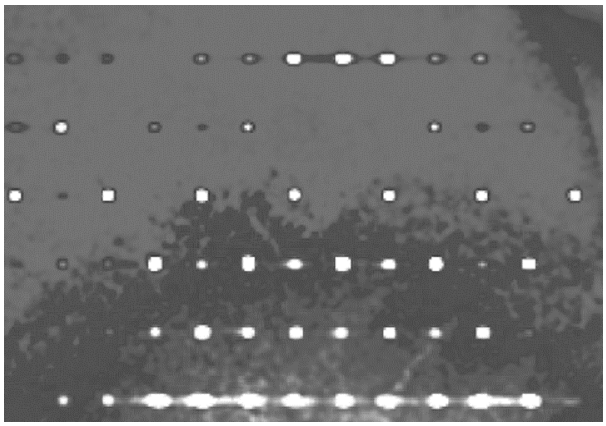

Figure 54: *Reconstruction of reciprocal lattice plane 0kl.*

To assess the contributions of different types of intermolecular contacts, a Hirshfeld surface analysis was conducted for both the polymorphs. This method enabled the generation of fingerprint plots and the calculation of the relative contributions of various interactions to the Hirshfeld surfaces.

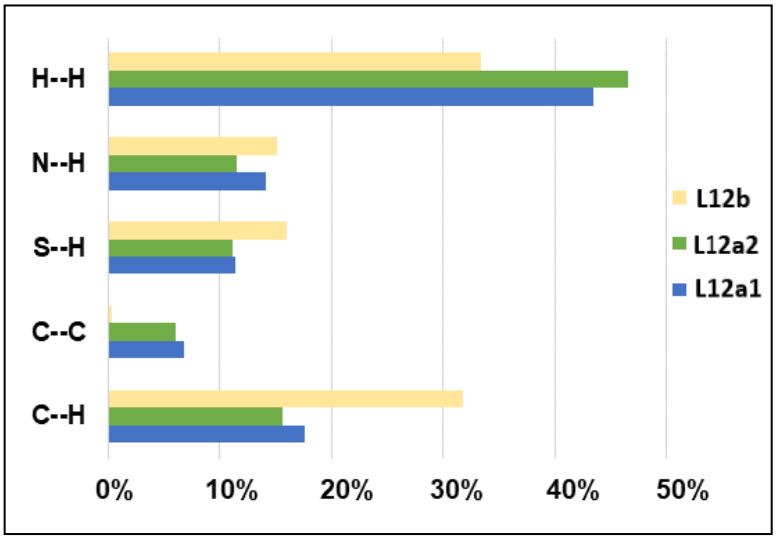

Figure 55: *Estimated contributions of selected intermolecular forces stabilizing the formation of* ***L12a1***, ***L12a2*** *and* ***L12b****.*

The analysis revealed that in **L12b**, weak hydrogen bonds are the predominant stabilizing interactions, while **L12a** is primarily stabilized by van der Waals forces, supplemented by weak hydrogen bonds and π-π interactions. Notably, π-π interactions were absent in **L12b** (Figure 55). The analysis also showed that in **L12a2**, van der Waals forces play an even greater role than in **L12a1**, with a correspondingly reduced contribution from hydrogen bonding (Figure 55). These findings are further supported by enrichment ratio calculations [209]. Specifically, C–H···N interactions are more pronounced in **L12a1**, with an enrichment ratio of 1.47 compared to 1.11 in **L12a2**. Conversely, H···H contacts are slightly more favored **in L12a2** (1.07) than in **L12a1** (1.03). This trend is consistent with the reduced involvement of C–H···N hydrogen bonds in **L12a2** relative to **L12a1**, as summarized in Table S1 (where identical atom labeling was applied to both components).

11.3.2. Bulk Solid-State Studies

Powder X-ray diffraction (PXRD) analysis of the bulk crystalline material revealed that the **L12b** phase is the predominant form. Notably, the PXRD pattern remained unchanged even after the sample was exposed to air for five days, implying that the **L12a** phase transforms rapidly into the **L12b** phase, as the single crystal analyzed was obtained directly from the solution.

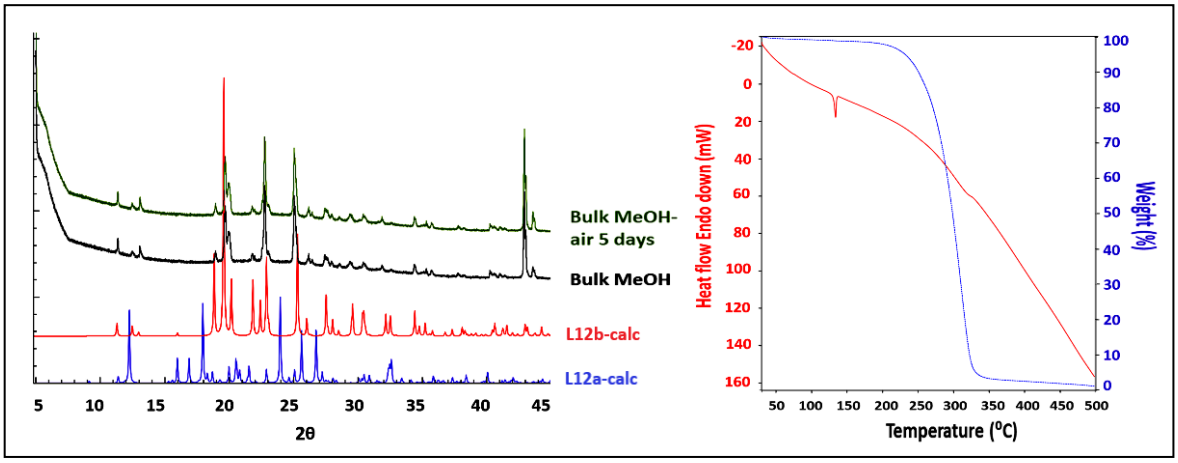

Figure 56: ***(On the left)****: simulated and experimental powder patterns;* ***(on the right)****: TG and heat flow-calibrated DTA curves.*

Furthermore, the DTA curve (Figure 56) demonstrated that the bulk material remains stable, showing no phase transitions from room temperature up to the melting point.

11.3.3. Crystal Lattice Energy Calculations

Crystal lattice energy calculations, carried out using Crystal Explorer, indicated that polymorph **L12a1** possesses lower stability relative to form **L12b**, with an energy

difference of approximately 9 kJ/mol. This result aligns with the calculated packing efficiencies (70.1% for **L12a1** versus 71.6% for **L12b**) and corresponding densities (1.398 g/cm³ for **L12a1** compared to 1.429 g/cm³ for **L12b**). In the case of **L12a2**, both CrystalExplorer and PIXEL indicated high values for the repulsion term, prompting the question of whether this is due to a software error (Table 8).

Table 8. *The results of the crystal lattice energy calculations for **L12a1, L12a2** and **L12b** (kJ/mol units).*

CrystalExplorer	E_ele	E_pol	E_dis	E_rep	E_tot
			Tonto wavefunction calc.		
L12a1	−55.6	−9.9	−154.6	80.5	−139.7
L12a2	−122.1	−10.8	−160.2	235.6	−57.5
L12b	−52.6	−10.3	−160.0	74.2	−148.8
			Gaussian wavefunction calc.		
L12a1	−57.4	−10.1	−154.6	80.6	−141.6
L12a2	−124.9	−11.1	−160.2	236.2	−60.0
L12b	−54.8	−10.4	−160.0	74.3	−150.9
Pixel (L12a2)	−156.1	−94	−218.9	476.8	7.8

Therefore, a search in CSD was performed for reported crystal structures exhibiting very short π-π stacking distances. Two coordination compounds, **ZOMSEB:** bis(2,4-dihydroxy-1-(hydroxy)-9,10-anthraquinonato)-copper(II) dihydrate and **OXUDES0:** bis(μ-4-(amino)-N-(3,4-dimethyl-1,2-oxazol-5-yl)benzenesulfonamidato)-di-silver(I) dihydrate, were identified with π-π separations of 2.94 Å and 2.96 Å, respectively. Additionally, two organic compounds (ref code: **ECUTUR09:** anthracene octafluoronaphthalene and **NPOFNP09:** naphthalene octafluoronaphthalene) featuring slightly longer but still notably short π-π contacts (approximately 3.1 Å) were selected. Lattice energy calculations were subsequently performed for these structures using the same computational methodology. The results obtained from Crystal Explorer and PIXEL resembled those determined for **L12a2** (Table 9), with prominent repulsion terms. These values suggest that the programs may not handle such short interactions well, which was further discussed with the authors of the software.

Table 9. *The results of the crystal lattice energy calculations for **ECUTUR09** and **NPOFNP09** (kJ/mol units).*

	E_ele	E_pol	E_dis	E_rep	E_tot
			ECUTUR09		
Pixel	−178.3	−80.5	−264.1	519.7	−3.2
CrystalExplorer	−153.5	−6.6	−217.1	296.2	−81.0

NPOFNP09					
Pixel	−137.8	−57.4	−218.9	418.3	4.3
CrystalExplorer	−120.2	−5.7	−187.3	234.7	−78.5

12. Structural Studies on the Metal Complexes: Porosity and Dynamics

Hundreds (approximately 800) metal-complexation and crystallization experiments were conducted aiming to obtain crystals of metallocycles. However, many crystallization attempts led to polycrystalline or amorphous precipitates, and in some cases, only the ligands or metal salts crystallized without forming the intended complex. Furthermore, in some cases coordination polymers were obtained instead of 0D metallocycles, as gaining control over the crystallization products and self-assembly process remains a formidable task and slight variations in crystallization conditions can result in entirely different products. **The presented series of metal complexes consist of 12 metallocycles (MC1-MC12) and 3 of 1D coordination polymers (CP1-CP3), which I was able to crystallize and which showed potential for further dynamics and porosity studies**.

12.1. Metallocycles (MCs)

12.1.1. Based on Naphthalene Core Ligands: 2,6-Bis((imidazol-1-yl)methyl)naphthalene (L2) and 2,6-Bis((2-methyl-imidazol-1-yl)methyl)naphthalene (L3)

The crystals of 2 metallocycles based on rigid naphthalene core suitable for SCXRD were obtained one with Cu(II) ion and **L2** and the other one with Co(II) ion and **L3**. The related crystallographic data are shown in Table 10.

Table 10. *Crystallographic data and structure refinement parameters for metallocycles based on naphthalene core ligands **MC1**, **MC2**, **MC2-a**, and **MC2-b**.*

Compound Reference	**MC1**	**MC2**	**MC2-a**	**MC2-b**
Chemical formula	$C_{36}H_{32}Cl_4Cu_2N_8$	$C_{41.6}H_{42.4}Cl_4Co_2N_{8.8}$	$C_{40}H_{40}Cl_4Co_2N_8$	$C_{40}H_{40}Cl_4Co_2N_8$
Formula mass	845.57	925.30	892.46	892.46
Crystal system	Monoclinic	Monoclinic	Monoclinic	Triclinic
a/Å	26.2905(35)	8.6819(3)	8.1764(2)	8.3472(5)
b/Å	14.3288(2)	15.6163(5)	16.3230(4)	10.8357(5)
c/Å	12.7203(3)	15.3308(6)	14.9045(3)	11.9070(5)
α/ ◦	90	90	90	85.199(4)
β/ ◦	117.818(3)	101.240(4)	97.506(2)	88.019(4)
γ/ ◦	90	90	90	81.204(5)
Unit cell volume/$Å^3$	4238.10(18)	2038.67(13)	1972.16(8)	1060.30(9)
Temperature/K	99.99(16)	100(2) K	100(2) K	100(1) K

Space group	*C2/c*	*P*2$_1$/*c*	*P*2$_1$/*c*	*P*-1
No. of formula units per unit cell, Z	4	2	2	1
Radiation type	CuK\α	CuK\α	CuK\α	CuK\α
Absorption coefficient, μ/mm^{-1}	3.826	9.129	9.408	8.749
No. of reflections measured	32237	12557	21591	7607
No. of independent reflections	4222	4000	3953	7607
Rint	0.0436	0.0408	0.0347	--
Final R1 [a] values (I > 2σ(I))	0.0561	0.0601	0.0376	0.0636
Final wR2 [b] values (I > 2σ(I))	0.1544	0.1584	0.0908	0.1621
Final R1 [a] values (all data)	0.0597	0.0722	0.0454	0.0931
Final wR2 [b] values (all data)	0.1583	0.1670	0.0949	0.1860
Goodness of fit on F^2	1.096	1.062	1.046	1.028

12.1.1.1. MC1: $[Cu_2(L2)_2Cl_4]\cdot xS$

12.1.1.1.1. Structural Analysis

The SCXRD study revealed that **MC1** is a metallocycle composed of two copper ions doubly bridged by two dipodal ligands and coordinated by chloride ions, resulting in a neutral complex of very distorted tetrahedral geometry with a τ_4 index of 0.52 (Table 11). τ_4 index is a geometric parameter proposed by Houser *et al.* to provide a straightforward and enhanced method for quantitatively assessing the geometry of four-coordinate complexes [210]. The proposed formula (as described below) is remarkably simple, allowing the τ_4 index to be calculated by hand using only the bond angles within the metal coordination sphere, where α and β are the two largest bond angles in the four-coordinate species. The values of τ_4 range from 1.00 for a perfect tetrahedral geometry to zero for a perfect square planar geometry.

$$\tau_4 = \frac{360^\circ - (\alpha + \beta)}{141^\circ}$$

Table 11: *Selected bond lengths [Å] and angles [°] for **MC1**.*

Compound	**Bond lengths**	**Bond angles**
MC1	Cu1-N1 1.958(3) Cu1-N20# 1.956(3) Cu1-Cl1 2.2647(10) Cu1-Cl2 2.2405(9)	N1-Cu1-N20# 148.37(11) N1-Cu1-Cl1 96.05(9) N1-Cu1-Cl2 94.68(9) N20#-Cu1-Cl1 95.93(8) N20#-Cu1-Cl2 95.54(8)

		Cl1-Cu1-Cl2 138.42(4)

[#]1-x,1-y,1-z

There is half of a metallocycle present in the asymmetric unit, with the other half being generated by an inversion center (Figure 57). The distance between Cu metal centers in the metallocycle formed is 11.94 Å. The metallocycles are stacked above each other along the crystallographic *c*-axis to form one-dimensional channels, as shown in Figure 57. The solvent molecules occupying the channels were very badly disordered, could not be modeled, and were treated with SQUEEZE as mentioned previously in section 8.1.

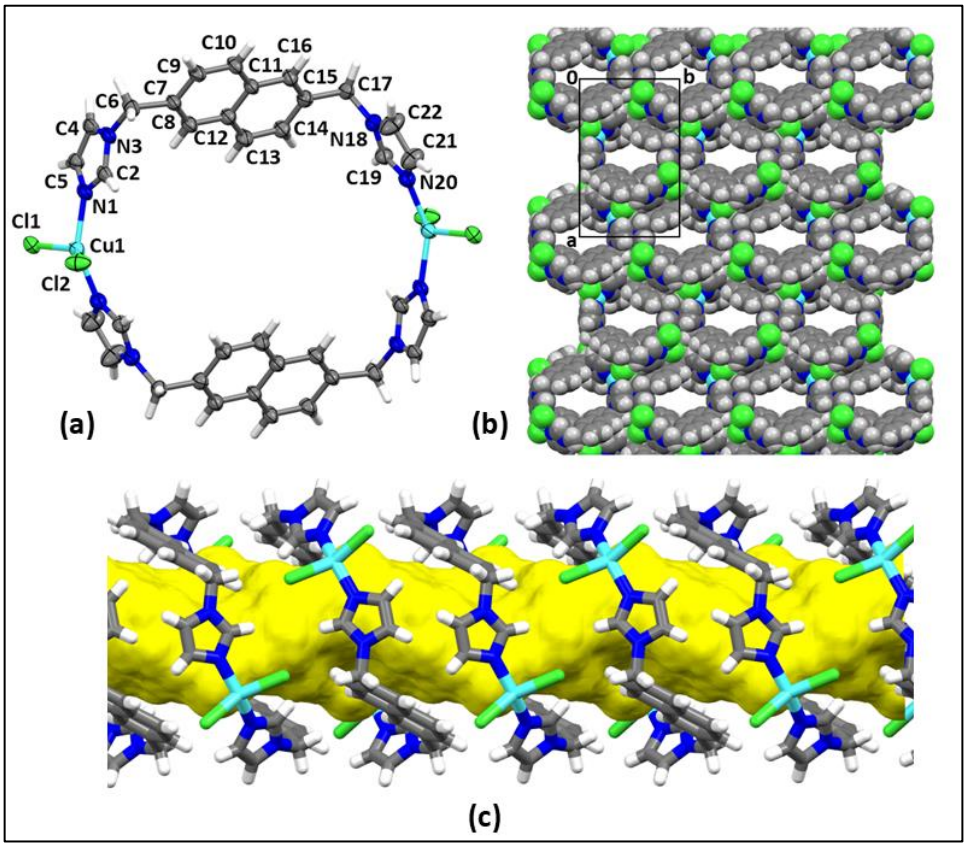

Figure 57: ***(a)*** *Representation of the molecular structure of* ***MC1*** *with displacement ellipsoids drawn at the 50% probability level, the unlabeled atoms are related to the labeled ones by the symmetry operation: 1-x,1-y,1-z;* ***(b)*** *space filling projection showing the packing arrangement of* ***MC1*** *along [001];* ***(c)*** *perspective view perpendicular to a one-dimensional channel (yellow surface) defined by a column of stacked above each other metallocycles shown in capped-sticks representation.*

Each column is in van der Waals contact with six neighboring columns to form a "brick wall" packing motif (Figure 57) as viewed along [001]. This arrangement is stabilized by intermolecular π-π interactions present between imidazole rings (N1-C5) with a centroid-centroid distance of 3.387(3) Å, symmetry operator 1-x,2-y,1-z and between imidazole

rings (N18-C22) at a distance of 3.4625(19) Å, symmetry operator 1/2-x,1/2-y,-z, respectively, C-H···π interactions involving imidazole rings (N18-C22) as donor and benzene rings (C7-C12) as acceptor, and C-H···Cl interactions involving H-atoms of the methylene group (C6) with Cl2 as acceptors and H-atoms of the benzene rings (C12-C16) with Cl1 as acceptors (Table S2).

12.1.1.1.2. Bulk Solid-State Studies

As the molecular packing indicated presence of channels thermogravimetric analysis (TGA) of **MC1** was performed to assess the removability occupying these solvent molecules.

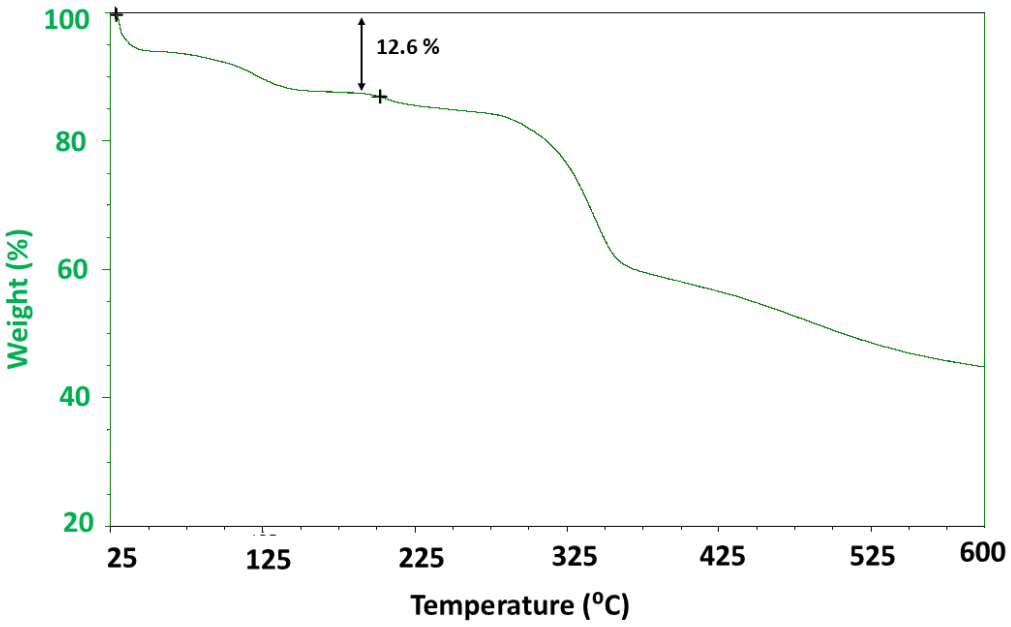

Figure 58: *Thermogram of **MC1**.*

The analysis revealed that the guest molecules were released stepwise up to the point of melting (around 210 ºC) corresponding to a weight loss of *ca*. 12.6% (predicted value of 12.7% for 3 acetonitrile molecule per metallocycle) (Figure 58). The obtained result from TGA indicated that the system could not be further analyzed towards porosity, as it was not possible to fully evacuate the solvent from this crystalline material. Thus, the material which after structural analyses was looking very promising for further sorption application appear to be not usable.

12.1.1.2. MC2: $[Co_2(L3)_2Cl_4]\cdot 0.8CH_3CN$

12.1.1.2.1. Structural Analysis

Good quality crystals of **MC2:** $[Co_2(\mathbf{L3})_2Cl_4]\cdot 0.8CH_3CN$, where **L3** differs from **L2** by presence of methyl substituents on imidazole rings were obtained by the slow evaporation from acetonitrile. Unfortunately, I was not able to obtain analogue of **MC1** with Cu(II) chloride. SCXRD revealed that **MC2** crystallizes in the monoclinic $P2_1/c$ space group, where the asymmetric unit consists of one ligand molecule, one Co(II) cation and two chloride ions coordinated with the metal center as well as acetonitrile molecule of partial occupancy present at the inversion center. The Co(II) ions in **MC2** exhibit an almost perfect tetrahedral geometry (τ_4 index of 0.97) [210]. These are coordinated with two N atoms originating from imidazole rings belonging to two symmetry related ligands **(L3)** and chloride ions with Cd-N and Cd-Cl distances in the range of 2.017(3)–2.023(3) Å and 2.2532(12)-2.26(12) Å, respectively, and bond angles ranging from 104.34(11)º to 112.07(13)º (Table 12) yielding once again a neutral cyclic complex $[M_2L_2Cl_4]$. Co---Co distance in this metallocycle is equal to 14.214(1) Å. The angle between the planes of the imidazole rings within a ligand is 63.75º, and between the planes of the naphthalene ring and the imidazole rings are 84.86º/76.71º.

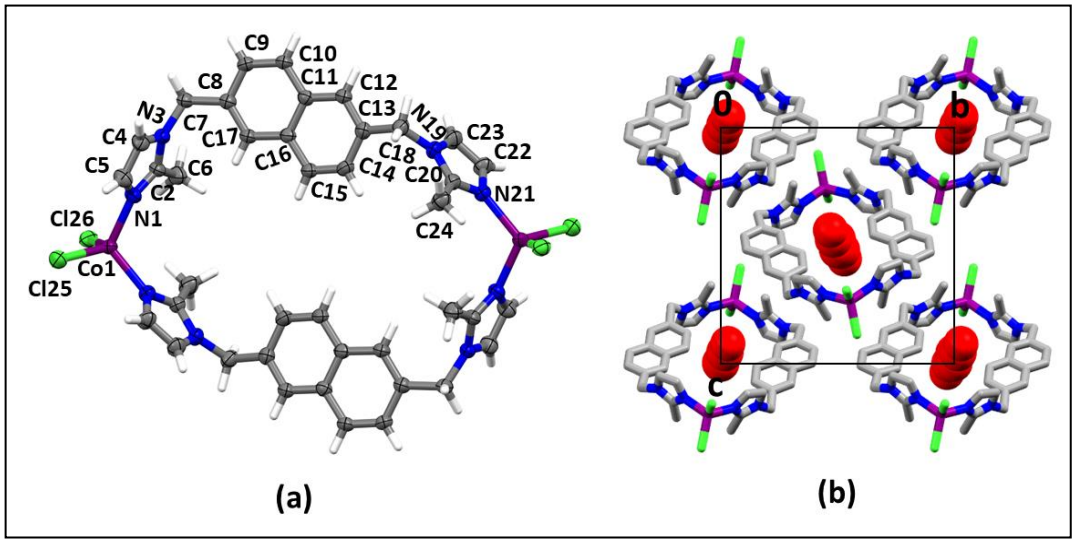

Figure 59: ***(a)*** *Representation of the molecular structure of* ***MC2*** *with displacement ellipsoids drawn at the 50% probability level, solvent molecules have been omitted for clarity;* ***(b)*** *Packing diagram of* ***MC2*** *shown along the a-axis, solvent molecules are shown in red, hydrogen atoms were omitted for clarity.*

The host metallocycles stack to form linear columns along [100] (Figure 59) with each metallocycle tilted at an angle of approximately 50° relative to this axis. **MC2** contains solvent-accessible voids with an estimated volume of ~13 $Å^3$ per unit cell (calculated using a spherical probe radius of 1.2 Å and a grid spacing of 0.3 Å in Mercury) which are

occupied by disordered acetonitrile molecules. The packing arrangement of **MC2** is stabilized by a range of weak hydrogen bonds, such as C–H···Cl and C–H···π involving H-atoms from the methyl group of acetonitrile molecule, imidazole ring (N1-C5), and methyl group of the same imidazole ring with imidazole (N19-C23) and benzene (C11-C16) rings, C–H···N interactions involving H-atoms from the methyl group of the acetonitrile molecule, methylene group (C18), both benzene rings and N-atoms from the acetonitrile molecule, and both the imidazole rings (refer Table S2 for details). There are also π-π interactions formed between the two different imidazole rings (N1-C5) and (N19-C23) with a distance of 3.629(3) Å, symmetry operator: -1+x,1/2-y,-1/2+z.

12.1.1.2.2. Bulk Solid-State Studies

To assess if it is possible to remove solvent molecules from the host thermogravimetric analysis (TG) has been applied. The analysis revealed a weight loss of approximately 4.6% uptill 130 °C (Figure 60), which correlates well with the theoretical value of 4.4% expected for the loss of 1 acetonitrile molecule per metallocycle. As in the crystal acetonitrile molecule shows partial occupancy it could indicate that the solvent molecules are coming out easily. The system remains stable up to 380°C, which marks the decomposition temperature.

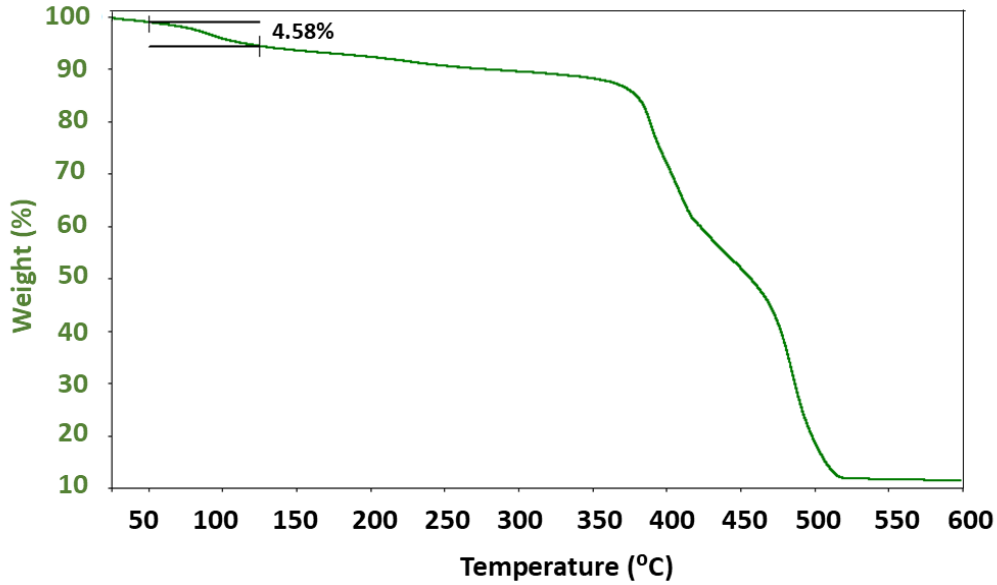

Figure 60: *Thermogram of **MC2**.*

A good match of the simulated PXRD patterns with the as-synthesized PXRD patterns was observed for **MC2** (Figure 61), indicating that the bulk sample is homogenous and can be used further for sorption studies.

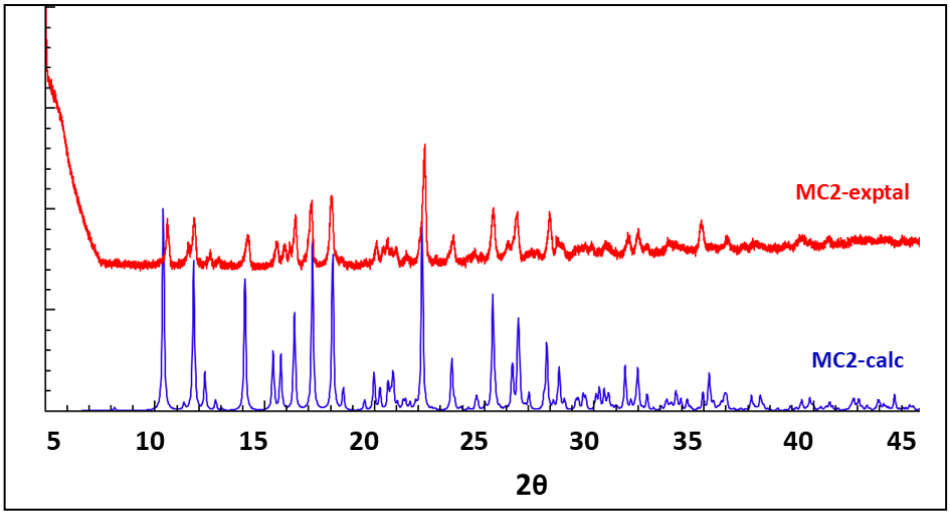

Figure 61: *Comparison of the calculated and experimental powder patterns of **MC2**.*

12.1.1.2.3. Triggered Structural Transformations of MC2 to MC2-a and MC2-b

Acetonitrile solvate **MC2** can be converted to a non-porous phase **MC2-a** upon heating for a 3-4 minutes at 100 ºC or leaving it in the air for a few weeks. The new phase shows the same space group as **MC2** with some differences in the unit cell parameters namely, reduction along the *a* (5.8%) and *c*-axis (2.8%) as well as elongation along the *b*-axis (4.3%), leading to approximately 3% decrease in the overall cell volume. The tetrahedral coordination geometry got a bit more distorted as indicated by a slightly lower value of τ_4 index (0.94) and values of the corresponding angles (see table 12). Particularly the value of N-Co-N angle decreased of 8° as compared to **MC2**. Moreover, one of the imidazole rings changed its orientation in **MC2-a** as evident by the value of the angle between the planes of the opposite imidazole rings within a ligand which is 83.94º in case of **MC2-a** as compared to 63.75º in **MC2** as mentioned before, and the values of torsion angles C8-C7-N3-C4 and C13-C18-N19-C23, which are 90º and 69º for **MC2** and 78º and 35º for **MC2-a**, respectively. Moreover, free space between the naphthalene cores in the metallocycle with C15---C15 distances is changing from 4.97 Å in **MC2** to 4.45 Å in **MC2-a**. The changes in molecular geometry reflect in differences in the molecular packing which are specially visible along [001] (see Figure 62). The intermolecular interactions stabilizing the crystal structure involve in **MC2-a** different atoms than in **MC2**. The packing of **MC2-a** is stabilized through interactions such as C–H···Cl, C–H···N involving methylene group (C18), and imidazole ring (N1-C5), and C–H···π involving H-atoms from the methyl group of imidazole ring (N1-C5), methylene group (C18), benzene ring (C8-C17) and imidazole

ring (N1-C15) with imidazole (N1-C5) and benzene (C11-C16) rings (Table S2). π-π stacking interactions which were present in **MC2** are absent in this case.

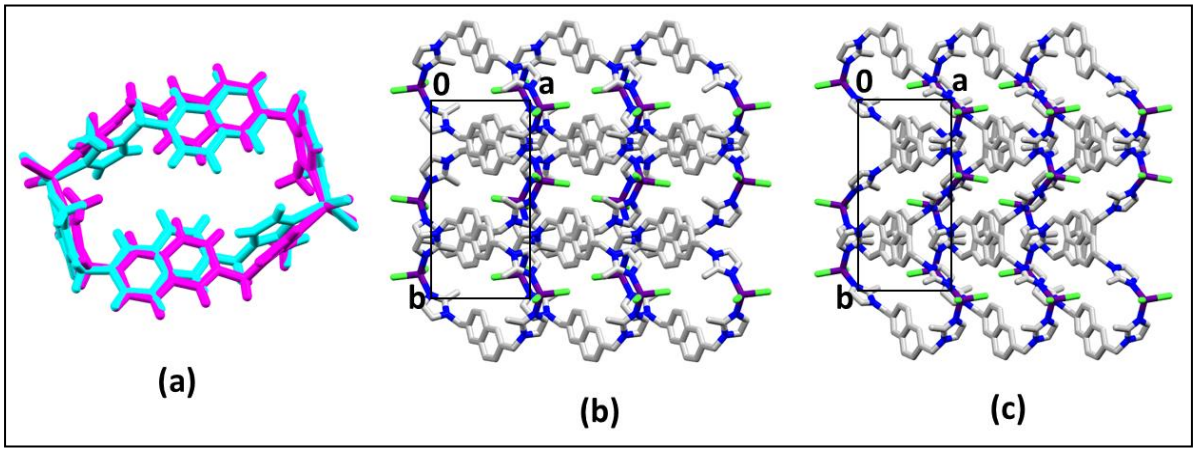

Figure 62: ***(a)*** *Molecular overlay of* ***MC2*** *(magenta) and* ***MC2-a*** *(blue), RMSD is 0.6915 Å;* ***(b)*** *Packing diagram of* ***MC2*** *and* ***(c)*** ***MC2-a*** *shown along the c-axis, hydrogen atoms and solvent molecules were omitted for clarity.*

This arrangement leads to a densely packed phase **MC2-a** upon solvent removal and thus mercury doesn't find any voids using a solvent-accessible surface with a probe radius of 1.2 Å and a grid spacing of 0.3 Å, upon decreasing a probe radius to 0.8 Å, it displays discrete voids of only around 3.38 $Å^3$ per unit cell.

Packing comparison of **MC2** and **MC2-a** was carried using the Mercury and XPac program, where Mercury showed an overlap of 11 molecules out of 15 with a root-mean-square (RMS) deviation of 1.02 Å on applying the standard settings with a 20% tolerance for bond lengths and angles, and XPac identified the formation of 3D supramolecular constructs with a dissimilarity index (x) of 12.0, wherein all the atomic coordinates (in crystal geometry) except for the hydrogen and solvent atoms were taken for the analysis. Previously, it was shown that dissimilarity values around 1 are typical when small substituents such as chlorine are replaced with bromine (x = 1), while more substantial changes, like the replacement of a methyl group with a trifluoromethyl group, yielded values around x = 2.8 in case of organic molecular crystals [208]. Although the dissimilarity index provides quantitative data, it does not exhibit a consistent pattern of maximum and minimum values. Systems of high similarity (three-dimensional, 3D) with dissimilarity values close to 10.0 and lower similarity with dissimilarity values close to 1.0 are observed. This inconsistency arises from the varying number of molecules considered in each case and does not allow a range of comparisons, as observed in recent studies [211-213]. As a

result, the *x* values do not always offer a reliable quantitative information for comprehensive crystal structure comparisons.

Interestingly one more phase **(MC2-b)** was isolated by changing desolvation conditions: the crystals of **MC2** were kept under the vacuum for 4 hours. The asymmetric unit of **MC2-b** is similar to **MC2-a**, however, in this case, symmetry breaks and the structure transforms from a higher symmetry monoclinic crystal system containing glide planes, two-fold-screw axes, and inversions to a lower symmetry triclinic crystal system containing only inversions. One of the 2-methylimidazole groups in this structure was found to be disordered and modelled into two positions with occupancies of 65% and 35% indicating that in one ligand two methyl groups sometimes are pointing out the same direction sometime opposite. The latter orientation was present in **MC2** and **MC2-a**. The cif file was split into two parts to facilitate a better comparison of **MC2-b** with **MC2** and **MC2-a**. The major component structure is denoted as **MC2-b1**, and the minor component structure is denoted as **MC2-b2**. The content of the asymmetric unit in **MC2-b** is very similar to **MC2** and **MC2-a**, however the values of angles forming coordination geometry show some differences particularly those involving nitrogen atoms from the disordered imidazole ring. For instance, the N1/1A-Co-Cl26 angle shows the most significant variation (see table 12), it is approximately 12° smaller in **MC2-b1** and 11° larger in **MC2-b2** compared to **MC2**. Relative to **MC2-a**, this angle is about 16° smaller in **MC2-b1** and 7° larger in **MC2-b2**. The τ index value decrease showing value ca.0.89 (0.90/0.88 for **MC2-b1** and **MC2-b2**, respectively). The bond lenght values for **MC2** series (**MC2**, **MC2-a** and **MC2-b**) do not deviate from typical values for comparable molecular fragments, as revealed by a Mogul geometry check in Mercury (CCDC).

Table 12: *Selected bond lengths [Å] and angles [°] for **MC2**, **MC2-a** and **MC2-b.***

Compound	Bond length	Bond angles
MC2	Co1-N1 2.023(3)	$N21^{\#}$-Co1-N1 112.09(4)
	Co1- $N21^{\#}$ 2.017(3)	N1-Co1-Cl25 104.35(11)
	Co1-Cl25 2.2600(12)	$N21^{\#}$-Co1-Cl25 106.74(11)
	Co1-Cl26 2.2532(12)	N1-Co1-Cl26 110.81(11)
		$N21^{\#}$-Co1-Cl26 111.21(11)
		Cl25-Co1-Cl26 111.38(5)

MC2-a	Co1-N1 2.005(2) Co1- N21$^{\#}$ 2.023(2) Co1-Cl25 2.2506(8) Co1-Cl26 2.2406(7)	N21$^{\#}$-Co1-N1 104.12(9) N1-Co1-Cl25 105.65(7) N21$^{\#}$-Co1-Cl25 110.26(6) N1-Co1-Cl26 115.04(7) N21$^{\#}$-Co1-Cl26 112.60(6) Cl25-Co1-Cl26 108.86(3)
MC2-b1	Co1-N1 2.018(8) Co1- N21$^{\#}$ 2.017(4) Co1-Cl25 2.2537(16) Co1-Cl26 2.2476(16)	N21$^{\#}$-Co1-N1 118.9(3) N1-Co1-C25 109.7(2) N21$^{\#}$-Co1-Cl25 103.08(13) N1-Co1-Cl26 98.8(3) N21$^{\#}$-Co1-Cl26 113.76(13) Cl25-Co1-Cl26 112.79(6)
MC2-b2	Co1-N1A 2.034(15) Co1- N21$^{\#}$ 2.017(4) Co1-Cl25 2.2537(16) Co1-Cl26 2.2476(16)	N21$^{\#}$-Co1-N25 102.1(4) N1A-Co1-C25 101.3(4) N21$^{\#}$-Co1-Cl25 103.09(12) N1A-Co1-Cl26 121.6(4) N21$^{\#}$-Co1-Cl26 113.75(13) Cl25-Co1-Cl26 112.79(6)

$^{\#}$1-x,1-y,1-z

Moreover, the metallocycle's shape is very different due to the rotation of one of the 2-methylimidazole groups on the ligand. The angle between the planes of the opposite imidazole rings within a ligand in **MC2-b1/b2** is 67.95º/69.85º, which is 63.75º and 83.94º in **MC2** and **MC2-a**, as mentioned before. The torsion angle from the disordered 2-methylimidazole group, C8-C7-N3-C4 is -72º for **MC2-b1**, and C8-C7-N3A-C4A is 87º for **MC2-b2**, respectively, indicating reorientation of the 2-methylimidazole group. The Co---Co distance in **MC2-b** is 13.21 Å which is around 1 Å shorter as compared to **MC2** and **MC2-a**. On the other hand, naphthalene rings in **MC2-b** are farther apart as compared to **MC2** and **MC2-a** with a C15---C15 distance of 6.69 Å, which was 4.97 Å in **MC2** and 4.45 Å in **MC2-a**, suggesting a significant expansion of metallocycle.

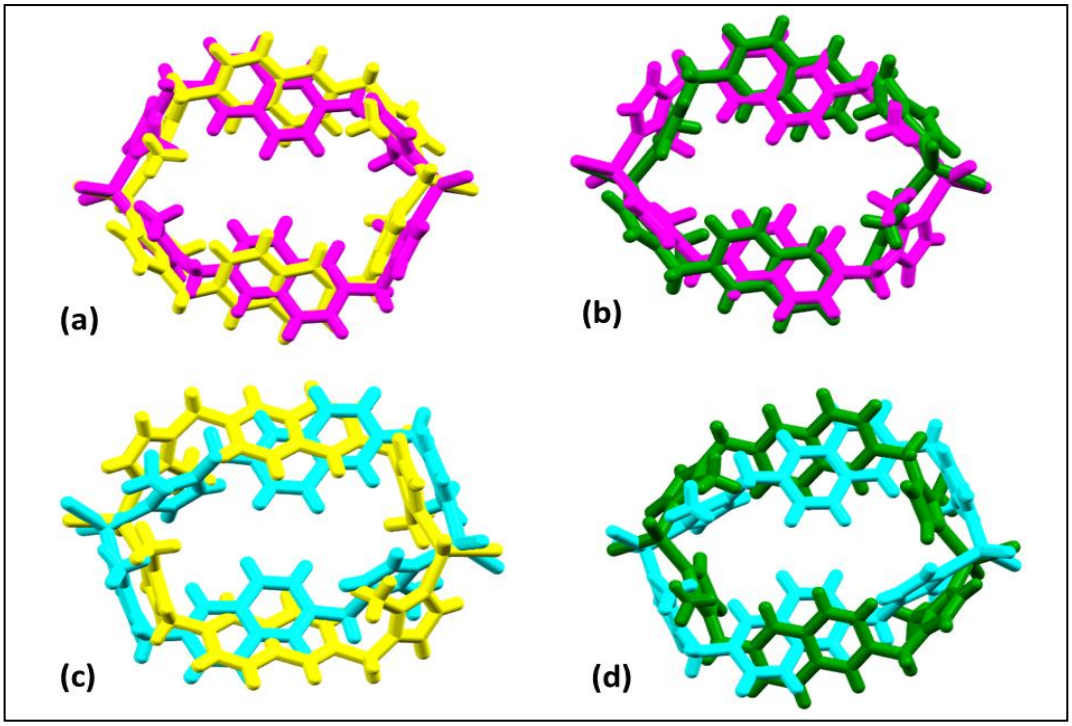

Figure 63: *Molecular overlay of **(a) MC2** (magenta) and **MC2-b1** (yellow), RMSD is 1.4252 Å; **(b) MC2** (magenta) and **MC2-b2** (green), RMSD is 1.3261 Å; **(c) MC2-a** (sky blue) and **MC2-b1** (yellow), RMSD is 1.8306 Å; **(d) MC2-a** (sky blue) and **MC2-b2** (green), RMSD is 1.7755 Å.*

The host metallocycles in **MC2-b** also stack to form linear columns along [100] but these are packed differently as the rotation of the ligand within the metallocycle alters the stabilizing interactions, resulting in the crystal structure of **MC2-b** being stabilized by a different set of interactions compared to **MC2** and **MC2-a**. π-π stacking interactions which were absent in **MC2-a** but present in **MC2** between the two different 2-methylimidazole groups of adjacent metallocycle, are now present between the same imidazole rings (N1-C5) at a distance of 3.675(6) Å, symmetry operator- -x,-y,1-z, and between (N19-C23) at a distance of 3.842(3) Å, symmetry operator- 1-x,2-y,-z. Moreover, C–H···Cl interactions involves methylene groups, and both imidazole rings as donors for Cl25 as acceptors and methylene groups, disordered imidazole rings, and C-H from benzene ring (C11-C15) as donor for Cl26 as acceptors. Additionally, C–H···N interaction involve the methyl groups of 2-methylimidazole rings (N1A-C5A) and N1A atoms of the same ring in adjacent metallocycle as acceptor (Table S2).

The structure of **MC2-b** contains discrete voids aligned along the columns formed by the stacked dinuclear rings along the *a*-axis with an estimated volume of ~12 Å^3 per unit cell (calculated using a solvent accessible surface having a probe radius of 1.2 Å in Mercury).

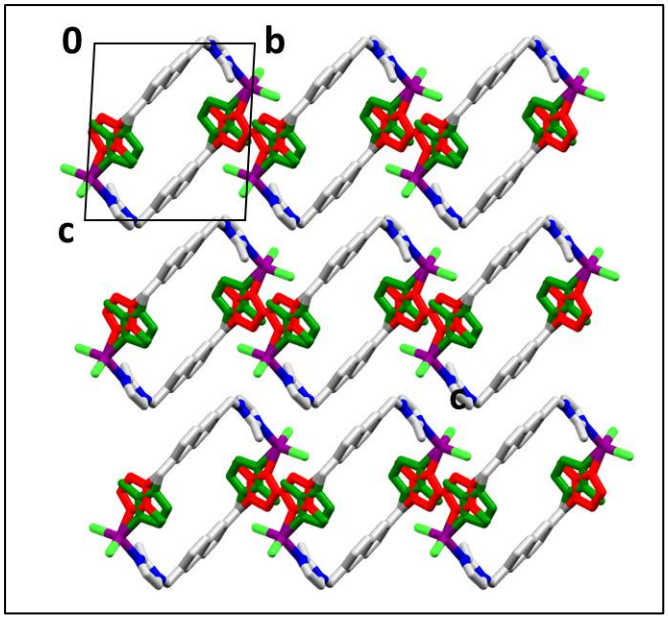

Figure 64: *Packing diagram of **MC2-b** shown along the a-axis, disordered 2-methylimidazole group is shown in red (major) and green (minor), hydrogen atoms were omitted for clarity.*

Hirshfeld surface analysis was performed using Crystal Explorer and two-dimensional fingerprint plots were generated to investigate and quantify the contributions of intermolecular interactions stabilizing the crystal structures of **MC2-a** and **MC2-b** (averaging MC2-b1 and MC2-b2). The analysis shows that H···H contacts represent the largest contribution to the Hirshfeld surface in both the cases, though this contribution is lower in **MC2-b** compared to **MC2-a**. Additionally, the analysis confirms the presence of π-π interactions in **MC2-b**, which are absent in **MC2-a**, while C–H···N, C–H···Cl, and C–H···π interactions are predominant in **MC2-a** (Figure 65).

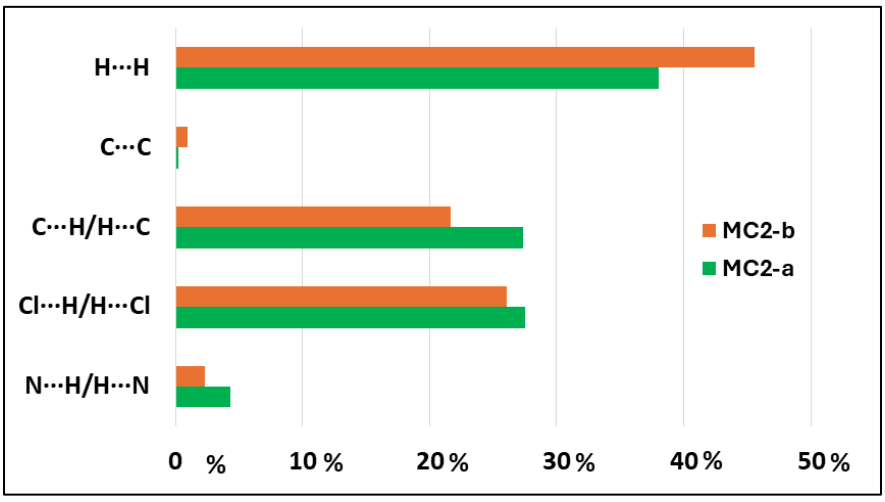

Figure 65: *Estimated contributions of selected intermolecular forces stabilizing the formation of **MC2-a** and **MC2-b** (average of **MC2-b1** and **MC2-b2**).*

Packing comparison of **MC2-a** with **MC2-b1** and **MC2-b2** showed an overlap of only 1 molecule out of 15 with a root-mean-square deviation of 2.036 Å calculated using the standard settings with a 20% tolerance for bond lengths and angles in Mercury, whereas XPac showed no structural similarity.

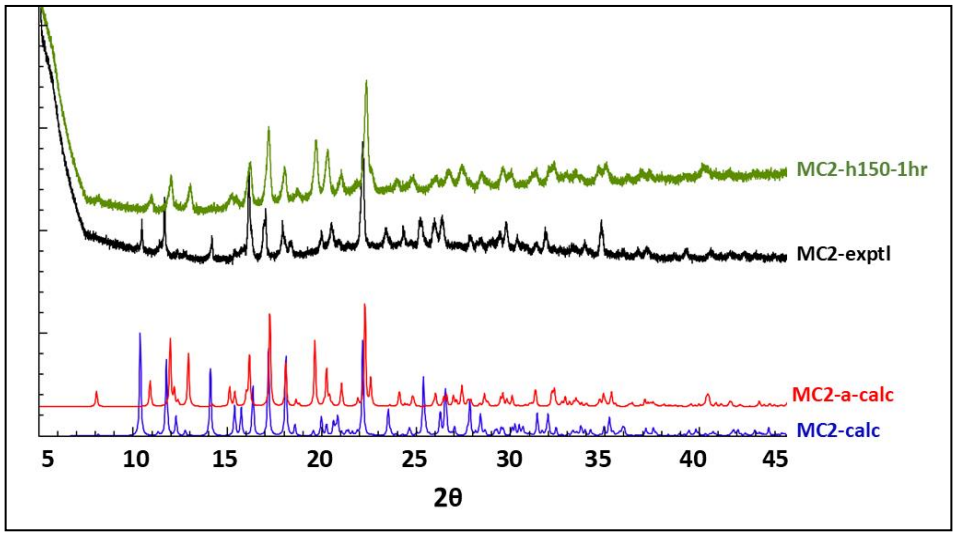

Figure 66: *Comparison of the calculated and experimental powder patterns of **MC2** and **MC2-a**.*

Desolvated crystals of **MC2** were exposed to acetonitrile vapour to test the reversibility of the desolvation process; however, they did not readsorb the solvent. Nevertheless, the conformational flexibility of **MC2** indicated its potential to exhibit permeability to small gas molecules. While not porous in the conventional sense, similar structures have demonstrated gas and guest permeability, prompting further investigation of the system through sorption studies [84, 86-91].

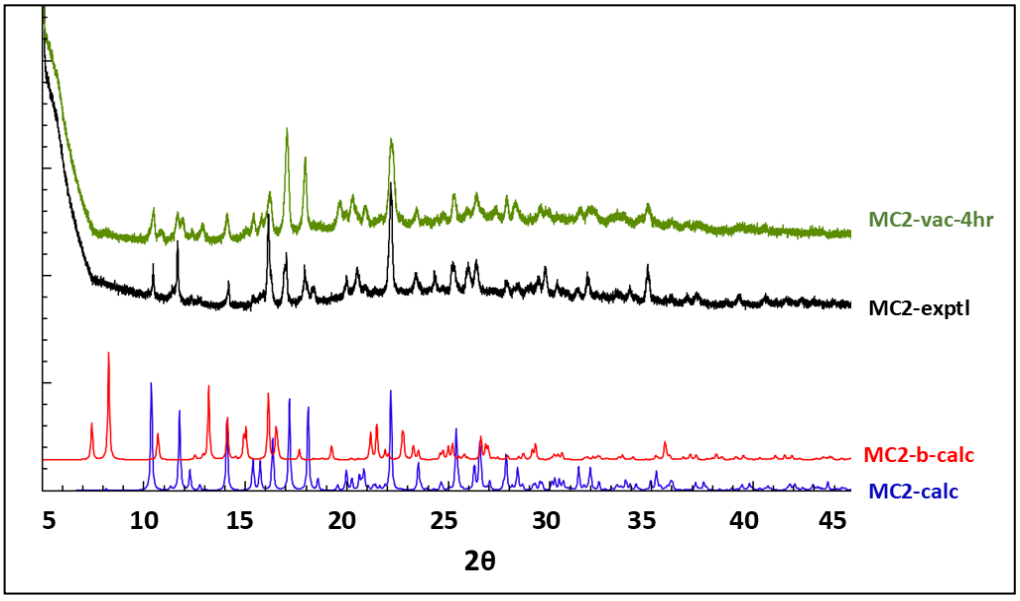

Figure 67: *Comparison of the calculated and experimental powder patterns of **MC2** and **MC2-b**, respectively.*

Moreover, the transformations were also followed in bulk using powder X-ray diffraction (PXRD). A good match of the simulated PXRD patterns with the as-synthesized PXRD patterns was observed for **MC2** as shown previously which upon heating match with **MC2-a** phase indicating the conversion of **MC2** to **MC2-a** (Figure 66). Unfortunately, the **MC2-b** phase was not captured via PXRD after exposure to vacuum for 4h instead we could notice the presence of **MC2-a** (Figure 67). We were able to catch this phase during SCXRD studies as the crystals were immediately immersed in oil and measured.

12.1.1.2.4. Porosity Studies

To explore the potential of **MC2** as a porous material the obtained crystalline material was activated by heating at 100 ºC for 1 hour under vacuum and exposed to various gases. Sorption isotherms for N_2, CO_2, and CH_4 were measured gravimetrically at room temperature. The system did not take any N_2, and CH_4, but interestingly shows some affinity for CO_2. The CO_2 adsorption shows isotherm type I which is the characteristic of microporous structures, where saturation uptakes were 0.47 and 0.495 mmol/g or 2.07 wt% and 2.18 wt% at temperatures of 34 ºC and 24 ºC, respectively, which roughly corresponds to 0.5 CO_2 per host molecule.

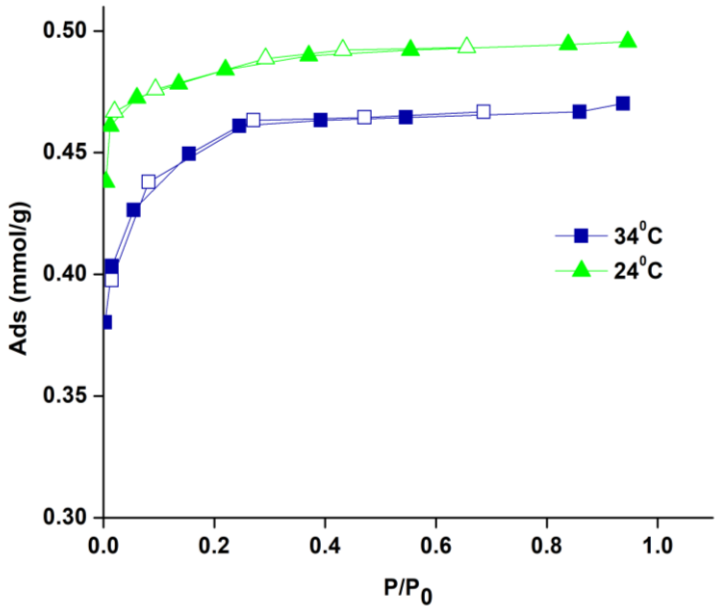

Figure 68: *CO_2 sorption isotherms recorded at 24 ºC and 34 ºC for **MC2**, wherein closed and open symbols represent adsorption and desorption, respectively.*

A particularly interesting observation is that gas uptake occurs even though the desolvated structures appear to lack continuous channels connecting the voids. This would indicate that this phenomenon could be attributed to the dynamic motion of the molecular crystal components, which transiently generate short-lived channels. This assumption is supported by isolation of **MC2-b**, where the **MC2** structure, upon prolonged exposure to vacuum, undergoes a significant expansion. In this state, channels can be mapped using a solvent-accessible surface with 0.8 Å probe radius, indicating that the voids might undergo further expansion when exposed to gases at higher pressures. This expansion is likely driven by the cooperative movement of the molecular crystal components [86] which is somewhat attributed to the flexibility of the ligands forming metallocycle. Furthermore, the selective adsorption of CO_2 over N_2 can be explained by differences in polarity, a trend that is well documented in MOFs [214-217]. The electrostatic and van der Waals interactions are more favorable for CO_2 due to its quadrupole moment and higher polarizability, which enable stronger binding to polar groups and charged sites. In contrast, N_2 is non-polar and interacts weakly with such sites. To accurately determine the specific CO_2 binding locations within a compound, advanced techniques are essential. These include computational methods such as Density Functional Theory (DFT) and Grand Canonical Monte Carlo (GCMC) simulations, as well as experimental approaches like in-situ single-crystal X-ray diffraction using an environmental gas cell have also been employed for study on single-crystals [88]. Morever it can have something to do with kinetic diameters. CO_2, with a smaller kinetic diameter (3.3 Å) [218], is able to diffuse through the transient channels, whereas N_2, with a kinetic diameter of 3.64 Å, is unable to pass through them.

12.1.2. Based on Partially Embedded Anthracene Moiety

12.1.2.1. MC3: $[Co_2(L4)_2Cl_4]\cdot CH_3CN$, MC4: $[Co_2(L4)_2Br_4]\cdot 4CH_3CN$ and MC5: $[Co_2(L5)_2Br_4]$

After exploring ligands based on a naphthalene core, the next planned step was to extend the core by introducing phenanthrene. However, despite attempting several multi-step synthetic routes, it was not possible to obtain these ligands. As an alternative, I turned to ligands featuring a partially embedded anthracene moiety. These ligands also offer a π-rich environment that promotes π–π interactions. Unfortunately, **L4** and **L5** exhibited poor solubility in organic solvents, which posed a significant challenge for crystallizing the resulting metal complexes.

Table 13. *Crystallographic data and structure refinement parameters for **MC3**, **MC4**, and **MC5**.*

Compound Reference	**MC3**	**MC4**	**MC5**
Chemical formula	$C_{62}H_{47}Cl_4Co_2N_9$	$C_{68}H_{56}Br_4Co_2N_{12}$	$C_{64}H_{52}Br_4Co_2N_8$
Formula mass	1177.74	1478.74	1370.63
Crystal system	Triclinic	Triclinic	Triclinic
a/Å	10.5487(1)	10.5557(2)	8.9323(2)
b/Å	10.5577(1)	13.3558(3)	12.2660(3)
c/Å	12.4906(2)	13.4158(3)	13.9350(4)
α/ ◦	105.141(1)	116.225(2)	68.391(2)
β/ ◦	100.577(1)	108.028(2)	76.608(2)
γ/ ◦	100.266(1)	93.512(2)	81.672(2)
Unit cell volume/$Å^3$	1281.93(3)	1569.30(7)	1377.87(6)
Temperature/K	99.99(10)	100(1)	100(1)
Space group	*P*-1	*P*-1	*P*-1
No. of formula units per unit cell, Z	1	1	1
Radiation type	CuK\α	CuK\α	CuK\α
Absorption coefficient, μ/mm^{-1}	7.405	7.534	8.504
No. of reflections measured	37276	17349	17977
No. of independent reflections	5140	5633	5633
Rint	0.0144	0.0148	0.0280
Final R1 [a] values (I > 2σ(I))	0.0227	0.0248	0.0358
Final wR2 [b] values (I > 2σ(I))	0.0611	0.0738	0.0987
Final R1 [a] values (all data)	0.0227	0.0251	0.0394
Final wR2 [b] values (all data)	0.0612	0.0740	0.1008
Goodness of fit on F^2	1.046	1.099	1.074

All three metallocycles **MC3**, **MC4** and **MC5** crystallize in the *P*-1 space group of triclinic crystal system.

12.1.2.1.1. Structural Analysis

The asymmetric unit of acetonitrile solvate **MC3** $[Co_2(\mathbf{L4})_2Cl_4]\cdot CH_3CN$, contains a ligand (**L4**) molecule, Co(II) cation, two chloride ions coordinated to a metal center, and a half of acetonitrile molecule which is located around the inversion center. The dinuclear neutral metallocycle formed contains two Co(II) ions which are connected by two bridging ligands (**L4**) through the N-atoms originating from the benzimidazole rings. The shape of the metallocycle reminds to some extend a cage as an effect of protruding phenyl rings. The geometry around the metal center is slightly distorted tetrahedral (τ_4 index of 0.93) as can be seen from the angles values in Table 14. The benzimidazole rings within a ligand in **MC3** are perpendicular to each other with an angle of 90º, while the angles between the planes of the anthracene ring and the benzimidazole rings are 86/88º, and the distance between the Co(II) metal centers is 11.1787(3) Å.

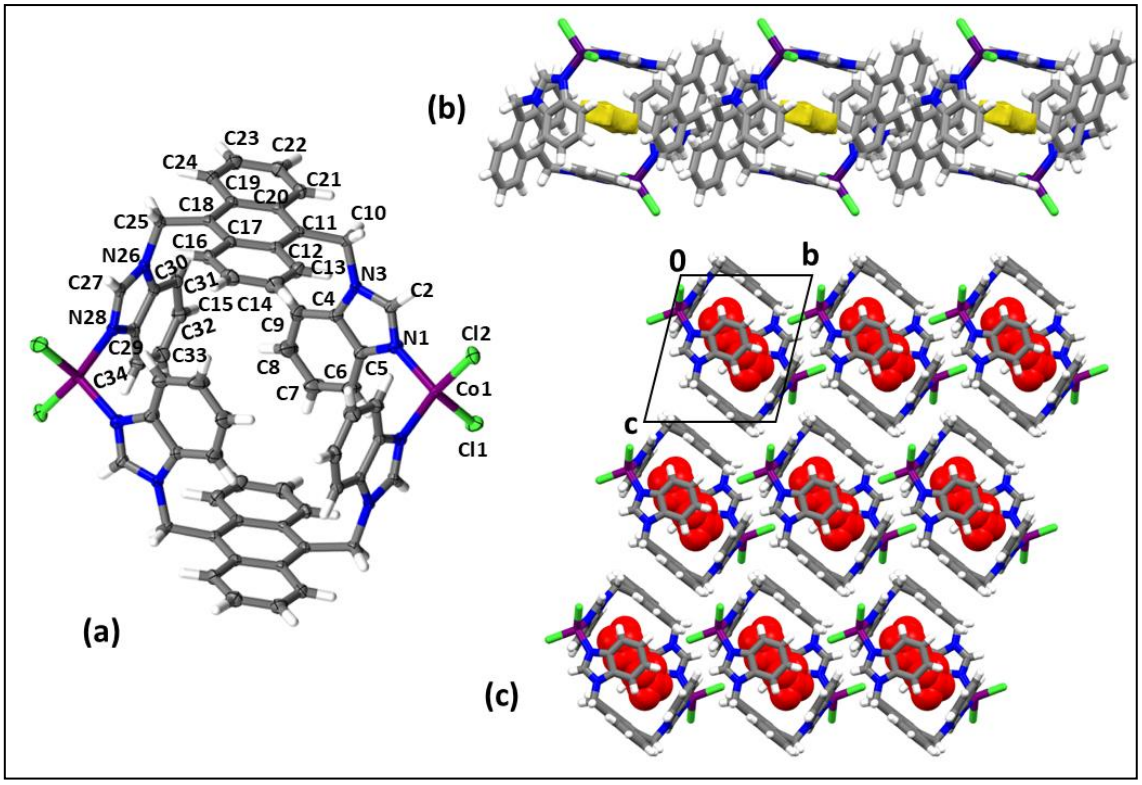

Figure 69: **(a)** *Representation of the molecular structure of **MC3** with displacement ellipsoids drawn at the 50% probability level, the unlabelled atoms are related to the labelled ones by the symmetry operation: 1-x,1-y,1-z;* **(b)** *Perspective view of **MC3** with solvent-filled pockets in yellow expanding along [001], calculated using a solvent accessible surface with a probe radius of 1.2 Å;* **(c)** *Capped-stick packing arrangement of **MC3** shown along the a-axis, the solvent molecules are shown in red in spacefill representation.*

The host metallocycles stack over top of one another to form columns along the *a*-axis resulting in motive highly reminiscent to the one present in **MC1**. However, in this case, because of introduction of bulky ligand and pseudo-cage formation instead of 1D channels, solvent molecules (acetonitrile) are present in the discrete pockets (Figure 69).

This arrangement is stabilized through C–H···N interactions extending along [011], between MCs involving CH- of anthracene rings and N-atoms originating from the benzimidazole rings, C–H···Cl interactions involving methylene groups (C25) and CH- originating from the imidazole ring of the benzimidazole moiety (N26-C34) as donor where C11 act as acceptor, and methylene groups (C10), CH- originating from the anthracene rings and benzene rings (C4-C9) as donor where Cl2 act as acceptor, C–H···π hydrogen bonds where CH- originating from the benzene rings (C19-C24) act as a donor and imidazole rings (N26-C30) as an acceptor (Table 15). There is also a variety of π-π interactions present between benzimidazole moiety and the anthracene moiety (Table S3).

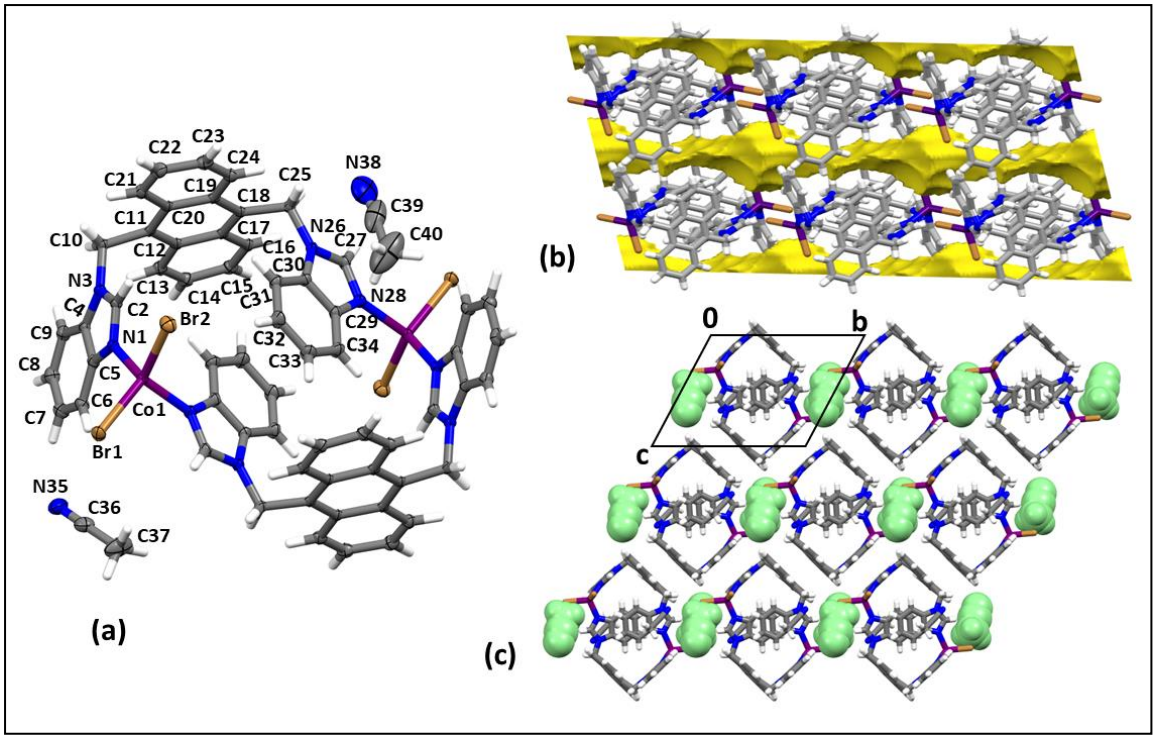

Figure 70: ***(a)*** *Representation of the molecular structure of* ***MC4*** *with displacement ellipsoids drawn at the 50% probability level, the unlabelled atoms are related to the labelled ones by the symmetry operation: 1-x,1-y,1-z;* ***(b)*** *Perspective view of columnar stacking of* ***MC4*** *along [100] (horizontal direction) viewed down the b-axis, solvent-filled channel are shown in yellow (calculated using a solvent accessible surface with a probe radius of 1.2 Å);* ***(c)*** *Capped-stick packing arrangement of* ***MC4*** *shown along the a-axis, the solvent molecules are shown in light green in spacefill representation.*

MC4 was obtained by applying the different counterion Br^- instead of Cl^- as in **MC3**. The compound crystallizes in *P*-1 space group like **MC3**. The asymmetric unit of **MC4** contains similar contents to **MC3** with different counterions and presence of two acetonitrile molecules instead of a half (Figure 70). The major difference in the shape of metallocycles **MC3** and **MC4** arises because of ligands adopts different conformation. This however does not really affect the coordination environment (Table 14). The geometry around the metal center remains slightly distorted tetrahedral with a τ_4 index of 0.93, where the largest angle difference is observed in the N-Co-N which is approximately 5° smaller as compared to **MC3**.

In case of **MC3**, the phenyl rings originating from benzimidazole units of the same ligand are pointing out the same direction and there are tilted towards each other, however, in the case of **MC4**, the benzimidazole units adopt other conformation and one benzene ring is pointing towards the metallocycle and the other outwards (see figure 72 for the comparison). In this case the angle between the planes of the benzimidazole rings within a

ligand in **MC4** is 73.99º, which was almost 90º in the case of **MC3** and the angles between the planes of the anthracene ring and the benzimidazole rings are 85.88/89.76º. The distance between the Co(II) metal centers in this case is 9.3678(6) Å which is almost 2 Å shorter as compared to **MC3**.

The packing shows similar columnar motive along *a*-axis as it was in **MC3**. However, in this case solvent molecules are not located inside of the metallocycles. They take the interstitial space (Figure 70). The packing is stabilized via intermolecular C–H···N interactions involving N-atoms from acetonitrile molecules, C–H···Br interactions involving methylene groups (C25) and CH- originating from the imidazole ring of the benzimidazole moiety (N26-C34) as donor where Br1 acts as acceptor, and CH- originating from the benzene rings (C4-C9) as donor where Br2 acts as acceptor (Table 15), as well as several π-π interactions which are present between the imidazole rings, benzene rings, and imidazole rings and benzene rings of the benzimidazole moiety, and the benzene rings of the anthracene moiety (Table S3). Intermolecular C–H···π forces involve solvent molecules interacting with benzimidazole moiety of the host.

Table 14: *Selected bond lengths [Å] and angles [°] for **MC3**, **MC4** and **MC5**.*

Compound	Bond length	Bond angle
MC3	Co1-N1 2.0085(12)	N1-Co1-N28$^{\#}$ 109.36(5)
	Co1-N28$^{\#}$ 2.0269(11)	N1-Co1-Cl1 112.81(4)
	Co1-Cl1 2.2476(4)	N1-Co1-Cl2 102.66(4)
	Co1-Cl2 2.2575(4)	N28$^{\#}$-Co1-Cl1 105.40(3)
		N28$^{\#}$-Co1-Cl2 110.75(3)
		Cl1-Co1-Cl2 115.87(2)
MC4	Co1-N1 2.004(2)	N1-Co1-N28$^{\#}$ 104.02(7)
	Co1-N28$^{\#}$ 2.011(1)	N1-Co1-Br1 114.34(5)
	Co1-Br1 2.3901(4)	N1-Co1-Br2 104.55(5)
	Co1-Br2 2.3602(4)	N28$^{\#}$-Co1-Br1 104.48(5)
		N28$^{\#}$-Co1-Br2 114.50(5)
		Br1-Co1-Br2 114.71(2)
MC5	Co1-N1 2.030(3)	N1-Co1-N29$^{\#}$ 108.19(11)
	Co1-N29$^{\#}$ 2.041(2)	N1-Co1-Br1 114.49(8)
	Co1-Br1 2.4054(5)	N1-Co1-Br2 101.79(8)
	Co1-Br2 2.4059(6)	N29$^{\#}$-Co1-Br1 104.81(7)
		N29$^{\#}$-Co1-Br2 118.49(7)
		Br1-Co1-Br2 109.50(2)

$^{\#}$1-x,1-y,1-z

Metallocycle **MC5** is related via metal center and counterion with **MC4**. There is a difference in the ligand composition where benzimidazole was substituted with a methyl group. Unfortunately, I was not able to get an analogue of **MC3** with this ligand.

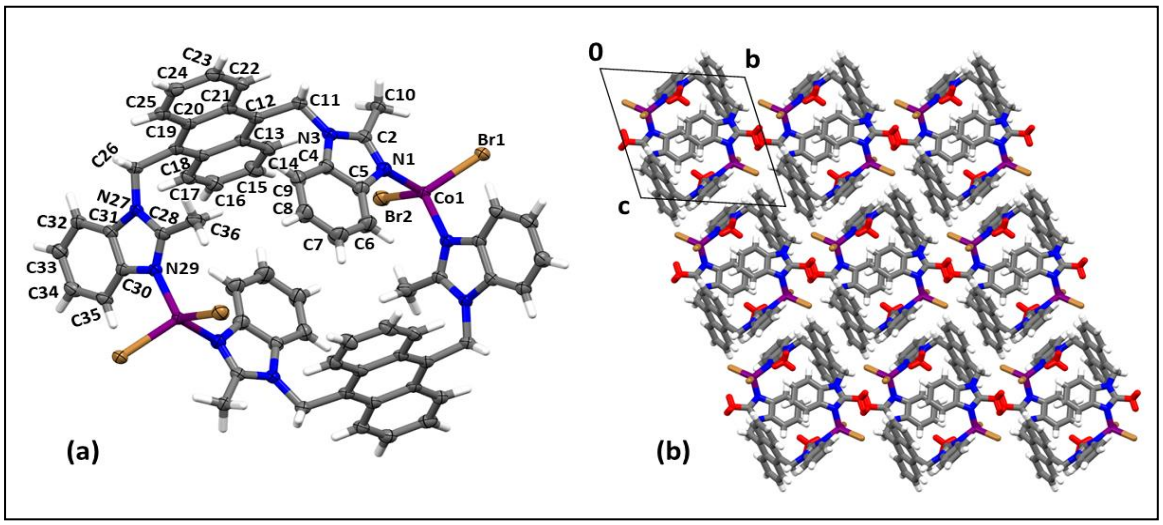

Figure 71: ***(a)*** *Representation of the molecular structure of* ***MC5*** *with displacement ellipsoids drawn at the 50% probability level, the unlabelled atoms are related to the labelled ones by the symmetry operation: 1-x,1-y,1-z;* ***(b)*** *Capped-stick packing arrangement of* ***MC5*** *shown along the a-axis, the methyl groups are shown in red colour.*

The asymmetric unit of **MC5** contains a ligand (**L5**) molecule, Co(II) cation, two bromide anions coordinated to a metal center. The Co(II) metal center also displays slightly distorted geometry in this case with a τ_4 index of 0.9, where the bond distances are nearly uniform, with a maximum variation of only 0.05 Å, while the largest deviation in bond angle is specifically in the Cl-Co-Cl angle which is approximately 5° smaller as compared to **MC4**. These bond distance values for **MC3**, **MC4** and **MC5** are in usual range revealed by Mogul geometry check in Mercury. Moreover, the shape of metallocycle **MC5** as well as packing also differs from **MC4** as a result of some small conformational changes within the ligand (see Figure 72 and 73). In **MC5**, the angle between the planes of the benzimidazole rings within a ligand is 80.74º as compared to 73.99º in **MC4** and an angle of 77/80.31º between the planes of the anthracene ring and the benzimidazole rings as compared to 85.88/89.76º in **MC4**. The distance between Co(II) metal centers does not change much and is equal to 9.6149(8) Å. **MC5** is forming a non-porous structure with no space for solvent molecules. Moreover, when analyzed using a spherical contact surface probe (radius of 1.2 Å), **MC5** shows no space available, in contrast to **MC4**, which exhibits approximately 34.53 Å^3 of free space, accounting for 2.2% of its unit cell volume. This comparison highlights the denser packing and reduced internal free volume in **MC5** (Figure 73).

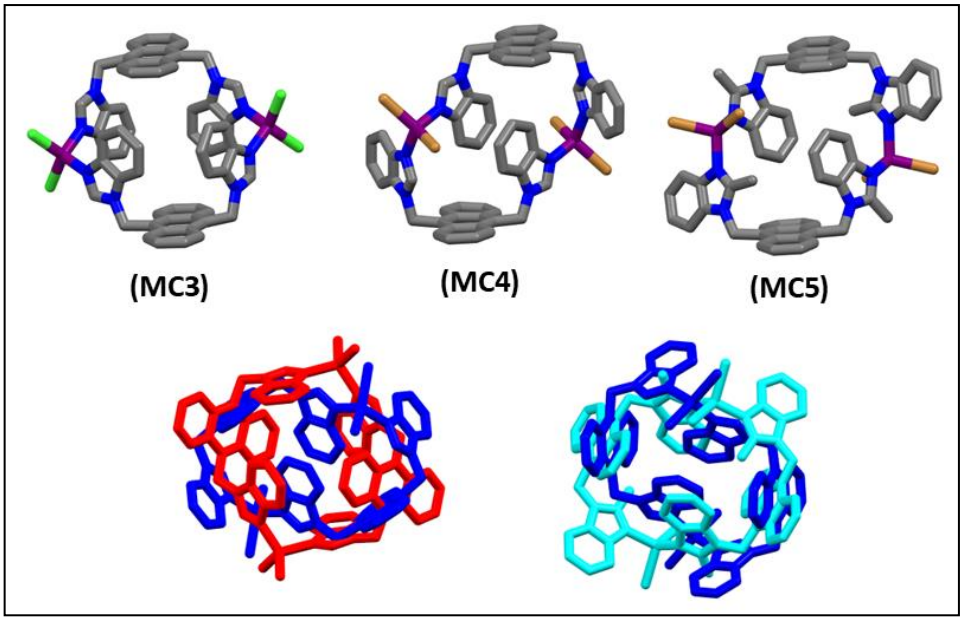

Figure 72: ***(Top):*** *Representation of the differently shaped metallocycles* ***MC3***, ***MC4*** *and* ***MC5****, the solvent molecules and hydrogen atoms were omitted for clarity;* ***(Bottom-left):*** *molecular overlays of metallocycle* ***MC3*** *(red) and* ***MC4*** *(blue), RMSD- 3.0647 Å;* ***(Bottom-right):*** *and* ***MC4*** *(blue) and* ***MC5*** *(cyan), RMSD- 2.9181 Å.*

Table 15: *Hydrogen bonding parameters for* ***MC3***, ***MC4*** *and* ***MC5.***

Compound	D-H···A	H···A (Å)	D···A (Å)	D-H-A (°)
MC3	O36-H36A···N26	2.80	3.448(3)	133
	O36-H36B···N28	2.50	3.226(3)	141
	C23-H23···N28^{i}	2.81	3.554(2)	136
	C25-H25A···Cl1^{ii}	2.99	3.749(1)	135
	C27-H27···Cl1^{ii}	2.78	3.497(1)	133
	C10-H10B···Cl2^{iii}	2.69	3.452(1)	138
	C14-H14···Cl2^{iv}	2.89	3.683(2)	146
	C33-H33···Cl2^{v}	2.93	3.711(1)	141
	C24-H24···Cg2^{i}	2.81	3.5677(16)	138
MC4	C6-H6···N35	2.60	3.340(4)	135
	C10-H10A···N35^{i}	2.71	3.614(2)	159
	C15-H15···N35^{ii}	2.98	3.851(3)	152
	C21-H21···N35^{i}	2.74	3.537(3)	142
	C14-H14···N38^{iii}	2.88	3.538(3)	127
	C25-H25B···N38	2.55	3.269(5)	134
	C37-H37B···N38^{iv}	2.64	3.491(7)	145
	C25-H25A···Br1^{ii}	2.95	3.856(2)	164
	C27-H27···Br1^{ii}	2.89	3.750(3)	151
	C7-H7···Br2^{iii}	2.863	3.600(2)	135
MC5	C11-H11B···Br1^{i}	2.93	3.687(4)	141
	C24-H24···Br2^{ii}	2.93	3.802(4)	154

(MC3): Cg2 is the centroid of the imidazole ring (N26-C30), Cg4 is the centroid of the benzene ring (C11-C20); (**MC4):** Cg1 is the centroid of the imidazole ring (N1-C5), Cg5 is the centroid of the benzene ring (C12-C17), Cg7 is the centroid of the benzene ring (C29-C34); (**MC5):** Cg2 is the centroid of the imidazole ring (N27-C31), Cg4 is the centroid of the benzene ring (C12-C21); **Symmetry codes (MC3):** (i) 1-x,-y,-z, (ii) x-1,y-1,z-1, (iii) 2-x,2-y,1-z, (iv) 1-x,2-y,1-z, (v) x,y-1,z; **(MC4)**: (i) 1-x,-y,-z, (ii) x,1+y,z, (iii) 1+x,y,z, (iv) 1-x,1-y,1-z; **(MC5)**: (i) 2-x,-y,1-z, (ii) x,y,1+z

MC5 also shows columnar packing along the *a*-axis, however, the arrangement is only stabilized by C–H···Br interactions involving methylene groups (C11) as donor whereas Br1 acts as acceptor and CH- from anthracene rings as donor with Br2 as acceptor (Table 15). There are also π-π interactions present between the imidazole rings and benzimidazole moiety and the anthracene moieties (Table S3). Intermolecular C–H···N and C–H···π interactions are absent in this case which in case of **MC3** and **MC4** were coming from the involvement of solvent molecules.

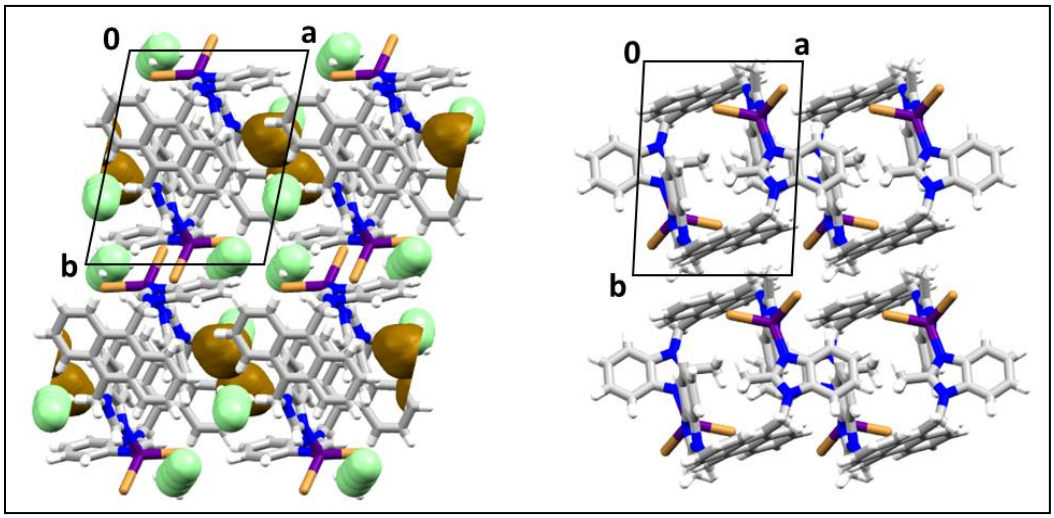

Figure 73: *Capped-stick packing arrangement of **MC4** (on the left) and **MC5** (on the right) shown along the c-axis, the solvent (acetonitrile) molecules in **MC4** are shown in light green in spacefill representation and the brown voids are the contact surface accessible voids calculated using a spherical probe radius of 1.2 Å.*

12.1.2.1.2. Bulk Solid-State Studies

PXRD analysis indicated that in the case of **MC3**, the precipitate taken out from the solution was not homogeneous, suggesting the presence of another form, which prevented further investigation of this system.

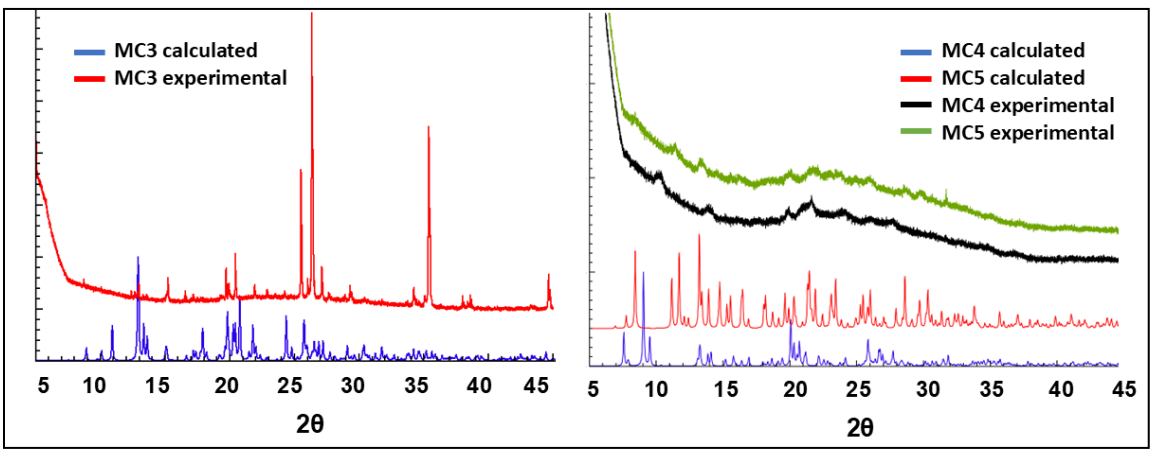

Figure 74: ***(On the left):*** *Comparison of the calculated (blue) and experimental (red) powder patterns of* ***MC3****,* ***(on the right):*** *calculated and experimental powder patterns of* ***MC4*** *and* ***MC5****.*

Moreover, for **MC4** and **MC5**, the crystalline materials lost their structural integrity upon removal from the solution, as evident from the PXRD patterns, which was also observed under the microscope, crystals of **MC4** upon leaving on the plate in air for some time were cracking and did not diffract anymore. Consequently, these systems could not be studied further.

12.1.3. Based on Biphenyl Core Ligands: 4,4′-Bis((1H-imidazol-1-yl)methyl)-1,1′-biphenyl (L6), 4,4′-Bis((2-methylimidazol-1-yl)methyl)-1,1′-biphenyl (L7), 4,4′-Bis((benzimidazol-1-yl)methyl)-1,1′-biphenyl (L9) and 4,4′-Bis((2-methylbenzimidazol-1-yl)methyl)-1,1′-biphenyl (L10)

Since the problem with crystallization and obtaining porous materials based on metallocycles with rigid naphthalene core, I have also tried working with ligands with relatively flexible cores (biphenyl) thereby to check if this would help in the formation of porous materials. This way I have obtained a series of metallocycles: **MC6**-**MC12** containing metal ions such as: Cu(II), Zn(II) and Cd(II).

Table 16: *Crystallographic data and structure refinement parameters for metallocycles based on biphenyl core ligands* ***MC6****,* ***MC7****,* ***MC8****,* ***MC8-a****,* ***MC9****,* ***MC10****,* ***MC10-a****,* ***MC11*** *and* ***MC12****.*

Compound Reference	**MC6**	**MC7**	**MC8 (reported)**	**MC8-a**	**MC9**	**MC10**	**MC10-a**	**MC11**	**MC12**
Chemical formula	$C_{40}H_{36}Cl_4Cu_2N_8$	$C_{40}H_{36}Cl_4Zn_2N_8$	$C_{46}H_{52}Cd_2Cl_4N_8O_2$	$C_{44}H_{44}Cl_4Cd_2N_8$	$C_{57}H_{46}Cl_6Cu_2N_8$	$C_{56}H_{44}Cl_4Zn_2N_8$	$C_{62}H_{58}Cl_4Zn_2N_{10}O_2$	$C_{72}H_{80}Cl_4Zn_2N_{12}O_4$	$C_{63}H_{59}Cl_4Zn_2N_9O$
Formula mass	897.65	901.31	1115.55	1051.47	1182.80	1101.53	1247.72	1450.02	1230.73
Crystal system	Triclinic	Monoclinic	Monoclinic	Monoclinic	Monoclinic	Monoclinic	Triclinic	Triclinic	Triclinic
a/Å	9.1970(8)	17.0375(8)	17.2080(16)	20.3000(4)	16.4190(9)	10.2927(10)	10.5809(4)	9.47700(10)	10.3821(2)
b/Å	11.3356(12)	15.6305(5)	15.5925(15)	14.8978(2)	16.7445(7)	15.9782(10)	11.8518(4)	14.80290(10)	14.4140(2)
c/Å	11.6132(11)	9.0980(4)	9.6635(9)	17.1809(4)	10.6245(5)	23.2708(10)	11.9336(5)	15.08200(10)	21.2946(4)
α/ ◦	85.796(8)	90	90	90	90	90	85.956(3)	68.6470(10)	75.1380(10)
β/ ◦	68.543(8)	116.012(6)	114.257(2)	119.201(3)	104.031(5)	96.6640(10)	81.510(3)	80.2720(10)	85.9720(10)
γ/ ◦	75.262(8)	90	90	90	90	90	78.534(3)	86.1000(10)	74.6360(10)
Unit cell volume/$Å^3$	1089.47(19)	2177.41(19)	2363.9(4)	4535.60(19)	2833.8(2)	3801.23(5)	1449.26(10)	1942.19(3)	2970.00(9)

Temperature/ K	100.15(1)	100.15(1)	100(2)	100.01(1)	100(2)	100(2)	100.01(1)	100(1)	100(1)
Space group	*P*-1	*C*2/*m*	*C*2/*m*	*C*2/*c*	*C*2/*m*	$P2_1/m$	*P*-1	*P*-1	*P*-1
No. of formula units per unit cell, Z	1	2	2	4	2	2	1	1	2
Radiation type	CuK\α	CuK\α	MoK\α	CuK\α	CuK\α	CuK\α	CuK\α	CuK\α	CuK\α
Absorption coefficient, μ/mm^{-1}	3.754	3.908	1.172	9.995	3.876	2.314	3.139	2.438	3.037
No. of reflections measured	11261	6994	n/a	13795	7820	71142	9629	53288	37499
No. of independent reflections	4252	2103		4240	2761	7876	9629	7680	11902
Rint	0.0486	-		0.0322	0.0313	0.0264	-	0.014	0.02
Final R1 [a] values ($I > 2\sigma(I)$)	0.0785	0.0428		0.0373	0.0696	0.0483	0.0528	0.0301	0.0721
Final wR2 [b] values ($I > 2\sigma(I)$)	0.2309	0.1122		0.1034	0.1898	0.1280	0.1440	0.0769	0.1996
Final R1 [a] values (all data)	0.0964	0.0453		0.0411	0.0776	0.0488	0.0569	0.0302	0.0738
Final wR2 [b] values (all data)	0.2488	0.1139		0.1060	0.1971	0.1283	0.1496	0.0769	0.2008
Goodness of fit on F^2	1.055	1.065		1.100	1.040	1.097	1.081	1.038	1.074

12.1.3.1. MC6:$[Cu_2(L6)_2Cl_4]\cdot xS$ and MC7:$[Zn_2(L6)_2Cl_4]\cdot xS$

12.1.3.1.1. Structural Analysis

MC6 crystallizes in the *P*-1 space group of the triclinic crystal system, whereas **MC7** crystallizes in the monoclinic crystal system of the *C*2/*m* space group. The asymmetric unit of **MC6** contains half a metallocycle, i.e., one Cu(II) ion, one **L6** molecule, and two chloride ions out of which one was modelled into two positions (80:20), whereas the asymmetric unit of **MC7** contains a Zn(II) ion located on a mirror plane with half of occupancy, half a molecule of **L6**, two chloride ions located on mirror plane with half of occupancy. The coordination geometry around the metal center is very different in both cases, **MC6** displays significantly distorted tetrahedral geometry (τ_4 index of 0.61), whereas **MC7** displays slightly distorted tetrahedral geometry (τ_4 index of 0.95) (Table 17).

The bond distances though remain within typical ranges, as revealed by Mogul geometry check in Mercury when compared to similar molecular fragments.

Table 17: *Selected bond lengths [Å] and angles [°] for **MC6** and **MC7**.*

Compound	Bond lengths	Bond angles
MC6	Cu1-N1 1.957(4)	N1-Cu1-N22$^{\#}$ 139.59(16)
	Cu1-N22$^{\#}$ 1.970(4)	N1-Cu1-Cl2 97.55(13)
	Cu1-Cl2 2.218(2)	N1-Cu1-Cl3 97.46(12)
	Cu1-Cl3 2.250(2)	N22$^{\#}$-Cu1-Cl2 98.65(13)
		N22$^{\#}$-Cu1-Cl3 98.0(13)
		Cl2-Cu1-Cl3 133.00(12)
MC7	Zn1-N1 2.011(2)	N1-Zn1-N1$^{\#}$ 110.98(12)
	Zn1-N1$^{\#}$ 2.011(2)	N1-Zn1-Cl2 109.05(7)
	Zn1-Cl2 2.2279(12)	N1-Zn1-Cl3 106.69(7)
	Zn1-Cl3 2.2461(13)	N1$^{\#}$-Zn1-Cl2 109.05(7)
		N1$^{\#}$-Zn1-Cl3 106.69(7)
		Cl2-Zn1-Cl3 114.35(6)

(MC6): $^{\#}$1-x,1-y,1-z; **(MC7):** $^{\#}$x,1-y,z

The conformation of the ligand within the metallocycle shows some small variations, as depicted in Figure 75. These differences are highlighted by the values of angles between the planes of the imidazole rings: 54° and 61°, and the angles between the planes of the benzene rings within the biphenyl moiety, recorded as 30° and 35° for **MC6** and **MC7**, respectively. Additionally, the torsion angles C2-N3-C6-C7 and C4-N3-C6-C7 are 113° and -64° for **MC6**, compared to 111° and -68° for **MC7**. Consequently, the distance between the metal centers in the metallocycle is almost 1 Å larger in **MC7** (15.83 Å) than in **MC6** (14.76 Å).

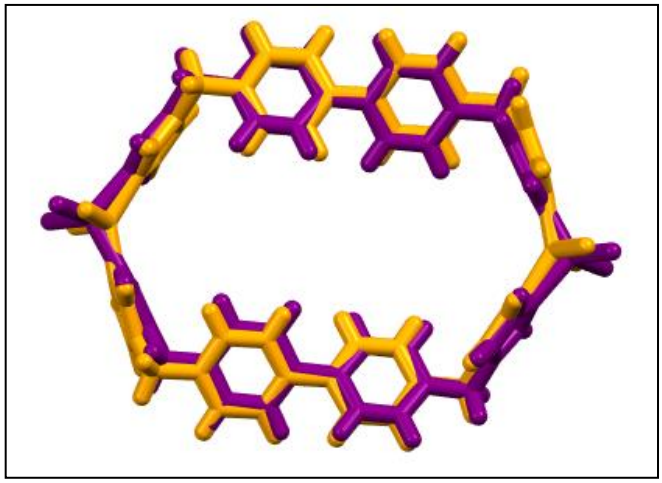

Figure 75: *Molecular overlay of **MC6** (orange) and **MC7** (purple), RMSD-0.6638 Å.*

The main difference lies in the packing of both the metallocycles. They display columnar stacking packing like previous metallocycles (**MC1-MC5**). The detailed analyses of intermolecular interactions in **MC6** and **MC7** will not be discussed as solvent molecules in both the metallocycles are not taken in consideration and because of that the analysis can not be correct.

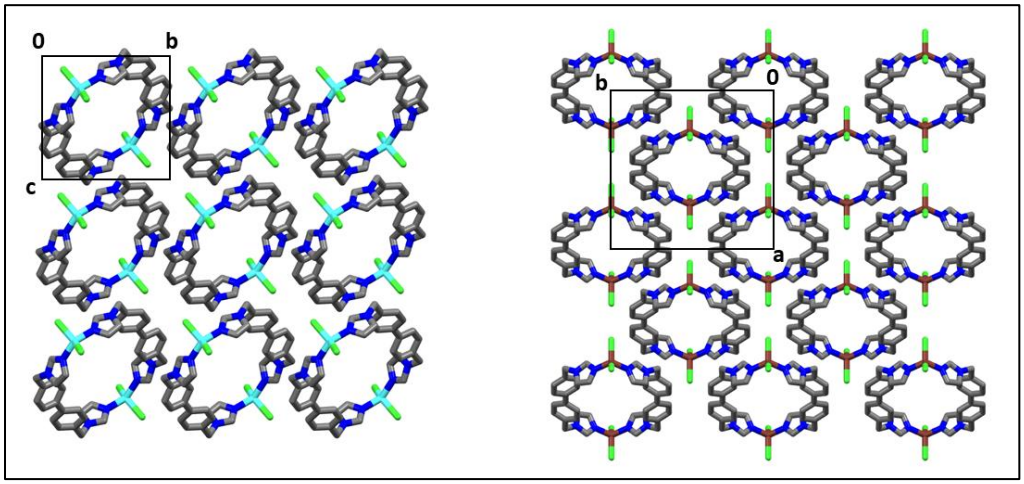

Figure 76: *Capped-stick packing arrangement of **MC6** (on the left) and **MC7** (on the right) shown along the a-axis and c-axis, respectively hydrogen atoms were removed for clarity.*

MC6 displays discrete voids with application of probe radius 1.2 Å solvent accessible surface, accounting for a volume of approximately 13 Å^3 per unit cell filled with solvent molecules whereas **MC7** display discrete voids filled with solvent molecules which accounts for a volume of 24 Å^3 per unit cell calculated with Mercury using probe radius 1.2 Å solvent accessible surface. The solvents molecules in both the structures were highly disordered and squeezed as already mentioned previously in section 8.1.

12.1.3.1.2. Bulk Solid-State Studies

PXRD analysis of the bulk obtained in the case of **MC6** from different solvents was performed (Figure 77) indicating that the patterns from most of the solvents are different and the one from methanol did not match with calculated pattern revealing the presence of another form(s). Moreover, PXRD patterns obtained from EtOH and acetonitrile indicated formation of the same product. As the phases shown by PXRD studies could not be isolated the porosity studies were not performed. Single-crystal to single-crystal transformation studies could also not be performed due to the lack of reproducibility of single crystals, meaning despite using the same and alternative solvents and methods, I was unable to get single crystals again, only polycrystalline material was obtained in all the setups. Initially,

we had just one low-quality crystal, which was used for SCXRD. These reasons posed a challenge to study this system further.

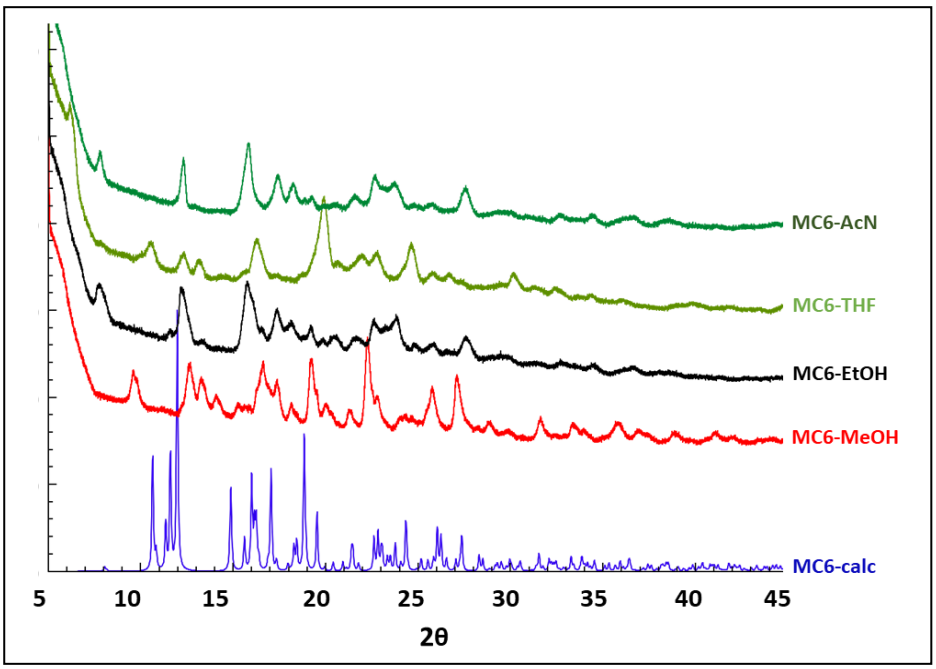

Figure 77: *Calculated and experimental powder patterns of the **MC6** bulk obtained from different solvents.*

In the case of **MC7**, simulated and experimental powder patterns do not show a perfect match as clear peak broadening is observed, most likely resulting from partial desolvation and the presence of collapsed regions. (Figure 78).

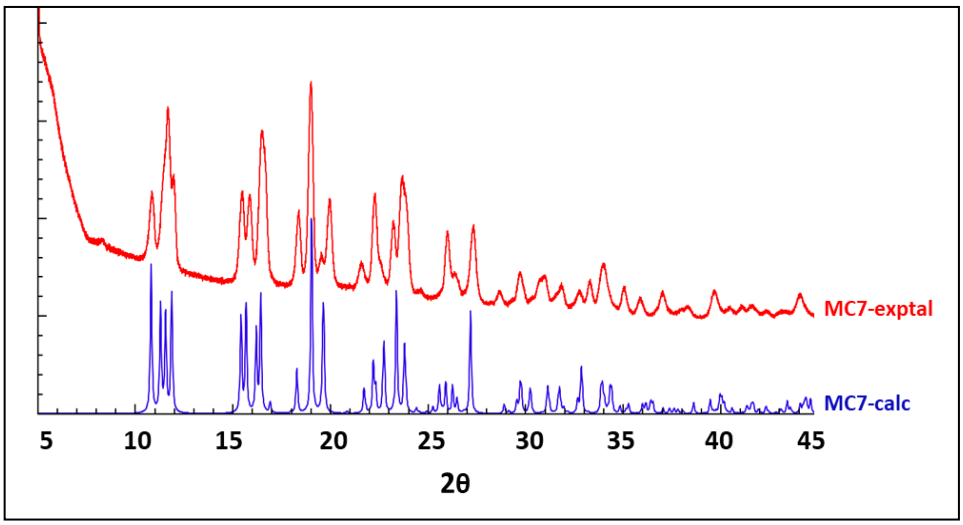

Figure 78: *Calculated and experimental powder patterns of the **MC7** bulk.*

Moreover, TGA revealed that the removal of solvent molecules starts already at RT and it does not cause decomposition of the compound until 350 ºC. Highlighting that this system is robust and suitable for further sorption studies (Figure 79).

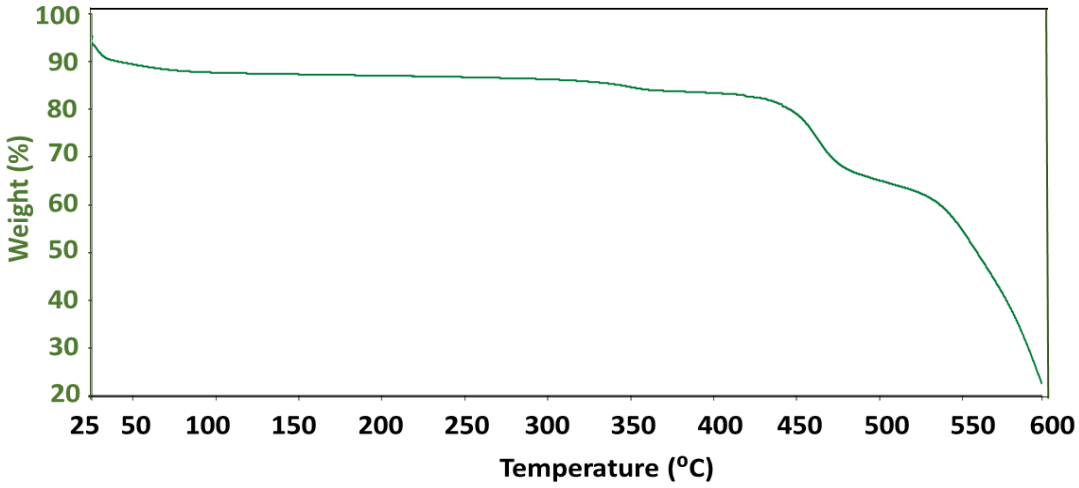

Figure 79: *Thermogram of **MC7**.*

12.1.3.1.3. Porosity Studies

MC7 was activated by heating at 100 ºC for 1 hour under vacuum and exposed to various gases. Sorption isotherms for H_2, N_2, CO_2, C_2H_2 and CH_4 were measured gravimetrically at room temperature.

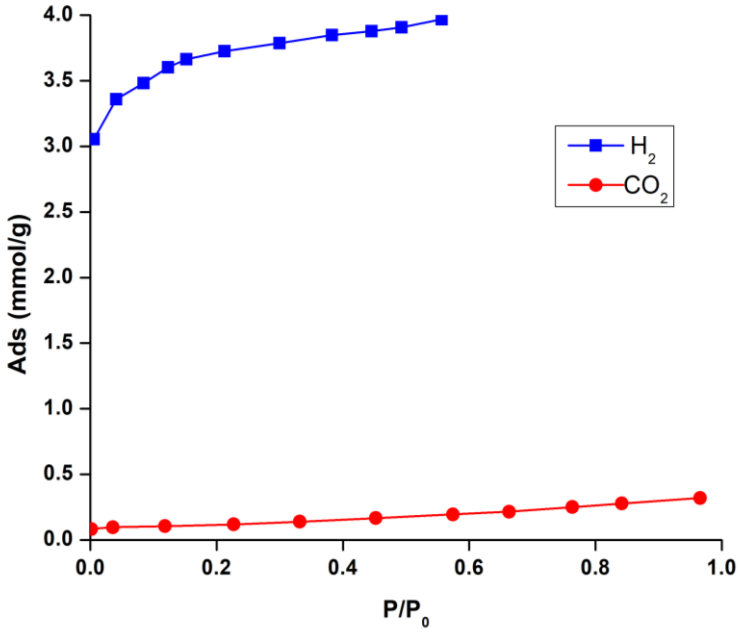

Figure 80: *H_2 and CO_2 adsorption isotherms for **MC7** at 25 ºC.*

The results show that system didn't take any N_2, C_2H_2, and CH_4, and showed very low uptake for CO_2 which was *ca.* 0.32 mmol/g (1.42 wt%). However, H_2 adsorption shows isotherm type I with a pretty high uptake (above average) of approximately 4 mmol/g or 0.80 wt%. In this case as well similar theory like in case of **MC2** could be postulated i.e.,

the formation of short-lived channels due to the dynamic cooperative motion of the molecular crystal component. In this case, the channels are not even big enough to accommodate CO_2 molecules, in fact, they can only allow H_2 diffusion, which has smaller kinetic diameter (2.89 Å) than CO_2 (3.30 Å) [219].

12.1.3.2. MC8: $[Cd_2(L7)_2Cl_4]\cdot 2CH_3OH$

12.1.3.2.1. Structural Analysis

This compound was already reported in the literature [88]. The reported metallocycle was obtained upon layering equimolar solution of the ligand in DCM and metal salt $CdCl_2\cdot 2.5H_2O$ in MeOH. It was shown that the desolvation occurs without any apparent change in the molecule's crystal structure and desolvated structure adsorbs gas molecules (CO_2 and C_2H_2) with a greater affinity for C_2H_2. The structural studies with incremental gas loading to locate and get details about host-guest interactions were conducted *in-situ* with single-crystal X-ray data equipped with an environmental gas cell which showed that CO_2 and C_2H_2 are accommodated in different orientations [88]. However, during our studies on this compound, another densely packed phase was revealed and we were not able to get the desolvated phase reported earlier. Interestingly, there are reports on two similar composition isostructural cobalt and zinc-based metallocycles and these metallocyclic hosts apparently are not robust to solvent removal since the ligand undergoes significant conformational changes upon desolvation to yield a non-porous apohost like we observed [219].

The solvated **MC8** structure used below for comparision of its structural features with the new desolvated form is the previously reported one. Interestingly, we observed that, over time or after short heating (2 min) of the methanol solvated crystals, the solvent partially leaves the structure resulting in crystals containing two or more different phases.

MC8 as **MC7** crystallizes in the monoclinic *C*2/*m* space group wherein the asymmetric unit of **MC8** contains $1/4^{th}$ of a metallocycle i.e., Cd(II) ion, two chloride anions coordinated to a metal center and a half of methanol molecule located on a mirror plane and showing half of occupancies as well as half a ligand molecule. The geometry around the Cd(II) metal center in **MC8** is distorted tetrahedral (τ_4 index of 0.89) with Cd-N bond distance of 2.208 Å and Cd-Cl in the range of 2.4423-2.4488 Å, and angles ranging from 101.86º to 119.61º (Table 18). **MC8** structure contains intrinsic solvent accessible discrete pockets accounting for around 1.3% of the total unit cell volume, which is approximately

32 Å^3 per unit cell (calculated using solvent accessible surface with a probe radius of 1.2 Å). The voids are filled with methanol molecules.

12.1.3.2.2. Bulk Solid-State Studies

Thermogravimetric analysis of **MC8** (Figure 81) reveals that the solvent loss starts to take place at *ca.* 45 °C and the material is completely desolvated at *ca.* 120 °C. The weight loss corresponds to *ca*. 5.5% which is equivalent to two MeOH molecules which agree with the determined structure (predicted- 5.7%). The material is stable till *ca.* 350 °C where the decomposition starts.

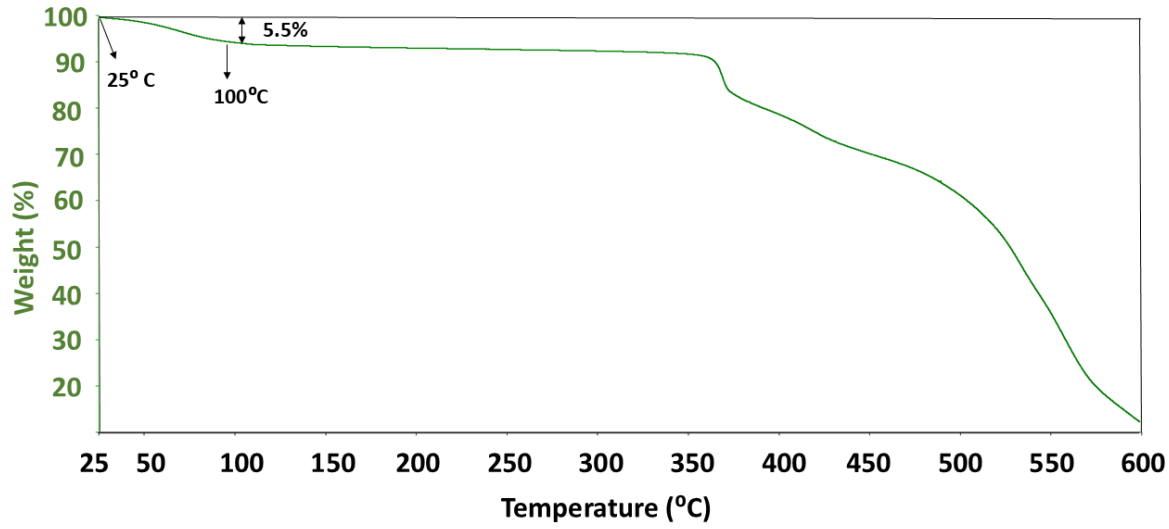

Figure 81: *Thermogram of **MC8**.*

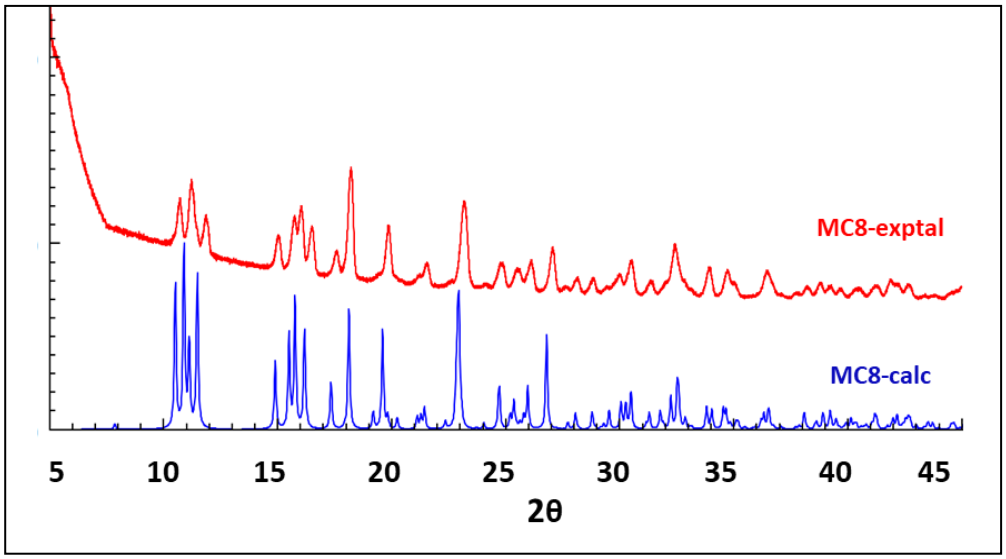

Figure 82: *Calculated and experimental PXRD patterns of **MC8** bulk.*

Furthermore, PXRD analysis verified the bulk phase purity of **MC8**, showing good agreement between the calculated and experimental patterns (Figure 82).

12.1.3.2.3. Structural Transformation of MC8 to MC8-a

After heating for 5h at 120 °C, **MC8** transforms into a densely packed phase (**MC8-a**) in an SC-SC fashion. **MC8-a** exhibits lower symmetry (*C*2/*c* space group) and as a result distinct unit cell parameters. The asymmetric unit of **MC8-a** contains two crystallographically independent halves of the ligand molecule, two chloride anions, and a Cd(II) metal ion.

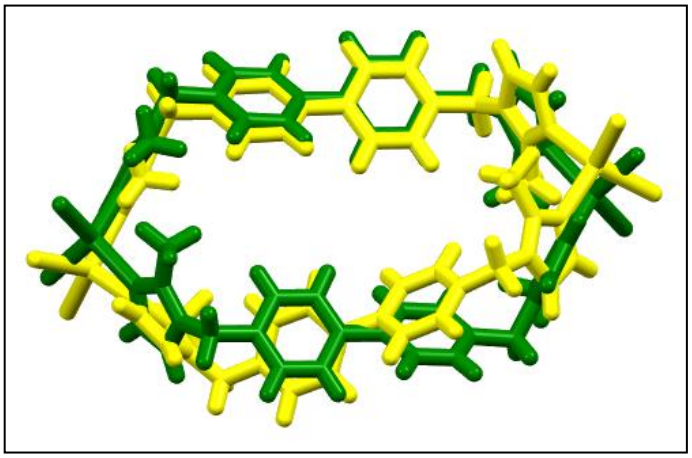

Figure 83: *Molecular overlay of **MC8** (green) and **MC8-a** (yellow), RMSD-1.3064 Å.*

During structural transformation the ligand conformation significantly changed as can be seen from the overlay (Figure 83) and highlighted by the values of angles between the planes of the imidazole rings which are 56° and 53°, and between the planes of the benzene rings within the biphenyl moiety which are 37° and 30° within the same ligand for **MC8** and **MC8-a**, respectively.

Table 18: *Selected bond lengths [Å] and angles [°] for **MC8** and **MC8-a**.*

Compound	Bond lengths	Bond angles
MC8	Cd1-N4 2.208(3) Cd1-N4$^{\#}$ 2.208(3) Cd1-Cl2 2.4423(13) Cd1-Cl3 2.4488(14)	N4-Cd1-N1$^{\#}$ 115.42(14) N4-Cd1-Cl2 109.09(7) N4-Cd1-Cl3 101.86(7) N4$^{\#}$-Cd1-Cl2 109.09(7) N4$^{\#}$-Cd1-Cl3 101.86(8) Cl2-Cd1-Cl3 119.61(5)
MC8-a	Cd1-N17 2.227(3) Cd1-N4 2.216(3) Cd1-Cl2 2.4396(10) Cd1-Cl3 2.4186(10)	N17-Cd1-N4 105.40(11) N17-Cd1-Cl2 107.28(8) N17-Cd1-Cl3 105.78(9) N4-Cd1-Cl2 108.52(9) N4-Cd1-Cl3 116.47(8)

		Cl2-Cd1-Cl3 112.73(4)

[#]x,1-y,z

Moreover, in **MC8**, the methyl groups of the coordinated imidazole moieties point in the same direction, whereas in **MC-8a**, they point in opposite directions. As a result of this change in the ligand orientation, the metallocycle gets more elongated with an increase in the distance between Cd(II) centers from 16.14 Å in **MC8** to 16.62 Å in **MC8-a**. The two ligands within a metallocycle are twisted relative to each other in **MC8-a** as compared to **MC8**. The geometry around the Cd(II) ion in **MC8-a** is also slightly distorted tetrahedral (τ_4 index of 0.93) but has different bond angles ranging from 105.40º to 116.47º (Table 18).

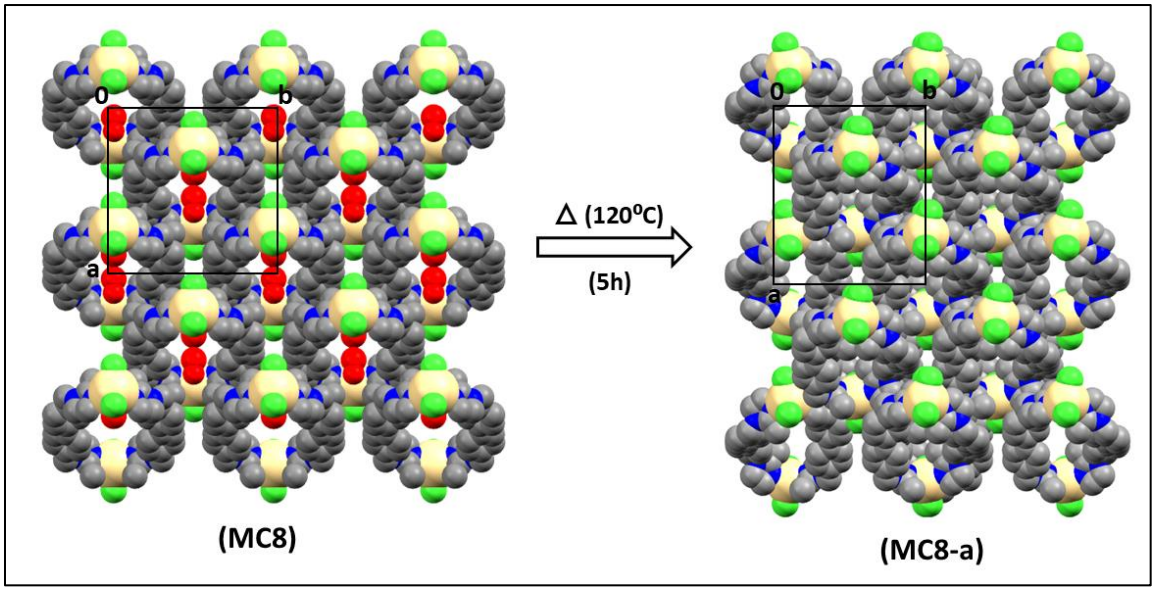

Figure 84: *Spacefill packing arrangement of **MC8** (on the left) and **MC8-a** (on the right) shown along the c-axis, methanol molecules are shown in red and hydrogen atoms were removed for clarity.*

As a result of the different conformation of the ligand in both **MC8** and **MC8-a**, the intermolecular interactions stabilizing the two structures vary significantly. π-π interactions are present between the imidazole rings (N4-C8) at a distance of 3.784(2) Å having a symmetry operator 1/2-x,1/2-y,1-z in **MC8**, and at a distance of 3.632(2) Å having a symmetry operator 1/2-x,3/2-y,1-z in **MC8-a**. Host-guest assembly in **MC8** is stabilized by O–H···Cl and C–H···O interactions. As could be expected, C–H···Cl and C–H···π interactions are more diverse in the case of **MC8-a** as compared to **MC8**. C–H···Cl interactions in **MC8** involve only methylene groups (C10) as donors while in case of **MC8-a** they involve methylene groups (C10) and both benzene rings as donor for Cl2 as acceptor. For Cl3 as acceptors, **MC8** involves benzene rings (C11-C16) as donor, whereas **MC8-a** involves 2-methylimidazole rings (N4-C9), methylene groups (C23) and benzene ring

(C24-C29) as donor. C–H···π interactions in **MC8** involve 2-methylimidazole rings (N4-C9) as donor for benzene rings (C11-C16) as acceptors, whereas in case of **MC8-a**, these also involve methylene groups as donor for benzene rings as acceptor in addition to the one present between 2-methylimidazole group and benzene rings (Table 19).

Table 19: *Hydrogen bonding parameters for **MC8** and **MC8-a**.*

Compound	D-H···A	H···A (Å)	D···A (Å)	D-H-A (°)
MC8	C6-H9C···O18	2.537	3.360(6)	141
	C16-H16···O18	2.725	3.572	149
	O18-H18···Cl3^{i}	2.340	3.176(5)	173
	C15-H15···Cl3^{i}	2.969	3.818	150
	C10-H10A···Cl2^{ii}	2.819	3.764(3)	160
	C6-H6···Cg2^{iii}	3.007	3.660	127
	C9-H9A···Cg2^{iv}	2.752	3.581(4)	143
MC8-a	C26-H26···Cl2^{i}	2.858	3.601(3)	136
	C10-H10A···Cl2^{ii}	2.825	3.711(5)	149
	C16-H16···Cl2^{i}	2.878	3.623(3)	136
	C23-H23A···Cl3^{iii}	2.628	3.588(5)	163
	C28-H28···Cl3^{iv}	2.937	3.513(3)	120
	C6-H6···Cl3^{ii}	2.911	3.757(5)	149
	C9-H9B···Cg3^{v}	2.833	3.789(5)	165
	C18-H18···Cg4^{vi}	2.766	3.502(4)	135
	C23-H23B···Cg4^{vii}	2.742	3.541(3)	138

(**MC8):** Cg2 is the centroid of the benzene ring (C11-C16); (**MC8-a):** Cg3 is the centroid of the benzene ring (C24-C29), Cg4 is the centroid of the benzene ring (C11-C16); **Symmetry codes (MC8):** (i) x,y,1+z, (ii) 1/2-x,1/2+y,1-z, (iii) -x,y,1-z, (iv) 1/2-x,1/2-y,2-z; **(MC8-a):** (i) x,1-y,-1/2+z, (ii) 1/2-x,3/2-y,1-z, (iii) 1/2-x,1/2-y,1-z, (iv) 1/2+x,-1/2+y,z, (v) 1/2-x,1/2+y,1/2-z, (vi) 1/2-x,-1/2+y,1/2-z, (vii) 1-x,1-y,1-z.

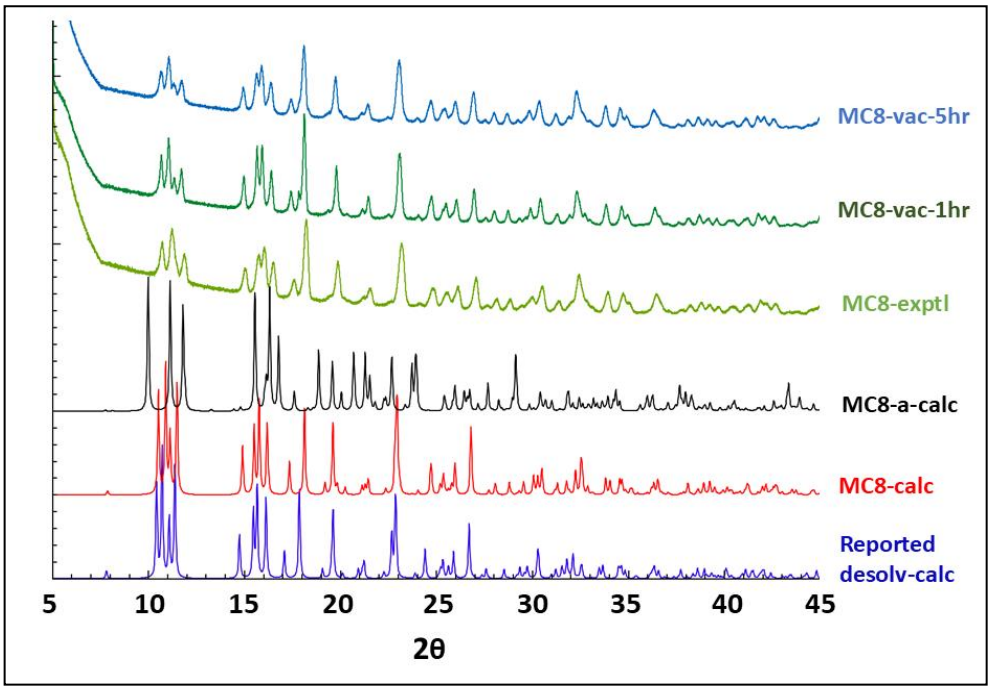

Figure 85: *Calculated and experimental powder patterns of the reported desolvated compound, **MC8**, **MC8-a** and the bulk sample obtained among others by placing **MC8** under vacuum.*

PXRD analysis was performed to monitor the transformation in the bulk material. A comprehensive evaluation of the PXRD results reveals that the patterns obtained after subjecting the **MC-8** sample to vacuum for 1 hour or even 5 hours remain consistent with the initial bulk sample patterns (Figure 85). The calculated patterns from the reported desolvated structure appear quite similar to those of the methanol solvate **MC8**, making it difficult to determine whether complete or only partial solvent removal occurred upon subjecting **MC8** to vacuum. When checked on SCXRD, it showed that methanol was still present in the structure, even after exposing the crystals to vacuum for 7 hours or heating at 120 °C for 10 minutes.

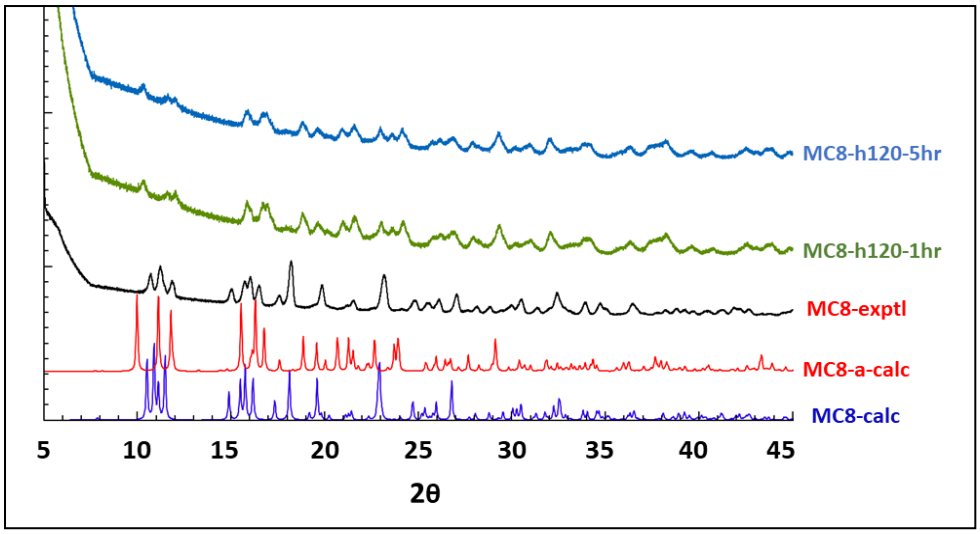

Figure 86: *Calculated and experimental powder patterns of the **MC8**, bulk, and upon heating it at 120 °C.*

However, heating the sample at 120 °C for 1 hour leads to noticeable changes in the pattern, which no longer match the initial bulk sample. Instead, it resembles the calculated patterns for **MC-8a**. Prolonged heating for 5 hours yields the same pattern (Figure 86). Notably, heating appears to reduce the crystallinity of the sample, as indicated by the peak broadening and intensity reduction observed in the PXRD patterns.

12.1.3.3. MC9: $[Cu_2(L9)_2Cl_4]\cdot CH_2Cl_2$

12.1.3.3.1. Structural Analysis

SCXRD analysis of the obtained crystals was carried out which revealed that **MC9** crystallizes in the *C*2/*m* space group of the monoclinic crystal system, wherein the asymmetric unit contains 1/4th of a metallocycle, i.e., half of Cu(II) ion two halves of chloride ions and a one quarter of DCM molecule located on the mirror plane as well as

half a molecule of **L6** with proper rotation axes passing through the middle of biphenyl moiety. The two bipodal ligands are bridging two Cu(II) centers through the N-atoms originating from the benzimidazole group to generate a full metallocycle with a Cu---Cu distance of 13.69 Å. The metal center Cu(II) displays a very distorted tetrahedral geometry (τ4 index of 0.56) with Cu-N and Cu-Cl distances of 1.917 Å and 2.25 Å, respectively, falling in usual range compared to similar fragments using Mogul geometry check in Mercury and the values of angles as presented in Table 20.

Table 20: *Selected bond lengths [Å] and angles [°] for **MC9**.*

	Bond lengths	**Bond angles**
MC9	Cu1-N1 1.971(3)	N1-Cu1-N1$^{\#}$ 143.01(19)
	Cu1-N1$^{\#}$ 1.971(3)	N1-Cu1-Cl2 95.98(9)
	Cu1-Cl2 2.247(2)	N1-Cu1-Cl3 96.96(9)
	Cu1-Cl3 2.251(2)	N1$^{\#}$-Cu1-Cl2 95.98(9)
		N1$^{\#}$-Cu1-Cl3 96.96(9)
		Cl2-Cu1-Cl3 138.36(7)

#x,1-y,z

Compound **MC9** $[Cu_2(\mathbf{L9})_2Cl_4]\cdot CH_2Cl_2$ is analogous to previously described **MC6** $[Cu_2(\mathbf{L6})_2Cl_4]\cdot xS$ which contains imidazole instead of benzimidazole in its composition. The distance between the metal centers in **MC9** is *ca.*1 Å shorter compared to **MC6**.

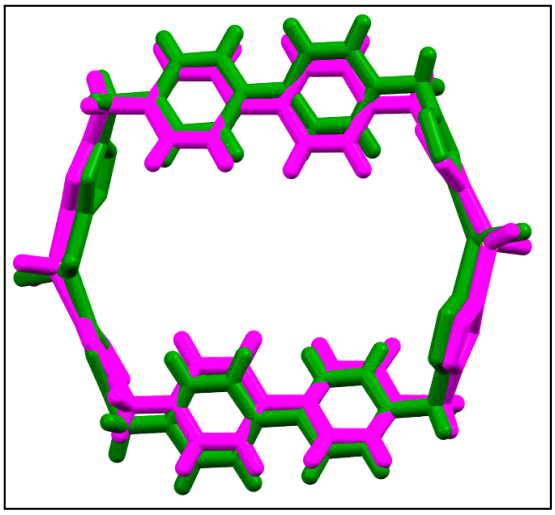

Figure 87: *Molecular overlay of **MC6** (pink) and **MC9** (green), RMSD- 0.5974 Å; extra benzene rings and H-atoms of the benzimidazole group in **MC9** were removed for better comparison.*

The angles between the planes of the benzene rings originating from biphenyl core are 30° and 31° in **MC6** and **MC9**, respectively, and the angle between the planes of the imidazole rings in case of **MC6** is 54° whereas it is 36° in case of **MC9** (measured after removing

benzene ring from benzimidazole moiety). Thus, the shape of metallocycle looks not so different in both the cases (see overlay in Figure 87). However, the crystal packing is different, and the structure features discrete voids which accounts for a volume of around 122 Å^3 per unit cell (4% of the total unit cell volume, calculated with Mercury software using a solvent-accessible probe with a radius of 1.2 Å) which are filled with DCM molecules (Figure 88).

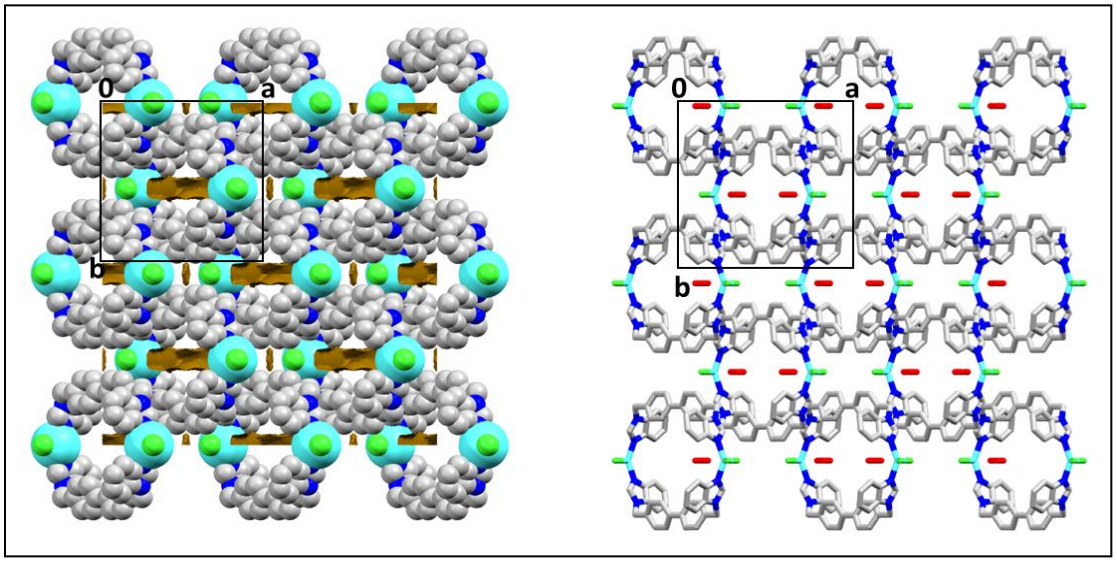

Figure 88: *Space-fill packing arrangement of **MC9** showing solvent-accessible discrete voids in dark yellow (on the left) which are filled with DCM molecules as shown in the capped-stick packing arrangement of **MC9** (on the right), shown along the c-axis. DCM guest molecules are highlighted in red, hydrogen atoms were omitted for clarity.*

The metallocycles in **MC9** expands into *bc* plane to form a 2D supramolecular assembly stabilized by π-π interactions present between the imidazole rings (N1-C9) with a centroid-centroid distance of 3.788(2) Å having a symmetry operator 1/2-x,1/2-y,2-z and between imidazole rings (N1-C9) and benzene rings (C4-C9) with a centroid-centroid distance of 3.582(2) Å and symmetry operator 1/2-x,1/2-y,2-z, and weak C–H···Cl hydrogen bonding interactions involving methylene groups and coordinated Cl3 atoms. These interactions are further supported by C–H···π interactions involving benzimidazole groups as donors and benzene rings of the biphenyl group as acceptors to form a 3D supramolecular assembly (Table 21).

Table 21: *Hydrogen bonding parameters for **MC9**.*

Compound	D-H···A	H···A (Å)	D···A (Å)	D-H-A (°)
MC9	C10-H10B···Cl3^{i}	2.79	3.762(4)	169
	C6-H6···Cg3^{ii}	2.72	3.558(4)	147

(**MC9):** Cg3 is the centroid of the benzene ring (C12-C17); **Symmetry codes:** (i) 1/2-x,-1/2+y,2-z, (iii) 1-x,y,2-z.

12.1.3.3.2. Bulk Solid-State Studies

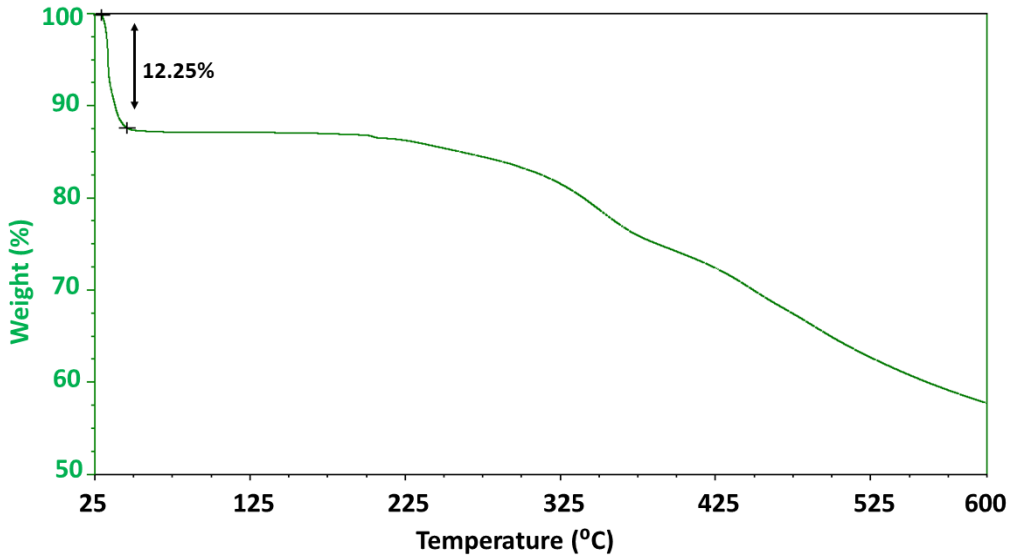

Figure 89: *Thermogram of **MC9**.*

Thermogravimetric analysis of **MC9** (Figure 89) reveals that the solvent loss starts to occur readily at room temperature and finishes at 45 ºC corresponding to a weight loss of 12.5% which corresponds to *ca.* 1.7 DCM molecule which doesn't exactly corresponds to the crystal structure data (1 molecule of DCM (7.2%) per metallocycle). The discrepancy between the observed and calculated values once again could be because of solvent loss from the crystal surface at ambient temperature during SCXRD sample preparation, leading to underestimation of solvent content in the crystallographic model relative to the bulk material analyzed by TGA. **MC9** is stable upto *ca.* 200 ºC after which the decomposition starts.

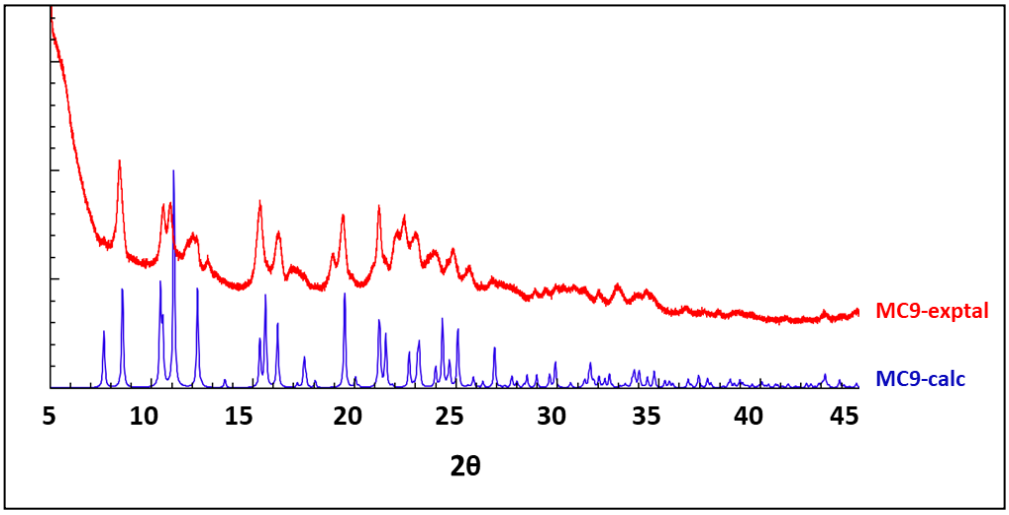

Figure 90: *Calculated and experimental PXRD patterns of the **MC9** and the bulk sample, respectively.*

PXRD studies were also carried out to check the homogeneity of the sample. The bulk was taken out from the solution, washed with crystallization solvent, and PXRD pattern was collected which didn't match perfectly with the calculated PXRD pattern, but that could be because of the sudden loss of the solvent molecules which come out already at the room temperature and might cause some changes in the structure and hence the PXRD patterns, for example peak broadening (Figure 90).

Based on these results, which show that the structure is stable after solvent loss up to 200 ºC, it was further given for the sorption studies, but unfortunately, it didn't adsorb any gases. The crystals were not of great quality and didn't diffract well upon heating so the structural transformation couldn't be followed in single-crystal to single-crystal mode for this system.

12.1.3.4. MC10: $[Zn_2(L9)_2(Cl)_4]\cdot xS$

12.1.3.4.1. Structural Analysis

Single-crystal X-ray diffraction (SCXRD) analysis of a crystal taken directly from the solution revealed that **MC10** crystallizes in the monoclinic space group $P2_1/m$. The asymmetric unit consists of two halves of crystallographically independent Zn(II) ions, four halves of chloride ions located on a mirror plane and one ligand molecule. The disordered solvent molecules were treated with SQUEEZE (described in section 8.1). **MC10** is a discrete neutral dinuclear metallocycle, with the cyclic units stacked above each other along the *a*-axis. One of the phenyl ring of the biphenyl core show disorder, which were modelled in two positions (65:35). Zn(II) metal center adopts a distorted tetrahedral coordination geometry (τ4 index of 0.90, Table 22) formed by two nitrogen atoms originating from 2 crystallographically independent ligand molecules and two chloride ions. The void volume within the channels of **MC10**, measuring approximately 563 $Å^3$ using a solvent-accessible probe with a radius of 1.2 Å, accounts for approximately 15% of the unit cell volume, and is filled with guest molecules (*ca.* 4.5 DMF molecules per formula unit, see chapter 8.1).

12.1.3.4.2. Bulk Solid-State Studies

Thermogravimetric analysis (TGA) revealed a stepwise weight loss pattern, indicating the difference in the interaction of guest molecules with the host, with an initial decrease of approximately 18% up to 80 °C (Figure 91). This was followed by an additional weight loss of around 8% until 230 °C, and a further decline beginning at 362 °C initiates

decomposition. Altogether (26% lost until decomposition), corresponds to the loss of roughly 4.5 DMF molecules per formula unit (predicted - 24.8%).

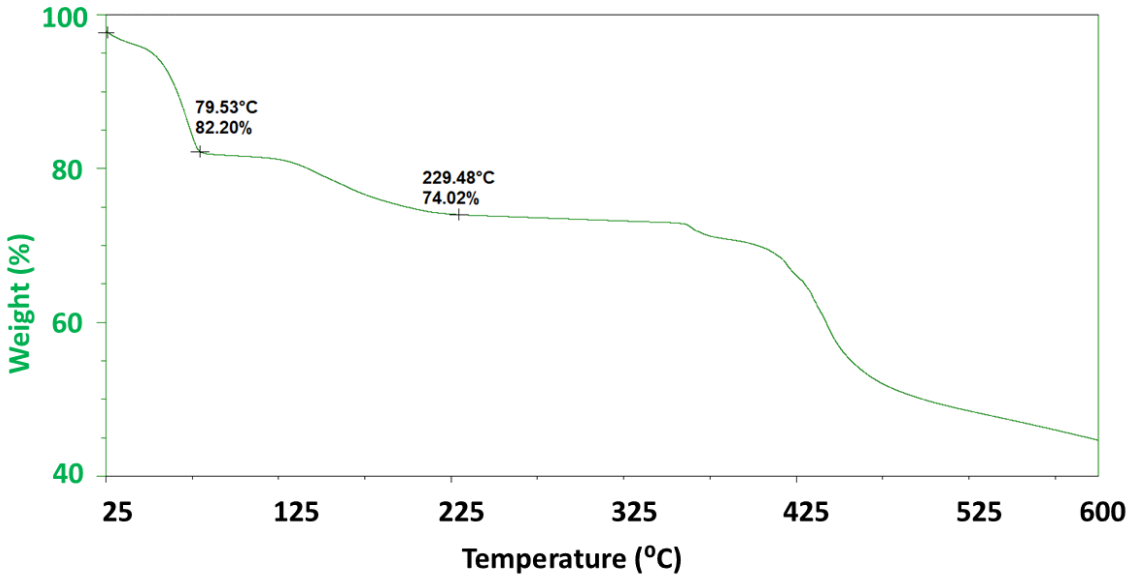

Figure 91: *Thermogram of **MC10**.*

Powder X-ray diffraction analysis was performed to verify the phase purity of **MC10**; however, the simulated and experimental patterns did not align, indicating the presence of another form/s (Figure 92). Challenges with sample homogeneity and solvent removal (discussed in section below) prevented sorption studies from being carried out on the system.

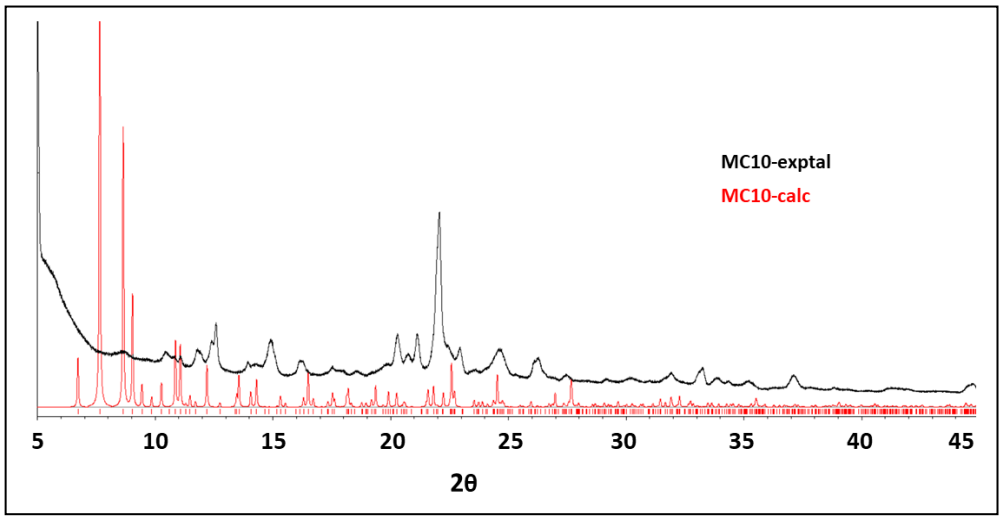

Figure 92: *Calculated and experimental PXRD patterns of the **MC10** and the bulk sample.*

12.1.3.4.3. Structural Transformation of MC10 to MC10-a

Thereby to check which process is taking place during the major weight loss observed on TGA the good quality crystal was heated at 100 ºC for 5 minutes. Morever, the full removal of solvent was approached by keeping the crystals under vacuum for 5 hours. Surprisingly not any attempt was successful in solvent removal; however, both of them resulted in significant SC-SC transformation revealing the drastic change in ligand's conformation within a metallocycle as described below.

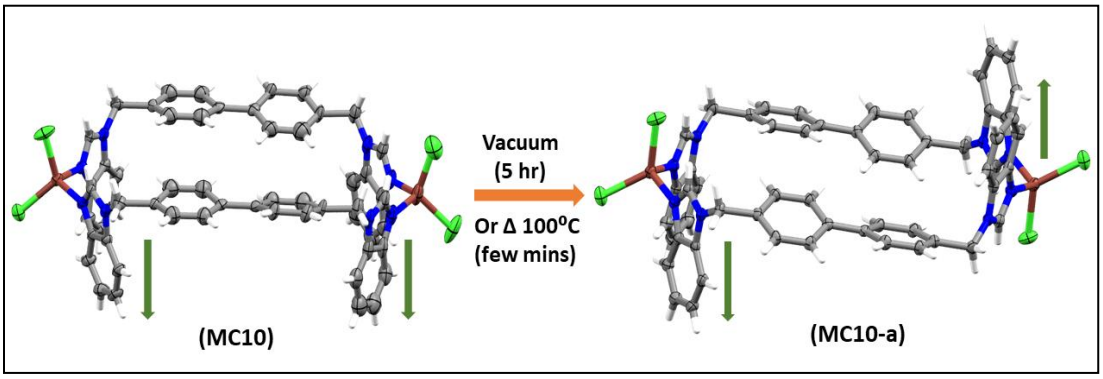

Figure 93: *Transformation of **MC10** to **MC10-a**.*

In **MC10**, both phenyl rings of benzimidazole units originating from the single ligand are oriented in the same direction, however, in **MC10-a**, it was observed that one phenyl ring is oriented upwards while the other is oriented downwards within a single ligand with respect to the plane of metallocycle, which is the result of the rotation of one of the benzimidazole groups within a ligand (Figure 93 and 94). This rotation of one of the benzimidazole groups is evidenced by torsion angle (C20-C23-N24-C25) which is 108.46º in **MC10** and -102.54º in case of **MC10-a**.

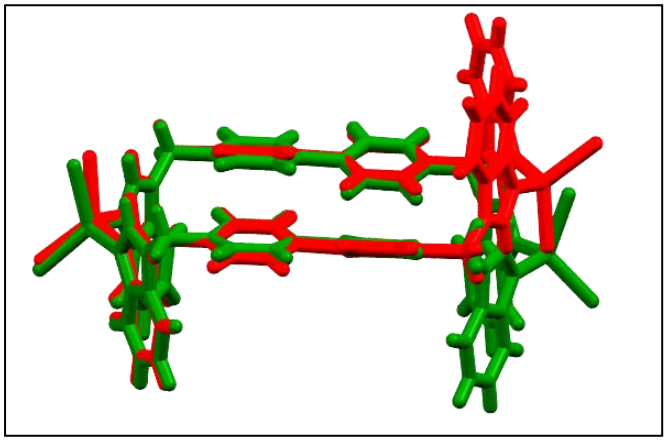

Figure 94: *Structure overlay of **MC10** (red) and **MC10-a** (green) highlighting rotation of benzimidazole group.*

MC10-a shows lower symmetry (triclinic system with space group *P*-1). The asymmetric unit of **MC10-a** consists of one Zn(II) cation, one ligand, two chloride ions, and 1 DMF

molecule (Platon showed 75 electron count per unit cell, roughly corresponding to 1 DMF molecule per asymmetric unit). Zn(II) ion in **MC10-a** displays more distorted tetrahedral coordination geometry (τ4 index of 0.85, Table 22) than **MC10**. The most notable difference is observed in the Cl1-Zn-Cl2 angle, which measures approximately 124° in **MC10-a** compared to 118° in **MC10**, resulting in a maximum angle deviation of around 6°.

Table 22: *Selected bond lengths [Å] and angles [°] for **MC10** and **MC10-a**.*

Compound	Bond lengths	Bond angles
MC10	Zn1-N1 2.0192(16)	N1-Zn1-N1$^{\#}$ 113.56(7)
	Zn1-N1$^{\#}$ 2.0192(16)	N1-Zn1-Cl1 108.04(5)
	Zn1-Cl1 2.2377(9)	N1-Zn1-Cl2 104.37(5)
	Zn1-Cl2 2.2354(9)	N1$^{\#}$-Zn1-Cl1 108.04(5)
		N1$^{\#}$-Zn1-Cl2 104.37(5)
		Cl1-Zn1-Cl2 118.64(4)
MC10-a	Zn1-N1 2.025(2)	N1-Zn1-N26$^{\#}$ 116.74(11)
	Zn1-N26$^{\#}$ 2.030(2)	N1-Zn1-Cl1 104.54(8)
	Zn1-Cl1 2.235(1)	N1-Zn1-Cl2 102.93(8)
	Zn1-Cl2 2.2413(9)	N26$^{\#}$-Zn1-Cl1 107.90(8)
		N26$^{\#}$-Zn1-Cl2 101.46(8)
		Cl1-Zn1-Cl2 124.06(4)

MC10: #x,1/2-y,z; **MC10-a**: #1-x,1-y,1-z

The discrete voids volume in **MC10-a**, measuring around 58 Å^3 per unit cell using a solvent-accessible probe with a radius of 1.2 Å, accounts for approximately 4% of the unit cell volume and contains DMF guest molecules. This indicates that during transformation, the ligand adjusts its conformation by releasing certain DMF molecules from its structure to achieve a denser packing. As a result of this rotation, the packing of **MC-10a** is stabilized by a different set of intermolecular interactions than **MC10**. The structure of both **MC10** and **MC10-a** is stabilized by a variety of π-π and C–H···Cl interactions with additional C–H···π interactions stabilizing **MC10-a**, which are absent in **MC10**. Solvent molecules are involved with the host via C–H···N and C–H···π interactions in **MC10-a**, but these won't be discussed for comparison as the solvent molecules were squeezed in **MC10**. The π-π interactions in both **MC10** and **MC10-a** are similar and involve both benzimidazole moieties (Table S3). Moreover, C–H···Cl interactions are more diverse in **MC10-a** than **MC10**. Both the methylene groups are involved as donors whereas Cl1/Cl3 as acceptors in both **MC10** and **MC10-a**. Furthermore in **MC10**, H-atoms from only one of the benzene

rings of the biphenyl group are involved, whereas in **MC10-a**, H-atoms from both the benzene rings of the biphenyl group are involved into interactions with Cl1 and Cl2 as acceptors. (Table 23).

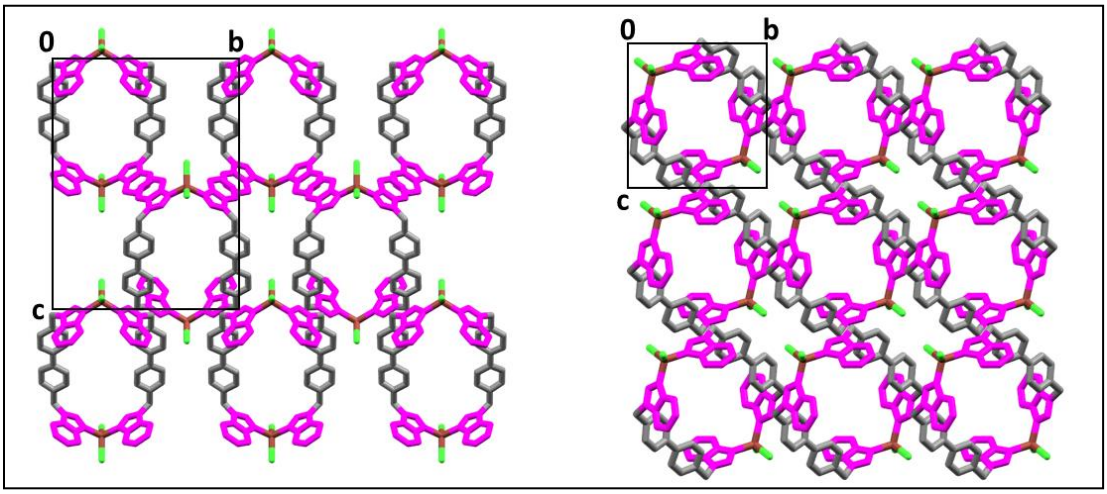

Figure 95: *Packing diagrams of **MC10** (left) and **MC10-a** (right), shown along the a-axis. Benzimidazole groups are highlighted in pink; hydrogen atoms were omitted for clarity.*

Table 23: *Hydrogen bonding parameters for **MC10** and **MC10-a**.*

Compound	D-H···A	H···A (Å)	D···A (Å)	D-H-A (°)
MC10	C10-H10A···Cl1^{i}	2.792	3.724	157
	C12-H12···Cl1^{i}	2.796	3.602	143
	C13-H13A···Cl2^{ii}	2.773	3.64	152
	C18-H18···Cl2^{ii}	2.892	3.706	144
	C23-H23B···Cl3^{iii}	2.730	3.677	160
MC10-a	C10-H10B···Cl1^{i}	2.952	3.873(3)	155
	C12-H12···Cl1^{i}	2.821	3.634(4)	144
	C19-H19···Cl1^{ii}	2.813	3.687(4)	153
	C23-H23B···Cl1^{ii}	2.727	3.689(4)	164
	C13-H13···Cl2^{iii}	2.943	3.560(3)	124
	C18-H18···Cl2^{iv}	2.755	3.628(4)	153
	C10-H10A···Cg4^{iv}	2.94	3.864(4)	160
	C30-H30···Cg4^{v}	2.90	3.727(4)	146
	C8-H8···Cg5^{vi}	2.954	3.720(5)	139

(**MC10-a):** Cg4 is the centroid of the benzene ring (C11-C16), Cg5 is the centroid of the benzene ring (C17-C22); Symmetry codes (**MC10):** (i) -x,1+y,-z, (ii) 1-x,1/2+y,-z, (iii) 2-x,1/2+y,1-z; (**MC10-a):** (i) 2-x,1-y,2-z, (ii) -1+x,-1+y,z, (iii) x,y-1,z, (iv) 1-x,1-y,2-z, (v) -1+x,y,z, (vi) 1+x,y,z.

In the solid state, molecular interactions play a crucial role in maintaining structural order. Any significant shift in molecular conformation or position that disrupts this stabilized arrangement can compromise the integrity of the crystal. Therefore, for a crystal to retain its monocrystalline nature during transformation, it is essential that either the changes to its core structure are minimal or that the molecules undergo a coordinated, collective reorganization. Previous studies on single-crystal to single-crystal transformations in metallocycles have typically involved only minor conformational adjustments [87, 89-91].

Some organic macrocycles though have demonstrated drastic conformational changes in SC-SC manner [220-222]. However, only one of the metallocycles [87] has exhibited a significant conformational change in an SC-SC manner upon heating or vacuum treatment. In contrast, our system exhibits substantial conformational changes, particularly the rotation of the benzimidazole group without compromising crystal integrity. This single-crystal to single-crystal (SCSC) transformation effectively demonstrated the cooperative molecular movements taking place in the crystals of presented Zn-metallocycle constructed with a **L9** ligand. Upon exposure to heat or vacuum, the system undergoes a significant conformational change, driven by the rotation of one of the benzimidazole groups, because of the removal of solvent molecules, leading to a reorganization of crystal structure to minimize free energy and stabilize the crystal structure. Moreover, to the best of our knowledge it is the first example reporting such a rotation of benzimidazole groups in the ligand within a metallocycle upon solvent removal. The ability of the crystals to withstand such a significant transformation is remarkable. This finding highlights the essential role of non-covalent interactions in driving structural rearrangements within single crystals. It also demonstrates that selecting an appropriate flexible ligand allows for the design of a dynamic metallocycle capable of undergoing considerable molecular and supramolecular changes in the solid state when exposed to external stimuli. Achieving control over the final product could lead to applications such systems in gas storage or separation. Moreover, substantial structural changes can be a base for development of new sensing materials.

12.1.3.5. MC11:$[Zn_2(L10)_2(Cl)_4]\cdot 4DMF\cdot xS$ and MC12: $[Zn_2(L10)_2(Cl)_4]\cdot 1DMF$

12.1.3.5.1. Structural Analysis

Both crystals were isolated from the same solution. They exhibited the same morphology, making it impossible to visually distinguish between them. However, as multiple crystals from the same beaker were selected for SCXRD study, the two different solvates were revealed.

Both **MC11** and **MC12** crystallize in the *P*-1 space group of the triclinic crystal system having different unit cell parameters. The asymmetric unit of **MC11** contains half a metallocycle i.e., one ligand, one Zn(II) cation, two chloride ions and two DMF molecules, out of which one is disordered over two positions (55:45). On the other hand, the asymmetric unit of **MC12** contains a whole metallocycle composed of two Zn(II) cations,

two bipodal ligands coordinated via N-atoms of the 2-methylbenzimidazole groups from both the ends with metal centers, four coordinated chloride ions and one DMF molecule (based on electron count from Platon as mentioned in the section 8.1). This metallocycle is highly disordered: one 2-methylbenzimidazole group, one Zn ion and two Cl ions are disordered over two positions with site occupancies of 80:20, while DMF is disordered with occupancies of 53:47. Such extensive disorder suggests dynamic behavior within the crystal of this molecule, likely triggered by partial solvent loss, which induces structural flexibility and positional rearrangement. The metal center displays slightly distorted tetrahedral geometry in both the cases (τ_4 indices of 0.98 for **MC11** and 0.93 for **MC12**) with major differences in the bond angles with N-Zn-N angle having largest difference of approximately 12º (Table 24).

Table 24: *Selected bond lengths [Å] and angles [°] for **MC11** and **MC12**.*

Compound	Bond lengths	Bond angles
MC11	Zn1-N1 2.0263(13)	N1-Zn1-N27$^{\#}$ 108.45(5)
	Zn1-N27$^{\#}$ 2.0363(12)	N1-Zn1-Cl1 109.79(4)
	Zn1-Cl1 2.2642(4)	N1-Zn1-Cl2 111.64(4)
	Zn1-Cl2 2.2656(4)	N27$^{\#}$-Zn1-Cl1 110.51(4)
		N27$^{\#}$-Zn1-Cl2 110.64(4)
		Cl1-Zn1-Cl2 105.81(2)
MC12	Zn1-N1 2.054(3)	N1-Zn1-N35 96.39(11)
	Zn1-N35 2.037(3)	N1-Zn1-Cl1 108.82(9)
	Zn1-Cl1 2.2356(11)	N1-Zn1-Cl2 113.96(9)
	Zn1-Cl2 2.2233(11)	N35-Zn1-Cl1 115.65(10)
		N35-Zn1-Cl2 108.36(9)
		Cl1-Zn1-Cl2 112.73(5)

MC11: #-x,1-y,1-z

The distance between the Zn(II) cation centers within a metallocycle is 15.742 Å and 16.545 Å in **MC11** and **MC12**, respectively. The angle between the 2-methylbenzimidazole rings within a ligand in **MC11** and **MC12** measures 54.95º and 7.16º, respectively. Moreover, the angle between the benzene rings of the biphenyl group within a ligand is 33.10º and 21.58º/26.15º for **MC11** and **MC12**, respectively. The orientation of 2-methylbenzimidazole rings within a ligand in **MC11** and **MC12** vary significantly as highlighted by torsion angles C12-C11-N3-C2 and C21-C24-N25-C26 which measure 103.52º and -106.26º for **MC11** and 99.05º and 67.6º for **MC12**, respectively. Additionally,

torsion angles C46-C45-N37-C36 and C55-C58-N59-C60 in **MC12** are equal to -104.04º and -102.7º, respectively.

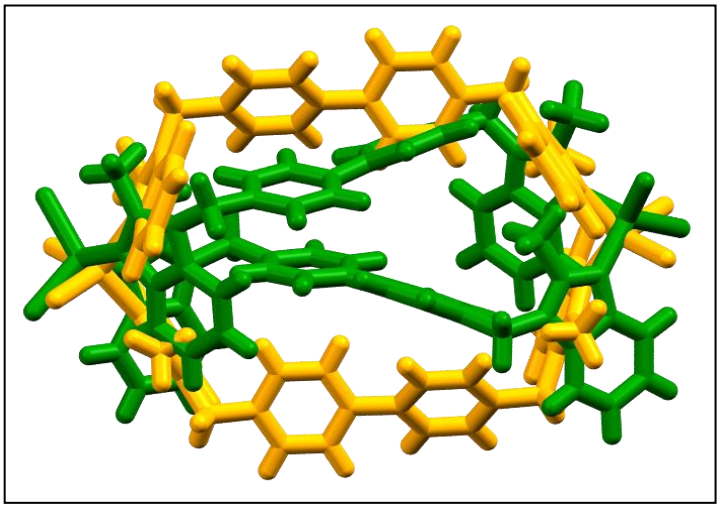

Figure 96: *Molecular overlay of **MC11** (orange) and **MC12** (green), RMSD-3.6854 Å.*

All these values highlight the distinct ligand conformation eventually leading to differently shaped metallocycles, 'open' in the case of **MC11** and partially 'closed' in the case of **MC12**, therefore leading to a differently packed structures. The comparison of the intermolecular interactions stabilizing the structure will not be discussed as **MC12** is highly disordered and it would not be feasible to compare the interactions in the two structures considering this disorder.

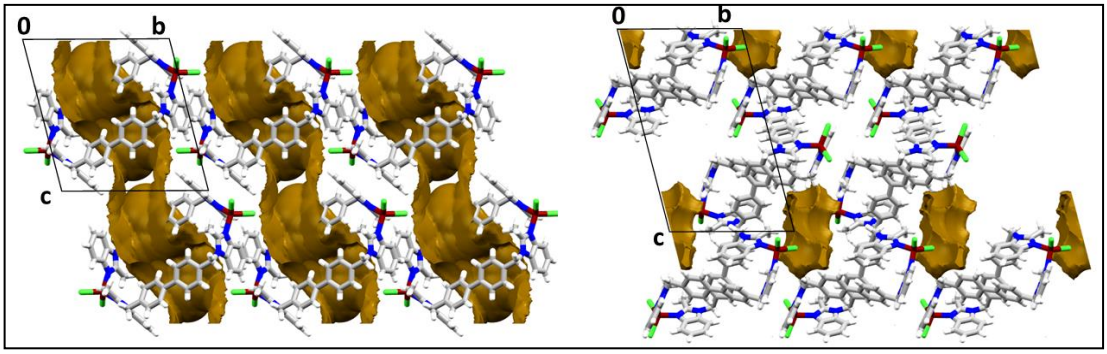

Figure 97: *Capped stick packing arrangement of **MC11** (on the left) and **MC12** (on the right) showing solvent-accessible channels in **MC11** and discrete voids in **MC12**, shown in brown which are filled with solvent molecules, shown along the a-axis.*

The structure of **MC11** displays channels expanding along *c*-axis corresponding to a volume of 317 Å^3 per unit cell, calculated using solvent-accessible surface with a probe radius of 1.2 Å, accounting for approximately 16% of the total unit cell, which totals is 1942.18 Å^3. The channels are filled with DMF molecules. On the other hand, **MC12**, displays only discrete voids corresponding to a volume of 97 Å^3, calculated using solvent-

accessible surface with a probe radius of 1.2 Å, accounts for approximately 3% of the total unit cell volume, which totals 2970 Å^3 and is filled with DMF guest molecules.

Table 25: *Hydrogen bonding parameters for **MC11**.*

Compound	D-H···A	H···A (Å)	D···A (Å)	D-H-A (°)
MC11	C16-H16···O44^{i}	2.701	3.298(4)	122
	C23-H23···O44^{i}	2.651	3.593(4)	171
	C38-H38···O44^{i}	2.992	3.726(6)	135
	C10-H10A···O44a^{i}	2.766	3.412(5)	125
	C17-H17···O44A^{i}	2.57	3.183(5)	123
	C38-H38···O44A^{i}	2.601	3.535(7)	168
	C7-H7···O39^{ii}	2.760	3.543(3)	140.5
	C10-H10B···O39^{iii}	2.765	3.689(2)	158
	C11-H11B···O39^{iii}	2.469	3.412(2)	159
	C22-H22···O39^{i}	2.875	3.610(3)	135
	C34-H34C···O39^{i}	2.476	3.453(2)	175
	C42A-H42D···N35	2.963	3.69(3)	131
	C43-H43···N35	2.924	3.87(2)	171
	C11-H11B···Cl1^{iv}	2.844	3.807(2)	164
	C13-H13···Cl1^{iv}	2.867	3.761(2)	157
	C20-H20···Cl2^{v}	2.875	3.772(1)	158
	C24-H24A···Cl2^{v}	2.894	3.838(2)	160
	C24-H24B···Cl2^{vi}	2.947	3.845(2)	151

Symmetry codes: (i) -x,1-y,1-z, (ii) -x,-y,1-z, (iii) 1+x,y,z, (iv) 1-x,-y,1-z, (v) x,1+y,z-1, (vi) 1-x,1-y,1-z.

12.1.3.5.2. Bulk-Solid-State Studies

This system couldn't be studied further on bulk due to the lack of homogeneity.

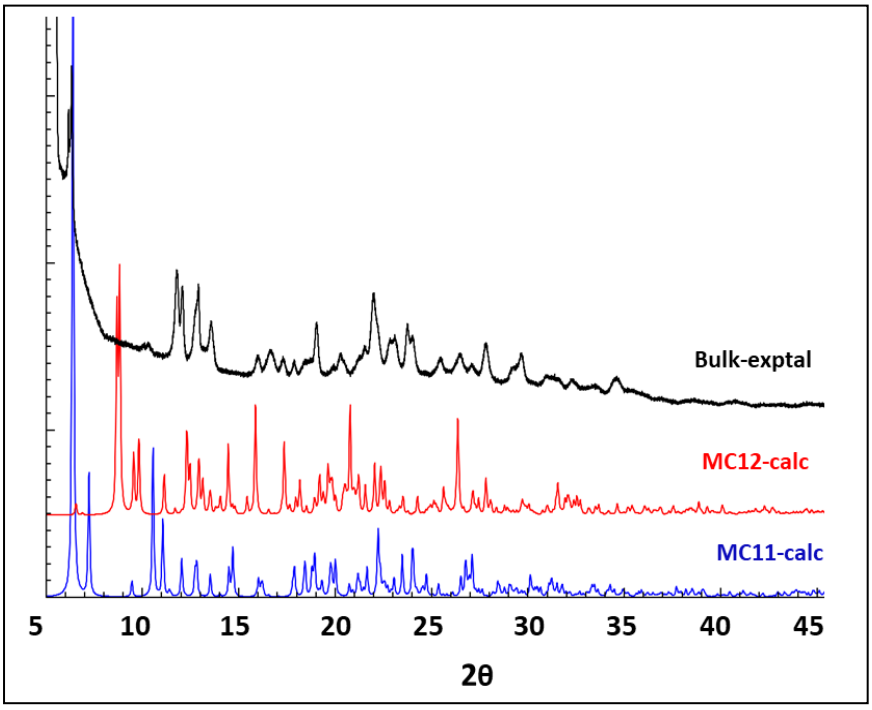

Figure 98: *Calculated and experimental powder patterns of the **MC11**, **MC12** and bulk.*

12.2. 1D Coordination Polymers

The primary objective of this thesis was to obtain and study sorption properties of crystalline materials based on 0D discrete metallocycles (MCs). However, as several 1D coordination polymers (CPs) were also isolated during the course of this research these results are presented below.

Table 26: *Crystallographic data and structure refinement parameters for presented CPs,* ***CP1***, ***CP2***, ***CP2-a***, ***CP3***, *and* ***CP3-a****.*

Compound Reference	**CP1**	**CP2**	**CP2 -a**	**CP3**	**CP3 -a**
Chemical formula	$C_{20}H_{20}Cl_2CoN_4$	$C_{22}H_{23}Cl_2CuN_5$	$C_{20}H_{20}Cl_2CuN_4$	$C_{22}H_{23.4}CdCl_2N_5O_{0.2}$	$C_{20}H_{20}N_4Cl_2CdN_4$
Formula mass	446.23	491.89	430.93	544.36	499.70
Crystal system	Orthorhombic	Monoclinic	Monoclinic	Monoclinic	Orthorhombic
a/Å	20.9350(2)	7.9786(2)	14.435(2)	7.97850(10)	10.3044(6)
b/Å	14.4387(2)	15.1761(4)	10.4268(14)	15.4909(2)	13.4369(6)
c/Å	13.0298(1)	9.0794(2)	13.2084(14)	9.39940(10)	15.1125(8)
α/ ◦	90	90	90	90	90
β/ ◦	90	98.300(2)	98.355(13)	97.7470(10)	90
γ/ ◦	90	90	90	90	90
Unit cell volume/$Å^3$	3938.57(7)	1087.86(5)	1967.0(4)	1151.11(2)	2092.46(19)
Temperature/K	100(2) K	100.15 K	100(1) K	100.15 K	100(2) K
Space group	*Pbcn*	$P2_1/m$	$P2_1/c$	$P2_1/m$	*Pbcn*
No. of formula units per unit cell, Z	8	2	4	2	4
Radiation type	CuK\α	CuK\α	CuK\α	CuK\α	CuK\α
Absorption coefficient, μ/mm^{-1}	9.421	3.825	4.157	9.886	10.797
No. of reflections measured	23713	6011	6264	13354	13136
No. of independent reflections	4042	2115	6264	2473	2195
Rint	0.0354	0.0201	-	0.0204	0.0950
Final R1 [a] values ($I > 2\sigma(I)$)	0.0372	0.0406	0.1127	0.0253	0.0873
Final wR2 [b] values ($I > 2\sigma(I)$)	0.0943	0.1199	0.2992	0.0679	0.2685
Final R1 [a] values (all data)	0.0434	0.0488	0.1417	0.0258	0.1273
Final wR2 [b] values (all data)	0.0978	0.1229	0.3259	0.0682	0.3060
Goodness of fit on F^2	1.054	1.099	1.073	1.097	1.099

12.2.1. CP1: $\{[Co(L3)Cl_2]\}_n$

12.2.1.1. Structural Analysis

SCXRD analysis revealed that **CP1** forms 1D chains. Thus, **MC2** and **CP1** have identical compositions except for the presence of an acetonitrile molecule in **MC2**, making them pseudo supramolecular isomers. However, **MC2-a**, **MC2-b**, and **CP1** can be termed genuine supramolecular isomers as they show identical composition. **CP1** crystallizes in the orthorhombic crystal system of the *Pbcn* space group, where the asymmetric unit consists of one Co(II) cation, one **L3** ligand molecule and two chloride ions. Similar to **MC2**, the Co(II) ion in **CP1** also exhibits a distorted tetrahedral geometry (τ_4 index of 0.91) with two N-atoms of imidazole rings belonging to two symmetry related ligand (**L3**) molecules and two chloride ions with Cd-N and Cd-Cl distances in the range of (2.006–2.025) Å and (2.006–2.025) Å, respectively, and angles ranging from 102.48º to 116.67º (Table 27).

Table 27: *Selected bond lengths [Å] and angles [°] for **CP1***.

Compound	Bonds	Angles
CP1	Co1-N2 2.006(2)	N2-Co1-N14 110.13(8)
	Co1- N14 2.025(2)	N2-Co1-C26 105.35(6)
	Co1-Cl26 2.2485(7)	N14-Co1-Cl26 113.84(6)
	Co1-Cl27 2.2628(7)	N2-Co1-Cl27 108.30(6)
		N1-Co1-Cl27 102.48(7)
		Cl26-Co1-Cl27 116.67(3)

2-methylimidazole rings in a bidentate ligand (**L3**) in **CP1** are oriented opposite ways towards the plane of naphthalene core and the ligand acts as a bridge between the metal ions to form a 1D wavy chain expanding along [201] with Co---Co separation of 15.3663(6) Å. The imidazole rings within a ligand in **CP1** are nearly parallel to each other, while the naphthalene ring and the imidazole rings are almost perpendicular to each other with an angle of 89.90º. The conformation of ligand in **CP1** differs significantly from the one observed in the related metallocycles: **MC2**, **MC2-a** and **MC2-b**.

The 1D chains are further stabilized by weak C–H···Cl hydrogen bonding interactions. These involve H-atoms from the methyl (C19) and methylene (C20) groups with Cl26 as the acceptor, as well as H-atoms from the imidazole rings (N1-C5), methyl groups (C6) and methylene groups (C8) with Cl27 as the acceptor, and C–H···π involving H-atoms from benzene rings (C9-C13) with benzene rings (C21-C25) as acceptor and H- atoms from imidazole rings (N14-C18) with benzene rings (C9-C13) as acceptor to form a 3D

supramolecular assembly. C–H···N interactions are absent in this case (Table S2). Moreover, π-π stacking interactions are present between adjacent imidazole rings (N14-C19) with a centroid to centroid distance of 3.6107(15) Å, symmetry operator- 1-x,y,1/2-z.

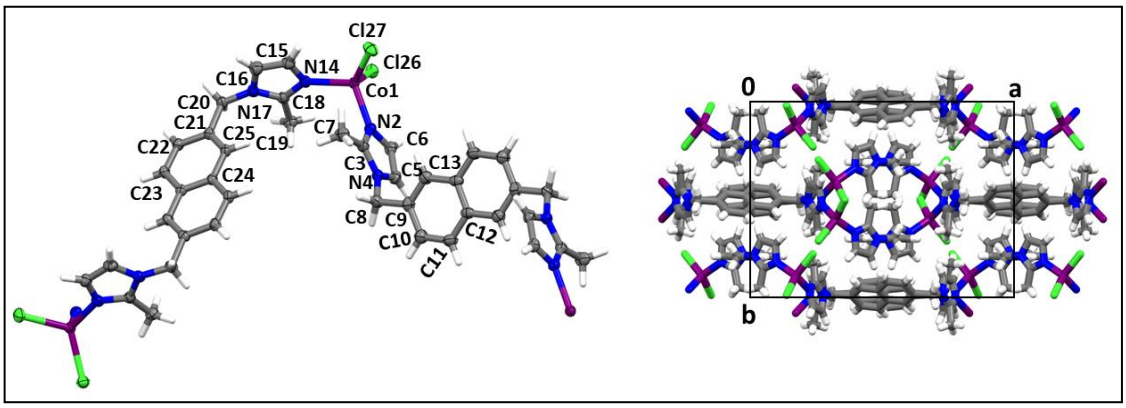

Figure 99: ***(On the left):*** *fragment of a 1D chain formed by* ***CP1*** *with atomic displacement ellipsoids drawn at the 50% probability levels, the unlabelled atoms are related to the labelled ones by the symmetry operation: -x,1-y,1-z,* ***(on the right):*** *packing diagram of* ***CP1*** *shown along the c-axis.*

12.2.1.2. Bulk Solid-State Studies

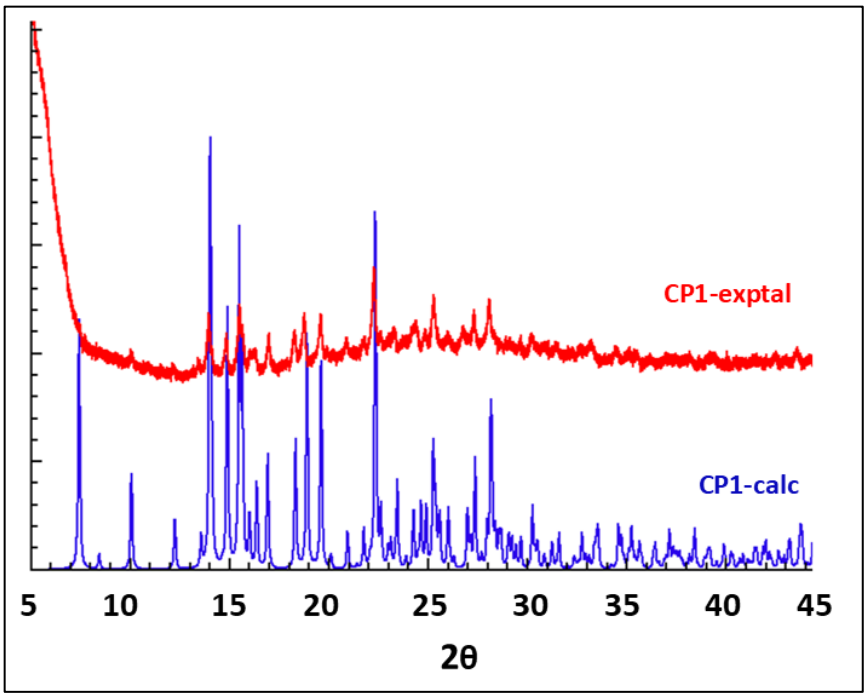

Figure 100: *Calculated and experimental PXRD patterns of the* ***CP1*** *and the bulk sample.*

A good match of the simulated PXRD patterns with the as-synthesized PXRD patterns was observed for **CP1** (Figure 100). Moreover, TGA analysis confirmed the absence of solvent in the structure. The compound melts at approximately 175 °C and decomposition starts around 360 °C (Figure 101).

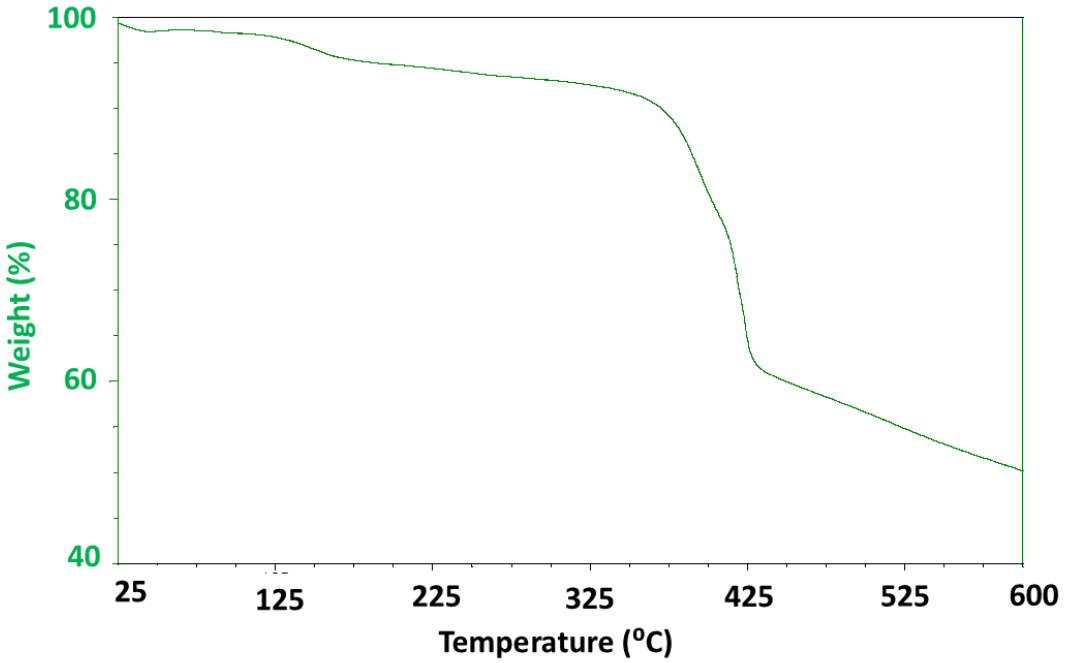

Figure 101: *Thermogram of **CP1**.*

12.2.2. CP2:{[Cu(L3)Cl_2]·CH_3CN}$_n$ and CP3:{[Cd(L3)Cl_2]·CH_3CN·0.2H_2O}$_n$

12.2.2.1. Structural Analysis

The slow evaporation of the mixture obtained by the equimolar complexation reaction of **L3** with $CuCl_2·6H_2O$ and $CdCl_2·2.5H_2O$ in acetonitrile gave good quality orange and colorless crystals (blocks) of **CP2** and **CP3**, respectively. SCXRD studies showed that **CP2** and **CP3** are isostructural and crystallize in the monoclinic $P2_1/m$ space group, with small differences in the unit cell parameters along the *b* (2%) and *c* (3.5%) axis. The asymmetric unit of both **CP2** and **CP3** contains two halves of chloride ions, half of metal ion (M= Cu(II) for **CP2** and Cd(II) for **CP3**), and half of acetonitrile molecule all located on the mirror plane, and half a molecule of the ligand with a two-fold screw axis passing through the naphthalene ring. (Figure 102). **CP3** additionally contains traces of water. The metal ions in both **CP2** and **CP3** are coordinated with two chloride ions and two N-atoms of the imidazole ring originating from two symmetry related **L3** ligand molecules resulting in a distorted tetrahedral geometry, with τ_4 indices of 0.7 and 0.88, respectively. The M–N distances measures 1.975 Å and 2.116 Å and M–Cl distances are in the range of (2.3076–2.367) Å and (2.0045–2.4462) Å for **CP2** and **CP3**, respectively, and the bond angles vary from 97.32° to 139.62° for **CP2** and 101.42° to 121.44° for **CP3** (Table 28). The 2-methylimidazole rings within a ligand are parallel to each other. Bidentate ligand (**L3**) in

both **CP2** and **CP3** and is acting as a bridge between the metal ions leading to the formation of polymeric 1D waved chains expanding along the *b*-axis, with M---M distances of 14.98 Å and 15.67 Å for **CP2** and **CP3**, respectively.

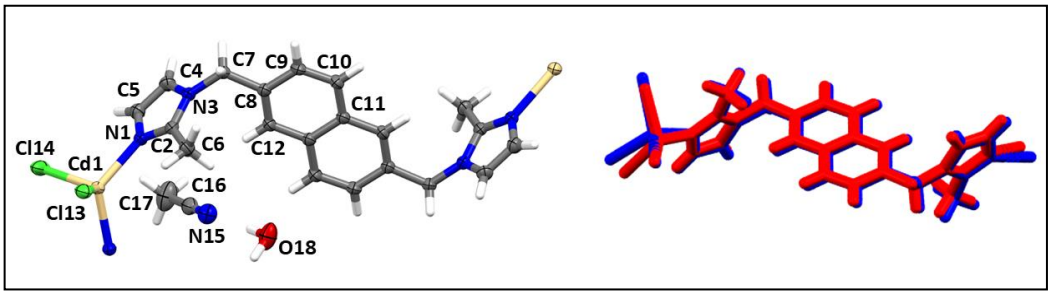

Figure 102: ***(a)*** *Fragment of a 1D chain formed by* ***CP3*** *with atomic displacement ellipsoids drawn at the 50% probability levels, the unlabelled atoms are related to the labelled ones by the symmetry operation: −x,1- y, 2−z,* ***(b)*** *overlay of 1D fragment of* ***CP2*** *(red) and* ***CP3*** *(blue), RMSD is 0.2119 Å, solvent molecules were omitted for clarity.*

In both the structures, 3D supramolecular assembly is stabilized by π-π stacking interactions between the imidazole rings with a distance of 3.4392(15) Å for **CP2** and 3.6360(14) Å for **CP3** and various C–H···Cl interactions (Table S2). The solvent molecules are involved in stabilizing the structure via weak C–H···N hydrogen bonds in both **CP2** and **CP3**, with additional C–H···O and O–H···N hydrogen bonds (Table S2) in the case of **CP3**, due to the presence of additional water molecule in the structure. The overall structures of both compounds are isostructural to some extent as evidenced by their unit cell parameters (the cell similarity index – Π is 0.0167, a value which approximates 0 for the identical unit cells of two crystal structures and isostructurality index is 67.8%- calculated without taking water molecules into account) [223, 224], and the similarity of their molecular packing and supramolecular interactions except for some subtle differences in the coordination geometry and the presence of more hydrogen bonding interactions involving additional water molecules in **CP3**.

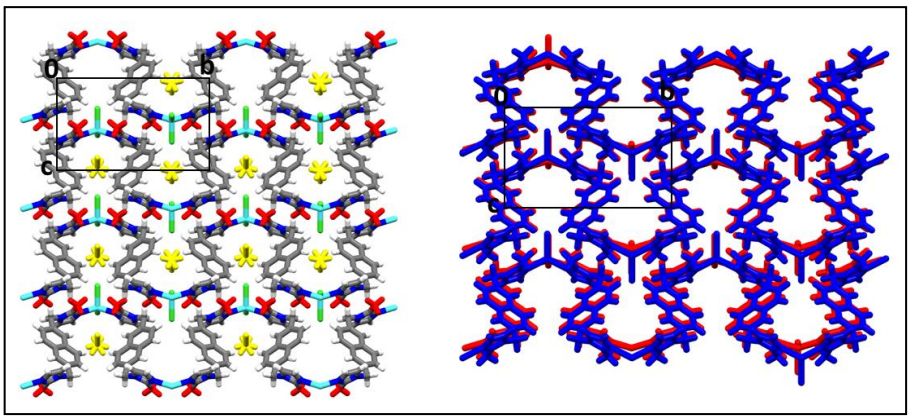

Figure 103: ***(On the left):*** *packing diagram of* ***CP2*** *shown along the a-axis; methyl groups shown in red, and acetonitrile molecules in yellow,* ***(on the right):*** *overlay of packing diagrams of* ***CP2*** *(red) and* ***CP3*** *(blue) shown along the a-axis.*

The solvent molecules in both **CP2** and **CP3** are present in discrete pockets accounting for a volume of 12 Å^3 per unit cell (*c.a.* 1% of the total unit cell volume) in case of **CP2** and a volume of 17 Å^3 per unit cell (*c.a.* 1.5% of the total unit cell volume), calculated using a solvent-accessible surface with a probe radius of 1.2 Å in Mercury.

12.2.2.2. Bulk Solid-State Studies

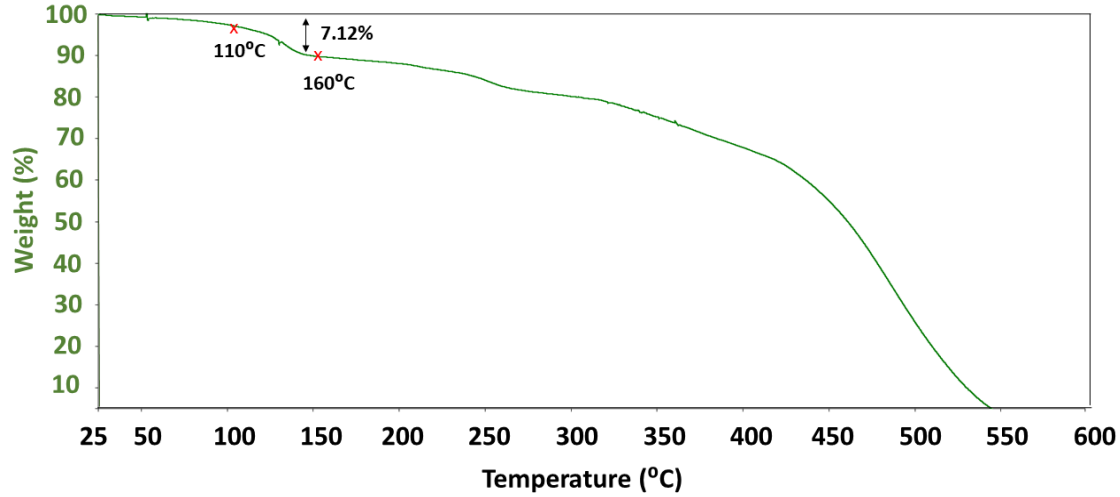

Figure 104: *Thermogram of* ***CP2****.*

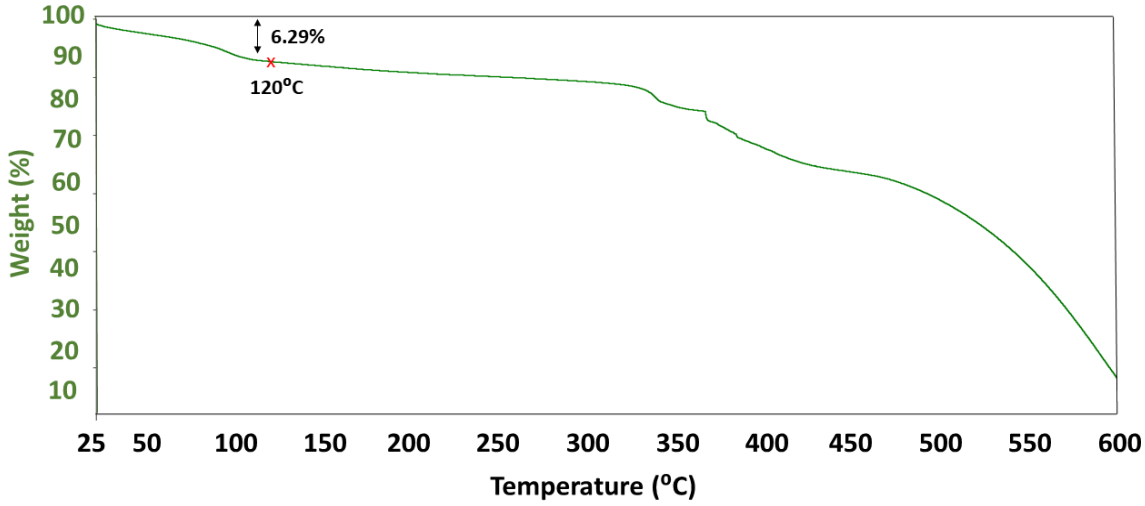

Figure 105: *Thermogram of* ***CP3****.*

Thermogravimetric analysis (TGA) of **CP2** and **CP3** revealed that it has different course in both solids. Solvent loss starts occurring near ambient temperature in both the cases and continues progressively until 160 ºC for **CP2** corresponding to a weight

loss of *c.a.* 7% (predicted 8.35%) (Figure 104) and until 120 ºC for **CP3** corresponding to a weight loss of *c.a.* 6.3% (predicted 7.9%) (Figure 105).

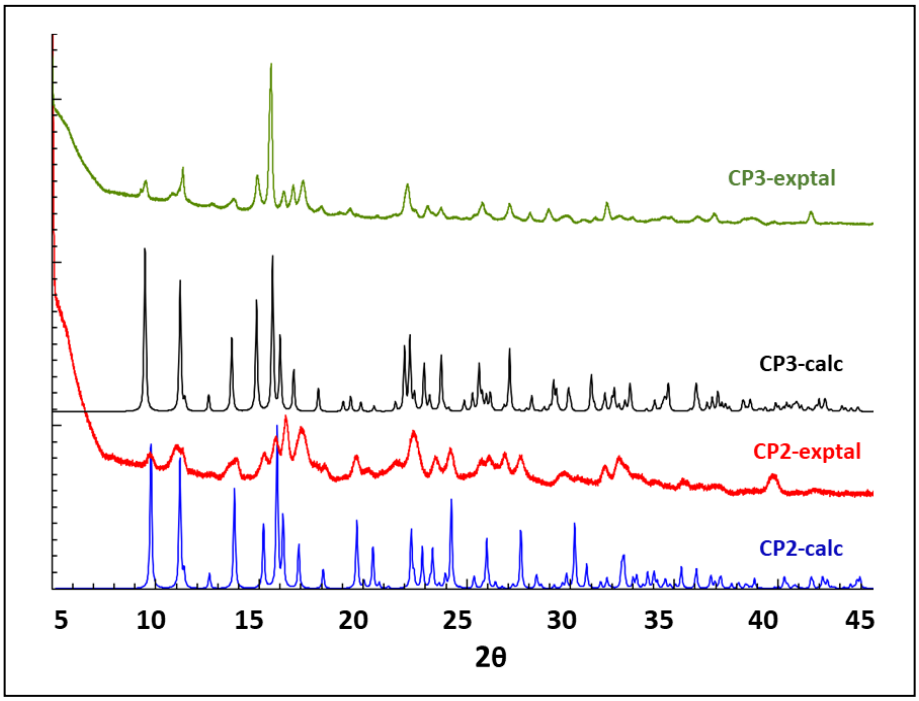

Figure 106: *Calculated and experimental PXRD patterns of **CP2**, **CP3** and bulk samples respectively.*

PXRD analysis show rather close match of the simulated PXRD patterns with the as-synthesized PXRD patterns indicating a higher amorphous character of **CP2** (Figure 106).

12.2.2.3. Trigerred Structural Transformations of CP2 to CP2-a and CP3 to CP3-a

As SCXRD analyses show presence of acetonitrile molecules in both crystal structures the attempts were undertaken to remove these in order to use the desolvated structures further for the sorption studies. Based on TGA data, crystals of **CP2** and **CP3** were heated at 150 ºC for around 2-3 minutes, resulting in the desolvated forms, **CP2-a** and **CP3-a**. These structures, upon solvent removal, reorganize into a more densely packed arrangement, and doesn't show any voids in the structure calculated using a solvent-accessible surface with a probe radius of 1.2 Å. Upon reducing the probe radius to 0.8 Å, **CP2-a** displays discrete voids with a volume of approximately 8 Å^3 per unit cell, and **CP3-a** displays discrete voids with a volume of approximately 21 Å^3 per unit cell. Thus, the structures obtained upon desolvation, are not porous in the conventional sense.

CP2 during transformation is changing space group from $P2_1/m$ to $P2_1/c$. The asymmetric unit of **CP2-a** contains two crystallographically independent half-molecules of the ligand, two chloride ions, and one Cu(II) ion. The 1D waved chains show an increased Cu---Cu separation of 15.717 Å (from 14.981 Å in **CP2**) and expand along the *a*-axis.

On the other hand, **CP3** transforms from a lower symmetry to a higher symmetry namely from monoclinic to orthorhombic crystal system of the *Pbcn* space group. The asymmetric unit of **CP3-a** contains half a molecule of the ligand, one chloride ion, and half of Cd(II) ion located on the 2-fold rotation axis. The formed 1D waved chain is expanding along the c-axis. It shows an increase of Cd---Cd distance of *ca.* 0.5 Å (16.18 Å in **CP3-a**, 15.67 Å in **CP3**). The geometry around the metal center in both **CP2-a** and **CP3-a** is still distorted tetrahedral (τ_4 indices of 0.85 and 0.93, respectively). However, significant changes are observed in bond angle values, specifically N-Cu-N bond angle which is almost 41° smaller in **CP2-a** as compared to **CP2**, whereas in **CP3-a**, it is around 10° smaller as compared to **CP3** (Table 28).

Table 28: *Selected bond lengths [Å] and angles [°] for **CP2**, **CP2-a**, **CP3** and **CP3-a**.*

Compound	Bond length	Bond angles
CP2	Cu1-N1 1.973(2) Cu1- N1$^{\#}$ 1.973(2) Cu1-Cl13 2.2939(11) Cu1-Cl14 2.2524(11)	N1$^{\#}$-Cu1-N1 139.43(12) N1-Cu1-Cl13 101.65(7) N1$^{\#}$-Cu1-Cl13 101.65(7) N1-Cu1-Cl14 97.55(7) N1$^{\#}$-Cu1-Cl14 97.55(7) Cl13-Cu1-Cl14 122.13(4)
CP2-a	Cu1-N1 1.941(10) Cu1- N15 1.969(11) Cu1-Cl13 2.245(4) Cu1-Cl14 2.237(3)	N1-Cu1-N15 98.7(4) N1-Cu1-Cl13 106.2(3) N15-Cu1-Cl13 116.7(4) N1-Cu1-Cl14 123.0(3) N15-Cu1-Cl14 107.5(3) Cl13-Cu1-Cl14 105.37(14)
CP3	Cd1-N1 2.2116(19) Cd1-N1$^{\#}$ 2.2116(19) Cd1-Cl13 2.4462(8) Cd1-Cl14 2.4352(9)	N1$^{\#}$-Cd1-N1 121.45(10) N1-Cd1-Cl13 108.82(5) N1$^{\#}$-Cd1-Cl13 108.82(5) N1-Cd1-Cl14 101.42(5) N1$^{\#}$-Cd1-Cl14 101.42(5) Cl13-Cd1-Cl14 114.84(4)

CP3-a	Cd1-N1 2.197(10) Cd1-N1$^{\#1}$ 2.197(10) Cd1-Cl13 2.441(3) Cd1-Cl13$^{\#1}$ 2.441(3)	N1$^{\#1}$-Cd1-N1 111.3(5) N1-Cd1-Cl13 107.9(2) N1$^{\#1}$-Cd1-Cl13 106.4(2) N1-Cd1-Cl13$^{\#2}$ 106.4(2) N1$^{\#1}$-Cd1-Cl13$^{\#2}$ 108.0(2) Cl13-Cd1-Cl13$^{\#2}$ 116.83(17)

(CP2, CP3): $^{\#}$1+x, 1/2-y,+z; **(CP3-a):** $^{\#1}$1-x,-y,1-z, $^{\#2}$1-x,y,3/2-z

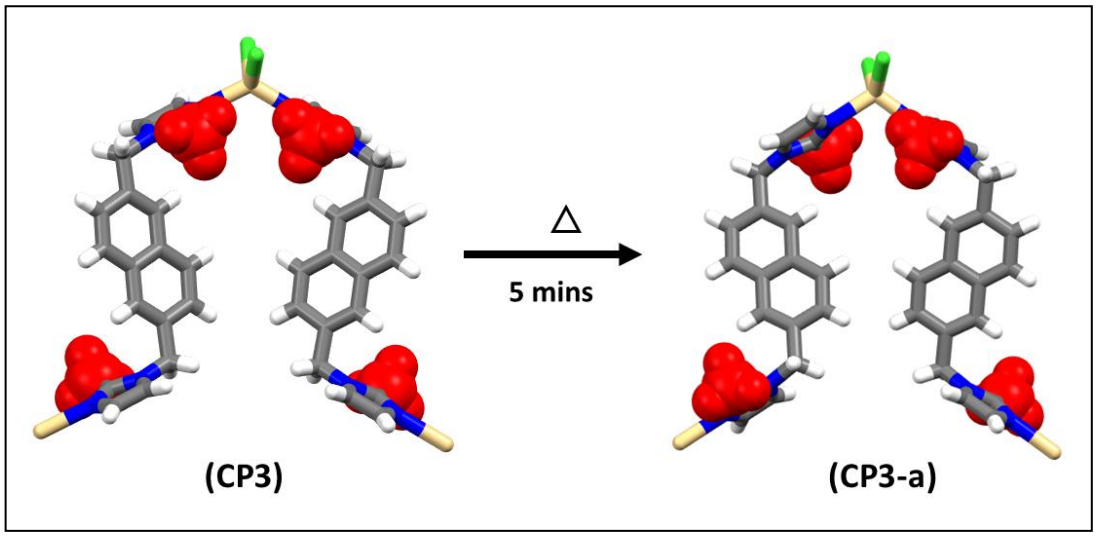

Figure 107: *Schematic transformation from **CP3** to **CP3-a**. The rotation of 2-methylimidazole group is highlighted by methyl group positions in red.*

The transformations from **CP2** and **CP3** to **CP2-a** and **CP3-a**, respectively result in the significant change in the ligand's conformation as a result of the rotation of one of the 2-methylimidazole groups within a ligand. In both **CP2-a** and **CP3-a**, the methyl groups of the two coordinated 2-methylimidazole groups from the different ligands are oriented opposite to each other, which in the case of **CP2** and **CP3** are pointing in the same direction (figure 107). The 2-methylimidazole rings within a ligand in both **CP2-a** and **CP3-a** are also parallel to each other like in **CP2** and **CP3**. The torsion angles C8-C7-N3-C4 within a ligand measure 51.90º/-51.90º in **CP2-a** and 79.97º/-79.97º in **CP3-a**, which was 99.34º/-99.34º in **CP2** and 101.36º/-101.36º in **CP3**. Moreover, the angle between the planes of the two coordinated 2-methylimidazole groups measures 84.53º in **CP2-a** and 71.24º in **CP3-a** which was 46.65º in **CP2** and 50.91º in **CP3**. All these values were quite similar in **CP2** and **CP3**, as they were isostructural. However, the values for **CP2-a** and **CP3-a** differ significantly from each other indicating different results of the structural transformations.

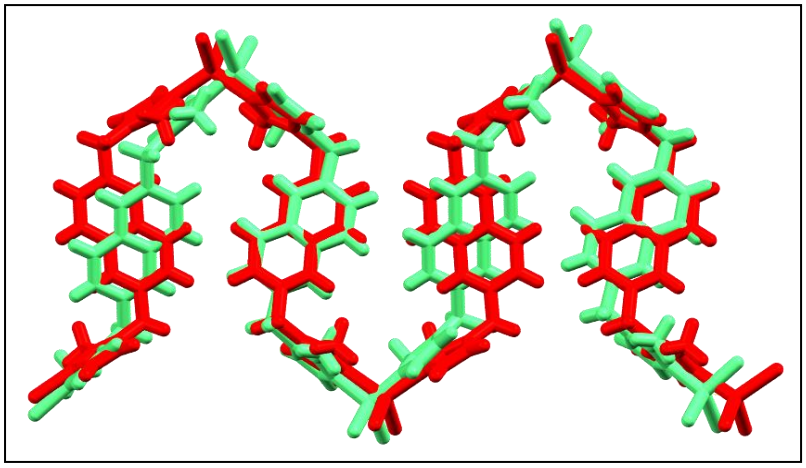

Figure 108: *Overlay of a fragment of 1D chain of **CP2-a** (light green) and **CP3-a** (red).*

As a result of solvent removal, the yielded phases are stabilized by a set of different interactions. **CP2-a** and **CP3-a** no longer contain C–H···N and C–H···O interactions which were involving solvent molecules in **CP2** and **CP3**. Instead, C–H···π hydrogen bonds which were absent in **CP2** and **CP3** are present in both new phases, in **CP2-a** methyl group (C20) act as their donors and benzene ring (C22-C26) as their acceptors, whereas in **CP3-a** both imidazole ring (N1-C5) and methyl group (C6) act as their donors and benzene ring (C8-C12) as acceptors. π-π interactions are present between imidazole rings in both the cases like in **CP2** and **CP3** which are as follows: between (N1-C5) imidazole rings at a distance of 3.4121(5) Å, symmetry operator 2-x,1-y,1-z and between (N15-C19) imidazole rings at a distance of 3.3874(5) Å, symmetry operator 1-x,1-y,1-z for **CP2-a**, as well as between (N1-C5) imidazole rings at a distance of 3.414(7) Å, symmetry operator 1-x,1-y,1-z for **CP3-a**. There are also some new C–H···Cl interactions (Table S2).

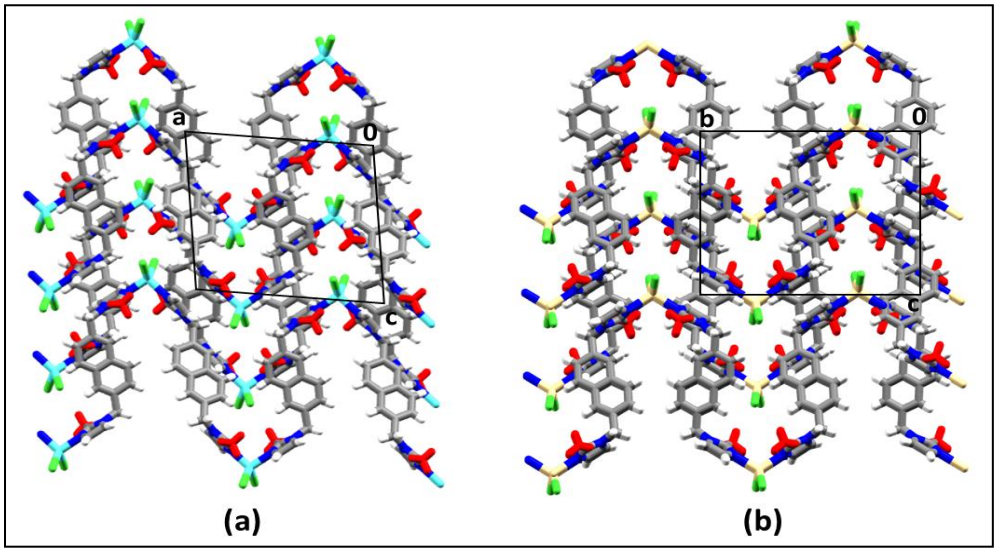

Figure 109: ***(a)** Packing diagram of **CP2-a** shown along the b-axis; **(b)** packing diagram of **CP3-a** shown along the a-axis; methyl groups are shown in red.*

Crystal Explorer was designed specifically for analyzing molecular crystals. However, it can also generate valuable comparative information by analysing equivalent molecular units in structurally related one-dimensional frameworks. Therefore, the input of intermolecular interactions stabilizing the structures of **CP2-a** and **CP3-a** was also estimated by Hirshfeld surface analysis using Crystal Explorer which showed the dominancy of H···H and C···C contacts in **CP2-a** whereas the dominance of H···Cl and H···C contacts in **CP3-a** (Figure 110), which agrees with the data of the structural analyses tabulated in Table S2.

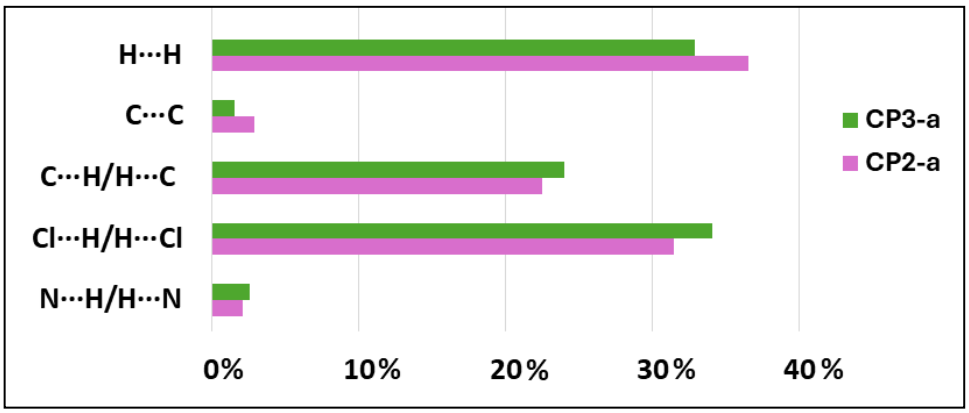

Figure 110: *Estimated contributions of selected intermolecular forces stabilizing the formation of **CP2-a** and **CP3-a**.*

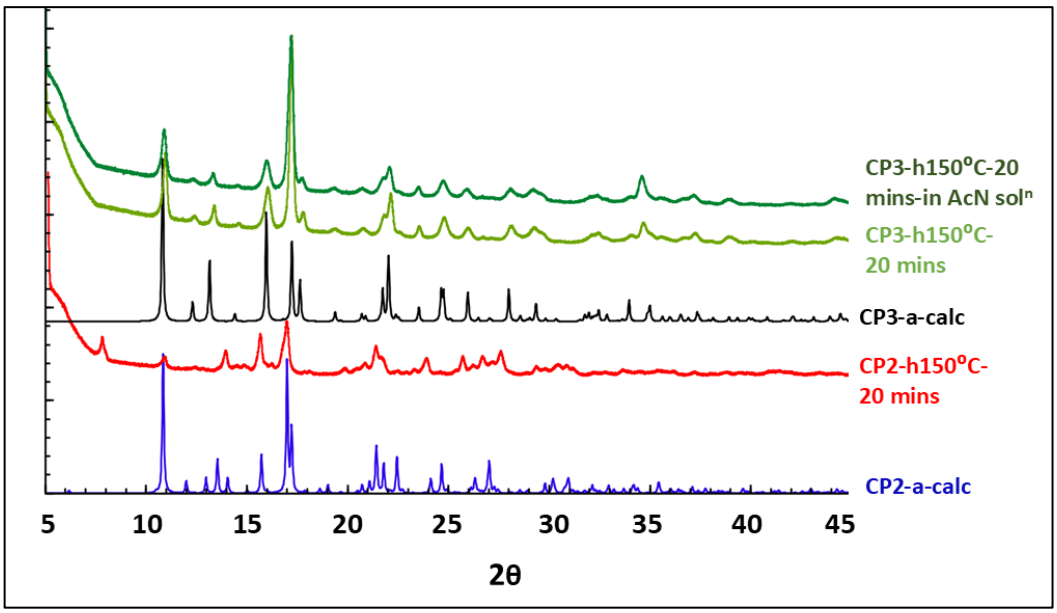

Figure 111: *Comparison of the calculated and experimental PXRD patterns of **CP2-a, CP3-a** and bulk sample upon heating, respectively.*

The transformations were also followed in bulk for both **CP2** and **CP3** using powder X-ray diffraction (PXRD). The PXRD patterns obtained upon heating the bulk

samples of **CP2** and **CP3** match with simulated **CP2-a** and **CP3-a** patterns, indicating the conversion of **CP2** and **CP3** to **CP2-a** and **CP3-a**, respectively (Figure 111). Moreover, the transformation is irreversible as the patterns do not change even after placing **CP2-a** or **CP3-a** in acetonitrile solution overnight.

Reports of conformational single-crystal to single-crystal (SC-SC) transformations in one-dimensional coordination polymers (1D CPs) are relatively scarce. Most studies rely on bulk characterization techniques like PXRD or focus on structural changes involving bond formation and cleavage, rather than purely conformational changes [142, 152]. The examples discussed here represent rare instances of conformational SC-SC transformations in 1D CPs. These findings are crucial for designing materials with tailored properties and selective applications.

12.2.2.4. Porosity Studies

Although the structures after desolvation are not conventionally porous, they still exhibit discrete voids which could indicate permeability to small molecular entities. Similar phenomena was reported previously for coordination polymers [166-168], however, none of them were 1D CPs. Furthermore, the molecules show dynamic behaviour in the crystals. To explore their potential as porous materials, we exposed bulk samples of **CP2-a** and **CP3-a** to various gases and water vapors. Sorption isotherms for H_2, CO_2, H_2O, and CH_4 were measured gravimetrically at room temperature.

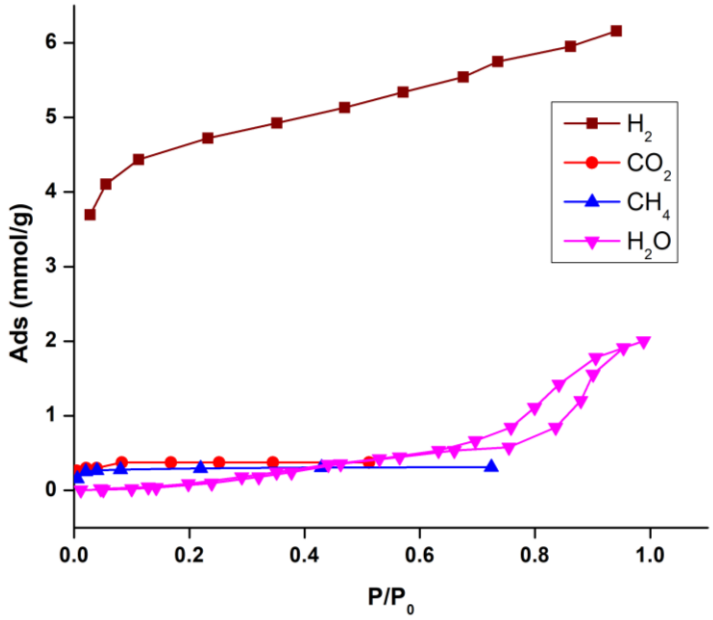

Figure 112: *H_2, CO_2, CH_4, and H_2O sorption isotherms recorded at room temp for* ***CP2-a****.*

Interestingly both structures exhibited different behaviors in their gas uptake properties. Both didn't adsorb any CO_2 and CH_4, but they show an affinity for H_2 and display type I isotherm, a characteristic of microporous structures, with a maximum uptake of 6.16 mmol/g corresponding to approximately 1.23 wt% in the case of **CP2-a** (Figure 112), and much lower uptake in case of **CP3-a** with a value of 2.9 mmol/g corresponding to 0.54 wt% (Figure 113). Current MOFs show impressive H_2 storage capacities at cryogenic temperatures (77 K), with examples such as MOF-210 [225] and NU-100 [226] achieving up to 17.6 wt% and 16.4 wt%, respectively, under high pressures. However, at ambient temperatures (298 K), their hydrogen uptake is significantly lower, typically below 2 wt% [227, 228]. To the best of my knowledge, to date, there are only two reports for 1D CPs reporting H_2 adsorption isotherms. The first, a permanently porous compound **[Ni(cyclam)(bpydc)]·5H₂O**, is composed of linear chains formed by the nickel–macrocyclic complex $Ni(cyclam)_2$ (cyclam = 1,4,8,11-tetraazacyclotetradecane) and 2,2′-bipyridyl-5,5′-dicarboxylate ($bpydc^{2-}$). This material exhibits H_2 uptake of **1.1 wt% at 77 K and 1 atm**, and undergoes a reversible single-crystal to single-crystal transformation upon dehydration and rehydration, accompanied by chromic changes [229]. The second example, solventless **$[Zn(phen)(SDC)]_n$**, where phen = 1,10-phenanthroline and H_2SDC = trans-4,4′-stilbenedicarboxylic acid, features a zig-zag chain structure with a polythreaded (entangled warp and-woof weaves) packing arrangement displaying narrow channels, and it demonstrates a a H_2 uptake of **0.49 wt% at 77 K and 1 atm** [230]. However, I couldn't find any reports of 1D CPs reporting H_2 adsorption isotherms at ambient temperature.

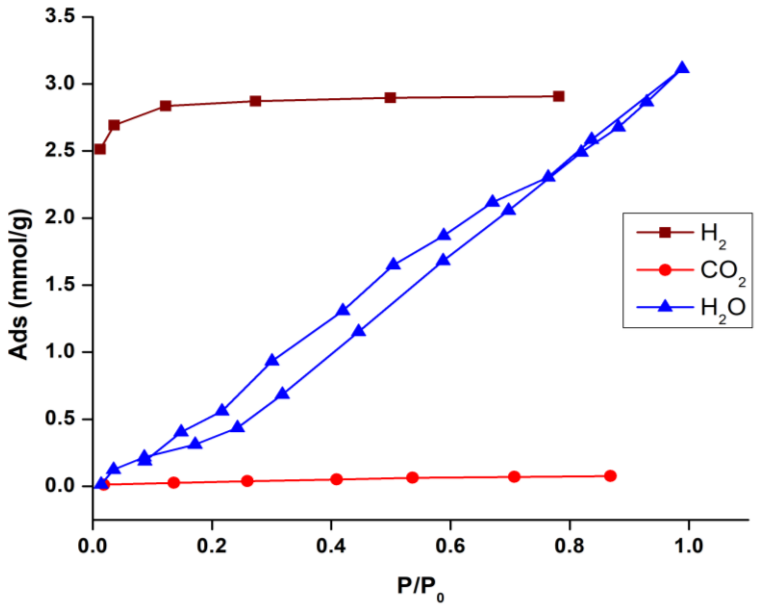

Figure 113: *H_2, CO_2, and H_2O sorption isotherms recorded at room temp for **CP3-a**.*

The different hydrogen uptakes for **CP2-a** and **CP3-a** once again highlight the differences in their crystal structures which clearly influence the adsorption capacity. Moreover, the difference in metal ions may also contribute to this effect.The Cu(II) based 1D coordination polymer (**CP2-a**) exhibit higher hydrogen adsorption compared to its Cd(II) based counterpart (**CP3-a**) probably due to the smaller ionic radius and higher charge density of Cu(II) (d^9 configuration versus d^{10} configuration) resulting in stronger polarizing power and enhanced interactions with H_2 molecules. Moreover, **CP2** and **CP3**, which were initially isostructural in their solvated forms, lose this structural similarity upon desolvation, resulting in distinct structures (**CP2-a** and **CP3-a**) with different pore environments. These differences likely influence how they interact with gas molecules and their hydrogen uptake capacities.Moreover, **CP2-a** and **CP3-a** also adsorbed water with a maximum uptake of approximately 2 mmol/g or 3.48 wt% and 3.11 mmol/g or 5.30 wt%, respectively, where both the isotherms display a hysteresis loop. Adsorption hysteresis occurs when the adsorption and desorption processes do not follow identical pathways, and there can be many reasons for this to happen, such as intrinsic framework flexibility, phase transitions, capillary condensation, or gas trapping within the pore apertures. In this case, we could attribute it to the intrinsic framework flexibility. Both compounds show high ligand flexibility, which enables dynamic structural adaptations that permit gas and water transport.

Section 3

Discussion and Concluding Remarks

"Every ending is a new beginning." – Marianne Williamson

Coordination bonds, known for their directionality and versatility, have emerged as powerful tool in designing crystalline frameworks, enabling the creation of diverse microporous systems. Our interest centered on leveraging coordination chemistry and crystal engineering to synthesize metallocycles that assemble in the solid state to form porous crystals. Based on previous studies [84-91], a key design feature in this approach was the formation of discrete metallocycles utilizing bipodal N-donor ligands, which often resist efficient packing in the solid state due to their irregular shapes. This characteristic can result in formation of voids or channels, and simultaneously potentially porous materials. Following the initial idea, a range of metallocycles was synthesized, crystallized and systematically analyzed towards porosity. However, my systematic studies revealed that certain factors limit the possibility of obtaining the bulk material which could be used for further porosity studies. The most important one being the formation of multiple products in the same complexation reaction. Controlling formation of the final product lies at the heart of crystal engineering and achieving precise control over the crystallization and self-assembly process remains a formidable task despite extensive research in designing controlled supramolecular architectures. However, the understanding of this phenomenon remains limited, making the rational design of crystal structures challenging. On the bright side, the lack of homogeneity allowed me to isolate 1D coordination polymers, which were also used in the studies on porosity and dynamics, extending our understanding of the behavior of related systems. Moreover, obtaining single crystals suitable for single-crystal X-ray diffraction analysis as well as crystals that can undergoe single-crystal to single-crystal transformations (maintain integrity upon subjecting to external stimuli) presents another significant hurdle. Sometimes crystals retain solvent molecules too strongly, preventing their effective exchange or removal or in some complete solvent removal was connected with melting or decomposition. However, despite the problems encountered, the set goals were achieved.

Evaluating the results in the context of the initial goals (see p.1):

1. Synthesis and characterization of the range of heterocyclic ligand was successfully performed **(L1-L12)**. Out of which 3 ligands **(L2**, **L3**, **L5)** were novel and used for the first time in obtaining metal-complexes. The ligands were crystallized allowing for further structural studies and and giving us some insight into the behavior of organic solid matter. Namely:
   a) The crystallization studies across the ligand series reveal two dominant phenomena: hydrate formation and polymorphism, each governed by distinct structural features. As it seems that ligand with rigid naphthalene core **L1: 2,7-bis(imidazol-1-ylmethyl)naphthalene** have tendency to form hydrates and ligands with flexible biphenyl core **L6: 4,4′-bis((1H-imidazol-1-yl)methyl)-1,1′-biphenyl, L8: 4,4′-bis((pyridin-4-yl)methyl)-1,1′-biphenyl, L11: 2,2′-bis((1H-imidazol-1-yl)methyl)-1,1′-biphenyl** to form polymorphs due to their higher conformational flexibility. The propensity for polymorphism correlates strongly with molecular flexibility. Ligands containing biphenyl spacers exhibit higher torsional degree of freedom, enabling alternative conformations that translate into distinct packing motifs. Conversely, ligands with rigid naphthalene core, show limited such structural diversity but readily accommodate water molecules in lattice voids, facilitating hydrate formation. This dichotomy highlights the importance of conformational adaptability in determining whether a ligand favors polymorphism or hydration.
   b) As could be expected across all ligands, dispersion forces constitute the primary stabilizing component of lattice energy, consistent with the aromatic nature of the ligands. However, the incorporation of water molecules introduces strong directional interactions, O–H···N and O–H···O hydrogen bonds and weak C–H···O interactions that significantly lower lattice energy and enhance thermodynamic stability of hydrates. Morever C–H···N and C–H···π hydrogen bonds which are present in anyhdrate form progressively diminish upon hydration. In polymorphic systems, tortional flexibility effects resulting C–H···N and C–H···π interactions and account for the diversity of packing arrangements. π–π stacking interactions appear selectively in polymorphs adopting planar conformations, suggesting that these interactions are secondary yet influential in stabilizing certain structures. The general trend of intermolecular interactions contributions in all the polymorphs of **L6, L8** and **L11** is in the order: H···H > C···H > N···H > C···C.

c) Thermal and PXRD analyses reveal that the most stable polymorphs predominate after heating or prolonged storage, whereas kinetically favored metastable polymorphs usually crystallize first in accordance with Ostwald's Rule of Stages.

d) The study on organic hydrates revealed that these are interesting group for vapour sorption studies. The reversible uptake and release of water observed in **L1** hydrates, coupled with the stepwise dehydration mechanism, a feature of type V isotherms commonly associated with hydrophobic porous materials. Such profiles indicate weak sorbent–water interactions at low humidity, followed by cooperative adsorption driven by water–water hydrogen bonding and capillary condensation within lattice voids. This mechanism is advantageous for applications where controlled uptake at high humidity is desired, such as indoor humidity regulation, and study on **L1** hydrate indicate potential for such sorption behavior and the future studies could go in this direction.

2. The range of metallocycles utilizing imidazole-based ligands of different aromatic core length and rigidity, as well as substituents on imidazole moieties with application of a variety of 3d transition metal salts was synthesized and successfully crystallised:

a) naphthalene core-based ligands (2 metallocycles) $[Cu_2(\mathbf{L2})_2Cl_4]\cdot xS$ **(MC1)** and $[Co_2(\mathbf{L3})_2Cl_4]\cdot 0.8CH_3CN$ **(MC2)**.

b) partially embedded anthracene moiety based (3 metallocycles) $[Co_2(\mathbf{L4})_2Cl_4]\cdot CH_3CN$ **(MC3)**, $[Co_2(\mathbf{L4})_2Br_4]\cdot 4CH_3CN$ **(MC4)**, $[Co_2(\mathbf{L5})_2Br_4]$ **(MC5)**.

c) biphenyl-based ligands (7 metallocycles) $[Cu_2(\mathbf{L6})_2Cl_4]\cdot xS$ **(MC6)**, $[Zn_2(\mathbf{L6})_2Cl_4]\cdot xS$ **(MC7)**, $[Cd_2(\mathbf{L7})_2Cl_4]\cdot 2MeOH$ **(MC8)**, $[Cu_2(\mathbf{L9})_2Cl_4]\cdot CH_2Cl_2$ **(MC9)**, $[Zn_2(\mathbf{L9})_2Cl_4]\cdot xS$ **(MC10)**, $[Zn_2(\mathbf{L10})_2(Cl)_4].4DMF$ **(MC11)** and $[Zn_2(\mathbf{L10})_2(Cl)_4].1DMF$ **(MC12)**.

A unifying feature among all the obtained metallocycles as anticipated in our strategy is their tendency to stack to form channels or discrete voids that encapsulated solvent molecules where the host molecules are stabilized by non-covalent interactions such as weak hydrogen bonds, such as C–H···Cl, C–H···N and C–H···π along with π-π interactions. However, the crystallization step seems to be challenging in case of ligands core containing more aromatic rings. The primary reason is their low solubility, which makes it difficult to achieve supersaturation, a prerequisite for successful crystallization. Attempts to improve solubility through

high-temperature dissolution followed by slow cooling often result in crystals that lack stability. This instability was evident in the case of **MC4** and **MC5**, which form irregularly shaped metallocycles and degrade rapidly outside solution. These observations suggest that the increased van der Waals forces in highly aromatic systems may lead to unfavorable packing arrangements, promoting amorphous or disordered solids rather than well-defined crystalline phases.

Morever some 1D coordination polymers were isolated during the synthesis of metallocycles: $\{[Co(L3)Cl_2]\}_n$ **(CP1)**, $Cu(L3)Cl_2]\cdot CH_3CN\}_n$ **(CP2)** and $\{[Cd(L3)Cl_2]\cdot CH_3CN\cdot 0.2H_2O\}_n$ **(CP3)**.

3. Studies encompassing the systematic investigation of the factors that influence the formation of particular supramolecular architectures (e.g. the effects of altering solvent, counterions etc.) were performed on organic ligands as well as on metal-complexes and the results can be find in the sections 11 and 12 respectively:

The results show that:

a) In case of the ligands containing naphthalene core: the solvent as well as crystallisation conditions do not effect too big extent the final products – the mixture of products is observed from almost all the solvents. In case of the ligands containing biphenyl core: solvent directs crystallisation, and changing it can lead to the formation of a new polymorph. Certain solvents stabilize metastable forms that later convert to thermodynamically favored phases upon heating or aging.

b) In case of the metal-complexes:

The **solvent** has huge influence on the final products formation. For example it can lead to the dimensionality change. Reaction of 2,7-bis(2-methylimidazol-1-ylmethyl)naphthalene **(L3)** with $CoCl_2\cdot 6H_2O$ in equimolar amount in acetonitrile resulted in the formation of 0D metallocycle (**MC2**). However, performing a similar reaction in a different solvent system ($CHCl_3$:MeOH) resulted in a 1D zig-zag chain coordination polymer (**CP1**).

The **metal ions** – if they have similar geometrical preferences they lead to formation of isostructural systems as shown in case of products of the complexation reaction of **L3** with $CuCl_2\cdot 6H_2O$ and $CdCl_2\cdot 2.5H_2O$ leading to 1D coordination polymers **CP2** and **CP3**, respectively. They can also show similar molecular structures and changes in packing as shown for **MC6** and **MC7**.

Ligand core modifications: Introducing ligand cores with a higher degree of aromaticity significantly influenced the nature of supramolecular architectures formed. Ligands **L3** and **L4** containing additional aromatic rings tend to produce metallocycles stabilized predominantly by π-π stacking interactions further supported by C–H···Cl/Br interactions, while the contribution of other directional interactions such as C–H···N and C–H···π becomes less pronounced. This shift reflects the dominance of dispersion forces and stacking interactions in highly aromatic systems.

Moreover, incorporating flexible cores, such as biphenyl units, imparts substantial conformational freedom to the ligand, enabling dynamic structural rearrangements within the crystal lattice of the metallocycles. These systems exhibit remarkable adaptability, as evidenced by single-crystal to single-crystal transformations and significant changes in packing upon desolvation (case of **MC8** and **MC10)**. While this flexibility supports the formation of more dynamic metallocycles, it also introduces challenges such as non-homogeneity in bulk samples. Metalocycles based on these flexible ligands are primarily stabilized by C–H···Cl and C–H···π interactions with limited π-π interactions.

In contrast, ligands with rigid core (e.g., naphthalene) favor the formation of metallocycles which packing is dominated via C–H···N forces. There are also π-π interactions. These systems show less dynamic behavior compared to the metallocycles based on flexible biphenyl core ligands, but offer homogeniety and structural integrity.

Changes in ligand substituents: It seems that substitution on the imidazole ring can effect packing efficiency for example introducing a methyl group into the benzimidazole moiety of the ligand in **MC5** results in a differently shaped metallocycle with a denser packing compared to **MC4**, which contains ligand with unsubstituted benzimidazole. Notably, the crystal structure of **MC5** lacks any included solvent molecules, in contrast to **MC4**, suggesting that the methyl substitution not only enhances lattice efficiency but also reduces the need for solvent stabilization.

The counterions effect: **MC4** was obtained by applying the different counterion Br^- instead of Cl^- as in **MC3** and it resulted in a differently shaped metallocycle as a result of different conformation of the ligand. The packing shows similar columnar motive along *a*-axis in both **MC3** and **MC4**. However, in case of **MC4** solvent molecules take the interstitial space, while they are located inside of the metallocycles in **MC3**.

4. Dynamics and sorption studies were performed on the selected crystalline material.

Structural dynamics was studied for $[Co_2(\mathbf{L3})_2Cl_4]\cdot 0.8CH_3CN$ **(MC2)**, $[Cd_2(\mathbf{L7})_2Cl_4]\cdot 2MeOH$ **(MC8)**, and $[Zn_2(\mathbf{L9})_2Cl_4]\cdot xS$ **(MC10)**, whereas sorption studies were performed for metallocycles: **MC2**, $[Zn_2(\mathbf{L6})_2Cl_4]\cdot xS$ **(MC7)**, $[Cu_2(\mathbf{L9})_2Cl_4]\cdot CH_2Cl_2$ **(MC9)**, and 1D coordination compounds: $Cu(L3)Cl_2]\cdot CH_3CN\}_n$ **(CP2)** and $\{[Cd(L3)Cl_2]\cdot CH_3CN\cdot 0.2H_2O\}_n$ **(CP3)**.

Dynamics: Performed studies revealed a lot of dynamics taking place in the crystals of metallocycles based on the imidazole derivative bipodal ligands. The metallocycles can undergo notable ligand conformational changes upon solvent loss; however, the extent of these changes depends strongly on ligand flexibility. For example, **MC2**, constructed from a rigid naphthalene-core ligand, exhibits minor conformational adjustments, and phases such as **MC2** and **MC2-a** retain similarities at the three-dimensional level. In contrast, metallocycles incorporating flexible biphenyl-core ligands, such as **MC8** and **MC10**, display significant conformational changes upon transformations. The metallocycle **MC8** adopted a bent conformation of the ligands relative to each other upon transformation to **MC8-a**. This structural shift driven by a significant conformational change in the ligand, ultimately resulted in a differently packed, non-porous metallocycle. Even more striking is the SC–SC transformation observed in **MC10**, where the ligand shifts from a C-shaped to an S-shaped conformation upon conversion to **MC10-a**, accompanied by a complete rearrangement of the packing motif. These results clearly demonstrates that the metallocycles incorporating flexible biphenyl core ligands, exhibit a remarkable ability to tolerate more substantial conformational changes compared to the metallocycles based on ligands with a rigid naphthalene core. These results are in agreement with earlier observations on ligand behavior, where biphenyl systems exhibit high conformational freedom and polymorphic tendencies. Interestingly, reports on single-crystal to single-crystal (SC–SC) transformations in dinuclear metallocycles during processes such as guest removal or substitution are relatively uncommon. This rarity stems from the fact that such transformations typically involve significant lattice rearrangements due to ligand reorientation, and one would expect that this would result in sufficient mechanical strain to fracture the crystal. Therefore, it is fascinating that desolvation occurs as single-crystal to single-crystal transformations withstanding such significant conformational changes. This phenomenon suggests that a high degree of cooperative motion among the molecules within the crystal must happen to preserve packing continuity in order to accomodate such large conformational changes. Consequently, it can be inferred that metallocycles featuring

flexible biphenyl-core based ligands possess a superior capacity to accomodate drastic structural changes without compromising their monocrystallinity. However, this flexibility also introduces challenges, as metallocycles based on biphenyl cores often suffer from non-homogeneity as seen in the case of **MC6**, **MC10, MC11** and **MC12**.

From a crystal engineering perspective:

- **Rigid cores (naphthalene)** favor structural integrity and reproducibility but limit dynamic adaptability.
- **Flexible cores (biphenyl)** enable dynamic responses and potential for stimuli-responsive materials, but require strategies to mitigate the phase control.

Sorption: Two of the metallocycles demonstrated measurable sorption behaviour. **MC2** shows selective CO_2 uptake (2.11 wt%, ambient conditions) despite having no channels in the structure, revealing so called transient porosity of this system. **MC7** on the other hand shows lower CO_2 uptake (1.42 wt%) however above average uptake of H_2 approximately 4 mmol/g or 0.80 wt%.

Two of 1D coordination polymers **CP2-a** and **CP3-a** also revealed sorption properties. These materials do not adsorb CO_2 as mentioned above metallocycles, but they show H_2 and H_2O uptake. The study revealed that H_2 uptake for **CP2-a** is among the highest reported numbers **in ambient conditions (1.23 wt%).** This affinity towards hydrogen is not so strong in case of **CP3-a** (0.54 wt%), highlighting the influence of metal ions and different structures of **CP2-a** and **CP3-a** on adsorption properties. **CP3-a** demonstrated higher water adsorption (5.30 wt%) than **CP2-a** (3.48 wt%), with both materials exhibiting hysteresis which once again could be related to different structures of **CP2-a** and **CP3-a** and how they interact with H_2O molecules. Similar to **MC1**, these structures adsorb H_2 and H_2O despite the absence of continuous channels, demonstrating transient porosity, which enables guest transport without permanent pores, relying on the flexibility of the host material to facilitate guest molecule diffusion.

Hydrogen gas stands out due to its high energy density, non-toxicity, and abundance [231]. Metal-organic frameworks (MOFs) have emerged as promising materials for hydrogen storage, thanks to their high surface area, tunable porous structures, and chemical stability [232-236]. Despite extensive research, only a few MOFs have been investigated to meet the U.S. Department of Energy's (DOE) 2025 criteria for hydrogen storage at room temperature and low pressures, which are 5.5 wt% (gravimetric) and 40 g/L (volumetric) [237]. To enhance hydrogen adsorption at room temperature, strategies such as modifying

metal centers, organic ligands, and counter-ions in MOFs have shown promise, improving adsorption interactions (isosteric heat of adsorption, Qst) to the ideal range of −15 to −25 kJ/mol [230, 238-240]. Despite these advancements, practical hydrogen storage remains challenging due to the current reliance on cryogenic temperatures or high pressures, limiting widespread adoption in transportation and other sectors. To date, no metal-organic materials have reached DOE's benchmark under near ambient conditions. In fact, 0D MCs, similar to the one described in this thesis, as well as 1D CPs and 3D MOFs, have not even reached hydrogen uptake above 2 wt% at near-ambient temperatures. See some as synthesized representative examples in table 29 that are reported in the literature to show highest uptakes from early 20s till date. Several strategies were employed to improve the sorption in some of these potential materials: **a)** incorporating a metal catalyst for hydrogen spillover with a MOF, for example IRMOF8 has been reported to have a hydrogen gravimetric uptake of just 0.5 wt% at 298 K and 100 bar but after combing with a Pt supported by activated carbon a response of 1.5 wt. % was observed. Further improvement with IRMOF-8 was achieved by forming a bridge between the activated carbon and MOF providing 4.0 wt% at same conditions [241]; **b)** post synthetic doping of MOFs with alkali metals, for instance a report in 2017 showed computationally that doping IRMOF-9 with Li^+ could substantially increased near-ambient hydrogen storage from just ~0.35 wt.% to ~4.5 wt. % at 298 K and 100 bar [242]; **c)** incorporation of open metal sites, an example of this was reported in 2021, $V_2Cl_{2.8}$(bttd) comprising of both saturated V(III) and unsaturated V(II) open sites shows one of the highest reported volumetric and gravimetric performance of 10.7 g/L and 1.64 wt% for H_2 at 298 K and100 bar and it was revealed that it is because of so-called Kubas interaction between he vanadium d_π and H_2 σ* orbital [243]. However, frameworks with open metal sites often face challenge of air sensitivity.

Developing cost-effective materials with higher gravimetric capacity and fast adsorption–desorption kinetics under ambient conditions could revolutionize hydrogen-based energy technologies. Given **CP2-a's** very promising hydrogen uptake at room temperature, further optimization through ligand modifications and alternative metal centers could enhance its potential for hydrogen storage applications. Future studies, including low-temp and high-pressure isotherms, DFT calculations or Monte Carlo simulations, and stability assessments, are necessary to determine its viability to improve H_2 storage [244]. Transitioning to renewable energy sources is critical for environmental sustainability and economic development.

Table 29: *List of selected metal-organic materials reporting H_2 sorption at near-ambient temperatures.*

Topo-logy	As-synthesized composition	Pore dimension	Sorption	Wt%	CSD refcode	Year	Ref
0D MCs	$[Ag_2(bib)_2](BF_4)_2 \cdot 2CH_3CN$	1D	H_2 (303 K)	1	DAMWIY	2005	85
1D CPs	$[Ni(cyclam)(bpydc)] \cdot 5H_2O$	1D	H_2 (77 K)	1.1	BEVYX	2004	229
	$[Zn(phen)(SDC)] \cdot DMSO$	1D	H_2 (77 K)	0.49	VOCSUC	2010	230
3D MOFs	IRMOF-8	-	H_2 (298 K)	0.5	-	2006	241
	MOF177	-	H_2 (298 K)	0.62	-	2007	245
	Cu^I-MFU-4l	-	H_2 (273 K)	0.34	JOJKOK	2014	246
	Ni_2(m-dobdc)	1D	H_2 (298 K)	0.98	KOSLUB	2018	247
	Ni50Co-IRMOF-74	1D	H_2 (298 K)	0.38	-	2019	248
	$V_2Cl_{2.8}$(bttd)	1D	H_2 (298 K)	**1.64**	OQETUC	2021	243

CP2 and **CP3** also shows dynamics in the crystal. Isostructural **CP2** and **CP3** upon heating result in the desolvated non-porous forms, **CP2-a** and **CP3-a** which are not isostructural. The transformations from **CP2** and **CP3** to **CP2-a** and **CP3-a**, respectively result in the significant change in the ligand's conformation as a result of the rotation of one of the 2-methylimidazole groups within a ligand. In both **CP2-a** and **CP3-a**, the methyl groups of the two coordinated 2-methylimidazole groups from the different ligands are oriented opposite to each other, which in the case of **CP2** and **CP3** are pointing in the same direction. This process kind of explains the guest diffusion without having continuous channels enabled by flexibility of the host material.

5. Studying how modification of the ligands relates to their sorption properties was conducted in the limited scope based on the results obtained. The compounds containing biphenyl core gain on the flexibility however even in the compound containing naphthalene core transient porosity was noticed. **MC7** and **MC9** show presence of biphenyl cores but differ via metal ions and imidazole derivatives. The metal ions exhibit similar coordination geometries; however, the introduction of more bulky benzimidazole units most likely leads to a loss of flexibility and preventing hosts molecules to cooperate in a dynamic and concerted fashion within the crystals to enable guest diffusion through closed pores. It can be concluded that flexible cores offer greater potential for structural transformations, but excessive bulk can negate this advantage.

Obtained results highlight that responsive crystalline materials based on 0D MCs and 1CPs hold great potential like their 2D and 3D counterparts and provide a foundation for the next-

generation porous materials. However, guest transport through discrete voids (closed pores) in crystalline solids is poorly understood and more systematic studies further in this direction are required to understand the underlying mechanisms governing their structural adaptability and to fully explore their potential in these areas. The presented work shown that imidazole-based ligands containing a rigid core, such as naphthalene could be promising candidates for constructing transiently porous metallocycles and 1D coordination polymers (CPs) suitable for small molecules adsorption. Future studies should explore the use of ligands with larger rigid cores, such as phenanthrene, in combination with various substituted imidazole's, to design porous metallocycles and CPs in combination with different metal salts, and varying metal-to-ligand ratios. Moreover, imidazolyl-based ligands with a flexible core also showed great potential for forming potentially porous metallocycles and can withstand more substantial conformational changes upon exposure to external stimuli, provided that precise control over crystallization product could be achieved which is still like "finding a needle in a haystack" and also using suitable building blocks allowing for the hosts molecules to cooperate in a dynamic and concerted fashion within the crystals to enable guest diffusion through closed pores. More systematic studies aimed at gaining this control and finding suitable ligands should be pursued, as they could unlock new applications in sensing, gas storage, and separation.

"*In many areas of chemistry, an X-ray single-crystal structure determination of a novel compound represents the solution to a particular problem, or the end of a specific project: the cynosure is usually the identity of the molecule itself, or some particular feature within its molecular structure. An alternative view, however, would be to treat the structural information as the beginning of a new venture, leading to questions of far reaching and fundamental importance regarding the interrelationships between molecules and ions in the solid state. Since the crystal structure represents a situation where all the bonding and nonbonding forces are poised at an energetic minimum (not necessarily a global minimum!), it contains all the information regarding the importance of, and balance between, intermolecular forces. If this information could be extracted and deconvoluted, then prospects of designing materials with specific properties would be vastly enhanced. Consequently, it is of great importance to improve our understanding of the forces that determine the structures of crystalline materials, and single-crystal data provide a natural starting point* [249].**"**

References:

[1] R. Pepinsky, *Phys. Rev.*, **1955**, 100, 971.
[2] G. M. J. Schmidt, *Pure Appl. Chem.*, **1971**, 27, 647.
[3] G. R. Desiraju, *Crystal Engineering, the Design of Organic Solids*, Elsevier, Amsterdam, **1989**.
[4] G. R. Desiraju, *Angew. Chem. Int. Ed. Engl.*, **1995**, 34, 2311–2327.
[5] B. Moulton, M. J. Zaworotko, *Chem. Rev.*, **2001**, 101, 1629–1658.
[6] G. R. Desiraju, *Angew. Chem. Int. Ed.*, **2007**, 46, 8342–8356.
[7] G. R. Desiraju, *J. Am. Chem. Soc.*, **2013**, 135, 9952–9967.
[8] M. J. Zaworotko, *Chem. Soc. Rev.*, **1994**, 23, 283–288.
[9] M. J. Zaworotko, L. R. MacGillivray, *Chem. Eur. J.*, ***2005***, 11, 401–410.
[10] G. R. Desiraju, J. J. Vittal, A. Ramanan, *Crystal Engineering: A Textbook,* World Scientific, **2011**.
[11] D. Braga, *Chem. Commun.*, **2003**, 2751–2754.
[12] M. Vasileiadis, C. C. Pantelides, C. S. Adjiman, *Chem. Eng. Sci.*, **2015**, 121, 60–76.
[13] M. K. Dudek, K. Drużbicki, *CrystEngComm*, **2022**, *24*, 1665–1678.
[14] R. Nikhar, K. Szalewicz, *Nat. Commun.*, **2022**, *13*, 3095.
[15] A. K. Nangia, G. R. Desiraju, *Angew. Chem. Int. Ed.*, **2019**, 58, 4100–4107.
[16] K. Biradha, C. Y. Su, J. J. Vittal, *Cryst. Growth Des.*, **2011,** 11, 875–886.
[17] C. B. Aakeröy, N. R. Champness, C. Janiak, *CrystEngComm*, **2010**, 12, 22–43.
[18] D. Braga, G. R. Desiraju, S. Miller, A. G. Orpen, S. L. Price, *CrystEngComm*, **2002**, 4, 500–509.
[19] D. Braga, F. Grepioni, *Chem. Commun.*, **2005**, 3635–3645.
[20] J. P. Brog, C. L. Chanez, A. Crochet, K. M. Fromm, *RSC Adv.*, **2013**, 3, 16905–16931.
[21] S. Aitipamula, R. B. H. Tan, "1. *Pharmaceutical co-crystals: crystal engineering and applications*". *Multi-Component Crystals: Synthesis, Concepts, Function*, edited by Edward Tiekink and Julio Zukerman, Berlin, Boston: De Gruyter, **2018**, pp. 1–31.
[22] G. Bolla, B. Sarma, A. K. Nangia, *Chem. Rev.*, **2022**, 122, 11514–11603.
[23] A. G. Shtukenberg, C. T. Hu, Q. Zhu, M. U. Schmidt, W. Xu, M. Tan, B. Kahr, *Cryst. Growth Des.*, **2017**, 17, 3562–3566.
[24] A. Schneemann, V. Bon, I. Schwedler, I. Senkovska, S. Kaskel, R. A. Fischer, *Chem. Soc. Rev.*, **2014**, 43, 6062.
[25] M. D. Allendorf, V. Stavila, *CrystEngComm*, **2015**, 17, 229.
[26] P. L. Garff, R. M. Losus, S. Chaudhary, L. Dobrzańska, *Acta Cryst.*, **2024**, B80, 19–26.
[27] A. Nangia, *J. Chem. Sci.*, **2010**, 122, 295–310.
[28] V. A. Adhav, K. Saikrishnan, *ACS Omega*, **2023**, 8, 22268–22284.
[29] A. Nangia, G. R. Desiraju, *Acta Cryst*., **1998**, A54, 934–944.
[30] A. Haque, K. M. Alenezi, M. S. Khan, W. Y. Wong, P. R. Raithby, *Chem. Soc. Rev.*, **2023**, 52**,** 454–472.
[31] G. R. Desiraju, *Comprehensive Supramolecular Chemistry, Vol. 6*, 1 ed. (Eds.: J. L. Atwood, J. E. D. Davies, D. D. MacNicol, F. Vögtle), Pergamon, Oxford, **1996**, pp. 1–22.
[32] G. R. Desiraju, *Acc. Chem. Res.*, **1991**, 24, 290–296.
[33] W. Wang, Y. Zhang, W. Liu, *Prog. Polym. Sci.* **2017**, 71, 1–25.
[34] F. H. Allen, J. E. Davies, J. J. Galloy, O. Johnson, O. Kennard, C. F. Macrae, E. M. Mitchell, G. F. Mitchell, J. M. Smith, D. G. Watson, *J. Chem. Inf. Comput. Sci.*, **1991**, 31, 187–204.

[35] F. H. Allen, O. Kennard, R. Taylor, *Acc. Chem. Res.*, **1983**, 16, 146–153.
[36] B. Venkataramanan, M. A. Saifudin, J. J. Vittal, V. Suresh, *CrystEngComm*, **2004**, 6, 284–289.
[37] J. M. Lehn, *Angew. Chem. Int. Ed. Engl.*, **1990**, 29, 1304–1319.
[38] G. R. Desiraju, *Cryst. Growth Des.*, **2011**, 11, 896–898.
[39] G. A. Jeffrey, W. Saenger, *Hydrogen Bonding in Biological Structure*, Springer-Verlag: Berlin, **1994**, p 29.
[40] A. Werner, *Z. Anorg. Allgem. Chem.*, **1893**, 3, 267–330.
[41] W. M. Latimer, W. H. Rodebush, *J. Am. Chem. Soc*., **1920**, 42, 1419–1433.
[42] L. Pauling, *The Nature of the Chemical Bond and the Structure of Molecules and Crystals An Introduction to Modern Structural Chemistry*, 2nd ed., Oxford University Press, London, **1940**.
[43] G. C. Pimentel, A. L. McClellan, *The Hydrogen Bond*, W. H. Freeman and Company, San Francisco, **1960**.
[44] P. W. Atkins, *Physical Chemistry*. Oxford University Press, London, **1989**.
[45] T. Steiner, *Angew. Chem. Int. Ed.*, **2002**, 41, 48–76.
[46] E. Arunan, G. R. Desiraju, R. A. Klein, J. Sadlej, S. Scheiner, I. Alkorta, D. C. Clary, R. H. Crabtree, J. J. Dannenberg, P. Hobza, H. G. Kjaergaard, A. C. Legon, B. Mennucci, D. J. Nesbitt, *Pure Appl. Chem.*, **2011**, 83, 1637–1641.
[47] J. L. Atwood, J. W. Steed, *Encyclopedia of Supramolecular Chemistry*, Vol 1&2, Marcel Dekker, Boca Raton, **2004**.
[48] J. W. Steed, D. R. Turner, K. Wallace, *Core Concepts in Supramolecular Chemistry and Nanochemistry*, Wiley, Chichester, **2007**.
[49] G. R. Desiraju, T. Steiner, T., *The Weak Hydrogen Bond in Structural Chemistry and Biology*. Oxford University Press, Oxford, **1999**.
[50] Z. Rahim, B. N. Barman, *Acta Cryst*., **1978**, A34, 761–764.
[51] G. A. Jeffrey, *An Introduction to Hydrogen Bonding*. Oxford University Press, Oxford, **1997**.
[52] R. Yamdagni, P. Kebarle, *J. Am. Chem. Soc.*, **1971**, 93, 7139–7143.
[53] S. Subramanian, M. J. Zaworotko, *Coord. Chem. Rev.*, **1994**, 137, 357–401.
[54] C. A. Hunter, K. R. Lawson, J. Perkins, C. J. Urch, *J. Chem. Soc., Perkin Trans.*, **2001**, 2, 651–669.
[55] E. A. Meyer, R. K. Castellano, F. Diederich, *Angew. Chem. Int. Ed.*, **2003**, 42, 1210–1250.
[56] R. Thakuria, N. K. Nath, B. K. Saha, *Cryst. Growth Des.*, **2019**, 19, 523–528.
[57] T. Chen, M. Li, J. Liu, *Cryst. Growth Des.*, **2018,** 18, 2765–2783.
[58] C. A. Hunter, J. K. Sanders, *J. Am. Chem. Soc.*, **1990**, 112, 5525–5534.
[59] J. H. Williams, J. K. Cockcroft, A. N. Fitch, *Angew. Chem. Int. Ed. Engl.*, **1992**, 31, 1655–1657.
[60] C. G. Claessens, J. F. Stoddart, *J. Phys. Org. Chem.*, **1997**, 10, 254–272.
[61] M. O. Sinnokrot, C. D. Sherrill, *J. Am. Chem. Soc.*, **2004**, 126, 7690–7697.
[62] S. E. Wheeler, K. N. Houk, *J. Am. Chem. Soc.*, **2008**, 130, 10854–10855.
[63] M. O. Sinnokrot, C. D. Sherrill, *J. Phys. Chem. A*, **2006**, 110, 10656–10668.
[64] L. M. Salonen, M. Ellermann, F. Diederich, *Angew. Chem. Int. Ed.*, **2011**, 50, 4808–4842.
[65] R. G. Huber, M. A. Margreiter, J. E. Fuchs, S. von Grafenstein, C. S. Tautermann, K. R. Liedl, T.Fox, *J. Chem. Inf. Model.*, **2014**, 54, 1371–1379.
[66] C. Janiak, *J. Chem. Soc., Dalton Trans.*, **2000**, 21, 3885-–3896.
[67] H. Li, X. Zhang, W. Zu, *J. Appl. Phys.*, **2014**, 115, 054510.

[68] W. Yu, X. Y. Wang, J. Li, Z. T. Li, Y. K. Yan, W. Wang, J. A. Pei, *Chem. Commun.*, **2013**, 49, 54–56.
[69] L. Liu, J. Hao, Y. Shi, J. Qiu, C. Hao, *RSC Adv.*, **2015**, 5, 3045–3053.
[70] S. Shanmugaraju, P. S Mukherjee, *Chem. Commun.*, **2015**, 51, 16014-16032.
[71] F. London, *Trans. Faraday Soc.*, **1937**, 33, 8b–26.
[72] A. Stone, *The Theory of Intermolecular Forces (2nd ed.)*, Oxford University Press, Oxford, **2013**.
[73] J. W. Steed, J. L. Atwood, *Supramolecular Chemistry (3rd ed.)*, John Wiley & Sons, **2022**.
[74] A. Y. Robin, K. M. Fromm, *Coord. Chem. Rev.*, **2006**, 250, 2127–2157.
[75] S. R. Batten, S. M. Neville, D. R. Turner, *Coordination Polymers: Design, Analysis and Application*, The Royal Society of Chemistry, **2008**.
[76] S. Henke, *Metal-Organic Frameworks with Additional Flexible Substituents – Modulating Responsiveness, Gas Sorption Selectivity & Network Topologies*, **2011**.
[77] A. Werner, *Z. Anorg. Allg. Chem.* **1893**, *3*, 267–330.
[78] E. C. Constable, C. E. Housecroft, *Chem. Soc. Rev.*, **2013**, 42, 1429–1439.
[79] T. R. Cook, P. J. Stang, *Chem. Soc. Rev.*, **2015**, 115, 7001−7045.
[80] L. J. Chen, H. B. Yang, *Acc. Chem. Res.*, **2018**, 51, 2699–2710.
[81] B. Li, T. He, Y. Fan, X. Yuan, H. Qiu, S. Yin, *Chem. Commun.*, **2019**, 55, 8036–8059.
[82] B. Therrien, *Chem.*, **2020**, 2, 565–576.
[83] C. Yin, J. Du, B. Olenyuk, P. J. Stang, Y. Sun, *Inorganics*, **2023**, 11, 54.
[84] V. I. Nikolayenko, L. J. Barbour, A. Arauzo, J, Campo, J. M. Rawson, D. A. Haynes, *Chem. Commun.*, **2017**, 53**,** 11310–11313.
[85] L. Dobrzańska, G. O. Lloyd, H. G. Raubenheimer, L. J. Barbour, *J. Am. Chem. Soc.*, **2005**, 127, 13134–13135.
[86] L. Dobrzańska, G. O. Lloyd, H. G. Raubenheimer, L. J. Barbour, *J. Am. Chem. Soc.*, **2006**, 128, 698–699.
[87] L. Dobrzańska, G. O Lloyd, C. Esterhuysen, L. J. Barbour, *Angew. Chemie - Int. Ed.* **2006**, 45, 5856– 5859.
[88] T. Jacobs, G. O. Lloyd, J. A. Gertenbach, K. K. Müller-Nedebock, C. Esterhuysen, L. J. Barbour, *Angew. Chemie - Int. Ed.*, **2012**, 51, 4913–4916.
[89] T. Jacobs, L. J. Barbour, *CrystEngComm*, **2013**, 15, 1512–1514.
[90] V. I. Nikolayenko, A. Heyns, L. J. Barbour, *Chem. Commun.*, **2017**, 53, 11306–11309.
[91] M. D. Plessis, V. I. Nikolayenko, L. J. Barbour, *J. Am. Chem. Soc.*, **2020**, 142, 4529–4533.
[92] L. J. Chen, Y. Y. Ren, N. W. Wu, B. Sun, J. Q. Ma, L. Zhang, H. Tan, M. Liu, X. Li, H. B. Yang, *J. Am. Chem. Soc.*, **2015**, 137, 11725–11735.
[93] L. J. Barbour, *Chem. Commun.*, **2006**, 1163–1168.
[94] M. Fujita, J. Yazaki, K. Ogura, *J. Am. Chem. Soc.*, **1990,** 112, 5645–5647.
[95] B. Chatterjee, J. C. Noveron, M. J. E. Resendiz, J. Liu, T. Yamamoto, D. Parker, M. Cinke, C. V. Nguyen, A. M. Arif, P. J. Stang, *J. Am. Chem. Soc.*, **2004**, 126, 10645–10656.
[96] L. Dobrzańska , G. O. Lloyd, L. J. Barbour, *New. J. Chem.*, **2007**, 31, 669–676.
[97] J. Alen , L. V. Meervelt , W. Dehaen, Liliana Dobrzańska, *CrystEngComm*, **2015**, 17, 8957–8964.
[98] M. D. Plessis, V. I. Nikolayenko, L. J. Barbour, *Inorg. Chem.*, **2018**, 57, 12331–12337.
[99] G. Gupta, J. Lee, R. Hadiputra, J. Jung, P. J. Stang, C. Y. Lee, *J. Am. Chem. Soc.*, **2024**, 146, 30222–30230.
[100] X. W. Zhu, D. Luo, X. P. Zhou, D. Li, *Coord. Chem. Rev.*, **2022**, 455, 214354.

[101] M. Arhangelskis, L. Van Meervelt, L. Dobrzańska, *CrystEngComm*, **2021**, 23, 317–323.
[102] L. Dobrzańska, *Materials*, **2021**, 14, 1–9.
[103] S. Chaudhary, D. Kędziera, L. Dobrzańska, *Polyhedron*, **2022**, 224, 115989.
[104] R. M. Losus, S. Chaudhary, L. Dobrzańska, *Crystals*, **2024**, 14, 248.
[105] L. Dobrzańska, D. J. Kleinhans, L. J. Barbour, *New J. Chem.*, **2008**, 32, 813–819.
[106] J. Zhao, J. Yuan, Z. Fang, S. Huang, Z. Chen, F. Qiu, C. Lu, J. Zhu, X. Zhuang, *Coord. Chem. Rev.*, **2022**, 471, 214735.
[107] W. L. Leong,J. J. Vittal, *Chem. Rev.*, **2011**, 111, 688–764.
[108] M. Lippi, M. Cametti, *Coord. Chem. Rev.*, **2021**, 430, 213661.
[109] J. Martí-Rujas, *Materials*, **2019**, *12*, 4088.
[110] E. Loukopoulos, G. E. Kostakis, *J. Coord. Chem.*, **2018**, 71, 371–410.
[111] F. Ahmed, B. Dutta, M. H. Mir, *Dalt. Trans.*, **2021**, 50, 29–38.
[112] Y. Dai, G. Zhang, Y. Peng, Y. Li, H. Chi, H. Pang, *Adv. Colloid Interface Sci.*, **2023**, 321, 103022.
[113] M. Tran, K. Kline, Y. Qin, Y. Shen, M. D. Green, S. Tongay, *Appl. Phys. Rev.*, **2019**, 6, 04131.
[114] G. Chakraborty, I. H. Park, R. Medishetty, J. J. Vittal, *Chem. Rev.*, **2021**, 121, 3751–3891.
[115] L. P. Tang, S. Yang, D. Liu, C. Wang, Y. Ge, L. M. Tang, R. L. Zhou, H. Zhang, *J. Mater. Chem. A*, **2020**, 8, 14356–14383.
[116] H. C. J. Zhou, S. Kitagawa, *Chem. Soc. Rev.*, **2014**, 43, 5415.
[117] S. Kitagawa, S. Kaskel, Q. Xu, *Small Struct.*, **2022**, 3, 2200072.
[118] O. M. Yaghi, M. O'Keefe, N. W. Ockwig, H. K. Chae, M. Eddaoudi, J. Kim, *Nature*, **2003**, 423, 705.
[119] T. Jia, Y. Gu, F. Li, *J. Environ. Chem. Eng.*, **2022**, 10, 108300.
[120] L. Jiao, Y. Wang, H. L. Jiang, Q. Xu, *Adv. Mater.*, **2018**, 30, 1–23.
[121] H. D. Lawson, S. P. Walton, C. Chan, *ACS Appl. Mater. Interfaces*, **2021**, 13, 7004–7020.
[122] P. Kumar, A. Deep, K.-H. Kim, *TrAC Trends Anal. Chem.*, **2015**, 73, 39–53.
[123] O. K. Farha, I. Eryazici, N. C. Jeong, B. G. Hauser, C. E. Wilmer, A. A. Sarjeant, R. Q. Snurr, S. T. Nguyen, A. Ö. Yazaydin, J. T. Hupp, *J. Am. Chem. Soc.*, **2012**, 134, 15016–15021.
[124] S. R. Batten, N. R. Champness, X. M. Chen, J. Garcia-Martinez, S. Kitagawa, L. Öhrström, M. O'Keeffe, M. P. Suh, J. Reedijk, *Pure Appl. Chem.*, **2013**, 85, 1715–1724.
[125] G. Maurin, C. Serre, A. Cooper, G. Férey, *Chem. Soc. Rev.*, **2017**, 46, 3104–3107.
[126] J. Bernstein, *Cryst. Growth Des.*, **2011,** 11, 632–650.
[127] A. J. Cruz-Cabeza, J. Bernstein, *Chem. Rev.*, **2014**, 114, 2170–2191.
[128] A. J. Cruz-Cabeza, S. M. Reutzel-Edens, J. Bernstein, *Chem. Soc. Rev.*, **2015**, 44, 8619–8635.
[129] R. Hilfiker, M. V. Raumer, *Polymorphism in the Pharmaceutical Industry: Solid Form and Drug Development*, Wiley-VCH Verlag GmbH & Co. KGaA, **2018,** 1–30.
[130] J. P. Zhang, X. C. Huang, X. M. Chen, *Chem. Soc. Rev.*, **2009**, 38, 2385–2396.
[131] IUCr. Available online: http://reference.iucr.org/dictionary/Isostructural_crystals
[132] A. Kálmán, L. Párkányi, G. Argay, *Acta Cryst.*, **1993**, B49, 1039–1049.
[133] L. Fábián, A. Kálmán, *Acta Cryst.*, **1999**, B55, 1099–1108.

[134] A. Kálmán, *In Fundamental Principles of Molecular Modeling*; (Ed: W. Gans), Plenum Press, New York, NY, USA, **1996**, p. 209.
[135] P. Bombicz, *IUCrJ*, **2024**, 11, 3–6.
[136] A. M. Healy, Z. A. Worku, D. Kumar, A. M. Madi, *Adv. Drug Deliv. Rev.*, **2017**, 117, 25–46.
[137] S. Horike, S. Shimomura, S. Kitagawa, *Nat. Chem.*, **2009**, 1, 695–704.
[138] S. Krause, N. Hosono, S. Kitagawa, *Angew. Chemie - Int. Ed.*, **2020**, 59, 15325–15341.
[139] A. Schneemann, V. Bon, I. Schwedler, I. Senkovska, S. Kaskel, R. A. Fischer, *Chem. Soc. Rev.*, **2014**, 43, 6062–6096.
[140] L. J. Barbour, *Aust. J. Chem.*, **2006**, 59, 595–596.
[141] G. M. Schmidt, *J. Pure Appl. Chem.*, **1971**, 27, 647–678.
[142] W. W. He, S. L. Li , Y. Q. Lan, *Inorg. Chem. Front.*, **2018**, 5, 279–300.
[143] P. Naumov, P. K. Bharadwaj, *CrystEngComm*, **2015**, 17, 8775.
[144] C. P. Li, J. Chen, C. Sen Liu, M. Du, *Chem. Commun.*, **2015**, 51, 2768–2781.
[145] E. Fernandez-Bartolome, A. Martinez-Martinez, E. Resines-Urien, L. Piñeiro-Lopez, J. S. Costa, *Coord. Chem. Rev.*, **2022**, 452, 214281.
[146] J. P. Zhang, P. Q. Liao, H. L. Zhou, R. B. Lin, X. M. Chen, *Chem. Soc. Rev.*, **2014**, 43, 5789–5814.
[147] A. Chaudhary, A. Mohammad, S. M. Mobin, *Cryst. Growth Des.*, **2017**, 17, 2893–2910.
[148] S. Ehrling, I. Senkovska, A. Efimova, V. Bon, L. Abylgazina, P. Petkov, J. D. Evans, A. Gamal Attallah, M. T. Wharmby, M. Roslova, Z. Huang, H. Tanaka, A. Wagner, P. Schmidt, S. Kaskel, *Chem. - A Eur. J.*, **2022**, 28, 1–10.
[149] Y. Li, B. Zhao, J. P. Xue, J. Xie, Z. S. Yao, J. Tao, *Nat Commun.*, **2021**, 12, 6908.
[150] X. Wei, S. de Beer and L. J. Barbour, *Cryst. Growth Des.*, **2023**, 23, 6258–6262.
[151] J. J. Vittal, *Coord. Chem. Rev.*, **2007**, 251, 1781–1795.
[152] G. K. Kole, J. J. Vittal, *Chem. Soc. Rev.*, **2013**, 42, 1755–1775.
[153] S. L. Huang, T. S. A. Hor, G. X. Jin, *Coord. Chem. Rev.*, **2017**, 346, 112–122.
[154] B. B. Rath and J. J. Vittal, *J. Am. Chem. Soc.*, **2020**, 142, 20117–20123.
[155] T. D. Bennett, F. X. Coudert, S. L. James, A. I. Cooper, *Nat. Mater.*, **2021**, 20, 1179–1187.
[156] A. Schoedel, O. M. Yaghi, *Porosity in Metal-Organic Compounds*, In *Macrocyclic and Supramolecular Chemistry*, (Ed: R.M. Izatt), Wiley, **2016**, pp. 200–219.
[157] G. Slater, A. I. Cooper, *Science*, **2015**, 348, aaa8075.
[158] S. R. Batten, R. Robson, *Angew. Chem.*, **1998**, 110, 1558–1595.
[159] S. Kitagawa, R. Kitaura, S. I. Noro, *Angew. Chemie - Int. Ed.*, **2004**, 43, 2334–2375.
[160] H. Furukawa, K. E. Cordova, M. O'Keeffe, O. M. Yaghi, *Science*, **2013**, 341, 1230444.
[161] M. Ding, X. Cai, H. L. Jiang, Chem. Sci., **2019**, 10, 10209–10230.
[162] K. S. W. Sing, D. H. Everett, R. A. W. Haul, L. Moscou, R. A. Pierotti, J. Rouquerol, T. Siemieniewska, *Pure Appl. Chem.*, **1985**, 57, 603–619.
[163] J. Rouquerol, D. Avnir, C. W. Fairbridge, D. H. Everett, J. H. Haynes, N. Pernicone, J. D. F. Ramsay, K. S. W. Sing, K. K. Unger, *Pure Appl. Chem.*, **1994**, 66, 1739–1758.
[164] M. J. Bojdys, M. E. Briggs, J. T. A. Jones, D. J. Adams, S. Y. Chong, M. Schmidtmann, A. I. Cooper, *J. Am. Chem. Soc.*, **2011**, 133, 16566–16571.

[165] N. B. McKeown, *J. Mater. Chem.*, **2010**, 20, 10588–10597.
[166] D. P. van Heerden, V. J. Smith, H. Aggarwal, L. J. Barbour, *Angew. Chem. Int. Ed.*, **2021**, 60, 13430–13435.
[167] V. I. Nikolayenko, D. C. Castell, D. Sensharma, M. Shivanna, L. Loots, K. A. Forrest, C. J. Solanilla-Salinas, K. I. Otake, S. Kitagawa, L. J. Barbour, B. Space, M. J. Zaworotko, *Nat. Chem.*, **2023**, 15, 542–549.
[168] K. Koupepidou, A. C. Eaby, D. Sensharma, S. Javan Nikkhah, T. He, M. Lusi, M. Vandichel, L. J. Barbour, S. Mukherjee, M. J. Zaworotko, *Angew. Chem. Int. Ed.*, **2025**, 64, e202423521.
[169] M. Thommes, K. Kaneko, A. V. Neimark, J. P. Olivier, F. Rodriguez-Reinoso, J. Rouquerol, K. S. W. Sing, *Pure Appl. Chem.*, **2015**, 87, 1051–1069.
[170] A. H. Berger, A. S. Bhown, *Energy Procedia*, **2011**, 4, 562–567.
[171] S. I. Noro, R. Kitaura, M. Kondo, S. Kitagawa, T. Ishii, H. Matsuzaka, M. Yamashita, *J. Am. Chem. Soc.*, **2002**, 124, 2568–2583.
[172] S. S. Chen, *CrystEngComm*, **2016**, 18, 6543–6565.
[173] X. W. Zhu, D. Luo, X. P. Zhou, D. Li, *Coord. Chem. Rev.*, **2022**, 455, 214354.
[174] S. Kouser, A. Hezam, M. J. N. Khadri, S. A. Khanum, *J. Porous Mater.*, **2022**, 29, 663–681.
[175] Rigaku Oxford Diffraction. *CrysAlisPro Software System*, version 1.171.38.41; Rigaku Corporation: Oxford, UK **2015**.
[176] G. M. Sheldrick, *Acta Crystallogr. Sect. A Found. Crystallogr.*, **2015**, 71, 3–8.
[177] G. M. Sheldrick, *Acta Crystallogr. Sect. C Struct. Chem*, **2015**, 71, 3–8.
[178] O. V. Dolomanov, L. J. Bourhis, R. J. Gildea, J. A. K. Howard, H. Puschmann, *J. Appl. Crystallogr.*, **2009**, 42, 339–341.
[179] C. F. MacRae, I. Sovago, S. J. Cottrell, P. T. A. Galek, P. McCabe, E. Pidcock, M. Platings, G. P. Shields, J. S. Stevens, M. Towler, P. A. Wood, *J. Appl. Crystallogr.*, **2020**, 53, 226–235.
[180] http://www.povray.org/
[181] Match! - Phase Analysis using Powder Diffraction, Crystal Impact - Dr. H. Putz & Dr. K. Brandenburg GbR, Kreuzherrenstr. 102, 53227 Bonn, Germany, https://www.crystalimpact.de/match.
[182] W. Kraus, G. Nolze, *J. Appl. Crystallogr.*, **1996**, 29, 301–303.
[183] N. Döeblin, R. Kleeberg, *J. Appl. Cryst.*, **2015**, 48, 1573-1580.
[184] M. A. Spackman, D. Jayatilaka, *CrystEngComm*, **2009**, 11, 19–32.
[185] P. R. Spackman, M. J. Turner, J. J. McKinnon, S. K. Wolff, D. J. Grimwood, D. Jayatilaka and M. A. Spackman, *J. Appl. Crystallogr.*, **2021**, 54, 1006–1011.
[186] A. Gavezzotti, *J. Phys. Chem. B*, **2003**, 107, 2344–2353.
[187] M. G. Reeves, P. A. Wood, S. Parsons, *J. Appl. Crystallogr.*, **2020**, 53, 1154–1162.
[188] M. J. Frisch, G. W. Trucks, H. B. Schlegel, G. E. Scuseria, M. A. Robb, J. R. Cheeseman, G. Scalmani, V. Barone, B. Mennucci, G. A. Petersson, H. Nakatsuji, *et al.*, *Gaussian 09, Revision D.01*, Gaussian, Inc., Wallingford CT, **2013**.
[189] M. J. Frisch, G. W. Trucks, H. B. Schlegel, G. E. Scuseria, M. A. Robb, J. R. Cheeseman, G. Scalmani, V. Barone, B. Mennucci, G. A. Petersson, H. Nakatsuji, *et al.*, *Gaussian 16, Revision C.01*; Gaussian, Inc.: Wallingford, CT, USA, **2016**.
[190] S. Feng and T. Li, *J. Chem. Theory Comput.*, **2006**, 2, 149–156.
[191] T. Gelbrich, M. B. Hursthouse, *CrystEngComm*, **2005**, 7, 324–336.
[192] M. Cook, P. Cranwell, *Nucleophilic substitution*, Org. Chem., **2017**.

[193] C. Caron, X. N. T. Duong, R. Guillot, S. Bombard, A. Granzhan, *Chem. – Eur. J.*, **2019**, 25, 1949–1962.
[194] S. Kumar, P. Singh, S. Kumar, *Tetrahedron Lett.*, **2012**, 53, 2248–2252.
[195] P. K. Dhal and F. H. Arnold, *Macromolecules*, **1992**, 25, 7051–7059.
[196] P. Branná, M. Rouchal, Z. Prucková, L. Dastychová, R. Lenobel, T. Pospíšil, K. Maláč, R. Vícha, *Chem. Eur. J.*, **2015**, 21, 11712-11718.
[197] M. Fujita, M. Aoyagi, F. Ibukuro, K. Ogura and K. Yamaguchi, *J. Am. Chem. Soc.*, **1998**, 120, 611–612.
[198] L. X. Xie, M. L. Wei, C. Y. Duan, Q. Z. Sun, Q. J. Meng, *Inorg. Chim. Acta*, **2007**, 360, 2541.
[199] W. G. Trankle, M. E. Kopach, *Org. Process Res. Dev.*, **2007**, 11, 913–917.
[200] R. Sanii, E. Patyk-Kaźmierczak, C. Hua, S. Darwish, T. Pham, K. A. Forrest, B. Space, M. J. Zaworotko, *Cryst. Growth Des.*, **2021**, 21, 4927–4939.
[201] J. Thomas, G. Reekmans, P. Adriaensens, L. Van Meervelt, M. Smet, W. Maes, W. Dehaen, L. Dobrzańska, *Angew. Chem., Int. Ed.*, **2013**, 52, 10237–10240.
[202] D. E. Braun, P. G. Karamertzanis, S. L. Price, *Chem. Commun.*, **2011**, 47, 5443–5445.
[203] L. Carlucci, G. Ciani, S. Maggini and D. M. Proserpio, *CrystEngComm*, **2008**, 10, 1191–1203.
[204] L. N. Kuleshova, D. W. M. Hofmann, M. Y. Antipin, *Crystallogr. Rep.*, **2005**, 50, 167–176.
[205] T. Y. Nguyen, E. A. Roessler, K. Rademann, F. Emmerling, *Zeitschrift Fur Krist. - Cryst. Mater.*, **2017,** 232, 15–24.
[206] I. S. Antonijević, G. V. Janjić, M. K. Milčić, S. D. Zarić, *Cryst. Growth Des.*, **2016**, 16, 632–639.
[207] A. Bondi, *J. Phys. Chem.*, **1964**, 68, 441–451.
[208] T. Gelbrich, T. L. Threlfall, M. B. Hursthouse, *CrystEngComm*, **2012**, 14, 5454–5464.
[209] C. Jelsch, K. Ejsmont, L. Huder, *IUCrJ*, **2014**, 1, 119–128.
[210] L. Yang, D. R. Powell, R. P. Houser, *Dalton Trans.*, **2007**, 955–964.
[211] P. R. S. Salbego, C. R. Bender, T. Orlando, G. A. Moraes, J. P. P. Copetti, G. H. Weimer, H. G. Bonacorso, N. Zanatta, M. Hoerner, M. A. P. Martins, *ACS Omega*, **2019**, 4, 9697–9709.
[212] P. R. S. Salbego, C. R. Bender, M. Hoerner, N. Zanatta, C. P. Frizzo, H. G. Bonacorso, M. A. P. Martins, *ACS Omega*, **2018**, 3, 2569–2578.
[213] D. Dey, D. Chopra, *CrystEngComm*, **2017**, 19, 47–63.
[214] W. M, Bloch, R. Babarao, M. R. Hill, C. J. Doonan, C. J. Sumby, *J. Am. Chem. Soc.*, **2013**, 135, 10441-10448
[215] H. H. Wang, W. J. Shi, L. Hou, G. P. Li, Z. Zhu, Y. Y. Wang, *Chem. Eur. J.*, **2015**, 21, 16525-16531.
[216] D. Lv, J. Chen, K. Yang, H. Wu, Y. Chen, C. Duan, Y. Wu, J. Xiao, H. Xi, Z. Li, Q. Xia, *Chemical Engineering Journal*, **2019**, 122074.
[217] T. Di, Y. Yoshida, K. Otake, S. Kitagawa, H. Kitagawa, *Chem. Sci.*, **2024**, 15, 9641-9648.
[218] R. W. Broach, Zeolite Types and Structures. In Zeolites in Industrial Separation and Catalysis; *John Wiley & Sons*: Hoboken, NJ, USA, **2010**, 27–59.
[219] T. Jacobs, L. J. Barbour, *New J. Chem.*, **2013**, 37, 71–74.
[220] L. D. Shirtcliff, H. Xu, F. Diederich, *Eur. J. Org. Chem.*, **2010**, 2010, 846–855.
[221] J. Thomas, G. Reekmans, P. Adriaensens, L. V. Meervelt, M. Smet, W. Maes, W. Dehaen, L. Dobrzańska, *Angew. Chemie - Int. Ed.*, **2013**, 52, 10237–10240.

[222] J. Thomas, L. Dobrzańska, L. Van Meervelt, M. A. Quevedo, K. Woźniak, M. Stachowicz, M. Smet, W. Maes, W. Dehaen, *Chem. Eur. J.*, **2016**, 22, 979.
[223] A. Kálmán, L. Párkányi, G. Argay, *Acta Cryst.*, **1993**, B49, 1039–1049.
[224] P. Bombicz, N. V. May, D. Fegyverneki, A. Saranchimeg, L. Bereczki, *CrystEnggComm*, **2020**, 22, 7193–7203.
[225] H. Furukawa, N. Ko, Y. B. Go, N. Aratani, S. B. Choi, E. Choi, A. Ö. Yazaydin, R. Q. Snurr, M. O'Keeffe, J. Kim, O. M. Yaghi, *Science*, **2010**, 329, 424–428.
[226] O. K. Farha, A. Ö. Yazaydin, I. Eryazici, C. D. Malliakas, B. G. Hauser, M. G. Kanatzidis, S. T. Nguyen, R. Q. Snurr, J. T. Hupp, *Nat. Chem.*, **2010**, 2, 944–948.
[227] A. L. Sutton, J. I. Mardel, M. R. Hill, *Chem. Eur. J.*, **2024**, 30, e202400717.
[228] M. T. Kapelewski, T. Runčevski, J. D. Tarver, H. Z. H. Jiang, K. E. Hurst, P. A. Parilla, A. Ayala, T. Gennett, S. A. Fitzgerald, C. M. Brown, J. R. Long, *Chem. Mater.*, **2018**, 30, 8179–8189.
[229] E. Y. Lee, M. P. Suh, *Angew. Chem., Int. Ed.*, **2004**, 43, 2798–2801.
[230] G. G. Kole, A. J. Cairns, M. Eddaoudi, J. J. Vittal, *New J. Chem.*, **2010**, 34, 2392–2395.
[231] M. Momirlan, T. N. Veziroglu, *Int. J. Hydr. Energy*, **2005**, 30, 795–802.
[232] N. L. Rosi, J. Eckert, M. Eddaoudi, D. T. Vodak, J. Kim, M. O'Keeffe, O. M. Yaghi, *Science*, **2003**, 300, 1127–1129.
[233] L. J. Murray, M. Dinca, J. R. Long, *Chem. Soc. Rev.*, **2009**, 38, 1294–1314.
[234] J. Sculley, D. Yuan, H. C. Zhou, *Energy Environ. Sci.*, **2011**, 4, 2721–2735.
[235] M. P. Suh, H. J. Park, T. K. Prasad, D. W. Lim, *Chem. Rev.*, **2012**, 112, 782–835.
[236] X. Zhang, P. Liu, Y. Zhang , *Inorg. Chim. Acta*, **2023**, 557, 121683.
[237] *https://www.energy.gov/eere/fuelcells/articles/target-explanation-document-onboard-hydrogen-storage-light-duty-fuel-cell.*
[238] N. T. X. Huynh, V. Chihaia, D. N. Son, *Adsorption*, **2020**, 26, 509–519.
[239] D. Sengupta, P. Melix, S. Bose, J. Duncan, X. Wang, M. R. Mian, K. O. Kirlikovali, F. Joodaki, T. Islamoglu, T. Yildirim, R. Q. Snurr, O. K. Farha, *J. Am. Chem. Soc.*, **2023**, 145, 20492–20502.
[240] N. T. Xuan Huynh, V. T. Ngan, N. T. Yen Ngoc, V. Chihaia, D. N. Son, *RSC Adv.*, **2024**, 14, 19891–19902.
[241] Y. Li, R. T. Yang, *J. Am. Chem. Soc.*, **2006**, 128, 8136–8137.
[242] Z. Meng, R. Lu, D. Rao, E. Kan, C. Xiao, K. Deng, *Int. J. Hydrogen Energy*, **2013**, 38, 9811–9818.
[243] D. E. Jaramillo, H. Z. H. Jiang, H. A. Evans, R. Chakraborty, H. Furukawa, C. M. Brown, M. Head-Gordon, J. R. Long, *J. Am. Chem. Soc.*, **2021**, 143, 6248–6256.
[244] V. Zeleňák, I. Saldan, *Nanomaterials*, **2021**, 11, 1638.
[245] Y. Li, R. T. Yang, *Langmuir*, **2007**, 32, 12937–12944.
[246] D. Denysenko, M. Grzywa, J. Jelic, K. Reuter, D. Volkmer, *Angew. Chem.Int. Ed.*, **2014**, 53, 5832–5836.
[247] M. T. Kapelewski, T. Runcevski, J. D. Tarver, H. Z. H. Jiang, K. E. Hurst,P. A. Parilla, A. Ayala, T. Gennett, S. A. Fitzgerald, C. M. Brown, J. R. Long, *Chem. Mater.*, **2018**, 30, 8179–8189.
[248] H. Montes-Andrés, G. Orcajo, C. Martos, J. A. Botas, G. Calleja, *Int. J. Hydrogen Energy*, **2019**, 44, 18205–18213.
[249] C. B. Aakeröy, K. R. Seddon, *Chem. Soc. Rev.*, **1993**, 22, 397–407.

Appendix:

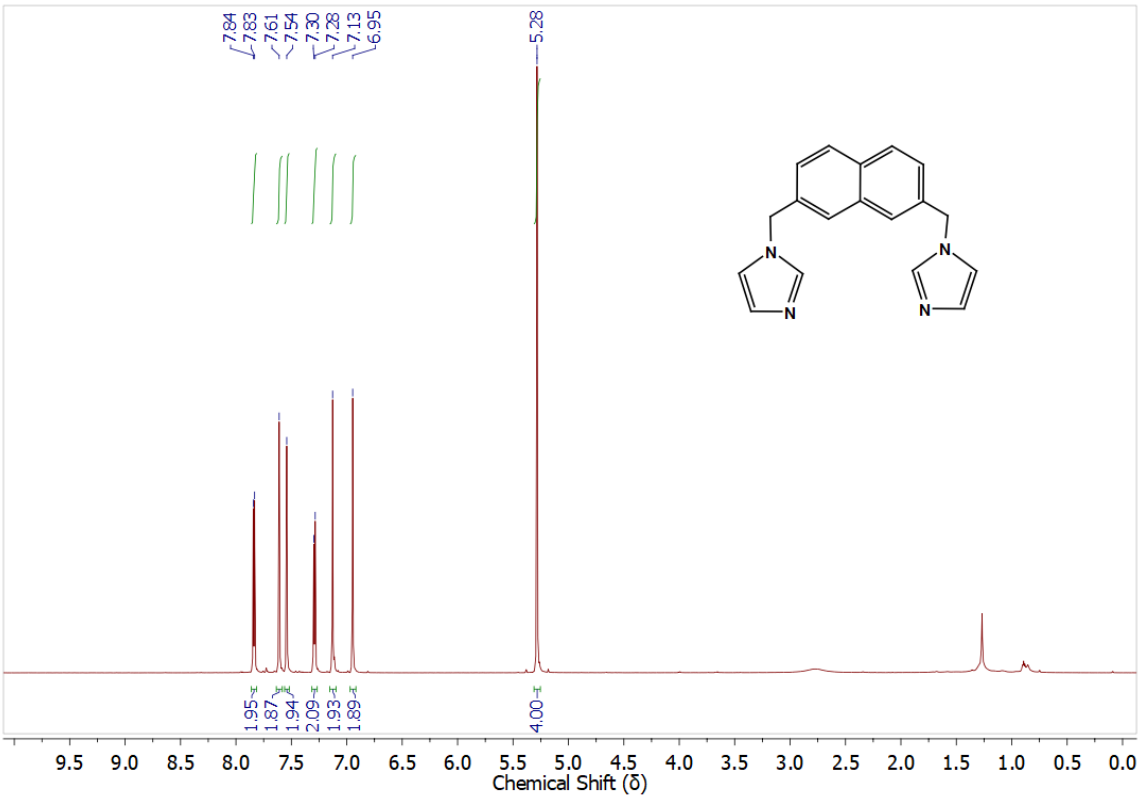

Figure S1: *^{1}H NMR spectra of L1.*

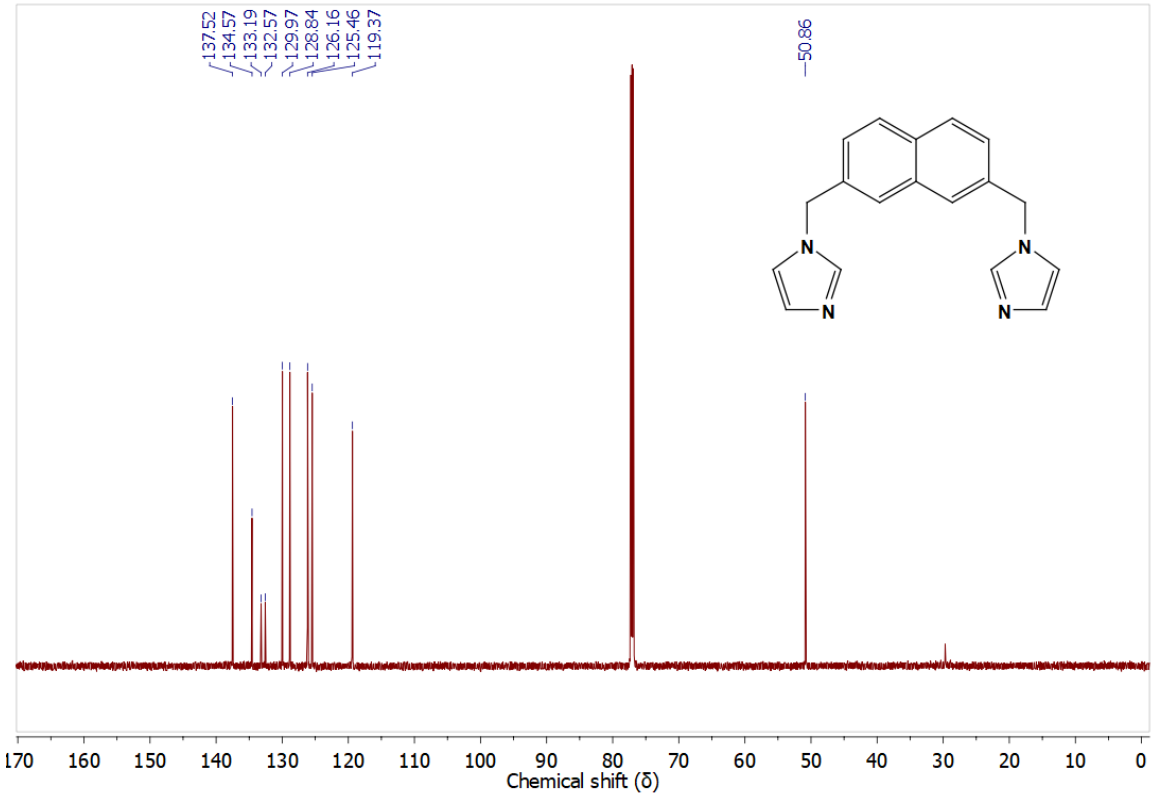

Figure S2: *^{13}C NMR spectra of L1.*

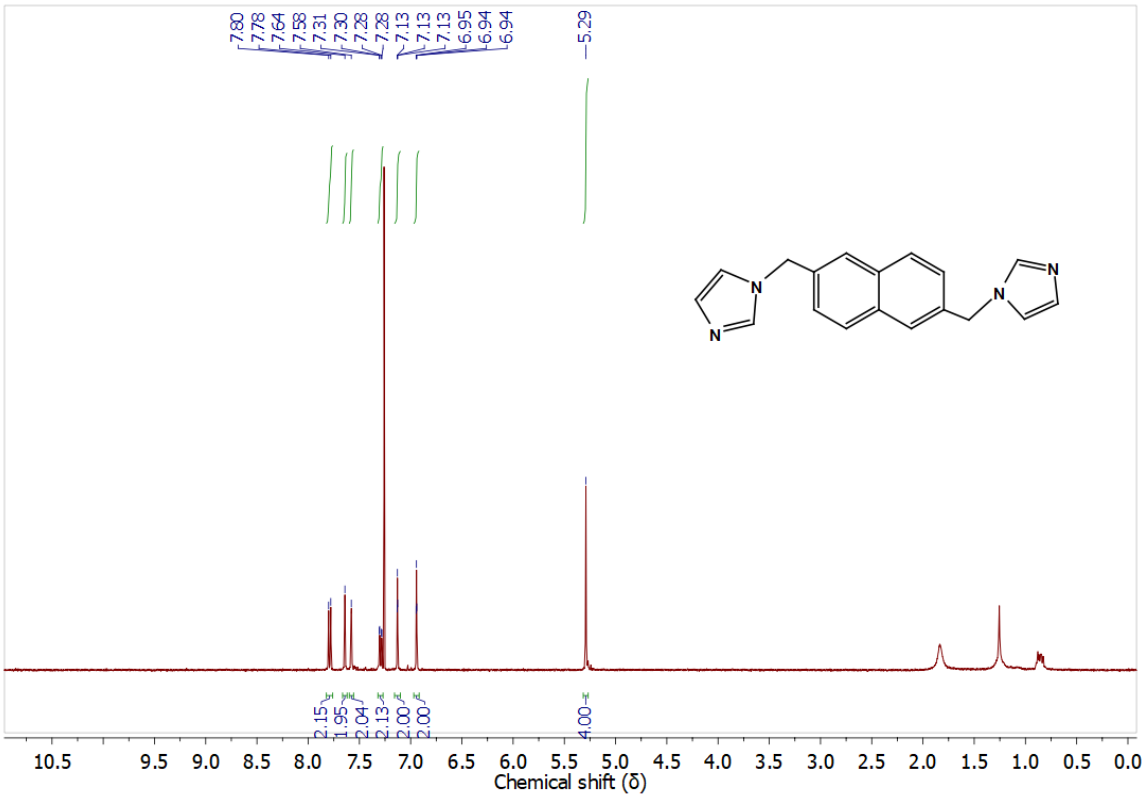

Figure S3: *^{1}H NMR spectra of L2.*

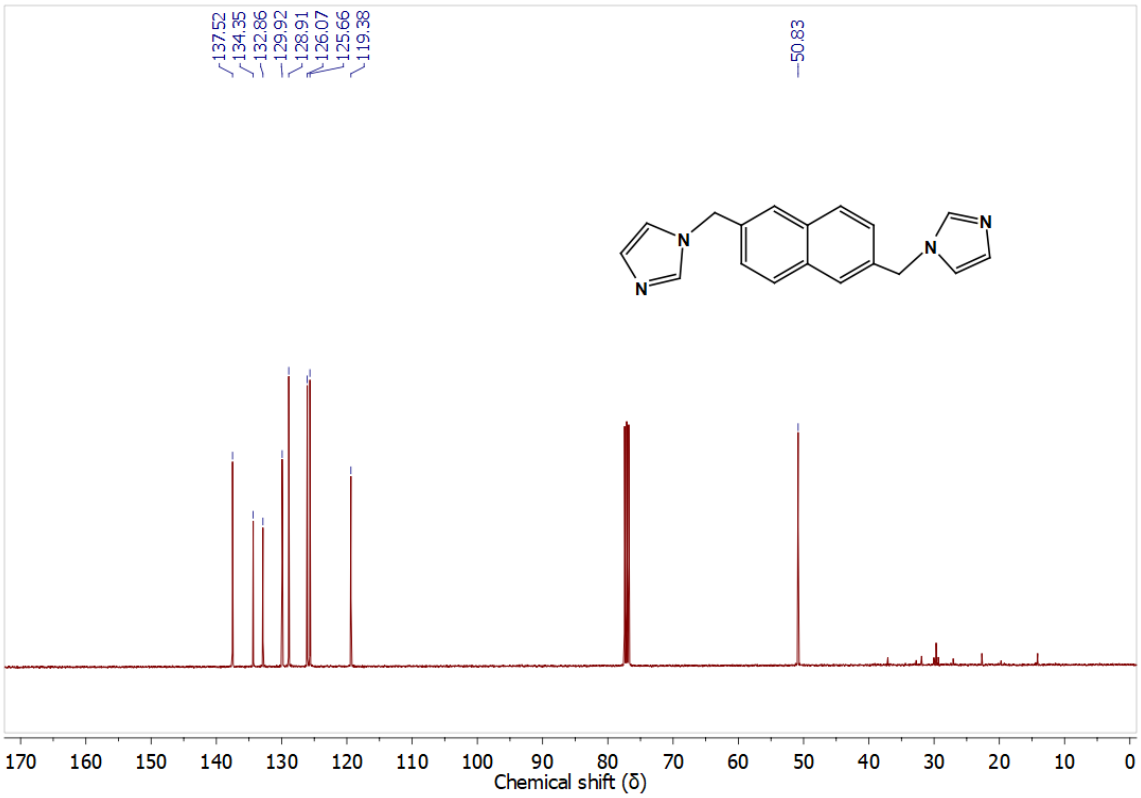

Figure S4: *^{13}C NMR spectra of L2.*

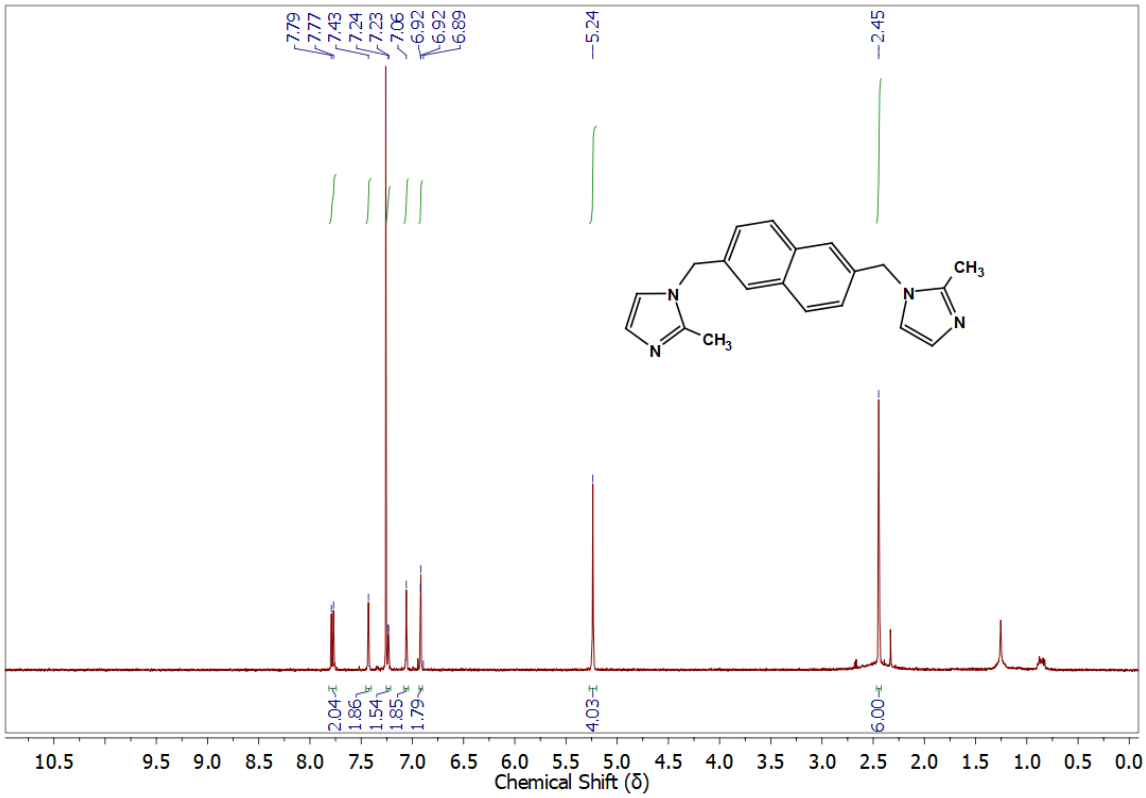

Figure S5: *^{1}H NMR spectra of L3.*

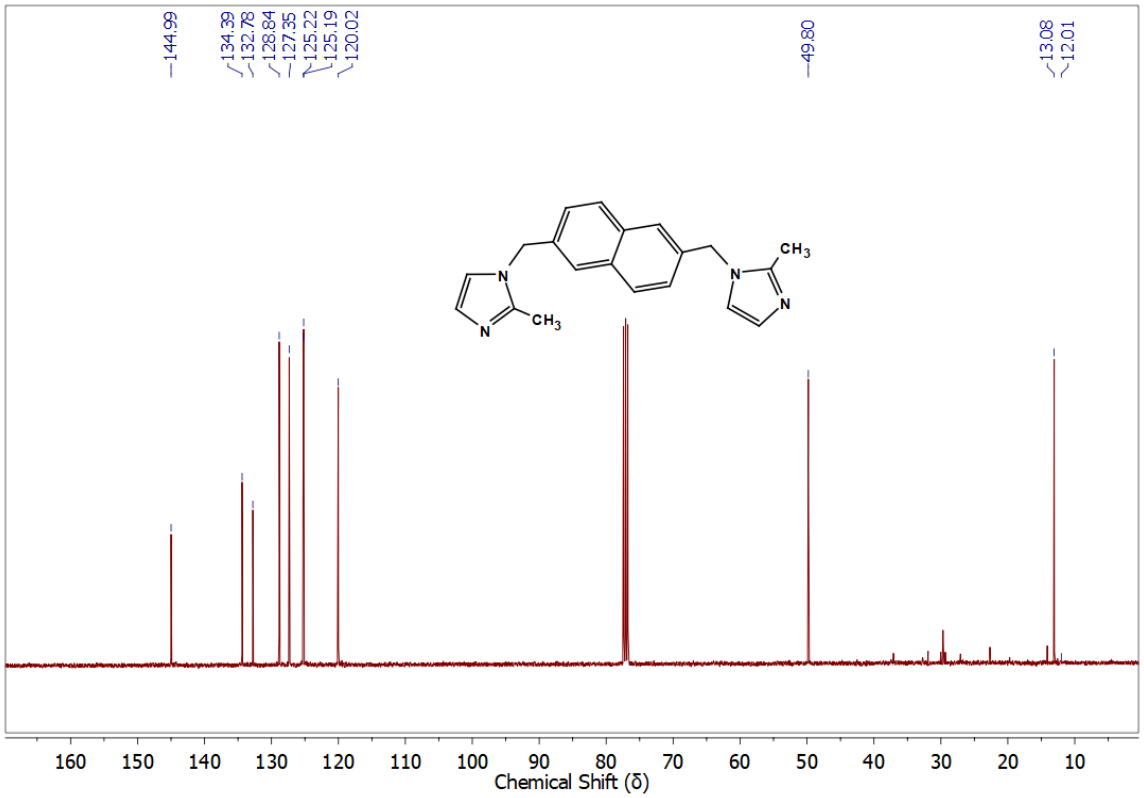

Figure S6: *^{13}C NMR spectra of L3.*

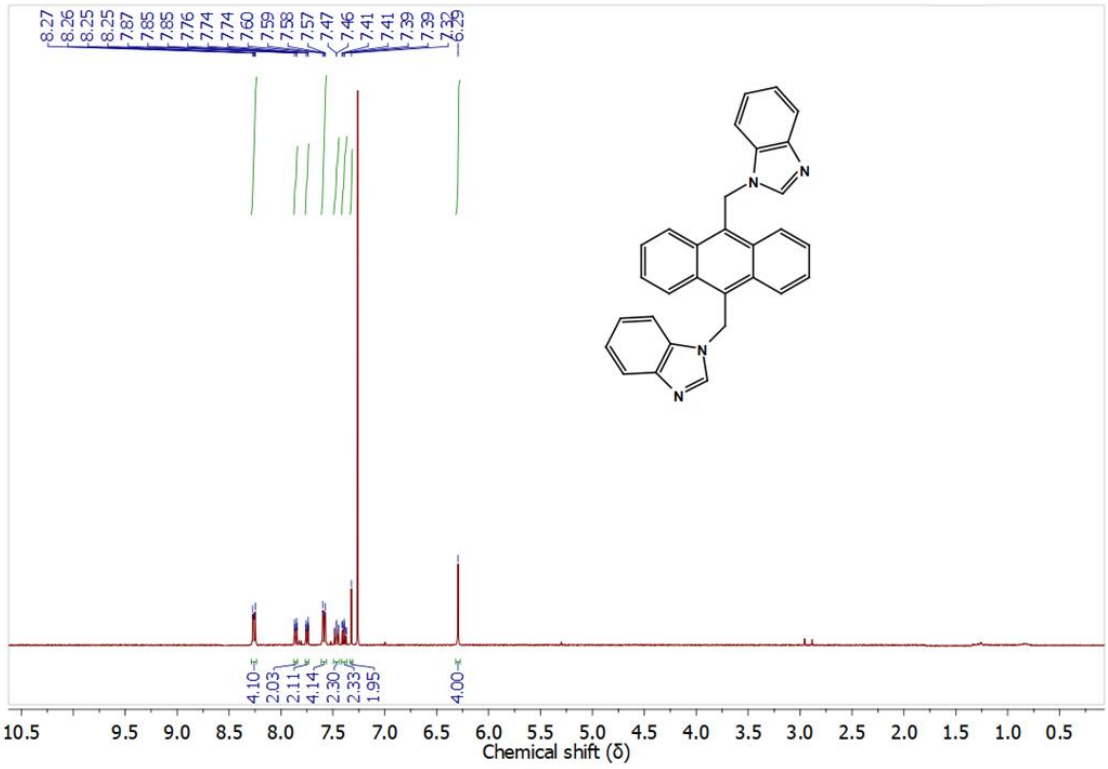

Figure S7: *^{1}H NMR spectra of L4.*

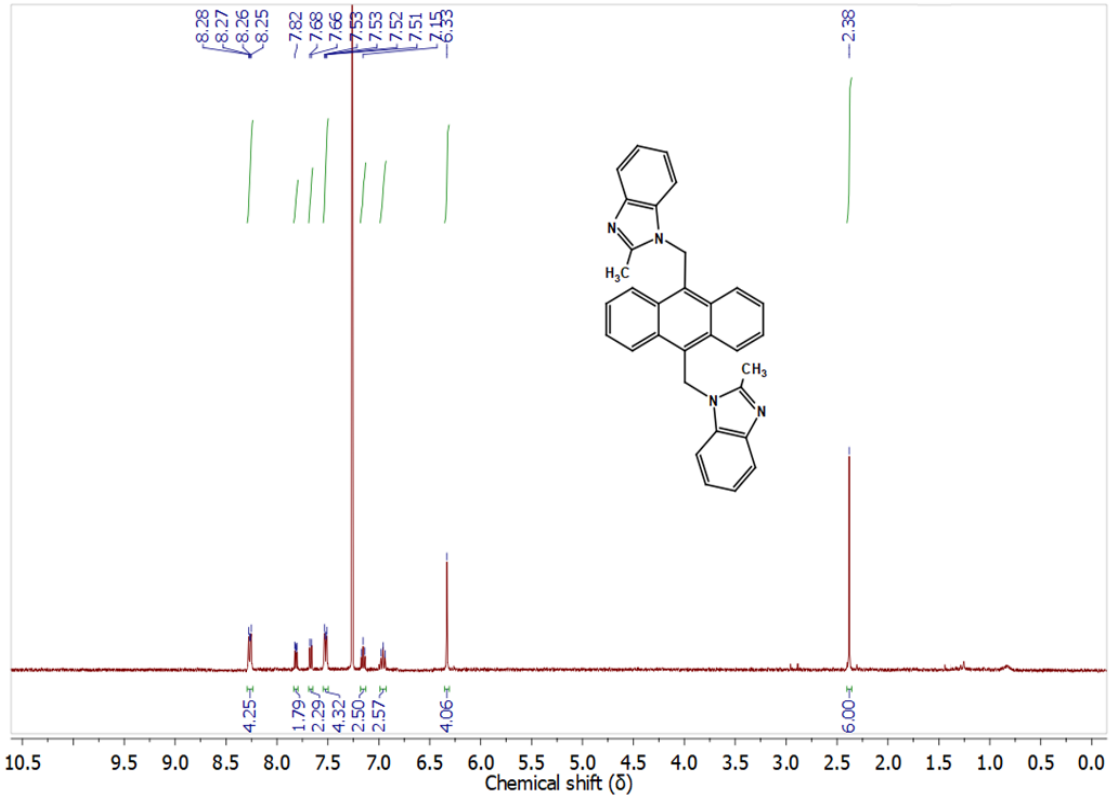

Figure S8: *^{1}H NMR spectra of L5.*

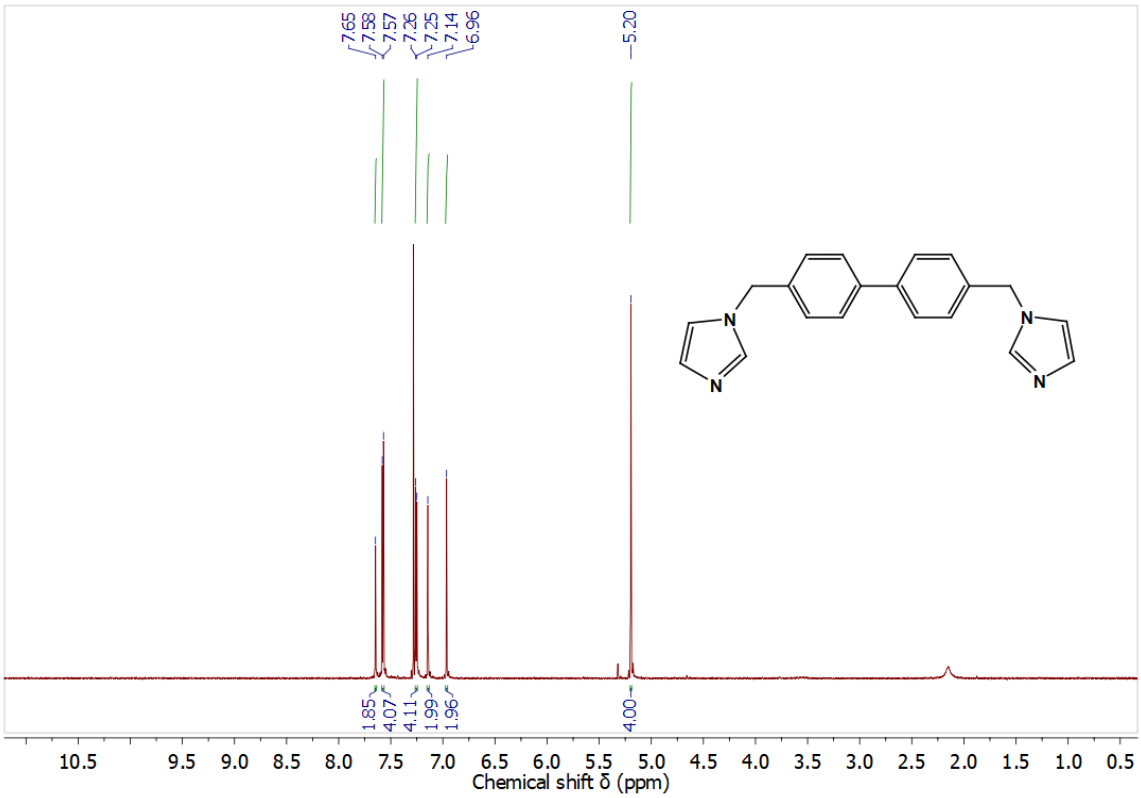

Figure S9: *^{1}H NMR spectra of L6.*

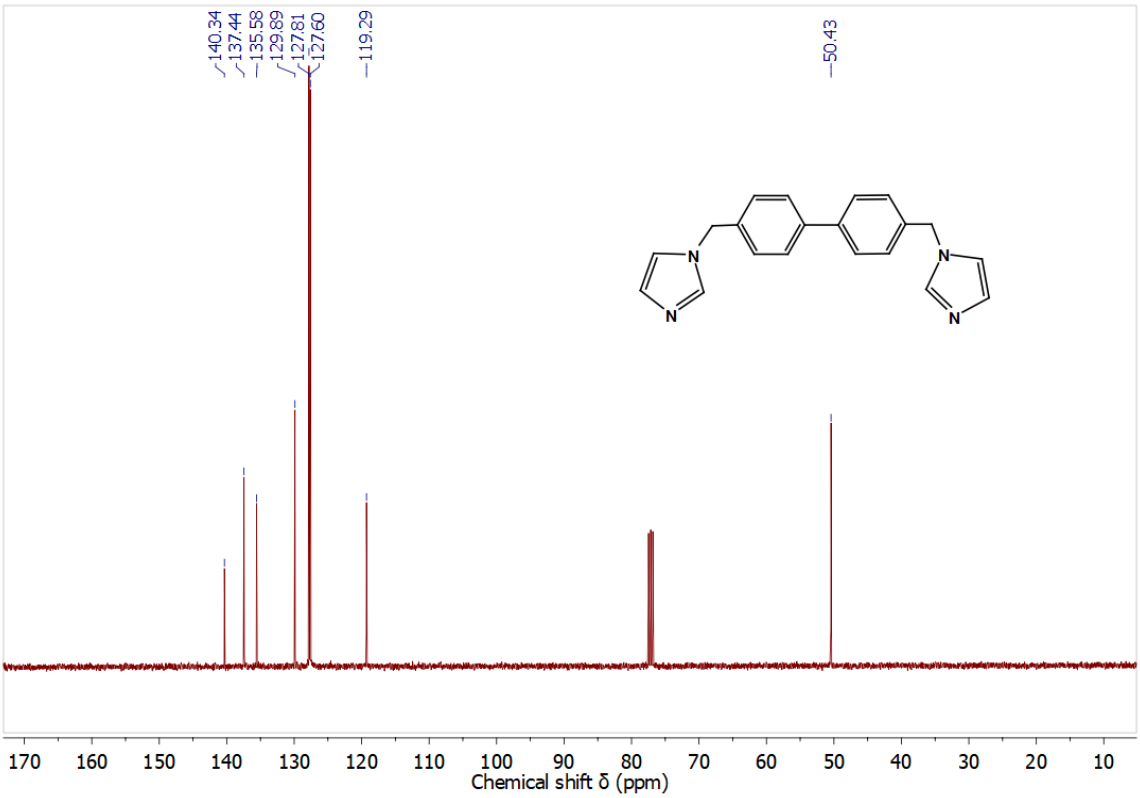

Figure S10: *^{13}C NMR spectra of L6.*

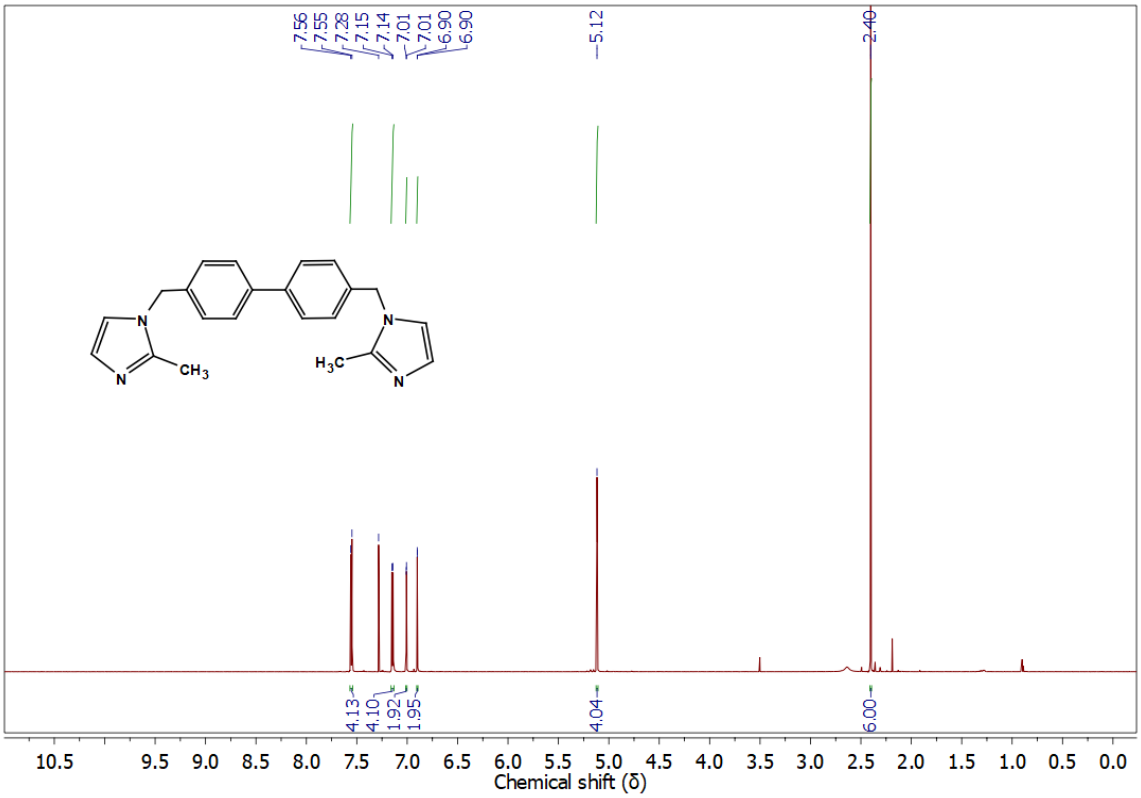

Figure S11: *^{1}H NMR spectra of L7.*

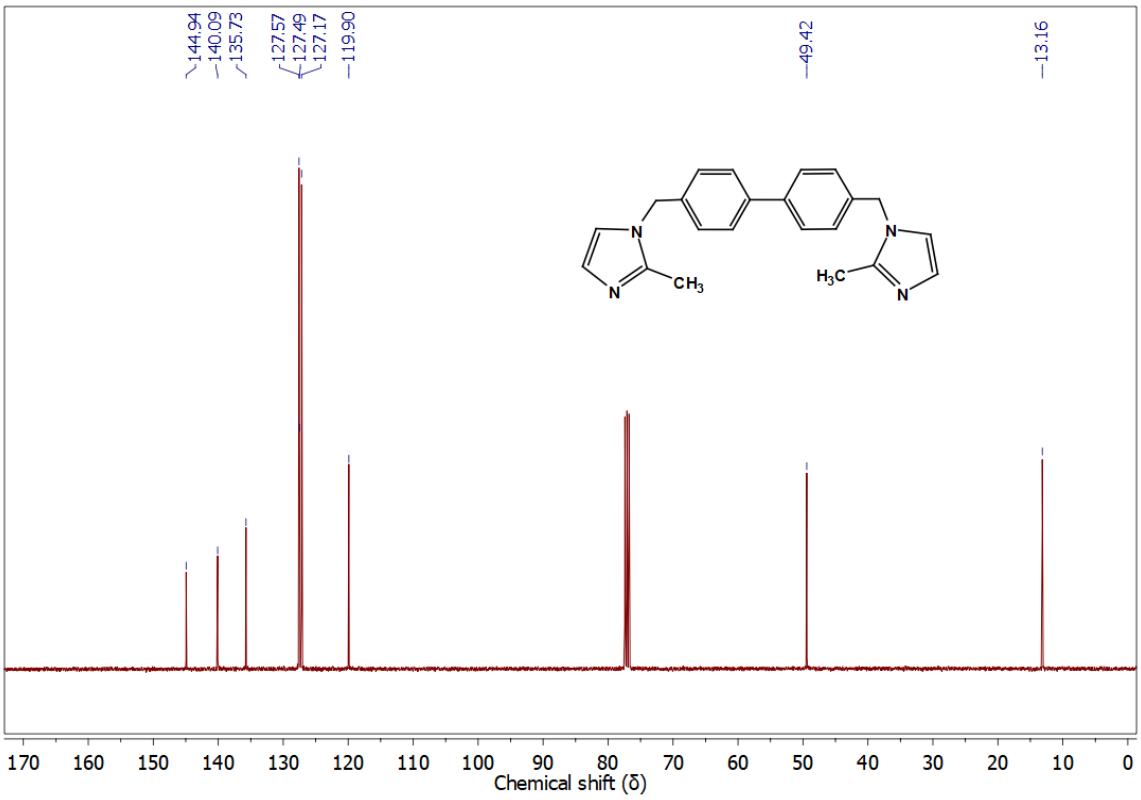

Figure S12: *^{13}C NMR spectra of L7.*

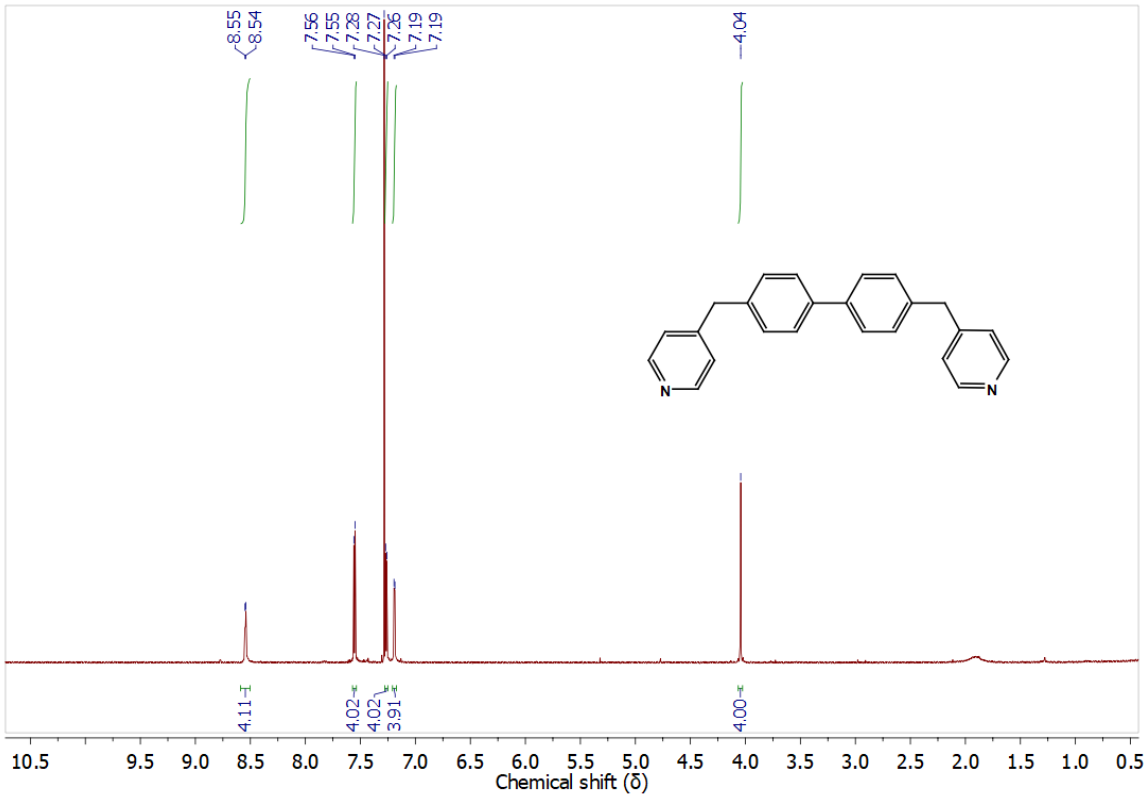

Figure S13: *^{1}H NMR spectra of L8.*

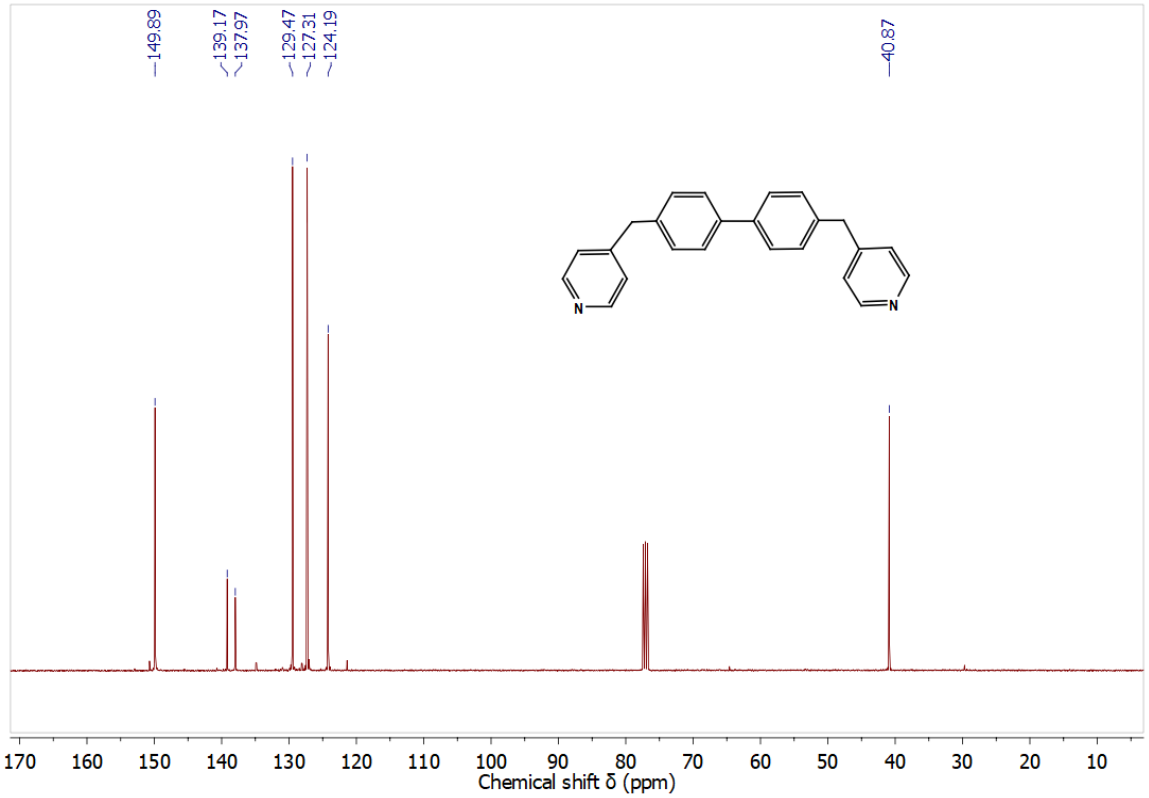

Figure S14: *^{13}C NMR spectra of L8.*

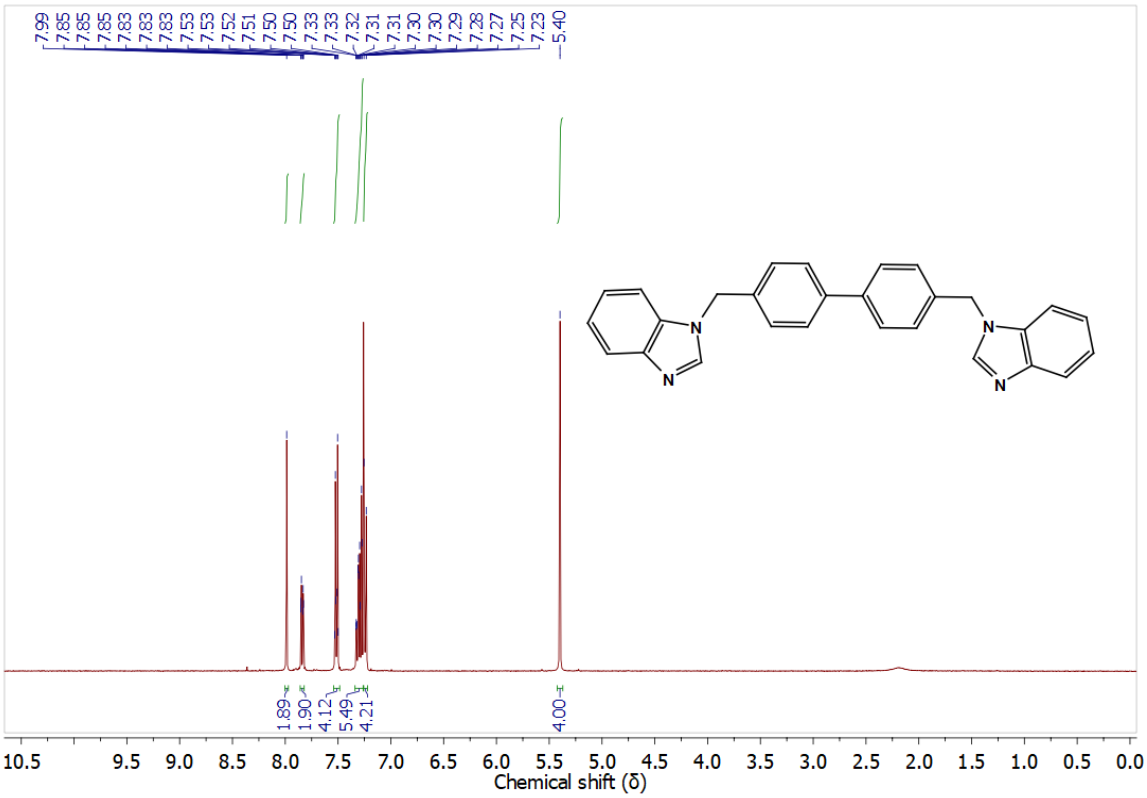

Figure S15: *^{1}H NMR spectra of L9.*

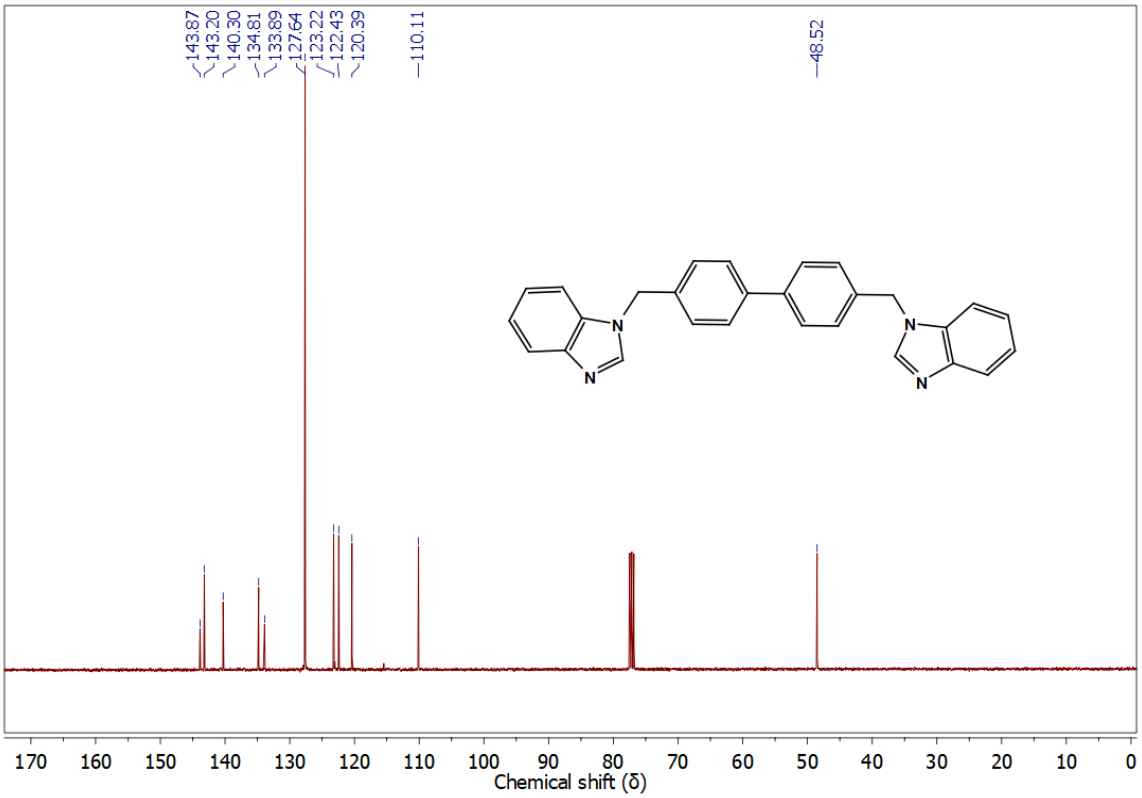

Figure S16: *^{13}C NMR spectra of L9.*

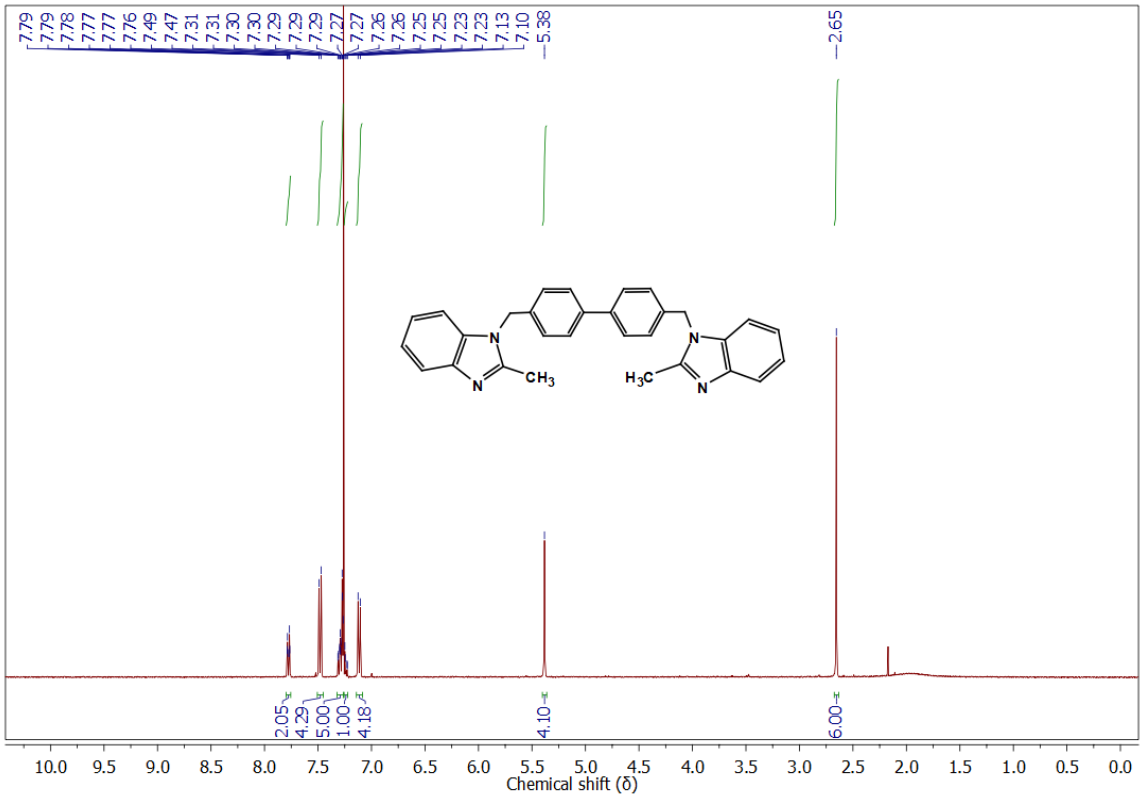

Figure S17: *^{1}H NMR spectra of L10.*

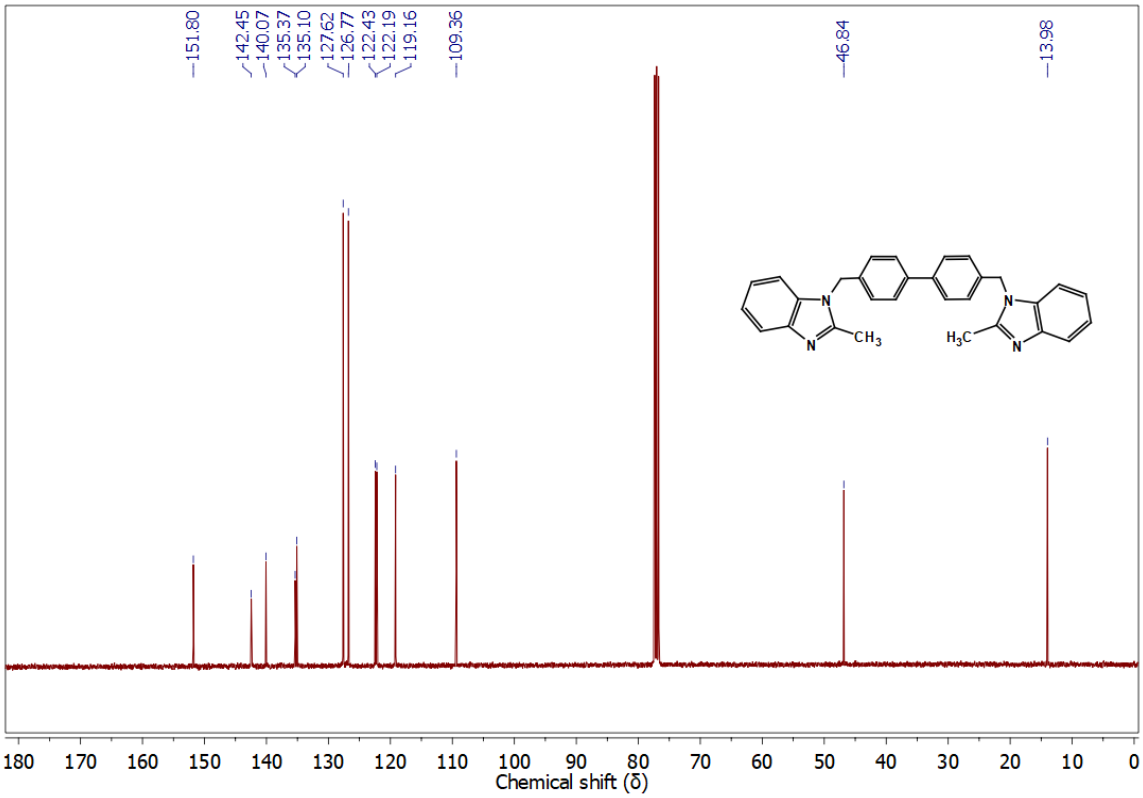

Figure S18: *^{13}C NMR spectra of L10.*

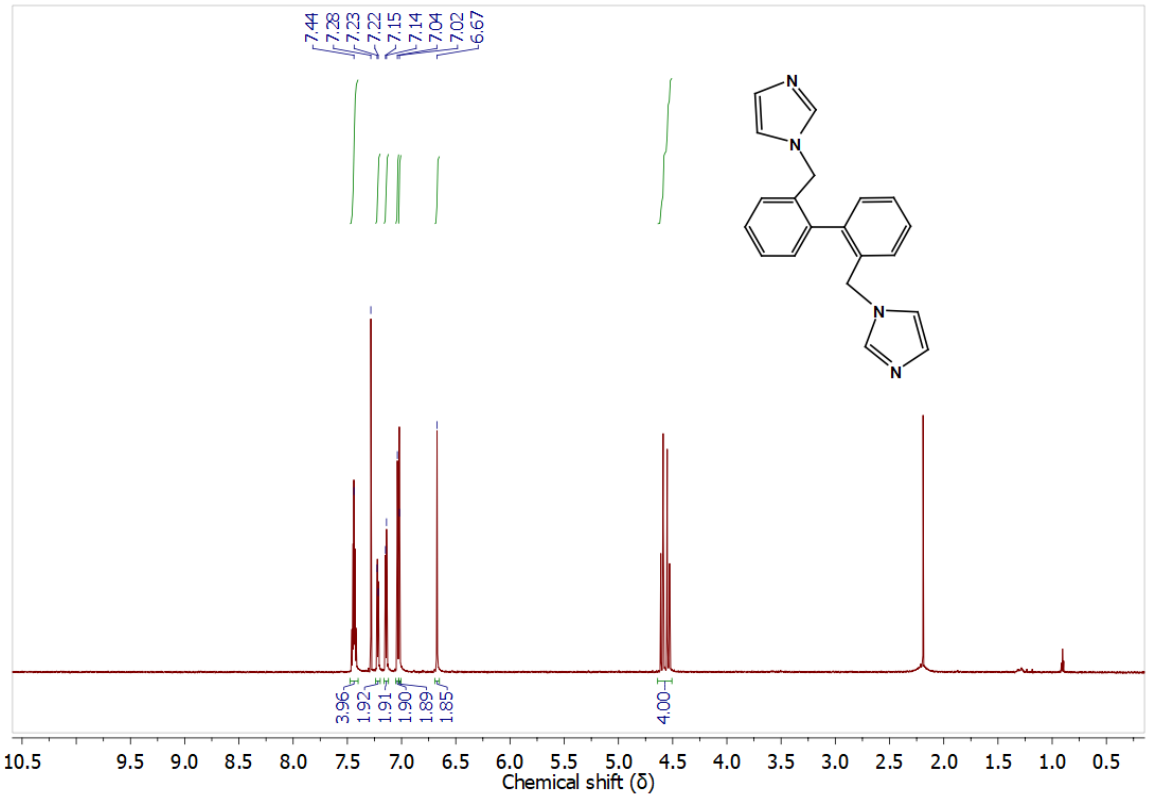

Figure S19: *^{1}H NMR spectra of L11.*

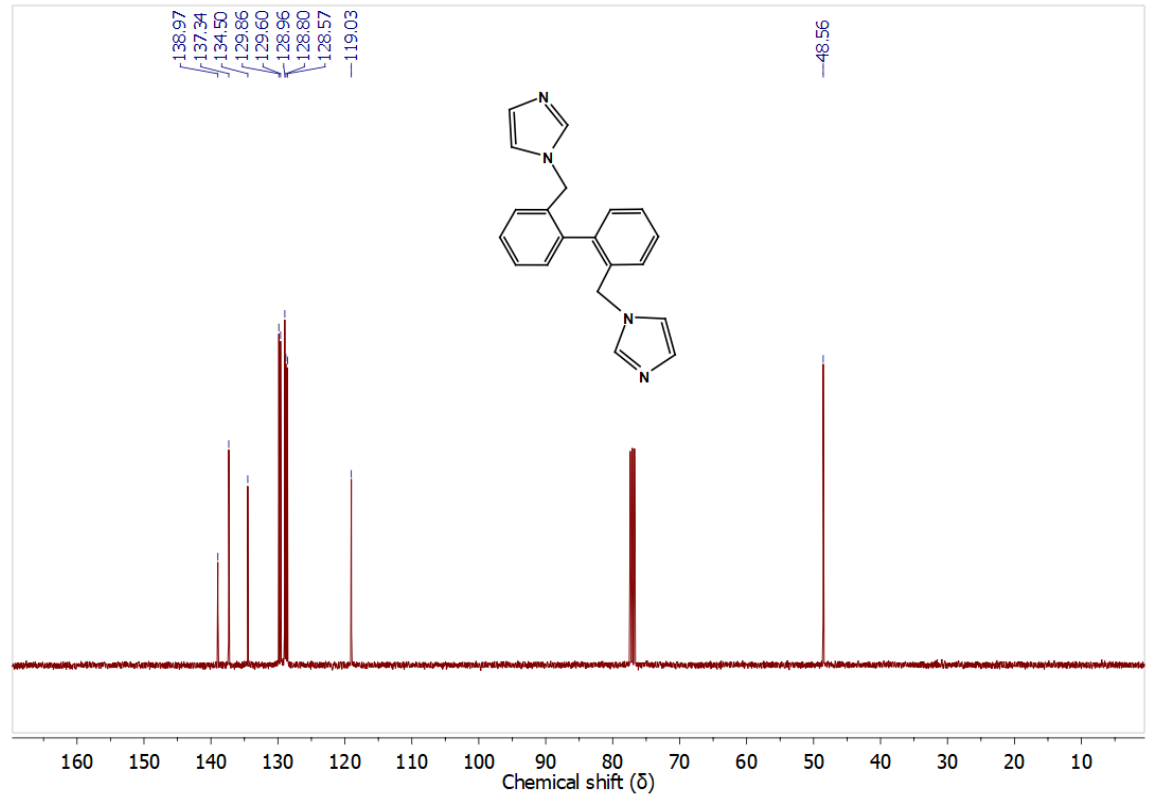

Figure S20: *^{13}C NMR spectra of L11.*

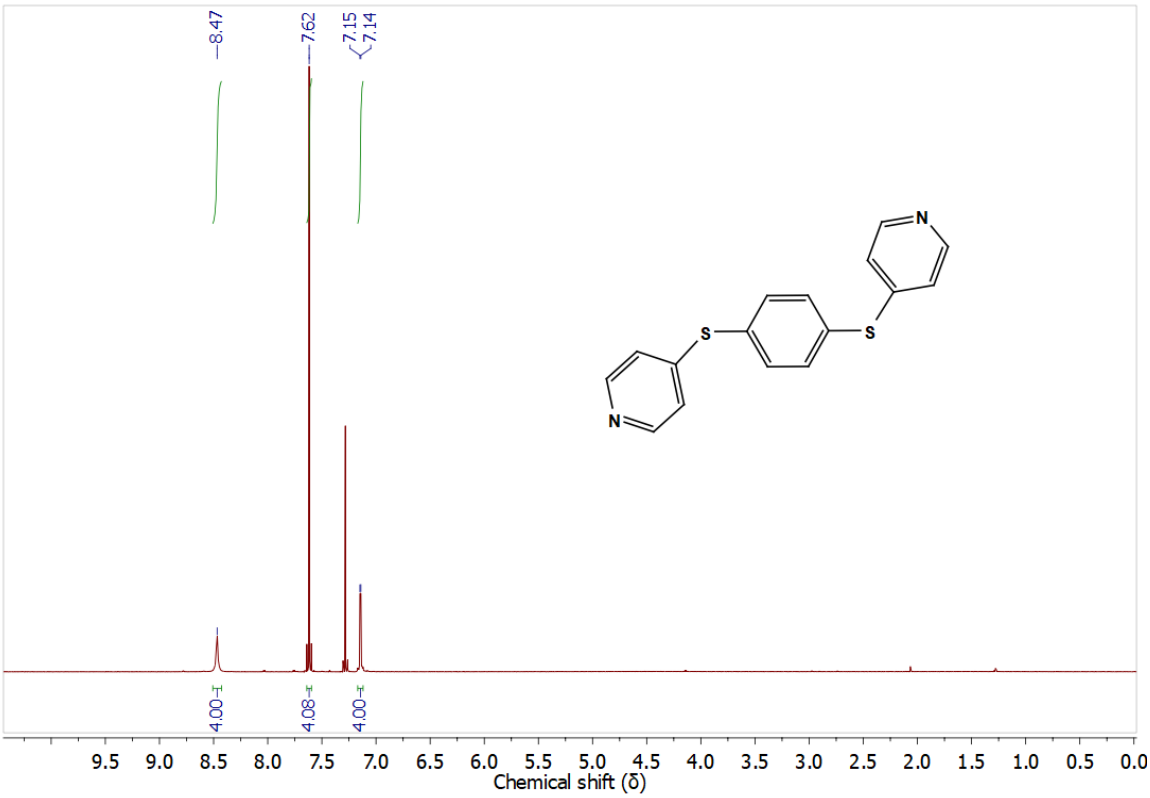

Figure S21: *^{1}H NMR spectra of L12.*

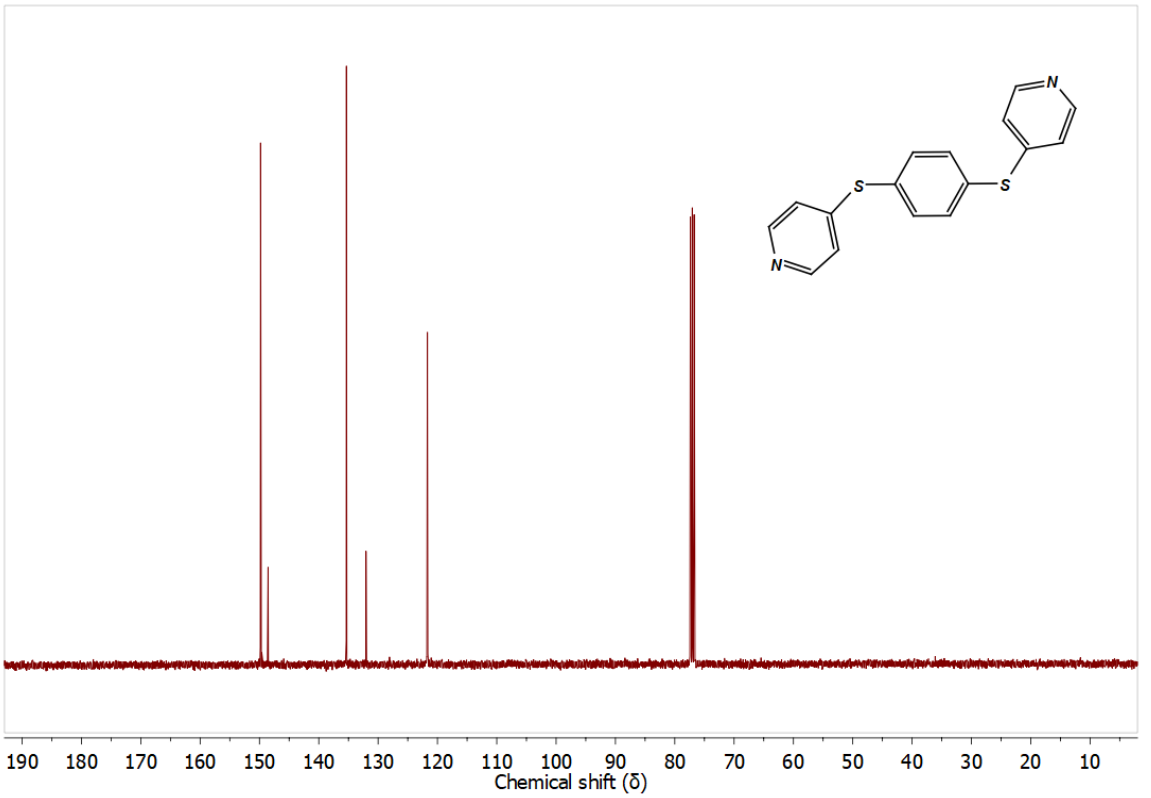

Figure S22: *^{13}C NMR spectra of L12.*

Table S1: *Hydrogen bonding parameters for different forms of **L1**, **L6**, **L8**, **L11**, and **L12**.*

Ligand	Polymorphs/hydrates	D-H···A	H···A (Å)	D···A (Å)	D-H-A (°)
L1	**L1a**	C8-H8···N3^{i}	2.61	3.532(2)	164
		C13-H13···N3^{ii}	2.76	3.708(1)	172
		C21-H21···N3^{iii}	2.77	3.605(2)	148
		C22-H22···N3^{iv}	2.99	3.915(2)	165
		C4-H4···N20^{v}	2.90	3.675(2)	139
		C5-H5···N20^{vi}	2.69	3.557(2)	156
		C12-H12···N20^{vi}i	2.53	3.471(1)	169
		C17-H17B···N20^{viii}	2.76	3.446(1)	127
		C13-H13···Cg1^{ii}	2.76	3.599(1)	148
		C6-H6A···Cg3^{iv}	2.62	3.524(2)	151
		C19-H19···Cg3^{vi}	2.59	3.517(1)	166
		C2-H2···Cg4i^{v}	2.89	3.780(1)	156
	L1b	O23-H23A···N3	1.99	2.896(1)	156
		O23-H23B···N3^{i}	1.94	2.896(1)	168
		C17-H17A···N3^{ii}	2.76	3.723(2)	164
		C2-H2···N18^{iii}	2.67	3.399(2)	134
		C9-H9···N20^{iv}	2.82	3.632(2)	144
		C21-H21···N20^{v}	2.81	3.571(1)	138
		C22-H22···N20^{vi}	2.64	3.439(2)	142
		C16-H16···O23^{ii}	2.94	3.787(1)	149
		C17-H17B···O23^{vii}	2.53	3.273(1)	132
		C2-H2···Cg2^{iii}	2.71	3.372(1)	128
		C19-H19···Cg4^{viii}	2.85	3.753(1)	160
	L1c	O23-H23B···N3	2.01	2.887(1)	170
		O23-H23A···N20^{i}	1.99	2.873(1)	178
		C6-H6A···N3^{ii}	2.67	3.649(1)	170
		C9-H9···N3^{iii}	2.88	3.741(1)	152
		C16-H16···N20^{iv}	2.90	3.538(1)	125
		C17-H17A···N20^{v}	2.75	3.503(2)	133
		C4-H4···O23^{vi}	2.55	3.371(2)	145
		C9-H9···O23^{iii}	2.85	3.666(1)	145
		C13-H13···O23^{iii}	2.52	3.421(1)	158
		C16-H16···O23^{ii}	2.92	3.802(1)	155
		C21-H21···O23^{vii}	2.33	3.143(2)	143
	L1d	O23-H23A···N3	1.93	2.856(3)	165
		O23-H23B···O24	1.82	2.754(3)	174
		O24-H24B···N20^{i}	1.82	2.776(2)	168
		O24-H24A···O23^{ii}	1.86	2.791(3)	167
		C17-H17A···N20^{iii}	2.71	3.693(4)	170
		C4-H4···O23^{ii}	2.93	3.784(3)	150
		C6-H6A···O23^{iv}	2.71	3.515(3)	138
		C12-H12···O23^{iv}	2.91	3.712(3)	143
		C16-H16···O23^{v}	2.85	3.412(3)	118
		C9-H9···O24^{vi}	2.72	3.585(3)	153
		C12-H12···O24^{iv}	2.81	3.686(3)	153
		C13-H13···O24^{vi}	2.77	3.624(3)	150
		C16-H16···O24^{iv}	2.82	3.692(3)	153
		C21-H21···O24^{vii}	2.74	3.548(3)	144

L6	**L6a1**	C6-H6···N3^{i}	2.94	3.82	158
		C10-H8···N3^{ii}	2.96	3.798	150
		C18-H15···N3^{i}	2.931	3.792	155
		C3-H1···N5^{iii}	2.897	3.752	153
		C8-H8···N5^{iv}	2.666	3.524	154
		C13-H11···N5^{v}	2.759	3.675	168
		C4-H2···Cg1^{vi}	2.69	3.575(2)	159
		C10-H8···Cg1^{vii}	2.73	3.565(2)	150
		C12---H10···Cg2^{viii}	2.95	3.677(2)	136
	L6a2	C9-H6···N4^{i}	2.950	3.598	128
		C10-H8···N4^{ii}	2.928	3.853	173
		C3-H1···N5^{iii}	2.897	3.752	153
		C8-H5···N5^{iv}	2.666	3.524	154
		C13-H11···N5^{v}	2.759	3.675	169
		C4-H2···Cg4^{vi}	2.69	3.5751	159
		C10-H8···Cg1^{Vii}	2.73	3.5650	150
		C12-H10···Cg2^{viii}	2.95	3.6773	136
	L6b	C17-H17···N3^{i}	2.851	3.264	107
		C18-H18···N3^{ii}	2.933	3.681	137
		C19-H19B···N3^{i}	2.733	3.318	118
		C19-H19A···N3^{iii}	2.57	3.5366(16)	164
		C8-H8···N22^{iv}	2.687	3.589	154
		C6-H6B···N22^{iv}	2.833	3.708	159
		C5-H5···Cg2^{v}	2.70	3.3852(13)	129
		C14-H14···Cg3^{vi}	2.94	3.6560(12)	133
		C18-H18···Cg1^{ii}	2.90	3.7143(12)	144
		C21-H21···Cg4^{vii}	2.90	3.8349(12)	167
	L6c	C19-H19B···N3^{i}	2.702	3.572	147
		C21-H21···N3^{ii}	2.852	3.629	140
		C2-H2···N22^{iii}	2.825	3.577	137
		C6-H6A···N22^{iii}	2.494	3.399(1)	152
		C6-H6B···N22^{iv}	2.809	3.677	147
		C12-H12···N22^{iv}	2.960	3.642	130
		C12-H12···Cg2^{v}	2.78	3.5513(1)	139
		C19-H19A···Cg4^{vi}	2.83	3.8111(1)	169
		C23-H23···Cg4^{vii}	2.82	3.7605(1)	173
L8	**L8a**	C5-H5···N1^{i}	2.61	3.553(2)	174
		C13-H13···N1^{i}	2.56	3.485(2)	163
		C10-H10···N24^{ii}	2.86	3.626(2)	139
		C16-H16···N24^{iii}	2.74	3.617(2)	153
		C20-H20A···N24^{iv}	2.70	3.474(2)	135
		C25-H25···N24^{v}	2.94	3.790(2)	150
		C7-H7A···Cg1^{vi}	2.85	3.767(1)	154
		C23-H23···Cg1^{ii}	2.95	3.829(1)	155
	L8b	C7-H7B···N1^{i}	2.73	3.521(2)	137
		C13-H13···N1^{i}	2.74	3.585(2)	149
		C22-H22···N1^{ii}	2.73	3.507(2)	140
		C5-H5···N24^{iii}	2.68	3.381(2)	131
		C2-H2···Cg2^{iv}	2.90	3.572(2)	129
		C16-H16···Cg1^{v}	2.78	3.683(2)	158
		C23-H23···Cg2^{vi}	2.89	3.680(2)	141
		C25-H25···Cg1^{vii}	2.95	3.697(2)	136

L11	**L11a**	C10-H10···N3^{i}	2.71	3.434(2)	134
		C15-H15···N3^{ii}	2.85	3.568(2)	134
		C6-H6B···N22^{iii}	2.98	3.851(2)	147
		C8-H8···N22^{iii}	2.56	3.363(2)	142
		C15-H15···N22^{iv}	2.57	3.521(2)	176
		C4-H4···Cg3^{v}	2.84	3.724(2)	155
		C6-H6A···Cg3^{vi}	2.92	3.688(2)	135
		C10-H10···Cg1^{vii}	2.78	3.666(2)	156
		C19-H19A···Cg1^{viii}	2.83	3.632(2)	139
		C21-H21···Cg4^{ix}	2.50	3.384(2)	156
	L11b	C2-H2···N3^{i}	2.99	3.624(2)	126
		C6-H6A···N3^{i}	2.52	3.384(2)	145
		C14-H14···N3^{ii}	2.59	3.475(2)	154
		C5-H5···N22^{iii}	2.59	3.478(2)	156
		C9-H9···N22^{iv}	2.45	3.348(2)	158
		C21-H21···N22^{v}	2.76	3.666(2)	159
		C4-H4···Cg3^{vi}	2.62	3.540(1)	162
		C23-H23···Cg4^{vi}	2.75	3.584(1)	147
	MIDJEPLN	C35-H35···N1^{i}	2.989	3.712(1)	134
		C14-14···N3^{i}	2.843	3.772(1)	166
		C33-H33···N3^{ii}	2.624	3.469(2)	148
		C43-H43A···N3^{i}	2.885	3.814(1)	156
		C45-H45···N3^{i}	2.820	3.647(1)	146
		C11-H11···N20^{iii}	2.991	3.781(1)	142
		C5-H5···N22^{iv}	2.796	3.739(1)	172
		C9-H9···N22^{v}	2.503	3.411(2)	160
		C21-H21···N22^{iii}	2.640	3.528(1)	156
		C30-H30B···N27^{vi}	2.513	3.355(1)	143
		C38-H38···N27^{i}	2.676	3.568(1)	157
		C2-H2···N46	2.898	3.656(1)	138
		C6-H6B···N46	2.625	3.534(1)	153
		C29-H29···N46^{ii}	2.337	3.178(1)	147
		C17-H17···Cg2	2.80	3.434(1)	125
		C4-H4···Cg3^{vii}	2.74	3.625(1)	154
		C23-H23···Cg4^{vii}	2.91	3.781(1)	153
		C6-H6B···Cg6	2.98	3.7898(1)	140
		C41-H41···Cg6	2.98	3.59(1)	123
		C47-H47···Cg8^{vii}	2.84	3.661(1)	145
L12	**L12a1**	C9-H9···N1^{i}	2.793	3.465(2)	129
		C10-H10···N1^{i}	2.923	3.528(2)	123
		C13-H13···N1^{ii}	2.662	3.506(2)	148
		C17-H17···N1^{iii}	2.729	3.547(2)	145
		C6-H6···N18^{iv}	2.914	3.639(2)	134
		C12-H12···N18^{v}	2.551	3.386(2)	147
	L12a2	C12A-H12A···N1A^{i}	2.216	2.915(4)	130
		C19A-H19A···N1A^{ii}	2.785	3.609(3)	145
		C6A-H6A···N18A^{iii}	2.875	3.619(4)	136
	L12b	C5-H5···N1^{i}	2.997	3.471(2)	112
		C6-H6···N1^{i}	2.859	3.414(2)	118
		C10-H10···N1^{ii}	2.573	3.446(2)	153

L1: **(L1a)** Cg1 is the centroid of the imidazole ring N1-C5, Cg3 is the centroid of the benzene ring C7-C12, Cg4 is the centroid of the benzene ring C10-C16, **(L1b)** Cg2 is the centroid of the imidazole ring N18-C22, Cg4 is the centroid of the benzene ring C10-C16, **(L1c)** Cg1 is the centroid of the imidazole ring N1-C5, Cg2 is the centroid of the imidazole ring N18-C22, **(L1d)** Cg1 is the centroid of the imidazole ring N1-C5, Cg3 is the centroid of the benzene ring C7-C12, Cg4 is the centroid of the benzene ring C10-C16, Symmetry codes **(L1a):** (i) 1-x,2-y,1-z, (ii) x,y,z-1, (iii) x,y-1,z-1, (iv) 1-x,1-y,1-z, (v) x,1+y,1+z, (vi) 2-x,1-y,-z, (vii) x,y,1+z, (viii) 2-x,-y,-z; **(L1b):** (i) -x,y,1/2-z, (ii) 1/2+x,1/2+y,z, (iii) x-1/2,y-3/2,z, (iv) 1-x,2-y,1-z, (v) 3/2-x,5/2-y,1-z, (vi) x,y-1,z, (vii) 1/2+x,3/2+y,z, (viii) x,1+y,z; **(L1c):** (i) 3/2-x,1-y,z-1/2, (ii) x-1/2,3/2-y,1-z, (iii) 1/2+x,3/2-y,1-z, (iv) 1-x,1/2+y,3/2-z, (v) x-1/2,y,3/2-z, (vi) 3/2-x,y-1/2,z, (vii) x,3/2-y,1/2+z; **(L1d):** (i) x-1,y,z-1, (ii) x,3/2-y,z-1/2, (iii) 2-x,1/2+y,3/2-z, (iv) 1-x,1/2+y,1/2-z, (v) 1-x,2-y,1-z, (vi) 1-x,y-1/2,1/2-z, (vii) 1+x,3/2-y,1/2+z; **L6:** (**L6a**) Cg1 is the centroid of imidazole ring N1-C5, Cg2 is the centroid of imidazole ring N20-C24, Cg3 is the centroid of benzene ring C7-C12, Cg4 is the centroid of benzene ring C13-C18, (**L6c**) Cg2 is the centroid of imidazole ring N20-C24, Cg4 is the centroid of benzene ring C13-C18, Symmetry codes **(L6a1):** (i) 1-x,1/2+y,1/2-z, (ii) 1-x,y-1/2,1/2-z, (iii) 2-x,y-1/2,-z-1/2, (iv) -x+2,-x,-y, (v) 2-x,1/2+y,-z-1/2, (vi) 1-x,-y,-z, (vii) 1-x,-1/2+y,1/2-z, (viii) 2-x,1/2+y,-1/2-z; **(L6a2):** (i) 1-x,1/2+y,1/2-z, (ii) 1-x,y-1/2,1/2-z, (iii) 2-x,y-1/2,-z-1/2, (iv) 2-x,-y,-z, (v) 2-x,1/2+y,-z-1/2, (vi 1-x,-y,-z, (vii) 1-x,1/2+y,-1/2-z, (viii) -x,-1/2+y,1/2-z; **(L6b):** (i) 1/2-x,1/2+y,1/2-z, (ii) 3/2-x,1/2+y,1/2-z, (iii) x-1/2,1/2+y,1/2-z, (iv) -x,-y,1-z, (v) 3/2+x,1/2-y,-1/2+z, (vi) 1-x,-y,1-z, (vii) -1+x,y,z ;**(L6c):** (i) x,1/2-y,1/2+z, (ii) 3/2-x,1-y,1/2+z, (iii) x,3/2-y,z-1/2, (iv) 2-x,1-y,1-z, (v) 1-x,1-y,-z,(vi) 1/2-x,1/2+y,z, (vii) 1-x,2-y,-z; **L8:** (**L8a**) Cg1 is the centroid of benzene ring C14-C19; (**L8b**) Cg1 is the centroid of benzene ring C8-C13, Cg2 is the centroid of pyridine ring N1-C6, symmetry codes **(L8a):** (i) -x,1/2+y,-1/2-z, (ii) 1-x,1-y,1-z, (iii) 1-x,1/2+y,1/2-z, (iv) 1-x,1-y,-z, (v) x,1/2-y,-1/2+z, (vi) x,y,-1+z; **(L8b):** (i) -x+1,y-1/2,-z+1, (ii) x,y,z+1, (iii) -x,y+1/2,-z+2, (iv) 1+x,y,-1+z, (v) 1-x,1/2+y,2-z (vi) 1-x,-1/2+y,2-z, (vii) -x,-1/2+y,2-z; **L11:** (**L11a**) Cg1 is the centroid of the imidazole ring N1-C5, Cg3 is the centroid of the benzene ring C7-C12, Cg4 is the centroid of the benzene ring C13-C18, (**L11b**) Cg3 is the centroid of the benzene ring C7-C12, Cg4 is the centroid of the benzene ring C13-C18, (**MIDJEPLN**) Cg2 is the centroid of the imidazole ring N20-C24, Cg3 is the centroid of the benzene ring C7-C12, Cg4 is the centroid of the benzene ring C13-C18, Cg6 is the centroid of the imidazole ring N44-C48, Cg8 is the centroid of the benzene ring C37-C42, Symmetry codes (**L11a**): (i) x,y-1,z, (ii) 1-x,1-y,1-z, (iii) 1/2+x,1/2-y,z-1/2, (iv) 1+x,y,z, (v) 1/2-x,1/2+y,1/2-z, (vi) 3/2-x,1/2+y,1/2-z, (vii) x,-1+y,z, (viii) x,y,z, (ix) 1-x,-y,1-z, (**L11b**): (i) x-1/2,1/2-y,1-z, (ii) x-1,y,z, (iii) 1/2-x,y-1/2,z, (iv) -x,y-1/2,1/2-z, (v) x-1/2,y,1/2-z, (vi) 1+x,y,z; (**MIDJEPLN**): (i) x-1,y,z, (ii) 1/2-x,y-1/2,z, (iii) x-1/2,y,3/2-z, (iv) 3/2-x,y-1/2,z, (v) 1-x,y-1/2,3/2-z, (vi) x-1/2,1/2-y,1-z, (vii) 1+x,y,z; **L12:** Symmetry codes: **(L12a1):** (i) 1-x,-y,1-z, (ii) 1-x,1/2+y,3/2-z, (iii) x-1,1/2-y,z-3/2, (iv) 1+x,1/2-y,3/2+z, (v) -x,1-y,-z; **(L12a2):** (i) -x,y-1/2,-z-1/2, (ii) 1+x,1/2-y,3/2+z, (iii) x-1,1/2-y,z-3/2, **(L12b):** (i) 2-x,y-1/2,1/2-z, (ii) x-1,3/2-y,z-1/2.

Table S2: *Hydrogen bonding parameters for* ***MC1***, ***MC2***, ***MC2-a***, ***MC2-b1***, ***MC2-b2***, ***CP1***, ***CP2***, ***CP2-a***, ***CP3***, *and* ***CP3-a***.

Compound	D-H···A	H···A (Å)	D···A (Å)	D-H-A (°)
MC1	C16-H16···Cl1^{i}	2.957	3.893(3)	169
	C6-H6B···Cl2^{ii}	2.671	3.612(4)	159
	C21-H21···Cg3^{iii}	2.88	3.639(4)	137
MC2	C18-H18A···N1^{i}	2.775	3.566(6)	137
	C27-H27B···N19^{ii}	2.80	3.76(1)	167
	C27-H27B···N21^{ii}	2.845	3.47(2)	122
	C14-H14···N25	2.81	3.54(1)	134
	C17-H17···N25^{iii}	2.785	3.65(1)	152
	C14-H14···Cl25^{iv}	2.89	3.535(5)	126
	C4-H4···Cl26^{v}	2.96	3.762(5)	143
	C12-H12···Cl26^{vi}	2.99	3.676(5)	130

	C23-H23···Cl26^{vi}	2.97	3.794(5)	145
	C27-H27B···Cg2^{ii}	2.56	3.390(15)	143
	C5-H5-Cg4^{vii}	2.96	3.640(5)	130
	C6-H6B···Cg4^{v}	2.80	3.471(5)	126
MC2-a	C18-H18A···N1^{i}	2.793	3.711(4)	154
	C14-H14···Cl25^{ii}	2.79	3.553(3)	138
	C24-H24B···Cl25^{ii}	2.80	3.712(3)	155
	C4-H4···Cl26^{iii}	2.63	3.516(3)	155
	C18-H18A···Cg1^{i}	2.82	3.433(3)	121
	C5-H5-Cg4^{iv}	2.88	3.452(3)	119
	C6-H6B···Cg4^{iii}	2.79	3.627(3)	142
MC2-b1	C4-H4···Cl25^{i}	2.72	3.51(1)	141
	C7-H7B···Cl25^{i}	2.89	3.612(6)	130
	C18-H18B···Cl25^{ii}	2.76	3.684(5)	155
	C22-H22···Cl25^{iii}	2.74	3.466(5)	134
	C7-H7B···Cl26^{i}	2.97	3.852(6)	148
	C15-H15···Cl26^{iv}	2.95	3.560(5)	123
	C18-H18A···Cl26^{ii}	2.95	3.596(5)	124
	C6-H6B···Cg3^{v}	2.86	3.536(15)	127
MC2-b2	C6A-H6AB···N1A^{i}	2.92	3.84(3)	157
	C7-H7B···Cl25^{i}	2.89	3.612(6)	130
	C18-H18B···Cl25^{ii}	2.76	3.684(5)	155
	C22-H22···Cl25^{iii}	2.74	3.466(5)	134
	C7-H7B···Cl26^{i}	2.97	3.852(6)	148
	C15-H15···Cl26^{iv}	2.95	3.560(5)	123
	C18-H18A···Cl26^{ii}	2.95	3.596(5)	124
	C6A-H6AA···Cl26^{iv}	2.84	3.80(2)	166
	C6A-H6AB···Cg1^{i}	2.93	3.70(2)	136
	C4A-H4A···Cg3^{v}	3.00	3.576(18)	121
CP1	C19-H19B···Cl26^{i}	2.91	3.883(3)	174
	C19-H19C···Cl26^{ii}	2.89	3.833(3)	162
	C20-H20A···Cl26^{i}	2.74	3.719(3)	172
	C6-H6···Cl27^{iii}	2.98	3.806(3)	147
	C7-H7A···Cl27^{iv}	2.89	3.756(3)	148
	C7-H7B···Cl27^{iv}	2.90	3.417(3)	114
	C8-H8A···Cl27^{ii}	2.81	3.729(3)	155
	C16-H16···Cg3^{v}	2.98	3.715(3)	136
	C11-H11···Cg5^{iii}	2.82	3.509(3)	130
CP2	C10-H10··· N15^{i}	2.885	3.719	147
	C12-H12··· N15	2.81	3.657	150
	C7-H7B···Cl13^{ii}	2.74	3.681(3)	160
	C6-H6A···Cl14^{iii}	2.93	3.700	136
CP2-a	C6-H6C···Cl13^{i}	2.842	3.57(1)	131.5
	C7-H7B···Cl13^{i}	2.99	3.83(1)	143
	C21-H21A···Cl13^{ii}	2.918	3.69(1)	135
	C20-H20A···Cl14^{iii}	2.903	3.86(2)	167
	C21-H21A···C14^{ii}	2.996	3.89(2)	151

	C20-H20B···Cg5^{iv}	2.81	3.4782(5)	126
CP3	C5-H5···O18^{i}	2.935	3.702	139
	C17-H7A···O18^{i}	2.303	3.124	141
	O18-H18B···N15	2.161	2.89	140
	C10-H10··· N15^{ii}	2.981	3.804	146
	C12-H12··· N15	2.879	3.722	148
	C7-H7B···Cl13^{iii}	2.842	3.794	162
	C6-H6A···Cl13^{iv}	2.882	3.801	111
	C6-H6C···Cl14^{v}	2.890	3.503	121
CP3-a	C4-H4···Cl13^{i}	2.957	3.78(1)	146
	C6-H6A···Cl13^{ii}	2.872	3.82(1)	162
	C7-H7B···Cl13^{iii}	2.825	3.61(1)	137
	C5-H5···Cg2^{iv}	2.881	3.595(12)	133
	C6-H6C···Cg2^{v}	2.81	3.625(12)	141

(MC1) Cg3 is the centroid of the benzene ring C7-C12; **(MC2)** Cg2 is the centroid of the imidazole ring N19-C23, Cg4 is the centroid of the benzene ring C11-C16, **(MC2-a)** Cg1 is the centroid of the imidazole ring N1-C5, Cg4 is the centroid of the benzene ring C11-C16, **(MC2-b1)** Cg3 is the centroid of the benzene ring C8-C17**, (MC2-b2)** Cg1 is the centroid of the imidazole ring N1A-C5A**,** Cg3 is the centroid of the benzene ring C8-C17**, (CP1)** Cg3 is the centroid of the benzene ring C9-C13, Cg5 is the centroid of the benzene ring C21-C25, **(CP2-a)** Cg5 is the centroid of the benzene ring C22-C26, **(CP3-a)** Cg2 is the centroid of the benzene ring C8-C12; **Symmetry codes (MC1)**: (i) 1-x,y,1/2-z, (ii) -1-x,y,3/2-z, (iii) 1/2-x,-1/2+y,1/2-z; **(MC2)**: (i) x-1,1/2-y,1/2+z, (ii) -x,1-y,1-z, (iii) 1-x,1-y,1-z, (iv) 2-x,1-y,1-z, (v) x,1/2-y,1/2+z, (vi) x-1,1/2-y,1/2+z, (vii) 1+x,y,z ; **(MC2-a)**: (i) x-1,1/2-y,1/2+z, (ii) 2-x,1-y,1-z, (iii) x,1/2-y,1/2+z, (iv) 1+x,y,z; **(MC2-b1)**: (i) -x,-y,1-z, (ii) x,1+y,-1+z, (iii) 1+x,1+y,-1+z, (iv) 1-x,-y,1-z, (v) -x,1-y,1-z; **(MC2-b2)**: (i) -x,-y,1-z, (ii) x,1+y,-1+z, (iii) 1+x,1+y,-1+z, (iv) 1-x,-y,1-z, (v) -x,1-y,1-z; **(CP1)**: (i) 1-x,y,1/2-z, (ii) x,1-y,1/2+z, (iii) 1/2-x,1/2+y,z, (iv) 1/2-x,1/2-y,1/2+z, (v) 1/2+x,1/2-y,1-z; **(CP2)**: (i) -x,1/2+y,2-z, (ii) 1-x,1/2+y,1-z, (iii) x-1,y,z; **(CP2-a)**: (i) x,3/2-y,z-1/2, (ii) 1-x,1-y,1-z, (iii) x,1/2-y,z-1/2, (iv) x,1/2-y,1/2+z; **(CP3)**: (i) 1+x,y,z, (ii) -x,1/2+y,2-z, (iii) 1-x,1/2+y,1-z, (iv) x,1/2-y,z, (v) x-1,y,z; **(CP3-a)**: (i) 1-x,1-y,1-z, (ii) 3/2-x, y-1/2, z, (iii) x,1-y,-1/2+z, (iv) -1/2+x,1/2-y,1-z, (v) 1/2+x,1/2-y,1-z.

Table S3: *π-π interactions present in the crystal structures of **MC3**, **MC4**, **MC5**, **MC10**, **MC10-a** and **MC11**.*

Compound	Cg—Cg	Cg—Cg (Å)	Symmetry operator
MC3	Cg3—Cg3	3.7469(10)	2-*x*,1-*y*,1-*z*
	Cg4—Cg4	3.8646(8)	1-*x*,1-*y*,-*z*
	Cg4—Cg5	3.7558(8)	1-*x*,1-*y*,-*z*
	Cg5—Cg6	3.7894(9)	1-*x*,1-*y*,-*z*
MC4	Cg1—Cg1	3.5052(14)	1-*x*,-*y*,-*z*
	Cg1—Cg3	3.4130(14)	1-*x*,-*y*,-*z*
	Cg4—Cg5	3.8514(13)	1-*x*,1-*y*,-*z*
	Cg5—Cg5	3.7858(12)	1-*x*,1-*y*,-*z*
	Cg7—Cg7	3.6200(15)	1-*x*,1-*y*,1-*z*
MC5	Cg2—Cg7	3.7448(18)	*x*,1-*y*,2-*z*
	Cg4—Cg6	3.4998(18)	*x*,1-*y*,2-*z*
	Cg6—Cg6	3.852(2)	*x*,1-*y*,2-*z*
MC10	Cg1—Cg1	3.7599(13)	-x,1-y,-z
	Cg1—Cg3	3.5509(13)	-x,1-y,-z
	Cg2—Cg2	3.7050(17)	2-x,1-y,1-z
	Cg2—Cg6	3.5947(19)	2-x,1-y,1-z
MC10-a	Cg1—Cg1	3.968(2)	2-*x*,1-*y*,2-*z*
	Cg1—Cg3	3.664(2)	2-*x*,1-*y*,2-*z*

	Cg2—Cg2 Cg2—Cg6	3.695(2) 3.610(2)	-*x*,-*y*,1-*z* -*x*,-*y*,1-*z*
MC11	Cg1—Cg3 Cg2—Cg2 Cg2—Cg6	3.5360(9) 3.7395(8) 3.5992(9)	1-*x*,-*y*,1-*z* -*x*,2-*y*,-*z* -*x*,2-*y*,-*z*

MC3: Cg3 (C4-C9), Cg4 (C11-C20), Cg5 (C12-C17), Cg6 (C19-C24); **MC4:** Cg1 (N1-C5), Cg3 (C4-C9), Cg4 (C11-C20), Cg5 (C12-C17), Cg7 (C29-C34) ; **MC5:** Cg2 (N27-C31), Cg4 (C12-C21), Cg6 (C20-C25), Cg7 (C30-C35); **MC10:** Cg1 (N1-C5), Cg2 (N24-C28), Cg3 (C4-C9), Cg6 (C27-C32); **MC10-a:** Cg1 (N1-C5), Cg2 (N24-C28), Cg3 (C4-C9), Cg6 (C27-C32); **MC11:** Cg1 (N1-C5), Cg2(N25-C29), Cg3 (C4-C9), Cg6 (C28-C33).

- Structural data relating to the final refinement of all single-crystal structures elucidated in this manuscript is provided separately along with the thesis. Included files are '.hkl', '.RES' and the Crystallographic Information File (.CIF) along with checkcif reports.